Transport and Non-Equilibrium Dynamics in Optical Lattices

from Expanding Atomic Clouds to Negative Absolute Temperatures

Inaugural-Dissertation

zur

Erlangung des Doktorgrades

der Mathematisch-Naturwissenschaftlichen Fakultät

der Universität zu Köln

vorgelegt von

Stephan Mandt

aus Köln

Köln 2012

Berichterstatter: Prof. Dr. Achim Rosch
Prof. Dr. Alexander Altland
Prof. Dr. Ralf Schützhold

Tag der mündlichen Prüfung: 16.5.2012

Kurzzusammenfassung

Transporteigenschaften und Nichtgleichgewicht in stark korrelierten Materialien sind für gewöhnlich schwer zu berechnen. Dies gilt sogar für minimalistische Modelle dieser Systeme wie das fermionische Hubbard Modell.

Ultrakalte Atome in optischen Gittern ermöglichen eine alternative Realisierung des Hubbard Modells und haben den Vorteil, frei von zusätzlichen Komplikationen wie Phononen, Gitterdefekten oder Verunreinigungen zu sein. Auf diese Weise können kalte Atome als *Quantensimulatoren* stark korrelierter Materialien fungieren. Wir zeigen jedoch, dass sich kalte Atome in optischen Gittern als thermisch isolierte Systeme auch sehr *anders* als Festkörper verhalten können und eine Fülle neuer dynamischer Effekte aufweisen.

In dieser Doktorarbeit werden mehrere Nichtgleichgewichtsprozesse mit fermionischen Atomen in optischen Gittern vorgestellt. Als erstes untersuchen wir die Expansion einer anfänglich gefangenen atomaren Wolke im untersten Band eines optischen Gitters. Während nichtwechselwirkende Atome ballistisch expandieren, expandiert die Wolke in Anwesenheit von Wechselwirkung mit einer drastisch reduzierten Geschwindigkeit. Markanterweise ist die Expansionsgeschwindigkeit unabhängig vom attraktiven oder repulsiven Charakter der Wechselwirkung, was eine neue dynamische Symmetrie des Hubbard Modells aufzeigt.

In einem zweiten Projekt diskutieren wir die Möglichkeit der Realisierung negativer absoluter Temperaturen in optischen Gittern. Negative absolute Temperaturen beschreiben Gleichgewichtszustände mit invertierter Besetzung der Energieniveaus. Hier schlagen wir einen dynamischen Prozess zur Umsetzung equilibrierter Fermionen bei negativen Temperaturen vor und untersuchen die Zeitskalen der globalen Relaxation ins Gleichgewicht, die mit der Umverteilung von Energie und Teilchen durch langsame Diffusionsprozesse verbunden sind.

Wir zeigen, dass Energieerhaltung einen großen Einfluss auf die Dynamik einer wechselwirkenden atomaren Wolke in einem optischen Gitter hat, die einem zusätzlichen schwachen linearen (Gravitations-)Potential ausgesetzt ist. Anstelle "herunterzufallen" diffundiert die Wolke symmetrisch im Gravitationspotential aufwärts und abwärts. Des Weiteren zeigen wir analytisch, dass der Radius R mit der Zeit t gemäß $R \sim t^{1/3}$ anwächst, was konsistent mit numerischen Simulationen der Boltzmanngleichung ist.

Abschließend untersuchen wir die Dämpfung von Bloch-Oszillationen durch Wechselwirkung. Für ein homogenes System diskutieren wir die Möglichkeit, die Dynamik des Teilchenstroms auf eine klassische gedämpfte harmonische Oszillatorgleichung abzubilden, wodurch wir eine analytische Erklärung für den Übergang von schwach gedämpften zu überdämpften Bloch-Oszillationen geben. Wir zeigen analytisch, dass die Dynamik einer stark Bloch-oszillierenden und schwach gedämpften, wechselwirkenden atomaren Wolke durch eine neuartige "stroboskopische" Diffusionsgleichung beschrieben werden kann. In dieser Näherung wächst der Wolkenradius R asymptotisch in der Zeit t gemäß $R \sim t^{1/5}$ an.

Abstract

Transport properties and nonequilibrium dynamics in strongly correlated materials are typically difficult to calculate. This holds true even for minimalistic model Hamiltonians of these systems, such as the fermionic Hubbard model.

Ultracold atoms in optical lattices enable an alternative realization of the Hubbard model and have the advantage of being free of additional complications such as phonons, lattice defects or impurities. This way, cold atoms can be used as *quantum simulators* of strongly interacting materials. Being thermally isolated systems, however, we show that cold atoms in optical lattices can also behave very *differently* from solids and can show a plethora of novel dynamic effects.

In this thesis, several out-of equilibrium processes involving interacting fermionic atoms in optical lattices are presented. We first analyze the expansion dynamics of an initially confined atomic cloud in the lowest band of an optical lattice. While non-interacting atoms expand ballistically, the cloud expands with a dramatically reduced velocity in the presence of interactions. Most prominently, the expansion velocity is independent of the attractive or repulsive character of the interactions, highlighting a novel dynamic symmetry of the Hubbard model.

In a second project, we discuss the possibility of realizing negative absolute temperatures in optical lattices. Negative absolute temperatures characterize equilibrium states with an inverted occupation of energy levels. Here, we propose a dynamical process to realize equilibrated Fermions at negative temperatures and analyze the time scales of global relaxation to equilibrium, which are associated with a redistribution of energy and particles by slow diffusive processes.

We show that energy conservation has a major impact on the dynamics of an interacting cloud in an optical lattice, which is exposed to an additional weak linear (gravitational) potential. Instead of ‘falling downwards‘, the cloud diffuses symmetrically upwards and downwards in the gravitational potential. Furthermore, we show analytically that the radius R grows with the time t according to $R \sim t^{1/3}$, consistent with numerical simulations of the Boltzmann equation.

Finally, we analyze the damping of Bloch oscillations by interactions. For a homogeneous system, we discuss the possibility of mapping the dynamics of the particle current to a classical damped harmonic oscillator equation, thereby giving an analytic explanation for the transition from weakly damped to over-damped Bloch oscillations. We show that the dynamics of a strongly Bloch oscillating and weakly interacting atomic cloud can be discribed in terms of a novel effective “stroboscopic” diffusion equation. In this approximation, the cloud’s radius R grows asymptotically in time t according to $R \sim t^{1/5}$.

Contents

0 General Introduction 1

1 Fundamentals 5
1.1 Introduction to ultracold atoms . . . 5
1.1.1 Scattering . . . 5
1.1.2 Feshbach resonances . . . 6
1.1.3 Optical potentials . . . 8
1.2 Modeling cold atoms in optical lattices . . . 12
1.2.1 Band theory . . . 12
1.2.2 Tight-binding approximation . . . 12
1.2.3 Hubbard model . . . 13
1.3 Transport theory . . . 15
1.3.1 Introduction . . . 15
1.3.2 The semiclassical picture . . . 15
1.3.3 Elementary transport theory . . . 16
1.3.4 Introduction to Boltzmann formalism . . . 17
1.3.5 Relaxation-time approximation . . . 18
1.3.6 Umklapp scattering . . . 19
1.3.7 Full Boltzmann equation . . . 20
1.3.8 Linearized Boltzmann equation . . . 21
1.3.9 Variational principle . . . 22
1.3.10 Physical interpretation of the variational principle . . . 23
1.3.11 Variational ansatz and solution . . . 24

2 Hydrodynamics and the Boltzmann equation 27
2.1 Introduction . . . 27
2.2 Relaxation-time approximation for an isolated system . . . 28
2.3 Numerical Boltzmann simulations . . . 29
2.4 Transport scattering rate . . . 31
2.4.1 Definition of the transport scattering rate . . . 31
2.4.2 Variational conductivity of the Hubbard model . . . 32
2.5 From Boltzmann to hydrodynamics . . . 36
2.5.1 Formal derivation . . . 36
2.5.2 General case . . . 37
2.5.3 High temperature expansion . . . 38

3 Fermionic transport in a homogeneous Hubbard model 41
3.1 Introduction 41
3.2 Experiment 43
3.3 Non-interacting case 43
  3.3.1 Free expansion rate 43
  3.3.2 Minimal model of free expansion 45
  3.3.3 Lattice inhomogeneities 46
3.4 Interacting case 47
  3.4.1 Experimental observation 47
  3.4.2 Theoretical interpretation 47
3.5 Numerical simulations 49
  3.5.1 Geometry 49
  3.5.2 Adjusting initial parameters 50
3.6 Comparison of numerical and experimental data 51
  3.6.1 Expansion velocities 51
  3.6.2 Momentum distribution 52
3.7 Dynamic symmetry of the Hubbard model 52
3.8 Nonlinear diffusion equation 55
  3.8.1 Validity of hydrodynamics 55
  3.8.2 Fast diffusion equation 56
  3.8.3 Scaling solutions 57
  3.8.4 Universal particle loss rate 57
  3.8.5 Interplay of the diffusive and ballistic regime 60
3.9 Discrepancies between theory and experiment 62
3.10 Summary and outlook 64

4 Equilibration rates and negative absolute temperatures 65
4.1 Introduction 65
4.2 Qualitative discussion 66
  4.2.1 General properties of negative temperatures 66
  4.2.2 Negative temperatures in the Hubbard model 68
  4.2.3 Proposed scheme of realizing $T < 0$ 69
4.3 Quantitative analysis 70
  4.3.1 Numerical simulations 70
  4.3.2 Instantaneous quench 70
  4.3.3 Time scales of global equilibration 71
  4.3.4 Continuous ramping and adiabaticity 73
4.4 Summary 75

5 Symmetric expansion in a gravitational potential 77
5.1 Introduction 77
5.2 Qualitative discussion 79
5.3 Numerical analysis 80
5.4 Hydrodynamic theory 81
5.5 Analytic solution of the hydrodynamic equations 83
  5.5.1 Scaling ansatz 83
  5.5.2 Particle number continuity 85
  5.5.3 Energy continuity equation 86
  5.5.4 Formulas for the scaling functions 87

5.5.5 Comparison of the analytical and numerical results 90
5.6 Summary and outlook 90

6 Damping of Bloch oscillations and stroboscopic diffusion 93
6.1 Introduction 93
6.2 Two perturbative limits for the homogeneous system 94
6.2.1 Over-damped Bloch oscillations 94
6.2.2 Weakly damped Bloch oscillations 96
6.3 Generalized continuity equations 100
6.3.1 Reproducing conventional diffusion 102
6.3.2 Damping of Bloch oscillations and the harmonic oscillator 104
6.3.3 Comparison with Boltzmann simulations 106
6.4 The stroboscopic diffusion equation 110
6.4.1 Introduction 110
6.4.2 Decomposition of the distribution function 112
6.4.3 Relaxation-time approximation 116
6.4.4 Scaling solution 117
6.4.5 Approximate solution of the scaling function 118
6.4.6 Comparison of the analytic and numerical results 119
6.5 Summary and outlook 122

7 Summary 125

A Fundamentals and Method 127
A.1 Variational principle 127
A.2 Stability analysis of the Boltzmann equation 128

B Expansion in a homogeneous lattice 129
B.1 Effects of the laser beam curvature 129
B.2 Validity of the diffusion equation 131
B.3 Geometric interpretation of the universal loss rate 132

C Negative absolute temperatures in optical lattices 135
C.1 Final temperatures, two limiting cases 135

D Expansion in a gravitational potential 137
D.1 Short time dynamics 137
D.2 Scaling analysis of the energy continuity equation 138

E Damping of Bloch oscillations 141
E.1 Linearized collision integral 141
E.2 Damping of the particle current 142
E.3 Oscillatory integrals 144

Bibliography 146

Danksagung 155

0

General Introduction

"I want to talk about the possibility that there is to be an *exact* simulation, that the computer will do *exactly* the same as nature" - with these words, Richard Feynman promoted his idea of quantum simulation. He suggested to try to build a quantum mechanical machine - a quantum computer - that would help to simulate and understand *all* other, more complicated quantum systems [1]. Since Feynman promoted his idea in the 1980ies, the construction of such a quantum computer is still not within reach. However, physicists are currently exploring different options for a physical realization, and ideas range from quantum dots and novel topological materials to trapped ions and neutral atoms.

Why is it so difficult to simulate a quantum system on a *classical*, i.e. conventional computer? Typically, the computational costs for an *exact* simulation of a quantum system increase exponentially with the number of involved particles. This applies in particular e.g. to simulating the dynamics of *interacting* quantum systems, whose properties can not be reduced to the properties of individual particles. As nowadays, both classical and quantum computation fail in many respects, it is highly desirable to explore alternative, more direct ways of simulating these systems. This is of great interest for modern condensed matter physics, where many effects such as high temperature superconductivity or quantum magnetism are *collective* phenomena and require a *large* number of particles.

Instead of trying to construct a universal machine that allows to study *all* other systems, there is a modern field of research that tries to explore a different path: designing simpler quantum systems to model *specific* more complex systems, such as strongly interacting materials. This is the field of quantum simulation with ultracold atoms. Cold atoms in optical lattices consist of neutral atoms that are trapped in the light of an interfering laser beam. The intensity pattern of the laser forms a lattice structure in space, in which the atoms are confined by an effective electromagnetic interaction. Also interactions *between* the atoms can be induced in a controlled way. This artificial system of atoms confined to a "crystal of light" resembles a crystalline solid, where the ultracold atoms play the role of the lattice electrons. This way, condensed matter systems can be imitated with ultracold atoms. The artificial solids can be used to examine many aspects of condensed matter theory, such as exploring phase diagrams and extracting thermodynamic quantities or - as done in the context of this thesis - transport properties.

Exploring condensed matter physics indirectly with cold atoms may answer long-standing questions, such as the question if certain minimalistic models for strongly correlated materials, such as the two-dimensional Hubbard model, suffice to explain the emergence of high temperature superconductivity. Recently, a Mott insulator has been realized with fermionic ultracold atoms, which mimics the insulating behavior of strongly repulsive electrons in certain materials [2,3]. Among many other examples, also the phenomena of Anderson localization [4], gauge fields [5], and the analog of vortices in superconductors [6] have been transfered from the condensed-matter world to the field of cold atoms. But not only realizing equilibrium phases of condensed matter physics is feasible with cold atoms: they also have a special potential to address problems far from thermal equilibrium. While electrons tunnel between the the sites of an atomic lattice within femtoseconds which is very difficult to resolve, atoms tunnel between the optical lattice sites typically within milli-seconds, which makes the direct observation of the collective dynamics experimentally possible. This way, old unsolved problems involving non-equilibrium dynamics in condensed matter systems can be explored in a new way.

There is an overall increasing interest in understanding non-equilibrium quantum systems for various reasons. Parts of the motivation came from the possibility of studying the transport through mesoscopic devices such as quantum dots, which are also theoretically accessible due to their reduced spatial dimensionality. For some of these systems, it has been recently claimed that they are *exactly* solvable by the Bethe ansatz [7]. Apart from that, transport through quantum dots can also be studied in the Kondo regime, which has been addressed analytically using non-equilibrium versions of the renormalization group approach [8,9]. For bulk electronic transport, one has been mostly interested in the linear response regime in the previous decades, exemplified by calculating the electronic or thermal conductivity. More recently, new sorts of experiments such as pump and probe spectroscopy have also changed this focus. In this novel kind of measurement, the electrons are excited locally, and it is even possible to observe the relaxation of those electrons to equilibrium, which happens on the time scale of femtoseconds. In addition to pump and probe spectroscopy, far-from-equilibrium electronic transport in strongly correlated solids plays a role in the context of breaking the Mott insulating state by strong electric fields [10,11]. Understanding and predicting non-equilibrium transport through those materials may open the possibility of building novel, promising electronic devices.

Apart from the possibility of *simulating* non-equilibrium processes with cold atoms, they are already very interesting systems in their own right, *especially* in the field of quantum non-equilibrium dynamics. Ultracold atoms in optical lattices have enriched this field in many respects. One of the first and most prominent non-equilibrium experiment with ultracold atoms has been the quench from the Mott insulating state to a superfluid state for interacting bosonic atoms in optical lattices. It has been observed that the superfluid order parameter periodically collapses and revives after the quench, until its dynamics gets washed out by damping and decoherence [12]. This experiment has inspired much theoretical research on quenches through a quantum phase transition. Especially, the dynamics of thermalization after a quantum quench are a topic of growing theoretical interest due to the relevance in the field of ultracold atoms: for many practical purposes, non-adiabatic manipulations on a trapped cloud of atoms are unavoidable in experiment. Hence it is important for experimentalists to know when the system has reached a thermal state, or how slow they have to change magnetic fields or laser intensities in order to avoid excitations in the gas of atoms. It has been also demonstrated experimentally with cold atoms that certain integrable systems seem to show no tendency of equilibration at all, such as one-dimensional tubes of hard-core bosons [13]. Integrability and thermalization has been since a very active field of theoretical research.

This thesis especially focuses on the out of equilibrium dynamics that is related to fermionic quantum transport. However, one of the main messages of this thesis is that instead of showing the analogue effects of condensed matter systems, ultracold atoms show very *different* dynamics, parts of the reason being the strict conservation of energy. Dissipation occurs only due inter-particle scattering processes with momentum transfer to the lattice, so-called umklapp processes. In condensed matter systems, these umklapp processes are known to give an important contribution the thermal resistivity in crystals, but they can also contribute significantly to the electronic conductivity.

The thesis is organized as follows. In chapter 1, we give a brief introduction to the basics of ultracold atoms and their description in terms of the fermionic Hubbard model. We also give a more extensive review of transport theory and the Boltzmann equation, with special emphasis on the variational method of approximating its solution. In chapter 2, we introduce the numerical and analytic tools that we use to study several non-equilibrium processes involving driven ultracold fermionic atoms. First, we describe our numerical variant of solving the Boltzmann equation which is based on a variational estimate of the conductivity of the Hubbard model. We then derive coupled diffusion equations for the energy and particle density that are valid at high temperatures. These and other methods are then practically applied in chapters 3 - 6. In chapter 3, we review a joint theoretical-experimental project where the expansion of a fermionic cloud in a homogeneous Hubbard model was studied. Interactions modify the expansion velocity of the cloud strongly, but in a way *independent* of the repulsive or attractive character of interactions, revealing a novel dynamic symmetry of the Hubbard model. In chapter 4 we propose and quantitatively model the time scales, on which states at negative absolute temperatures, i.e. equilibrium states with an inverted occupation of energy levels, can be realized in optical lattices. We also propose a dynamical scheme to realize lower negative temperatures and estimate the time scales to reach those temperatures. In chapter 5, we study the dynamics of a finite cloud of atoms in an optical lattice with an additional linear potential, as realized by gravity. Here, we study the regime of a small potential gradient, such that the cloud is only weakly driven out of equilibrium. We find that energy conservation affects the dynamics of the cloud drastically: the cloud expands symmetrically upwards and downwards the gravitational potential, and the cloud's radius R grows sub-diffusively in time t according to $R \sim t^{1/3}$. Finally, in chapter 6, we study the damping of Bloch oscillations that emerge in tilted lattice systems. For a homogeneous system, we show a limit where the system's dynamics can be systematically mapped to a classical damped harmonic oscillator equation, giving an analytical explanation for the transition from weakly damped to over-damped Bloch oscillations by increasing the interaction strength. We also analyze the situation of a finite cloud in a tilted optical lattice that we studied in chapter 5, but we now consider the regime, where Bloch oscillations are only weakly damped and the system is in a state far from thermodynamic equilibrium. Here, we find that the cloud expands according to the scaling law $R \sim t^{1/5}$ by deriving an effective, “stroboscopic” diffusion equation for the clouds dynamics on top of its rapid oscillatory movement.

1

Fundamentals

1.1 Introduction to ultracold atoms

The notion of ultracold atom systems usually refers to a new field of research in atomic physics, where interactions and coherence between atoms and molecules is in the focus of research, rather than their individual microscopic properties [14]. Being cooled to unprecedently low temperatures, collective quantum states of matter have been realized both with bosonic and fermionic atoms, which also had an enormous influence on theoretical research in condensed matter physics.

Cold atoms in optical lattices consist of neutral atoms that are trapped in the light of an interfering laser beam. The intensity pattern of the laser forms a lattice structure, in which the atoms are confined by an effective electromagnetic interaction. Interactions *between* the atoms can be induced by the use of Feshbach resonances, as will be explained below. This artificial system of atoms confined to a crystal of light resembles a crystalline solid, where the ultracold atoms play the role of the lattice electrons.

This introductory chapter reviews some facts and tools that are used to describe cold atomic systems in optical lattices or realize them in experiment, respectively. Here, we largely follow the review article by Bloch, Dalibard and Zwerger [14] as well as the book of Ashcroft and Mermin [15] with experimental inputs from the PhD thesis of Ulrich Schneider [16].

1.1.1 Scattering

Let us start our introductory chapter by reviewing the basics of *scattering* among ultracold atoms, which is a necessary requirement to understand the emergence of strong correlations in these systems. Collisions of two atoms in the quantum regime do in priori include scattering processes in states at finite relative angular momentum. In order to scatter in these states, the incoming states need to have enough energy to surmount a centrifugal barrier, which is given by the quantized angular momentum of the final state. The characteristic energy of this barrier usually corresponds to a temperature in the milli-Kelvin regime for the typical atomic masses that are used in experiment [14]. Below that temperature, only s-wave scattering processes are possible. This temperature regime *defines* the regime of ultracold collisions, relevant for our studies.

Throughout this thesis, we will be interested in the physics of *fermionic* atoms. Due to Pauli's exclusion principle, one needs a mixture of fermions which are in different internal states to allow for ultracold collisions, exemplified by a "spin"-mixture of fermionic atoms in two different hyperfine states, as is studied in this thesis. Alternatively, one can also use a mixture of bosonic and fermionic atoms to allow for scattering.

The scattering two-body wave function for s-wave collisions does not depend on the scattering angle, and it can be described by the following ansatz:

$$\Psi(k,t) \approx e^{i\,kz} + \frac{f(k)}{r} e^{ikr} \tag{1.1}$$

The first term describes the incoming state, which is assumed to be a plane wave in z-direction. The outgoing state is rotationally invariant around the scattering center at the origin and is determined by the momentum-dependend function $f(k)$. In the regime of ultracold collisions and for very small momenta k, this function assumes the form [14, 17]

$$f(k) \approx \frac{-a}{1+ika} \tag{1.2}$$

The parameter a that characterizes this function uniquely is called the *s-wave scattering length*. For a trapped interacting quantum gas in absence of an optical lattice, the scattering length is the relevant parameter that characterizes the interaction strength. It yet has also another important meaning: In most cases, a realistic two-body interaction potential can be approximated by a contact interaction potential

$$V(\mathbf{r}) = \frac{4\pi\hbar^2\, a}{m} \delta(\mathbf{r}) \tag{1.3}$$

such that the low energy scattering properties are still the same (m is the atomic mass) [14, 16]. Note that the limit $a \to \infty$ the scattering function $f(k) \to i/k$ becomes independent of the scattering length. This limit is called the *unitary limit*, and it has been largely explored theoretically and experimentally, as the system shows many universal characteristics; for a review see Ref. [18].

1.1.2 Feshbach resonances

The use of Feshbach resonances allowed experimentalists to increase the scattering lengths for attractive and repulsive interactions drastically; hence they have revolutionized the field of ultracold atoms and have paved the way to exploring strongly correlated systems. Feshbach resonances have first been proposed in 1958 [19] in the context of nuclear reactions, where they occur when in a scattering process a compound nucleus is formed and decays. For cold atom systems, Feshbach resonances were first proposed by Tiesinga et al. in 1993 [20] and were first experimentally realized in 1998 by several groups [21–24]. A theoretical review can be found in Ref. [25].

In general, Feshbach resonances occur in scattering problems when in a two-body problem, an *open channel* involving an unbound state is resonantly coupled to a *closed channel*, involving at least one bound state. This situation is depicted in Fig. 1.1. In experiments with cold atoms, these states are often realized by two different hyperfine states of the two-particle wave function, which have different magnetic moments. This has the advantage that the energies of these two states can be shifted relative to each other by varying an external magnetic field. The Feshbach resonance occurs when the bound state's energy coincides with the unbound state's energy. In this case, the scattering length *diverges*, and interactions become very strong. Alternatively, Feshbach resonances can also be induced optically [14].

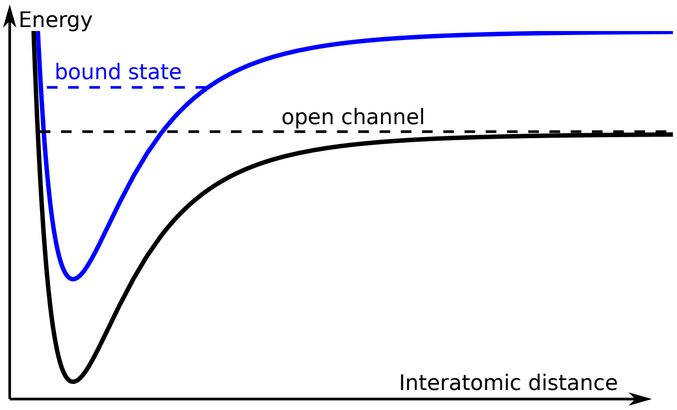

Figure 1.1: Schematic plot of a two-channel picture for a Feshbach resonance. The system is characterized by an open channel (black) which has an unbound state, and a closed channel with a bound state (blue). When the energy of the bound state coincides with the energy of the scattering state of the open channel, a Feshbach resonance occurs. As the two states have different magnetic moments, magnetic fields can be used to tune the resonance.

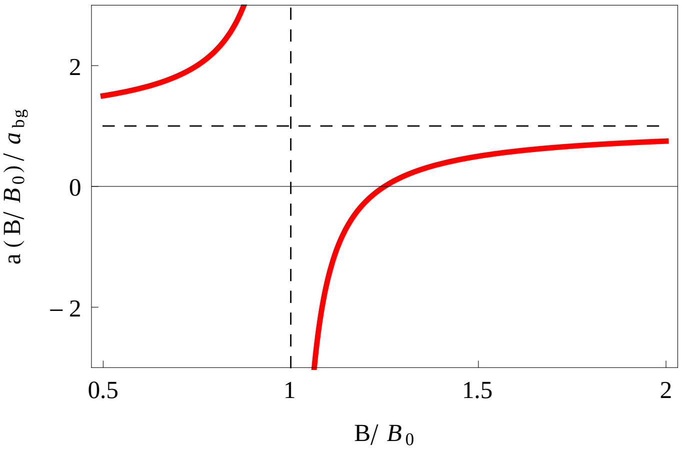

Figure 1.2: Rescaled scattering length a as a function of the magnetic field B. The Feshbach resonance B_0 has a characteristic width ΔB. In typical experiments, Feshbach resonances occur at several hundred Gauss.

On a phenomenological level, the dependence of the scattering length a on the magnetic field B as a tuning parameter is given by [14, 18]

$$a(B) = a_{bg}\left(1 - \frac{\Delta B}{B - B_0}\right) \tag{1.4}$$

The parameters ΔB and B_0 are the width and the position of the resonance, respectively. a_{bg} is the background scattering length, i.e. the scattering length in absence of the resonance. The corresponding plot is shown in Fig. 1.2. If the bound state's energy is slightly below the energy of the open channel, a molecular state exists. This molecular state has a finite extend in position space and grows larger and larger when approaching the Feshbach resonance. As an eigenstate of the Hamiltonian, it must have no overlap with the unbounded scattering states, which are also an eigenstates. This is an intuitive explanation of the fact that the effective interactions are *repulsive* in this case. Conversely, if the energy of the bound state of the closed channel is above the threshold, no molecular state exists and the effective interaction is attractive.

1.1.3 Optical potentials

There are different ways of trapping neutral atoms, the most important ones involve either magnetic or optical traps. In optical traps, neutral atoms are exposed to a spatially varying laser light intensity pattern. For experiments related to strongly interacting systems, they have the huge advantage of not involving external magnetic fields, which are already used to induce the Feshbach resonances. The present section reviews how the interaction between light and atoms is used for the purpose of creaing an almost conservative potential for the atoms, following [14, 26].

An optical potential is created by a laser that creates stationary intensity pattern of light in space:

$$I(\mathbf{r}) = \frac{1}{2}\langle \mathbf{E}(\mathbf{r})^2\rangle \tag{1.5}$$

Here, the brackets denote a time-average over the square of the time-dependent electric field $\mathbf{E}$ that oscillates at the laser frequency ω. We are considering a two-level atom with an atomic ground state $|g\rangle$ and the first excited state $|e\rangle$, which are energetically separated by the atomic transition frequency ω_0. The oscillating electric field induces a polarization $\mathbf{p}$ on the atoms, such that $\mathbf{p} = \alpha\,\mathbf{E}$, involving the atomic polarizability α. It is energetically favorable for the polarized atoms to align with the electric field. Therefore, the atoms feel a potential that is proportional to the light intensity distribution in space:

$$V(\mathbf{r}) = \frac{1}{2}\langle \mathbf{p}\,\mathbf{E}\rangle = \alpha\, I(\mathbf{r}) \tag{1.6}$$

This is already the basic mechanism of optical trapping, but let us review the mechanism in more detail. It can be shown that in the vicinity of the resonance, i.e. for $|\omega - \omega_0| \ll \omega_0$,

$$\alpha(\omega) = \frac{\Gamma}{\omega - \omega_0} \tag{1.7}$$

where $\Gamma \propto \langle e|\hat{d}_{\mathbf{E}}|g\rangle$ is proportional to the matrix element of the polarization operator $\hat{d}_{\mathbf{E}}$ between the ground state and the first excited state in direction of the electric field [26]. Most importantly, the polarizability $\alpha(\omega)$ changes sign at $\omega = \omega_0$. This means that the detuning parameter $\Delta = (\omega - \omega_0)$ decides about whether the optical potential is attractive or repulsive. For $\Delta < 0$, the laser is called *red-detuned*, and the atoms are attracted to the intensity maxima. Conversely, for $\Delta > 0$ the laser is called *blue-detuned*: here, the atoms are attracted to the intensity *minima* of the standing laser wave.

Note that the potential $V(\mathbf{r})$ is strictly speaking not conservative: at long times, atoms get heated up by absorption and spontaneous re-emission of laser photons. One can also show [26] that the rate τ_{heat}^{-1}, at which the atoms heat up, satisfies the proportionality

$$\tau_{\text{heat}}^{-1} \sim \left(\frac{\Gamma}{\Delta}\right)^2 \tag{1.8}$$

The emergence of heating due to photon absorption is an undesired effect: to realize an almost ideal conservative potential, we want to make the heating rate τ_{heat}^{-1} as small as possible. Luckily, this is always possible, because $\tau_{\text{heat}}^{-1} \sim \Delta^{-2}$ decays faster than the effective potential $V(\mathbf{r}) \sim \Delta^{-1}$ upon increasing Δ. Therefore, the laser light frequencies are typically tuned *far from resonance* by choosing a large $|\Delta|$. To conclude, a trapping potential for neutral atoms can be realized by a spatially varying intensity profile of a laser. Yet, the potential is not fully conservative and will lead to heating of the atoms by spontaneous absorption and emmission of photons for long times.

Optical trap

Optical traps are optical potentials that keep the atoms confined in a three-dimensional region in space. Spacially varying intensity profiles naturally emerge due to the finite width of the laser beam, which usually has a Gaussian shape in the radial coordinate r vertial to its propagation,

$$I(r) = I_0 \, e^{-2\,r^2/w_0^2} \tag{1.9}$$

Depending on whether the laser is red or blue detuned, it creates a confining or anticonfining optical potential that is approximately harmonic around the intensity maximum. In the joint theoretical-experimental project on an expanding cloud that will be described later in this thesis, the optical trap is *red-detuned.*

Optical lattices

Optical lattices are optical potentials of a special type. They are created by counterpropagating beams of laser light of the same frequency and polarization that form a standing wave. Their intensity distribution forms a static interference pattern, whose period is given by half the laser wavelength $\lambda/2$. In the context of the expanding cloud to be described later, the optical lattice is *blue-detuned.*

The simplest version of such an optical lattices is created by two counterpropagating laser beams, which results in an intensity profile of the form

$$V(r, z) \approx V_0 \, e^{-2r^2/w_0^2} \sin^2(kz)\,, \tag{1.10}$$

where z is the longitudinal coordinate along the laser beam and r is the vertical coordinate. If the laser intensity is chosen sufficiently strong, the atoms are tightly confined in two-dimensional planes in the direction perpendicular to z. As atoms are also confined in the vertical direction due to the finite width of the laser beam, this construction yields a series of two-dimensional “pancakes”. Adding two counterpropagating beams in a perpendicular

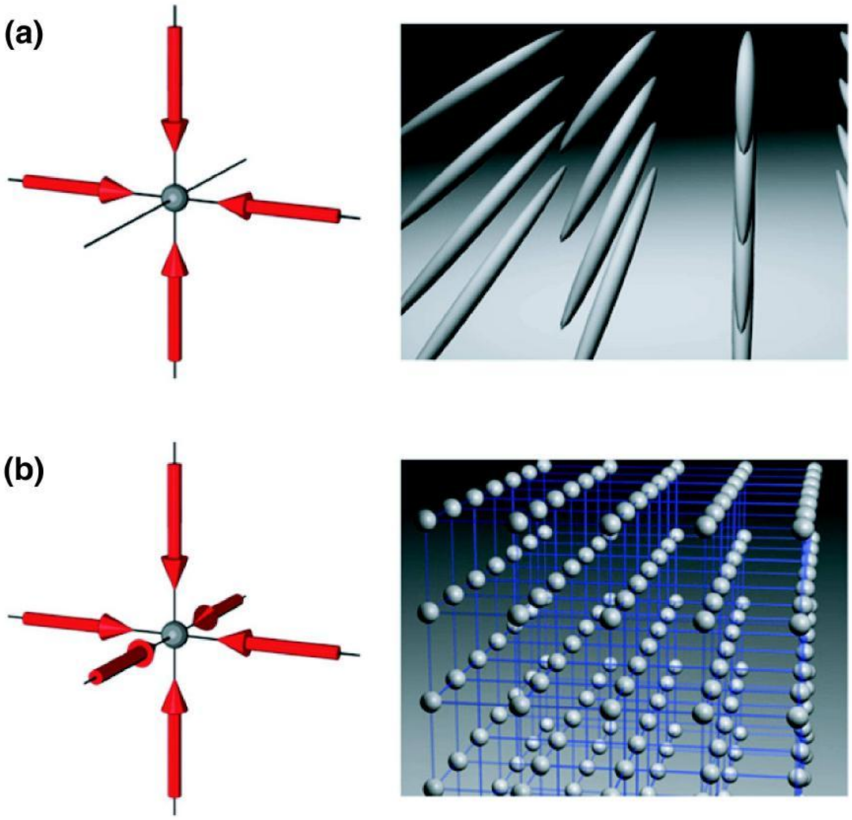

Figure 1.3: Optical potentials created by standing waves of laser light. In the upper panel, an array of one-dimensional quantum wires is created by superimposing two perpendicular standing waves. In the lower panel, a three-dimensional optical lattice is formed by three perpendicular standing waves. Picture taken from [14] (courtesy of I. Bloch).

angle to the original beams yields an array of tubes, each of them being one-dimensional. Here, one wants the orthogonal beams *not* to interfere. Therefore, one chooses slightly different frequencies or orthogonal polarizations. This way, quantum wires of ultracold atoms can be realized. Finally, if counterpropagating beams from all three perpendicular directions are superimposed, a three-dimensional lattice forms. The last two possibilities are depicted in Fig. 1.3. By choosing the laser intensities in z-direction stronger than in the perpendicular directions such that tunnelling in z-direction is completely suppressed, arrays of two-dimensional lattices can be formed.

1.2 Modeling cold atoms in optical lattices

1.2.1 Band theory

One of the hallmarks of condensed matter theory is Bloch's theorem [15] as a general statement about solutions of the Schrödinger equation in periodic potentials $V(\mathbf{r}+\mathbf{R}) = V(\mathbf{r})$ with period $\mathbf{R}$. The eigenstates are labeled by the following quantum numbers: A discrete index n that takes the band number and internal degrees of freedom such as spin into account, and a pseudo-momentum $\mathbf{k}$ that takes values in the first Brillouin zone. The eigenfunctions $\psi_{n,\mathbf{k}}(\mathbf{r})$ of the Schrödinger equation in a periodic potential are called Bloch functions, which can always be decomposed according to

$$\psi_{n,\mathbf{k}}(\mathbf{r}) = e^{i\mathbf{k}\mathbf{r}} u_{n,\mathbf{k}}(\mathbf{r}) \tag{1.11}$$

where the functions $u_{n,\mathbf{k}}$ satisfy $u_{n,\mathbf{k}}(\mathbf{r}+\mathbf{R}) = u_{n,\mathbf{k}}(\mathbf{r})$. The Fourier-transforms of the Bloch-functions are the *Wannier* functions,

$$w_{n,\mathbf{R}}(\mathbf{r}) = \frac{1}{(2\pi)^d} \int d\mathbf{k}\, e^{-i\mathbf{k}\mathbf{R}} \psi_{n,\mathbf{k}}(\mathbf{r}) \tag{1.12}$$

Wannier functions depend only on the relative coordinate $(\mathbf{r}-\mathbf{R})$ with respect to the lattice site $\mathbf{R}$. Importantly, they are also exponentially localized and orthogonal to each other with respect to the site and band index.

Wannier functions build the link to discrete lattice models. This can be conveniently shown in second quantization. The annihilation operator $\hat{\psi}(\mathbf{r})$ for a particle at position $\mathbf{r}$ can be expressed by a set of annihilation operators $\hat{c}_{\mathbf{R},n}$ on the *lattice sites* $\mathbf{R}$ using the Wannier functions:

$$\hat{\psi}(\mathbf{r}) = \sum_{\mathbf{R},n} w_{n,\mathbf{R}}(\mathbf{r})\, \hat{c}_{\mathbf{R},n} \tag{1.13}$$

Consequently, the noninterating Hamiltonian for free motion on a lattice can be expressed as

$$\hat{H}_0 = -\sum_{\mathbf{R}\mathbf{R}',n} J_n(\mathbf{R}-\mathbf{R}')\, \hat{c}^\dagger_{\mathbf{R}',n} \hat{c}_{\mathbf{R},n} \tag{1.14}$$

$$J_n(\mathbf{R}-\mathbf{R}') = \int d\mathbf{r}\; w^*_{n,\mathbf{R}'}(\mathbf{r}) \left(-\frac{1}{2m}\Delta_{\mathbf{r}} + V(\mathbf{r})\right) w_{n,\mathbf{R}}(\mathbf{r}) \tag{1.15}$$

The functions $J_n(\mathbf{R})$ are the hopping matrix elements and can be calculated numerically, using the above formula and the periodic potential $V(\mathbf{r})$. They are the Fourier transforms of the band energies, which are given by

$$\epsilon_n(\mathbf{k}) = \sum_{\mathbf{R}} J_n(\mathbf{R})\, e^{i\mathbf{k}\mathbf{R}} \tag{1.16}$$

1.2.2 Tight-binding approximation

Let us concentrate on a d dimensional simple-cubic lattice for simplicity. The deeper the periodic potential $V(\mathbf{r})$, the larger is the energy gap from the lowest energy band to higher bands. At low energies and for a sufficiently deep potential, only the lowest Bloch band $n = 1$ will play a role. Therefore we ommit the band index n. As we are interested in Fermions, we need to keep track of a spin index $\sigma = \uparrow, \downarrow$ instead. The tight-binding approximation relies on a further assumption: only the tunneling matrix elements between nearest-neighbouring sites are non-zero, i.e.

$$J(\mathbf{R}) = J \sum_{\mathbf{a}} \delta(\mathbf{R} \pm \mathbf{a}) \tag{1.17}$$

where the sum runs over the d base vectors $\mathbf{a}$ of the lattice. Therefore, we can express the tight-binding Hamiltonian in position space as

$$H_0 = -J \sum_{<ij>,\sigma} \hat{c}^{\dagger}_{i,\sigma} \hat{c}_{j,\sigma} \tag{1.18}$$

where the bracket denotes a sum over nearest-neighbour lattice sites. Fourier-transforming the Hamiltonian (1.15) yields

$$\epsilon_{\mathbf{k}} = -2\, J \sum_{i=1}^{d} \cos k_i \tag{1.19}$$

where we set the lattice constant $a = 1$. The tight-binding Hamiltonian in momentum representation thus reads

$$H_0 = \frac{1}{(2\pi)^d} \sum_{\sigma} \int d\mathbf{k}\; \epsilon_{\mathbf{k}}\, \hat{c}^{\dagger}_{\mathbf{k},\sigma} \hat{c}_{\mathbf{k},\sigma} \tag{1.20}$$

1.2.3 Hubbard model

One of the simplest models for interacting Fermions on a lattice is the Hubbard model, coined by J. Hubbard in 1963 [27]. The Hubbard model can be regarded as an extension of the tight-binding model to interacting systems: besides the hopping term H_0, the model contains an additional term that takes local contact interactions on the individual lattice sites into account,

$$H = -J \sum_{<ij>,\sigma} \hat{c}^{\dagger}_{i,\sigma} \hat{c}_{j,\sigma} \; + \; U \sum_{i} n_{i,\uparrow} n_{i,\downarrow} \tag{1.21}$$

where the operators $n_{i,\sigma} = \hat{c}^{\dagger}_{i,\sigma} \hat{c}_{i,\sigma}$ count the number of occupied states at site i and spin σ. Whenever both spin states at a given site are occupied, an interaction energy U is counted. U can either be negative or positive, favoring either empty and singly occupied sites or doubly occupied sites, respectively. Therefore, $U < 0$ models attractive interactions, while $U > 0$ models a repulsively interacting system.

The Hubbard model contains short-range interactions and is therefore applicable for ultracold atoms, which are only exposed to interactions when two atoms are in the same potential well of the optical lattice. Given the scattering length a and using (1.3), the on-site interaction U can easily be shown to be

$$U = \frac{4\pi\hbar^2 a}{m} \int d\mathbf{r}\; w(\mathbf{r})^4 \tag{1.22}$$

where w is the Wannier function of the lowest band. We will not review the rich physics and the phase diagram of the Hubbard model in this thesis, as we will be exclusively be interested in the model's metallic or band insulating phases for moderately strong interactions and high temperatures. In current experiments with fermionic atoms, entropies are still too high to exlore the relevant low-temperature phase diagram. There are many articles and books on the Hubbard model, among which we want to mention Gebhard's book on the Mott transition [28] and Essler's book on the one-dimensional Hubbard model [29].

Experiments with ultracold atoms are typically prepared in the presence of a harmonic trapping potential $V(\mathbf{r}) = V_0\,\mathbf{r}^2$, which addresses a different potential energy to each individual lattice site. Consequently, the system is describable in terms on an inhomogeneous Hubbard-model of the form

$$H = -J \sum_{<ij>,\sigma} \hat{c}^{\dagger}_{i,\sigma}\hat{c}_{j,\sigma} \; + \; U\sum_i n_{i,\uparrow}n_{i,\downarrow} + V_0 \sum_i (n_{i,\uparrow} + n_{i,\downarrow})\mathbf{r}_i^2 \tag{1.23}$$

The strength of the harmonic confinement is usually expressed in terms of the trapping frequencies ω, the atomic mass m and the lattice constant a [16]:

$$V_0 = \frac{1}{2}\, m\, \omega^2\, a^2 \tag{1.24}$$

The trap frequency ω is measured in experiments simply by observing the cloud's oscillatory movement in the parabolic trapping potential after having the cloud displaced from the trap center. When the potential is very shallow, it can be regarded as locally contant. In the local density approximation (LDA), the potential is absorbed by shifting the chemical potential,

$$\mu \longrightarrow \mu - V(\mathbf{x}) \tag{1.25}$$

As the system is assumed to be *locally translationally invariant*, quasi-momentum is kept as a quantum number in this approximation.

1.3 Transport theory

1.3.1 Introduction

From a technical point of view, we apply methods from the field of transport in condensed matter systems to ultracold atoms. The theory of transport in solids, involving Boltzmann equations, has been very successful for many practical purposes. We will review this method below and discuss its validity and the necessary modifications to apply it to analyze non-equilibrium in optical lattices: we will show, how the corresponding kinetic equations are motivated and how the emergent transport scattering rates are derived. This paragraph is inspired by the introductory books by Ziman [30] and Ashcroft and Mermin [15].

1.3.2 The semiclassical picture

To start our introduction to transport theory, we are going to derive and justify a semiclassical approach to quantum dynamics, starting from a single-particle picture. For simplicity, we start from a simple cubic lattice. To begin with, let us consider the analog of a *wave packet* for Fermions in a single band,

$$\psi(\mathbf{r},t) = \frac{1}{(2\pi)^d} \int d\mathbf{k}'\, g(\mathbf{k}-\mathbf{k}')\, \exp(i(\mathbf{k}'\,\mathbf{r} - \epsilon_{\mathbf{k}'}\,t)) \tag{1.26}$$

where $\epsilon_{\mathbf{k}}$ is the energy dispersion, and we set the lattice constant $a = 1$ and also $\hbar = 1$. We assume that the function $g(\mathbf{k}-\mathbf{k}')$ is a narrow distribution of momenta centered around $\mathbf{k}$ of width $\Delta k \ll 1$, such that its "support", i.e. its total mass, fits into the Brillouin zone. Due to the narrowness of $g(\mathbf{k}-\mathbf{k}')$, we can Taylor-expand the integrand to first order around $\mathbf{k}$, writing $\delta\mathbf{k} = \mathbf{k}-\mathbf{k}'$:

$$(\mathbf{k}'\,\mathbf{r} - \epsilon_{\mathbf{k}'}\,t) \approx (\mathbf{k}\,\mathbf{r} - \epsilon_{\mathbf{k}}\,t) + \delta\mathbf{k}\,(\mathbf{r} - \nabla_{\mathbf{k}}\epsilon_{\mathbf{k}}\,t) \tag{1.27}$$

which yields

$$\begin{aligned} \psi(\mathbf{r},t) &\approx \exp(i\,(\mathbf{k}\,\mathbf{r} - \epsilon_{\mathbf{k}}\,t)) \int \frac{d\,\delta\mathbf{k}}{(2\pi)^d}\, g(\delta\mathbf{k})\, \exp(i\,(\mathbf{r} - \nabla_{\mathbf{k}}\epsilon_{\mathbf{k}}\,t)\,\delta\mathbf{k}) \\ &= \exp(i(\mathbf{k}\,\mathbf{r} - \epsilon_{\mathbf{k}}\,t))\;\tilde{g}\,(\mathbf{r} - \nabla_{\mathbf{k}}\epsilon_{\mathbf{k}}\,t) \end{aligned} \tag{1.28}$$

where $\tilde{g}$ is the Fourier transform of g, which is a function of width $\Delta R \approx 1/\Delta k \gg 1$, centered around $\mathbf{r}$ in position space and spread over many lattice sites. Note that the probability density of the wave packet only depends on the argument of $\tilde{g}$, which allows us to identify

$$\mathbf{v}_{\mathbf{k}} = \nabla_{\mathbf{k}}\epsilon_{\mathbf{k}} \tag{1.29}$$

as the constant velocity of the wave packet. If we want to consider the wave packet as a semiclassical particle, external potentials $V(\mathbf{r})$ have to vary on length scales *even larger* than the width of the wave packet. This means that $J/F \gg \Delta R$ where we defined $F = |\nabla_{\mathbf{r}} V|$. To conclude, the three involved length scales must satisfy

$$1 \ll \Delta R \ll J/F \tag{1.30}$$

Schematically, the three involved length scales are depicted in Fig. 1.4. Combining Eq.

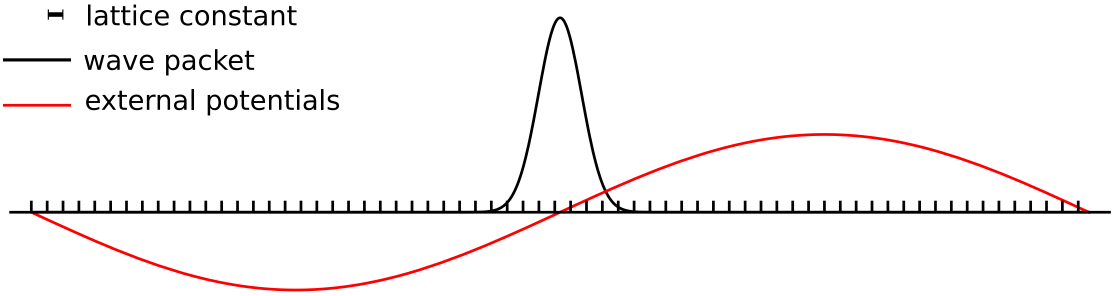

Figure 1.4: Schematic picture of the conditions required for the validity of semiclassics, following [15]. A hierarchy of three length scales has to be satisfied: while the extend of the wave packet ΔR has to be much larger than the lattice constant $\Delta R \gg 1$, external potentials $V(\mathbf{r})$ have to vary on even larger length scales, $\nabla_{\mathbf{r}} V/J \ll 1/\Delta R$ such that the system is locally translationally invariant and momentum is approximately a good quantum number.

(1.29) with the fact that potential gradients lead to a linear growth of momentum, we can write down the semiclassical equations of motion for a wave packet in a single band,

$$\begin{aligned} \dot{\mathbf{r}} &= \nabla_{\mathbf{k}} \epsilon_{\mathbf{k}} \\ \dot{\mathbf{k}} &= -\nabla_{\mathbf{r}} V \end{aligned} \tag{1.31}$$

The external potential V is treated classically, but the underlying lattice structure is treated fully quantum mechanically. In the multi-band case, semiclassical equations of motion generally neglect inter-band transitions. Note that Berry phases and magnetic fields have been neglected in the above equations of motion.

1.3.3 Elementary transport theory

Above, we have presented a semiclassical theory of noninteracting wave packets. In the remainder of this section we will be interested in a phenomenological theory of *interacting* particles. The goal of this section will be to explain how to calculate transport properties such as the mass, heat and momentum conductivity. The easiest theory that allows to do so is sometimes referred to as *elementary* transport theory [30], which is based on the semiclassical picture: lattice-Fermions are treated as semi-classical particles. For the moment, we will consider a simple model of transport, which relies on the notion of a *relaxation-time*. This is the characteristic time τ that measures, how long a particle travels freely between two scattering-events. The origin of scattering is left unspecified for the moment. On average, an particle that travels velocity $\mathbf{v}$ in a random direction will gain some additional energy from the force field $\mathbf{F}$ of the amount

$$\delta\mathcal{E} = \mathbf{v} \cdot \mathbf{F}\,\tau \tag{1.32}$$

At this point, let us consider a quadratic dispersion relation, i.e. $\mathcal{E} = m\,\mathbf{v}^2/2$, such that

$$\delta\mathcal{E} = \frac{\partial\mathcal{E}}{\partial\mathbf{v}}\,\delta\mathbf{v} = m\,\mathbf{v}\,\delta\mathbf{v} \tag{1.33}$$

which defines an average *drift velocity* $\delta\mathbf{v}$. The *mass current* is defined as $\mathbf{J} = n\,\delta\mathbf{v}$ and is related to the driving force $\mathbf{F}$ via the *mass conductivity* σ (assuming that $\mathbf{J} \parallel \mathbf{F}$),

$$\mathbf{J} = \sigma\,\mathbf{F} \tag{1.34}$$

This leads to the identification

$$\sigma = \frac{n\tau}{m} \tag{1.35}$$

The above model is greatly oversimplified, but it already shows important characteristics of the conductivity: it is proportional to the density of mass carriers and to the relaxation time. The above formula is sometimes used as a first estimate of the conductivity of a system when the some notion of a relaxation-time exists, e.g. from the imaginary part of some self-energy. As a next step, we will derive a more elaborate estimate for the conductivity, based on the notion of *distribution functions.*

1.3.4 Introduction to Boltzmann formalism

We will now review the Boltzmann equation approach to quantum dynamics in its full generality. In a seminal article [31], Ludwig Boltzmann coined the equation to describe the dynamics of classical gases already in 1872 and thereby laid the foundations for modern nonequilibrium statistical mechanics.

The Boltzmann approach is based on the semiclassical picture: particles move in phase-space and scatter among each other or among external obstacles. The method has proven to be very successful in the prediction of conductivities of metals. However, it also has some severe limitations, as e.g. it is based on the notion of (quasi-)particles [32]. This assumption breaks down in many cases, and in particular for strong interactions when symmetry is broken, or for certain one-dimensional systems [33]. In addition to the conditions for the validity of semi-classics, it e.g. also relies on second order perturbation theory in the interaction strength - hence on not too strong interactions - and on a sharply-peaked spectral function [34].

The goal of the Boltzmann approach is to calculate the non-equilibrium *distribution function* $f_{\mathbf{k}}(\mathbf{r}, t)$: it counts the average number of Fermions in the momentum state $\mathbf{k}$ in the neighborhood of position $\mathbf{r}$ at time t. Necessarily, there is some vagueness about the position $\mathbf{r}$ due to the uncertainty principle. Note that in equilibrium, this distribution function is nothing but the Fermi function, but out of equilibrium the distribution function is unknown and has to be calculated explicitly. There are three types of processes that may lead to the change of the distribution function in time: Drift, external fields and scattering. *Drift* takes into account that the individual momentum states travel in space according to their characteristic group velocity $\mathbf{v}_{\mathbf{k}}$,

$$\dot{f}_{\mathbf{k}}|_{drift} = -\mathbf{v}_{\mathbf{k}}\,\nabla_{\mathbf{r}}\,f_{\mathbf{k}}(\mathbf{r}) \tag{1.36}$$

External fields act as classical forces on the distribution function:

$$\dot{f}_{\mathbf{k}}|_{field} = -\mathbf{F}\,\nabla_{\mathbf{k}}\,f_{\mathbf{k}}(\mathbf{r}) \tag{1.37}$$

Finally, *scattering events* also lead to a change of the distribution function. At this point, we want to be general and let the specific origins of scattering unspecified for the moment. In the semiclassical picture, particles scatter locally in position space and only change their momenta during the collision event. Therefore, the scattering term is some functional I

of the distribution function, which is local in position space, but induces a change in the distribution of momenta:

$$\dot{f}_{\mathbf{k}}|_{scatt} = -I[f]_{\mathbf{k}} \tag{1.38}$$

We will specify the collision functional below for the case of fermionic inter-particle scattering. Usually, the collision functional $I[f]$ involves integrations overall several momentum coordinates. Adding these contributions, we arrive at the Boltzmann equation,

$$\partial_t\, f_{\mathbf{k}}(\mathbf{r}) + \mathbf{v}_{\mathbf{k}}\, \nabla_{\mathbf{r}}\, f_{\mathbf{k}}(\mathbf{r}) + \mathbf{F}\, \nabla_{\mathbf{k}}\, f_{\mathbf{k}}(\mathbf{r}) = -I[f]_{\mathbf{k}} \tag{1.39}$$

Note that up to now we have been very unspecific about the nature of the collision integral. The simplest approximation is the relaxation-time approximation, reviewed below.

1.3.5 Relaxation-time approximation

The probably simplest variant of the Boltzmann equation is the Boltzmann equation in relaxation time approximation. Hence, in analogy to elementary transport theory, it is based on the existence of a *relaxation time* τ, which measures the typical time between two subsequent scattering events. It is usually a general property of collisions that they tend to *equilibrate* the system. Let us regard τ^{-1} as the rate, at which the nonequilibrium distribution function gets effectively driven towards the equilibrium Fermi function $f^0_{\mathbf{k}}$, such that the Boltzmann equation reads

$$\partial_t\, f_{\mathbf{k}}(\mathbf{r}) + \mathbf{v}_{\mathbf{k}}\, \nabla_{\mathbf{r}}\, f_{\mathbf{k}}(\mathbf{r}) + \mathbf{F}\, \nabla_{\mathbf{k}}\, f_{\mathbf{k}}(\mathbf{r}) = -\tau^{-1}\left(f_{\mathbf{k}} - f^0_{\mathbf{k}}\right) \tag{1.40}$$

The relaxation-time approximation allows one to derive explicit formulas for the conductivities. This is what we want to do next. To this end, let us consider a homogeneous system in a *steady state*, i.e. where the distribution function does not change in time. This implies that $\partial_t\, f_{\mathbf{k}}(\mathbf{r}) = 0$, while homogeneity implies $\nabla_{\mathbf{r}}\, f_{\mathbf{k}}(\mathbf{r}) = 0$. Furthermore, let us assume that the driving force F is not too strong, such that we are close to equilibrium. In this case, it is justified to assume that deviations $\delta f_{\mathbf{k}}$ from the equilibrium distribution function $f^0_{\mathbf{k}}$ are small, so that we decompose $f_{\mathbf{k}}$ according to

$$f_{\mathbf{k}} = f^0_{\mathbf{k}} + \delta f_{\mathbf{k}} \tag{1.41}$$

Plugging this ansatz into (1.40) yields

$$\delta f_{\mathbf{k}} \approx -\tau\, \mathbf{F}\, \nabla_{\mathbf{k}}\, f^0_{\mathbf{k}} \tag{1.42}$$

where we used that the momentum-derivative acting on $f^0_{\mathbf{k}}$ gives already a non-vanishing contribution, so that $\delta f_{\mathbf{k}}$ can be neglected on the right hand side. Given this expression, we can derive a formula for the mass current:

$$\begin{aligned} \mathbf{j}_n &= \frac{1}{(2\pi)^d}\int d\mathbf{k}\ \mathbf{v}_{\mathbf{k}}\delta f_{\mathbf{k}} \\ &= -\frac{1}{(2\pi)^d}\int d\mathbf{k}\ \mathbf{v}_{\mathbf{k}}\frac{\partial \epsilon_{\mathbf{k}}}{\partial \mathbf{k}}\cdot \mathbf{F}\frac{\partial f^0_{\mathbf{k}}}{\partial \epsilon}\,\tau \\ &= -\frac{1}{(2\pi)^d}\int d\mathbf{k}\ \mathbf{v}_{\mathbf{k}}\mathbf{v}_{\mathbf{k}}\cdot \mathbf{F}\frac{\partial f^0_{\mathbf{k}}}{\partial \epsilon}\,\tau \end{aligned} \tag{1.43}$$

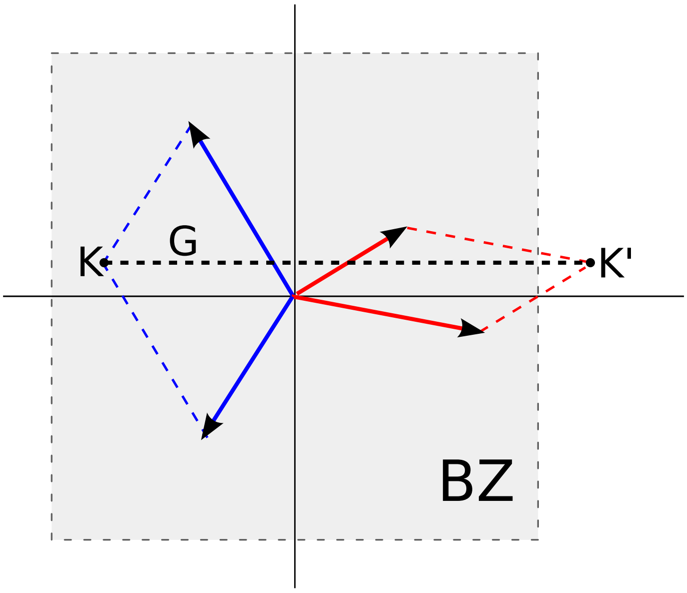

Figure 1.5: Schematic plot of a typical umklapp process. Two incoming momenta (red arrows) add up to a total momentum K', which lies outside the Brillouin zone (BZ). As all momenta are equivalent modulo reciprocal lattice vectors G, the two momenta equivalently add up to K. Therefore, they can scatter into the two momentum states indicated by the red arrows. As a result, the particles' center of mass changes its motion due to the umklapp process.

where we used that only $\delta f_{\mathbf{k}}$ carries a current: $f^0_{\mathbf{k}}$ is an even function and $\mathbf{v}_{\mathbf{k}}$ is an odd function of momentum; hence the integrated product vanishes. The above formula leads to the identification of the conductivity as

$$\sigma = -\frac{1}{(2\pi)^d}\int d\mathbf{k}\; \mathbf{v}_{\mathbf{k}}\mathbf{v}_{\mathbf{k}}\frac{\partial f^0_{\mathbf{k}}}{\partial \epsilon}\,\tau \tag{1.44}$$

Beyond the relaxation-time approximation, the conductivity can not be computed so easily. In this case, one has to find ways to approximate the complicated collision functional. A popular way to do so is based on a variational principle, presented below.

1.3.6 Umklapp scattering

Let us specify the scattering mechanism relevant for ultracold interacting fermionic atoms in optical lattices. To this end, it is important to realize that elastic two-body scattering processes do not alter the total momentum [30], but only induce relative changes in the momentum distribution. Very often, the current mode is proportional to the momentum mode, one exception being graphene [35]. Hence, scattering events that do not influence the system's total momentum do not alter the total mass current. As a consequence, an *infinite* conductivity emerges for those systems.

Lattice systems, however, *break* translational symmetry and are a priori not momentum-conserving: here, the total momentum is only conserved modulo reciprocal lattice vectors $\mathbf{G}$, i.e. processes of the form

$$\mathbf{k} + \mathbf{k_1} \longrightarrow \mathbf{k_2} + \mathbf{k_3} + \mathbf{G} \tag{1.45}$$

actually *do* have the potential to render the conductivities finite. These processes are called *umklapp* processes (as opposed to N-processes where $\mathbf{G} = 0$) and turn out to be essential for the discussion in the main part of this thesis.

A sketch of such a process is shown in Fig. 1.5: two momenta add up to a total momentum that exceeds the borders of the first Brillouin zone, such that it is equivalent to a different total momentum that lies within the Brillouin zone. This way, it can happen that both colliding particles *reverse* their velocities despite of the fact that both of them were originally traveling in the opposite direction. Thus, umklapp processes are the only processes that lead to finite conductivities and hence induce diffusive dynamics in the Hubbard model, as we are going to discuss in the main part of this thesis.

Away from half filling and for low temperatures, umklapp processes get exponentially suppressed: it becomes less and less likely that two momentum states are occupied such that they can add up to a total momentum large enough to wind around the Brillouin zone. However, despite of the fact that ultracold atoms in optical lattices are very cold on the Kelvin scale, their temperatures are high with respect to the band-width of the optical lattice: currently, typical temperatures in experiments are of the order of the hopping amplitude. Therefore, the particles' momentum distribution function is washed out among the whole Brillouin zone, and hence there is a large phase space for umklapp scattering processes - even away from half filling. For this reason, umklapp scattering rates can be expected to be very large and dominant for fermionic transport in optical lattices.

1.3.7 Full Boltzmann equation

We will now come to the actual Boltzmann equation that describes transport in fermionic lattice models at not too strong interactions, such as the Hubbard model. In contrast to the previous discussion that was based on the notion of an effective relaxation time, we will now motivate the origins of scattering microscopically. To this end, we specify the collision functional in Eq. (1.39). As stated previously, the collision term usually involves a high-dimensional integral in momentum space. This integral has to be evaluated at every point of the $2 \times d$ - dimensional phase space and for each time step, which makes the Boltzmann equation an *integro-differential equation.* Consequently, simulations of the full equation are numerically very demanding. The ultimate goal for the remainder of this section will be to calculate the conductivity *beyond* the relaxation-time approximation.

All scattering processes depend on the single-particle transition rates. Let therefore

$$\tilde{Z}_{\mathbf{k}\,\mathbf{k_1}}^{\mathbf{k_2}\mathbf{k_3}} \;=\; \mathrm{Prob}\left[(\mathbf{k},\mathbf{k_1}) \to (\mathbf{k_2},\mathbf{k_3})\right] \tag{1.46}$$

denote the probability that a certain scattering event takes place, involving two incoming and two outcoming momenta. The corresponding scattering processes have to conserve energy and momentum modulo reciprocal lattice vectors $\mathbf{G}$. Therefore, we define the *microscopic transition rates* $Z_{\mathbf{k}\,\mathbf{k_1}}^{\mathbf{k_2}\mathbf{k_3}}$ as

$$Z_{\mathbf{k}\,\mathbf{k_1}}^{\mathbf{k_2}\mathbf{k_3}} \;=\; \tilde{Z}_{\mathbf{k}\,\mathbf{k_1}}^{\mathbf{k_2}\mathbf{k_3}} \;\sum_{\mathbf{G}} \delta(\mathbf{k_0} + \mathbf{k_1} - \mathbf{k_2} - \mathbf{k_3} + \mathbf{G})\,\delta(\epsilon_{\mathbf{k_0}} + \epsilon_{\mathbf{k_1}} - \epsilon_{\mathbf{k_2}} - \epsilon_{\mathbf{k_3}}) \tag{1.47}$$

where the sum runs over all reciprocal lattice vectors, taking umklapp processes into account, but we also include $\mathbf{G} = 0$. Due to the principle of *microscopic reversibility*, the transition rates have to obey the relation

$$Z_{\mathbf{k}\,\mathbf{k_1}}^{\mathbf{k_2}\mathbf{k_3}} = Z_{\mathbf{k_2}\mathbf{k_3}}^{\mathbf{k}\,\mathbf{k_1}} \tag{1.48}$$

which can be checked straightforwardly. The microscopic transition rates are still not the physically realized transition rates: as we are dealing with *fermionic* particles, the outgoing states $\mathbf{k_2}$ and $\mathbf{k_3}$ have to be empty, while the original states $\mathbf{k}$ and $\mathbf{k_1}$ should be occupied. Hence, to obtain the actual probability of this event, the microscopic transition rate has to be multiplied with the corresponding occupation probability for particles and holes, respectively. The collision functional will take into account the probability to scatter *out* of the original state, but also - with inverse sign - the reverse process of scattering *into* the state $\mathbf{k}$. These considerations allow us to write down the *full* Boltzmann equation for interacting Fermions on a lattice as

$$\begin{aligned}(\partial_t + \mathbf{v_k}\nabla_\mathbf{r} + \mathbf{F}\nabla_\mathbf{k})\, f_\mathbf{k} &= -\int \frac{d\mathbf{k_1}}{(2\pi)^d}\frac{d\mathbf{k_2}}{(2\pi)^d}\frac{d\mathbf{k_3}}{(2\pi)^d}\quad \tilde{Z}^{\mathbf{k_2}\mathbf{k_3}}_{\mathbf{k}\,\mathbf{k_1}} \\ &\times\ \left(f_\mathbf{k} f_\mathbf{k1}(1-f_\mathbf{k2})(1-f_\mathbf{k3})\ -\ (1-f_\mathbf{k})(1-f_\mathbf{k1})f_\mathbf{k2}f_\mathbf{k3}\,\right) \\ &\times\ \sum_\mathbf{G} \delta(\mathbf{k_0}+\mathbf{k_1}-\mathbf{k_2}-\mathbf{k_3}+\mathbf{G})\,\delta(\epsilon_\mathbf{k_0}+\epsilon_\mathbf{k_1}-\epsilon_\mathbf{k_2}-\epsilon_\mathbf{k_3})\end{aligned} \tag{1.49}$$

Unfortunately, solving the full Boltzmann equation numerically is very costly already in two dimensions. We will derive an approximation of this equation in the main part of the thesis which shares all important characteristics with the full Boltzmann equation, and which allows one to extract analytical predictions from it. We will proceed by introducing a variational approach to calculate the conductivity predicted by the above equation.

1.3.8 Linearized Boltzmann equation

While it is not possible to treat the full Boltzmann equation (1.49) analytically, there are analytical tools to treat a *linearized* version of it. We are going to linearize the collision integral in the deviations from the local equilibrium distribution $f^0_\mathbf{k}$. For weak driving forces, the deviation from local equilibrium can be expected to be small, and the nonequilibrium solution can be parametrized as

$$f_\mathbf{k} = f^0_\mathbf{k} - \frac{\partial f^0_\mathbf{k}}{\partial \epsilon_\mathbf{k}}\phi_\mathbf{k} = f^0_\mathbf{k} + \beta f^0_\mathbf{k}(1-f^0_\mathbf{k})\phi_\mathbf{k} \tag{1.50}$$

where $\beta = 1/T$ is the inverse temperature and $\phi_\mathbf{k}$ is a smooth function around the Fermi surface. Before we proceed, we also note that the principle of *detailed balance* holds for the Fermi function:

$$f^0_\mathbf{k} f^0_\mathbf{k_1}(1-f^0_\mathbf{k_2})(1-f^0_\mathbf{k_3}) = (1-f^0_\mathbf{k})(1-f^0_\mathbf{k_1})f^0_\mathbf{k_2}f^0_\mathbf{k_3} \tag{1.51}$$

provided that $\epsilon_k + \epsilon_{k_1} - \epsilon_{k_2} - \epsilon_{k_3} = 0$. Given the *microscopic transition rates* Z, we define the *equilibrium transition rates* P as the many-body transition rates involving Pauli-blocking:

$$P^{\mathbf{k_2}\mathbf{k_3}}_{\mathbf{k}\,\mathbf{k_1}} := f^0_\mathbf{k} f^0_\mathbf{k_1}(1-f^0_\mathbf{k_2})(1-f^0_\mathbf{k_3})\; Z^{\mathbf{k_2}\mathbf{k_3}}_{\mathbf{k}\,\mathbf{k_1}} \tag{1.52}$$

Note that the principle of detailed balance holds also here due to (1.48) and (1.51):

$$P^{\mathbf{k_2}\mathbf{k_3}}_{\mathbf{k}\,\mathbf{k_1}} = P^{\mathbf{k}\,\mathbf{k_1}}_{\mathbf{k_2}\mathbf{k_3}} \tag{1.53}$$

We are now in a position to formulate the *linearized* Boltzmann equation. For later purposes, it will be enough to consider the equation for a *homogeneous* system in a *steady-state*:

we will use the linearized Boltzmann equation to extract an estimate for the *conductivity* or diffusion constant in terms of the full Boltzmann Eq. (1.49). Therefore, we set

$$\partial_t f_{\mathbf{k}} = 0, \qquad \nabla_{\mathbf{r}} f_{\mathbf{k}} = 0 \tag{1.54}$$

The generalization to the inhomogeneous case is straightforward [30], but not of interest to us. We use the ansatz (1.50), plug it in the full collision integral (1.49) and expand it to first order in $\phi_{\mathbf{k}}$. One can straightforwardly derive the *linearized Boltzmann equation*, which reads

$$\mathbf{F}\,\nabla_{\mathbf{k}}\, f^0_{\mathbf{k}} \;\; = -\beta \int \tfrac{d\mathbf{k_1}}{(2\pi)^d}\tfrac{d\mathbf{k_2}}{(2\pi)^d}\tfrac{d\mathbf{k_3}}{(2\pi)^d}\,(\phi_{\mathbf{k}} + \phi_{\mathbf{k_1}} - \phi_{\mathbf{k_2}} - \phi_{\mathbf{k_3}})\, P^{\mathbf{k_2}\mathbf{k_3}}_{\mathbf{k}\,\mathbf{k_1}} \tag{1.55}$$

where one uses detailed balance (1.53). Here, we approximated $f_{\mathbf{k}} \approx f^0_{\mathbf{k}}$ on the left hand side of the Boltzmann equation, which already gives a non-vanishing contribution. In contrast, as $I[f^0_{\mathbf{k}}] = 0$, the terms *linear* in $\phi_{\mathbf{k}}$ give the first non-vanishing contributions on the right hand side of the Boltzmann equation. Note that $\phi_{\mathbf{k}}$ is a function of chemical potential and temperature, as $f^0_{\mathbf{k}}$ and the transition rates P are function of these variables.

The linearized Boltzmann equation is not an integro-differential equation any more, but only an *integral equation.* Note that if we were able to solve the equation for $\phi_{\mathbf{k}}$ by inverting the linearized collision integral, we could calculate the particle current:

$$\mathbf{j}_n = -\frac{1}{(2\pi)^d}\int d\mathbf{k}\,\mathbf{v}_{\mathbf{k}}\,\frac{\partial f^0_{\mathbf{k}}}{\partial \epsilon_{\mathbf{k}}}\phi_{\mathbf{k}} = \sigma\,\mathbf{F} \tag{1.56}$$

where we used Eq. (1.50). Using that $\phi_{\mathbf{k}} \propto \mathbf{F}$, we could therefore extract the *conductivity* σ in terms of the Boltzmann equation. Therefore, our goal will be to invert the linearized collision integral in Eq. (1.55). Unfortunately, this can usually not be done exactly. Instead, we will present a way to approximate the inversion of the linearized collision functional by making a proper variational ansatz for ϕ. This method will be presented in the subsequent paragraph.

1.3.9 Variational principle

The variational method gives an estimate for the conductivity of the linearized Boltzmann equation. It is based on a choice of certain momentum modes or *channels*, in which the deviation from equilibrium is most pronounced. To simplify notation, it will be convenient to introduce an operator-formalism for the momentum-dependent functions and matrices that we worked with earlier. To this end, we define scalar product of two functions of momentum **k** as

$$\langle f, g\rangle := \frac{1}{(2\pi)^d}\int d\mathbf{k}\, f(\mathbf{k})\, g(\mathbf{k}) \tag{1.57}$$

We also introduce the linear *scattering operator* on the space of **k**-dependent functions,

$$\phi \longmapsto P\,\phi \tag{1.58}$$

whose action shall be defined by the right hand side of Eq. (1.55). Furthermore, let X denote the left hand side of Eq. (1.55), such that

$$X = P\phi \tag{1.59}$$

is an equivalent reformulation of Eq. (1.55). Using the definition of the scalar product (1.57) and the identity $\nabla_{\mathbf{k}} f^0_{\mathbf{k}} = \beta\, \mathbf{v}_{\mathbf{k}}\, f^0_{\mathbf{k}}(1 - f^0_{\mathbf{k}})$, we can calculate the matrix elements of the right and left hand side of Eq. (1.59) for the test functions ϕ and ψ, which yields

$$\langle \phi, X \rangle = \mathbf{F}\, \frac{\beta}{(2\pi)^d} \int d\mathbf{k}\, \phi_{\mathbf{k}}\, \mathbf{v}_{\mathbf{k}}\, f^0_{\mathbf{k}}(1 - f^0_{\mathbf{k}}) \tag{1.60}$$

$$\begin{aligned}\langle \phi, P\psi \rangle &= \frac{\beta}{(2\pi)^{4d}} \int d\mathbf{k_0} d\mathbf{k_1} d\mathbf{k_2} d\mathbf{k_3} \quad \phi_{\mathbf{k_0}}\, P^{\mathbf{k_2 k_3}}_{\mathbf{k_0\, k_1}} \left(\psi_{\mathbf{k_0}} + \psi_{\mathbf{k_1}} - \psi_{\mathbf{k_2}} - \psi_{\mathbf{k_3}}\right) \qquad (1.61)\\ &= \frac{1}{4}\, \frac{\beta}{(2\pi)^{4d}} \int d\mathbf{k_0} d\mathbf{k_1} d\mathbf{k_2} d\mathbf{k_3} \\ &\quad \times \left(\phi_{\mathbf{k_0}} + \phi_{\mathbf{k_1}} - \phi_{\mathbf{k_2}} - \phi_{\mathbf{k_3}}\right) P^{\mathbf{k_2 k_3}}_{\mathbf{k_0\, k_1}} \left(\psi_{\mathbf{k_0}} + \psi_{\mathbf{k_1}} - \psi_{\mathbf{k_2}} - \psi_{\mathbf{k_3}}\right)\end{aligned}$$

For the second equation, we used Eq. (1.55) and the fact that the integral in the first line is unaltered under the substitution $\phi_{\mathbf{k_0}} \to \phi_{\mathbf{k_1}}$, but changes sign under $\phi_{\mathbf{k_0}} \to \phi_{\mathbf{k_2}}$ and $\phi_{\mathbf{k_0}} \to \phi_{\mathbf{k_3}}$. The above matrix elements will be an important building block for the variational principle to follow, and we will calculate the integrals explicitly in the main part of this thesis for a set of functions ϕ and ψ that we are going to specify.

A weaker version of the operator equation (1.59) is its projection onto its solution ϕ:

$$\langle \phi, X \rangle = \langle \phi, P\phi \rangle \tag{1.62}$$

To proceed further, we need the following
Theorem *The solution ϕ of the integral equation (1.59) minimizes the functional*

$$\phi \longmapsto \frac{\langle \phi, P\phi \rangle}{\langle \phi, X \rangle^2} \tag{1.63}$$

We present the proof in the Appendix (A.1). The variational principle states that in order to find the solution of the integral equation (1.59), we have to minimize the above functional. Before we do so, however, let us gain more physical understanding of this fact by a reformulation of the variational principle.

1.3.10 Physical interpretation of the variational principle

The proceeding subsection seemed rather formal and lacking in physical interest. Therefore, we will present a physical interpretation of the variational principle in the context of steady-state transport, i.e. for an open system at fixed temperature such as a metal. Recall the *Shannon entropy*, which is a measure of entropy out of equilibrium ($k_B = 1$):

$$S = -\frac{1}{(2\pi)^d} \int d\mathbf{k}\, \left[f_{\mathbf{k}} \log(f_{\mathbf{k}}) + (1 - f_{\mathbf{k}}) \log(1 - f_{\mathbf{k}})\right] \tag{1.64}$$

Now, we take the derivative of this expression with respect to time and consider only the leading order terms in ϕ, which yields

$$\dot{S} \approx -\frac{1}{T}\, \frac{1}{(2\pi)^d} \int d\mathbf{k}\, \phi_{\mathbf{k}} \dot{f}_{\mathbf{k}} = -\frac{1}{T}\, \langle \phi, \dot{f} \rangle \tag{1.65}$$

where we omitted a term that takes an average increase in energy due to heating into account, which drops out in a steady-state nonequilibrium situation at fixed temperature.

As we are facing a steady-state situation of an open system, the open system's total entropy will be constant. Therefore, the rate of entropy production decomposes into a contribution due to scattering and a contribution due to the field term which exactly cancel each other:

$$0 = \dot{S}|_{field} + \dot{S}|_{scatt} \tag{1.66}$$

Using Eq. (1.65), we can identify those two contributions as

$$\begin{aligned} \langle \phi, X \rangle &= -T\dot{S}|_{field} \\ \langle \phi, P\phi \rangle &= \ \ T\dot{S}|_{scatt} \end{aligned} \tag{1.67}$$

Hence, it follows from the Boltzmann equation that these two rates of entropy production are identical, i.e. scattering entropy production has to be Joule heating entropy production. This common value coincides with the overall rate of generated entropy.

The following considerations go beyond the above steady-state non-equilibrium situation. The explicit expression for the entropy production due to Joule heating is given by

$$\langle \phi, X \rangle = \frac{\mathbf{F}}{(2\pi)^d} \int d\mathbf{k}\, \mathbf{v_k}\, \phi_\mathbf{k} \frac{\partial f^0}{\partial \epsilon_\mathbf{k}} = \frac{\mathbf{F}}{(2\pi)^d} \int d\mathbf{k}\, \mathbf{v_k}\, \delta f_\mathbf{k} = \mathbf{j}_n \mathbf{F} \tag{1.68}$$

Using this relation, Eq. (1.62) and setting $|\mathbf{F}| = 1$, we can identify the functional (1.63) as

$$\frac{\langle \phi, P\phi \rangle}{\langle \phi, X \rangle^2} = \frac{1}{\langle \phi, X \rangle} = 1/|\mathbf{j}_n| = 1/\sigma \tag{1.69}$$

Hence, this expression yields a direct formula for the inverse *conductivity* in terms of the Boltzmann equation. To conclude, the evaluation of the functional (1.63) in its minimum automatically yields the inverse conductivity.

1.3.11 Variational ansatz and solution

Having gained an intuition about the variational principle, we want to calculate the conductivity of the linearized Boltzmann equation. To do so, we will minimize the functional (1.63) variationally, starting from the variational ansatz

$$\phi_\mathbf{k} = \sum_{i=1}^{N} \eta_i \, \phi_\mathbf{k}^{(i)} \tag{1.70}$$

where the functions $\phi_\mathbf{k}^{(i)}$ constitute the momentum modes in which we expect the deviation from equilibrium to be most pronounced. In order to have a good result for the conductivity, one has to make a good choice of modes based on physical arguments. The variables η_i are the variational parameters that we want to determine. Defining the $N \times N$ matrix elements and $N-$vector components, respectively,

$$\begin{aligned} P_{ij} &:= \langle \phi^{(i)}, P\phi^{(j)} \rangle, \\ X_i &:= \langle X, \phi^{(i)} \rangle, \end{aligned} \tag{1.71}$$

the inverse variational functional (1.63) becomes a function of $\vec{\eta}$ and can be written

$$\vec{\eta} \longmapsto \frac{(\sum_i \eta_i X_i)^2}{\sum_{ij} \eta_i P_{ij} \eta_j} \tag{1.72}$$

This functional is minimized by

$$X_i \;=\; \sum_j P_{ij}\bar{\eta}_j \tag{1.73}$$

which can easily be inverted for a not too large number of modes N, and can be solved for $\bar{\eta}$. The coefficients are given by

$$\bar{\eta}_i \;=\; \sum_j P_{ij}^{-1} X_j \tag{1.74}$$

which can be plugged into our expression for the functional (1.63). The inverse functional, evaluated at its extremal value, finally yields the variational conductivity

$$\sigma_{\text{var}} = \sum_{ij} X_i (P^{-1})_{ij} X_j \tag{1.75}$$

in a unit force field. This concludes discussion of the variational principle. The conductivity of the full Boltzmann equation can be estimated variationally by calculating integrals of the type (1.61). The quality of the approximation depends on the choice of the modes $\phi_{\mathbf{k}}$.

2

Hydrodynamics and the Boltzmann equation

2.1 Introduction

In this thesis, we will analyze several physical problems involving dynamics and transport in optical lattices. In the present chapter, we review the central tools that we will use in this context, which are spatially inhomogeneous Boltzmann equations and nonlinear hydrodynamic equations. Being second order partial differential equations, we also refer to the hydrodynamic equations synomymously as *diffusion* equations. In the theory of transport in solids, Boltzmann equations are established tools to predict electronic charge or heat conductivities in metals [30]. However, these approaches have to be slightly modified in the context of ultracold atoms, which are thermally isolated systems. The purpose of this chapter is to explain the correspondence between the hydrodynamic approach and the Boltzmann equation, and our numerical implementation of the latter.

Problems involving nonequilibrium dynamics are usually more difficult than their equilibrium counterparts. On a technical level, the difficulty lies in the fact that the nonequilibrium distribution function is not known out of equilibrium, while it is known in equilibrium. The weakest form of a non-equilibrium situation is the regime of *linear response* [15,36,37]: here, the deviation from equilibrium is assumed to be a small correction, which is linear in the driving force. In many physical applications, the determination of the linear currents is already a much harder problem than calculating thermodynamic quantities.

Nonequilibrium and transport in the simplest interacting model systems is still comparatively poorly understood. There are only few methods available that allow to predict transport beyond the linear response regime in dimensions larger than one, which holds true even for numerical methods. In one-dimensional systems, much progress has been achieved using the time-dependent density-matrix renormalization group (tDMRG) [38–40]. Several classes of problems out of equilibrium have been treated with this method, including thermalization [41,42], interaction quenches [43–45], dynamics in inhomogeneous systems [46,47] or excitation spectra [48]. In comparison with other numerical methods, the tDMRG has the advantage of being able to treat systems that are both spatially inhomogeneous *and* out of equilibrium. However, the method is limited to comparatively short times.

Dynamical mean-field theory (DMFT) is a further numerical tool to simulate *either* inhomogeneous [3,49] *or* out-of-equilibrium systems [10,50,51] in two or higher dimensions. To a certain extend, the dynamics of interacting quantum systems can also be studied using e.g. Quantum Monte Carlo simulations [52, 53], Gutzwiller approaches [54] or exact diagonalization [42].

For large systems and not too strong interactions, Boltzmann equations are robust and reliable tools to describe the semiclassical dynamics of inhomogeneous quantum systems in dimensions larger than one, if the external potentials vary slowly. Simulating these equations numerically without further approximations is computationally very costly [55]: as integro-differential equations, Boltzmann equations involve the evaluation of a high-dimensional collision integral at each point in discretized phase space and for each time step. In this thesis, we will therefore approximate the Boltzmann equation in the relaxation time approximation, where we determine the corresponding transport scattering rate variationally. The Boltzmann equation does not only serve us as a purely numerical tool, but it also allows for analytical limits. In the context of this thesis, we will study effective hydrodynamic equations which arise in the collision dominated regime of the Boltzmann equation and which describe the diffusion of the system's conserved quantities, such as the particle and energy density. In the end of this chapter, we will review how these hydrodynamic equations can be derived systematically from the Boltzmann equation.

2.2 Relaxation-time approximation for an isolated system

In order to study the dynamics of cold atoms in optical lattices, the usual relaxation-time approximation has to be modified. When studying transport in quantum systems which are thermally coupled to a bath, such as solids under usual experimental conditions, the energy densities or temperatures are homogeneously distributed and constant. In contrast, in *isolated* systems such as ultracold atoms in optical lattices, energy densities may be spatially varying. Even more importantly, the total energy in the system is *conserved.* Also, the filling in cold atom systems varies in space, e.g. due to the presence of a confining potential. Therefore, the reference equilibrium Fermi function that is required for the relaxation-time approximation cannot be constant any more: it must be a different Fermi function at each position in space. As only the particle number n and the total energy are conserved due to the presence of umklapp scattering events that violate momentum conservation, the reference equilibrium distribution function is characterized only by the two parameters $\mathbf{n} = (n, e)$, where e is the kinetic energy. The adjustment of the local Fermi function to $\mathbf{n}$ must be made such that the scattering term conserves the local particle and kinetic energy density:

$$\begin{aligned} \int d\mathbf{k} \ \ \left(f_{\mathbf{k}} - f^0_{\mathbf{k}}(\mathbf{n})\right) &= 0 \\ \int d\mathbf{k}\, \epsilon_{\mathbf{k}} \ \left(f_{\mathbf{k}} - f^0_{\mathbf{k}}(\mathbf{n})\right) &= 0 \end{aligned} \tag{2.1}$$

The above two equations suffice to uniquely determine the reference Fermi function, which is characterized by two parameters[1]. We will review below how we numerically implemented the determination of $f^0_{\mathbf{k}}(\mathbf{n})$.

Let us now address the scattering rate. While there are several mechanisms of scattering in solids such as scattering of phonons, impurities or lattice imperfections, ultracold atoms scatter only due to inter-particle collisions. Hence, the scattering rate will also depend implicitly on the position via the local densities $\mathbf{n}$: besides a dependence on the local energies, high density regions imply a high rate of collisions, while collisions are rare in low density regions. Therefore, we have to consider a scattering rate function instead of a single rate,

---

[1] usually, $f^0_{\mathbf{k}}$ is parametrized by μ and T

$$\tau^{-1} \longrightarrow \tau^{-1}(\mathbf{n}) \tag{2.2}$$

To conclude, in contrast to the simplest version of a Boltzmann equation in relaxation-time approximation that we introduced previously (1.40), the version required for a thermally isolated, inhomogeneous systems such as ultracold atoms in optical lattices reads

$$\partial_t f + \mathbf{v_k}\nabla_{\mathbf{r}} f + \mathbf{F}\nabla_{\mathbf{k}} f \quad = \quad -\tau^{-1}(\mathbf{n})(f - f^0(\mathbf{n})) \tag{2.3}$$

where $\mathbf{v_k}$ is the group velocity of the $2D$ Hubbard model,

$$\mathbf{v_k} = \nabla_{\mathbf{k}}\epsilon_{\mathbf{k}} = 2J \begin{pmatrix} \sin\, k_x \\ \sin\, k_y \end{pmatrix} \tag{2.4}$$

The force $\mathbf{F}$ is determined by external potential gradients, but it also takes interactions on the Hartree level into account, where the individual particles are exposed to gradients of the mean interaction potential of the surrounding particles:

$$\mathbf{F} = -\nabla_{\mathbf{r}} V(\mathbf{r}) - U\nabla_{\mathbf{r}} n(\mathbf{r}) \tag{2.5}$$

We are now going to review how we adjust the Fermi function and implement the equation numerically, assuming that $\tau^{-1}(\mathbf{n})$ is a known function. Afterwards we show how to appropriately determine the transport scattering rate function.

2.3 Numerical Boltzmann simulations

Local Fermi function

The numerical scheme discussed below was developed in collaboration with David Rasch and is also reviewed in [56]. Let us assume for the moment that $\tau^{-1}(\mathbf{n})$ is a known function of two parameters $\mathbf{n} = (n, e)$. The Boltzmann simulation relies on a discretization of phase space and time. Whenever we are writing integrals in thus section of the thesis, we are actually refering to a discrete variant. Given the nonequilibrium phase-space distribution function $f_{\mathbf{k}}$ at time t, we first compute the local particle and kinetic energy densities according to

$$n(\mathbf{r}, t) = \frac{1}{(2\pi)^d} \int d\mathbf{k}\, f_{\mathbf{k}}(\mathbf{r}, t) \qquad e(\mathbf{r}, t) = \frac{1}{(2\pi)^d} \int d\mathbf{k}\, \epsilon_{\mathbf{k}}\, f_{\mathbf{k}}(\mathbf{r}, t) \tag{2.6}$$

Given $\mathbf{n}$, we need to compute the difference between the nonequilibrium distribution function $f_{\mathbf{k}}$ and a reference Fermi function

$$f^0_{\mathbf{k}}(\beta, z) = \frac{1}{1 + z\, e^{\beta\epsilon_{\mathbf{k}}}} \tag{2.7}$$

expressed in terms of an local inverse temperature $\beta(\mathbf{r}, t)$ and a local fugacity [2] $z(\mathbf{r}, t)$, having the advantage that these variables do not diverge in the infinite temperature limit.

---

[2] We replace the more common variables T and μ by $\beta = 1/T$ and $z = exp(-\mu/T)$

These two parameters have to be adjusted at each point $\mathbf{r}$ in position space such that

$$\begin{aligned} n(\mathbf{r},t) &= \frac{1}{(2\pi)^d}\int d\mathbf{k}\, f^0_{\mathbf{k}}(\beta(\mathbf{r},t), z(\mathbf{r},t)) \\ e(\mathbf{r},t) &= \frac{1}{(2\pi)^d}\int d\mathbf{k}\, \epsilon_{\mathbf{k}}\, f^0_{\mathbf{k}}(\beta(\mathbf{r},t), z(\mathbf{r},t)) \end{aligned} \tag{2.8}$$

is satisfied: this is required to guarantee that the collision term preserves the particle number and the kinetic energy. In our numerical simulation, the set of equations is inverted numerically using Newton's algorithm.

Our physical applications involve inhomogeneous density distributions where large parts of phase space are characterized by a very low occupation. For very low densities or fugacities, the Fermi distribution function can be approximated by a Boltzmann distribution,

$$\frac{1}{1+z\,e^{\beta\epsilon_{\mathbf{k}}}} \approx z^{-1}\,e^{-\beta\epsilon_{\mathbf{k}}} \qquad (n \ll 1) \tag{2.9}$$

It turns out that the numerical effort of finding the right (β, z) for given (e, n) is much smaller in this case. Using the Bessel function $B(x) = \int_{-\pi}^{\pi} dk\, e^{x\cos(k)}$, we obtain

$$\begin{aligned} n &\approx \frac{1}{(2\pi)^2}\int d\mathbf{k}\, z^{-1}\, e^{-\beta\epsilon_{\mathbf{k}}} &&= z^{-1}\, B(2\beta)^2 \\ e &\approx \frac{1}{(2\pi)^2}\int d\mathbf{k}\, z^{-1}\, \epsilon_{\mathbf{k}}\, e^{-\beta\epsilon_{\mathbf{k}}} &&= -4\, z^{-1}\, B'(2\beta)\, B(2\beta) \end{aligned} \tag{2.10}$$

As a consequence, β is determined by the ratio of e/n,

$$e/n = -4B'(2\beta)/B(2\beta) \tag{2.11}$$

which can be inverted with much less numerical costs compared to the $2d$ Newton's Algorithm. Having obtained β, we use that $z^{-1} = n/B(2\beta)^2$. We use this low density limit whenever $n < 10^{-4}$. The error is estimated in [56] and can be neglected.

As mentioned above, phase-space and time have to be discretized. Note that this discretization has got nothing to do with the "physical" discretization of space by the underlying optical lattice. While for fixed time, discrete derivatives in the space and momentum coordinates are performed, the evolution in time-direction is performed using a fourth-order Runge-Kutta scheme.

Equilibrium in the trap

For the simulations used in the chapters 4 and 5 of this thesis, the system is initially prepared in equilibrium at a given β in the presence of a confining potential $V(\mathbf{r})$ and in presence of interactions that give rise to an extra potential $U\,n(x,t)$. The initial distribution function has to be prepared self-consistently, taking its interaction energies into account. This can be done using the local density approximation (LDA), which involves the assumption that potentials are smooth and flat such the the system is *locally translationally invariant*, implying that momentum remains approximately a good quantum number. Thus, in equilibrium, external potentials can be absorbed by shifting the local chemical according to

$$\mu_{eff}(\mathbf{r}) = \mu_0 - V(\mathbf{r}) - U\,n(\mathbf{r}) \tag{2.12}$$

Note that $\mu_{eff}(\mathbf{r})$ and a global inverse temperature β uniquely characterize the equilibrium distribution function of the trapped system as

$$f^0_{\mathbf{k}}(\mathbf{r}) = \frac{1}{1+e^{\beta(\epsilon_{\mathbf{k}}-\mu_{eff}(\mathbf{r}))}} \tag{2.13}$$

However, (2.13) is a self-consistent equation as μ_{eff} depends on the density and hence on the distribution function itself. We use an iterative procedure to achieve self-consistency: the distribution function is first prepared in absence of interactions,

$$f^0_{\mathbf{k}}(\mathbf{r})^{(0)} = \frac{1}{1+e^{\beta(\epsilon_{\mathbf{k}}-\mu_0+V(\mathbf{r}))}}, \tag{2.14}$$

followed by the iterated loop $(m = 0, ..., N)$

$$n^{(m)}(\mathbf{r}) = \frac{1}{(2\pi)^d}\int d\mathbf{k}\, f^0_{\mathbf{k}}(\mathbf{r})^{(m)}, \qquad f^0_{\mathbf{k}}(\mathbf{r})^{(m+1)} = \frac{1}{1+e^{\beta(\epsilon_{\mathbf{k}}-\mu_0+V_0\mathbf{r}^2+Un^{(m)}(\mathbf{r}))}} \tag{2.15}$$

After about $N \approx 10$ iterations, the distribution converges for the given values of β, $V(\mathbf{r})$ and μ_0, including interaction energies on the the Hartree-level.

Numerical errors

It is a known fact that a numerical instability occurs if a first-order partial differential equation is *explicitly* evolved in time. This property is discussed in the Appendix (A.2) and in [57]: Numerical errors grow exponentially in time at a rate determined by the ratio of $\Delta t/\Delta x$, where Δt and Δx are the discretizations in time and in phase space, respectively. This means that the accumulation of noise can be temporarily suppressed by choosing a high temporal discretization while making the spatial discretization not too high. This instability makes numerical simulations costly, as we are interested in times up to $5000\,J^{-1}$, and hence the temporal discretization has to be chosen very high.

2.4 Transport scattering rate

2.4.1 Definition of the transport scattering rate

Having explained the numerical implementation of the Boltzmann equation, we will now review how the transport scattering rate $\tau^{-1}(\mathbf{n})$ was determined. To start with, we should emphasize that strictly speaking, there exists no well-defined notion of a scattering rate in transport theory: In the linearized Boltzmann equation, the different momentum modes, such as the modes for the particle, energy or momentum current, are damped with different rates. Postulating a unique, momentum-independent scattering rate is a further simplifying approximation, that makes the problem numerically tractable.

There are different possible choices for a scattering rate. As the physical quantity of most interest and relevance is the particle density, we chose a transport scattering rate that it optimally adjusted to the damping of the *particle* current. Hence, our scattering rate correctly reproduces the *mass* conductivity (as opposed to e.g. the heat conductivity) of the Hubbard model in the diffusive limit. In the introductory paragraph, an expression for the conductivity in terms of the scattering rate $1/\tau$ was given in Eq. (1.44). Second, also a variational approximation of the conductivity σ_{var} in terms of the full Boltzmann Eq.

(1.49) was given in Eq. (1.75). We can match these two expressions for the conductivity by demanding

$$\sigma_{\text{var}} \overset{!}{=} \frac{\beta}{(2\pi)^d} \int d\mathbf{k}\; \mathbf{v}_{\mathbf{k}}\mathbf{v}_{\mathbf{k}}\, f^0_{\mathbf{k}}(1 - f^0_{\mathbf{k}})\,\tau \tag{2.16}$$

We use this matching as a *definition* of the transport scattering rate:

$$\tau^{-1}(\beta, z) := \left(\frac{\beta}{(2\pi)^d} \int d\mathbf{k}\; \mathbf{v}_{\mathbf{k}}\mathbf{v}_{\mathbf{k}}\, f^0_{\mathbf{k}}(1 - f^0_{\mathbf{k}}) \right) \Big/ \sigma_{\text{var}}(\beta, z) \tag{2.17}$$

This way, the conductivities in terms of the Boltzmann equation in relaxation time approximation and in terms of the full Boltzmann equation coincide *by construction.* It remains to determine the conductivity $\sigma_{\text{var}}(\beta, z)$, using the variational principle explained before.

Unfortunately, we are not aware of any non-perturbative analytical or numerical method that allows to calculate the conductivity of the two-dimensional Hubbard model. Even in the infinite-temperature limit this problem remains difficult, while all thermodynamic properties are exactly known. Note that dynamical mean field theory (DMFT) successfully describes thermodynamic properties [3], while it fails to describe transport properties quantitatively. The reason is that DMFT neglects vertex corrections to the response functions which are qualitatively important, both for finite and infinite temperatures.

Therefore we determine the transport scattering rate by calculating the conductivity $\sigma_{\text{var}}(\beta, z)$ of the linearized Boltzmann equation, which involves a collision integral of the form (1.55). Note that the transport coefficients of the linearized Boltzmann equation are the transport coefficients of the Hubbard model for not too strong interactions U, as can be formally derived in second-order Keldysh perturbation theory in the ratio of U/J [34].

2.4.2 Variational conductivity of the Hubbard model

Using the variational approach described in the introductory paragraph, we calculate the conductivity of the linearized Boltzmann equation, using an appropriate variational ansatz. Note that an alternative approach to calculating the conductivity is the *memory-matrix formalism* [36, 58, 59], which leads to the same final expressions in terms of integrals [56]. The memory-matrix approach in general is a more powerful technique and can also be applied when the Boltzmann formalism does not apply, as e.g. in one-dimensional situations [60]. It can be shown quite generally, however, that these approaches are equivalent whenever the Boltzmann approach is valid [61].

Only due to the presence of Umklapp processes, the conductivity of a clean isolated lattice system is finite. We use that for a local contact interaction, the Golden-rule transition coefficients $\tilde{Z}$ are isotropic and nothing but $2\pi\, U^2/\hbar$, where we set $\hbar = 1$. Therefore, the microscopic transition rates (1.47) are given by

$$Z^{\mathbf{k}_2\mathbf{k}_3}_{\mathbf{k}\mathbf{k}_1} = 2\pi\, U^2 \sum_{\mathbf{G}} \delta\left(\mathbf{k} + \mathbf{k}_1 - \mathbf{k}_2 - \mathbf{k}_3 + \mathbf{G}\right) \delta\left(\epsilon_{\mathbf{k}} + \epsilon_{\mathbf{k}_1} - \epsilon_{\mathbf{k}_2} - \epsilon_{\mathbf{k}_3}\right) \tag{2.18}$$

where the sum runs over all reciprocal lattice-vectors $\mathbf{G}$. The transition rates are needed later when we apply the variational method.

In the variational approach, we have to specify *generalized currents* $\phi^{(i)}_{\mathbf{k}}$ in which we expect the deviation from equilibrium to be most pronounced: these are the the momentum modes which are least damped by the linearized collision integral. The ansatz for the nonequilibrium distribution function following (1.70) reads

$$f_{\mathbf{k}} = f^0_{\mathbf{k}} - \frac{\partial f^0_{\mathbf{k}}}{\partial \epsilon_{\mathbf{k}}} \sum_{i=1}^{4} \eta_i \, \phi^{(i)}_{\mathbf{k}} \tag{2.19}$$

which involves four variational parameters η_i and the generalized currents $\phi^{(i)}_{\mathbf{k}}$, which we selected to be

$$\phi^{(1)}_{\mathbf{k}} = \mathbf{v_k}^x, \qquad \phi^{(2)}_{\mathbf{k}} = \epsilon_{\mathbf{k}} \mathbf{v_k}^x, \qquad \phi^{(3)}_{\mathbf{k}} = k_x, \qquad \phi^{(4)}_{\mathbf{k}} = (\pi - k_x) \tag{2.20}$$

This ansatz is justified as follows: $\phi^{(1)}$ and $\phi^{(2)}$ are chosen in order to to calculate the mass and thermal conductivity as well as the corresponding cross-terms. The two remaining momentum and hole momentum currents, $\phi^{(3)}$ and $\phi^{(4)}$, are important to take the low-temperature physics into account: At low temperatures and at low particle or hole densities, Umklapp scattering processes get exponentially suppressed. Therefore, momentum is almost conserved in these regions, and hence the distribution function will deviate strongly from the equilibrium distribution function in those modes. Note that the correct low-temperature physics is *not* taken into account by more conventional versions of the relaxation-time approximation: there, the relaxation-rate is often identified with a single-particle relaxation rate [30], neglecting the vertex corrections. The variational approach is known to give only a lower bound for the conductivity [30, 62], however, we believe that it gives an accurate result within a few percent in the regime where the linearized Boltzmann equation applies. We have checked this statement by reducing the number of variational parameters.

In the introductory paragraph, we have derived an approximate formula for the conductivity in terms of the linearized Boltzmann equation (1.71), involving a 4 × 4-matrix P_{ij} and a 4-vector X_i. For our specific choice of variational modes and transition rates, we arrive at

$$\begin{aligned} P_{ij} &= \frac{\pi\beta U^2}{2} \sum_{\mathbf{G}} \int \frac{d\mathbf{k_0}}{(2\pi)^2} \frac{d\mathbf{k_1}}{(2\pi)^2} \frac{d\mathbf{k_2}}{(2\pi)^2} \frac{d\mathbf{k_3}}{(2\pi)^2} \; f^0_{\mathbf{k_0}} f^0_{\mathbf{k_1}} (1 - f^0_{\mathbf{k_2}})(1 - f^0_{\mathbf{k_3}}) \\ &\quad \times \left(\phi^{(i)}_{\mathbf{k_0}} + \phi^{(i)}_{\mathbf{k_1}} - \phi^{(i)}_{\mathbf{k_2}} - \phi^{(i)}_{\mathbf{k_3}} \right) \left(\phi^{(j)}_{\mathbf{k_0}} + \phi^{(j)}_{\mathbf{k_1}} - \phi^{(j)}_{\mathbf{k_2}} - \phi^{(j)}_{\mathbf{k_3}} \right) \\ &\quad \times \delta(\mathbf{k_0} + \mathbf{k_1} - \mathbf{k_2} - \mathbf{k_3} + \mathbf{G}) \, \delta(\epsilon_{\mathbf{k_0}} + \epsilon_{\mathbf{k_1}} - \epsilon_{\mathbf{k_2}} - \epsilon_{\mathbf{k_3}}) \end{aligned} \tag{2.21}$$

$$X_i = \beta \int \frac{d\mathbf{k}}{(2\pi)^2} \; \phi^{(i)}_{\mathbf{k}} \, \mathbf{v_k} \, f^0_{\mathbf{k}} (1 - f^0_{\mathbf{k}}) \tag{2.22}$$

As we have shown below, the conductivity results as the matrix product

$$\sigma_{\text{var}} = X^t \hat{P^{-1}} X \tag{2.23}$$

Note that the dependence on inverse temperature β and fugacity z enters via the Fermi functions, and that the conductivity has an overall prefactor of U^{-2}. The remaining integrals (2.21,2.22) were solved numerically using a Monte-Carlo integration for a discrete set of values for T and μ.

Figure 2.1 shows the resulting transport scattering rate as a function of the density for different temperatures. The curves converge upon increasing temperature towards a limiting curve at $T = \infty$ or $\beta = 0$, which has the asymptotic form of

$$\begin{aligned} \tau^{-1}(n, 0) &= \tau_0^{-1} \, n \, (1 - n) \\ \tau_0^{-1} &\approx 0.609 \, U^2/J \end{aligned} \tag{2.24}$$

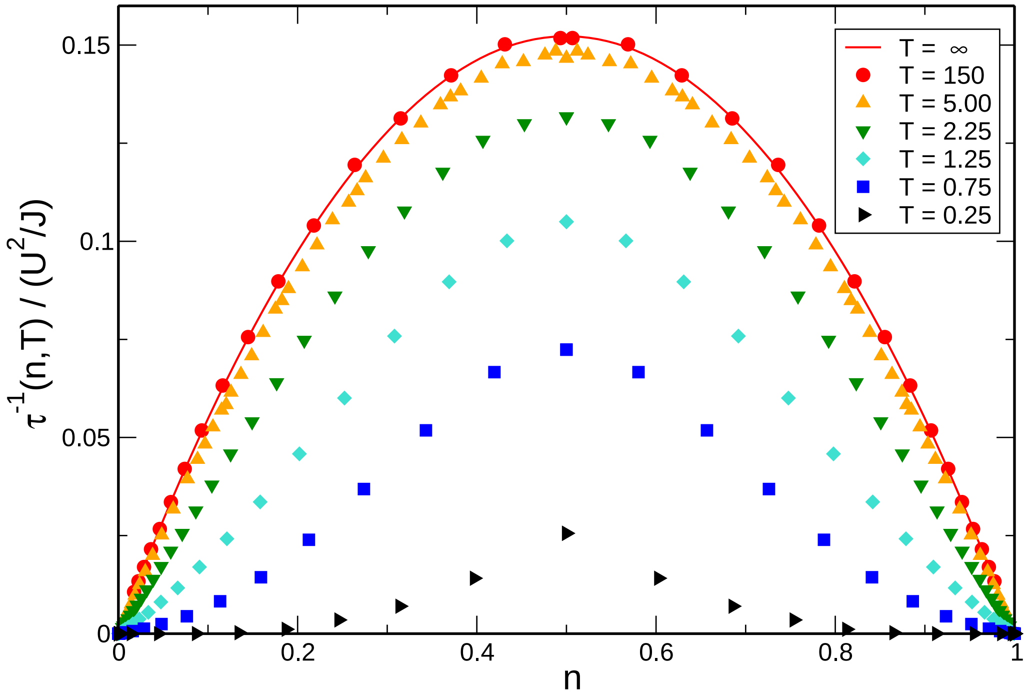

Figure 2.1: Scattering rate as a function of the density for various temperatures. Upon reducing temperature, Umklapp-scattering gets reduced and gets exponentially suppressed away from half filling at very low T. Approaching infinite T, a limiting inverted parabola with a non-universal prefactor results.

In our numerical implementation, the scattering rate function is interpolated by a smooth curve which is given in [56], such that the scattering rate can be evaluated for all values of n and β. This concludes the description of the numerical solution of the Boltzmann equation. We will now derive the hydrodynamic or diffusive limit of the Boltzmann equation formally.

2.5 From Boltzmann to hydrodynamics

2.5.1 Formal derivation

The Boltzmann equation in relaxation-time approximation is a very utile numerical tool, however, in spatially inhomogeneous situations, it is typically too complex to extract analytical information from it. It depends on several independent energy or time scales such as the bandwidth, interaction energy, scattering rate and the strength of external forces. Therefore, it is useful to study a *hydrodynamic* limit of the Boltzmann equation, which was derived in collaboration with Akos Rapp. Studying this limit amounts to deriving coupled diffusion equations for the conserved quantities of the system. In the hydrodynamic limit, the microscopic details of scattering are neglected and the system's dynamics is solely characterized by the flow of its conserved quantities. In the case of interacting particles on a lattice, the conserved quantities are the particle and energy densities, $\mathbf{n} = (n, e)$, but *not* momentum. Note that the Boltzmann equation is highly *nonlinear*, as the scattering rate itself depends on $\mathbf{n}$. Therefore we can expect the resulting diffusion equations also to be nonlinear, which will have a large impact on their mathematical properties.

The diffusive limit of the Boltzmann equation relies on the assumption of being always close to local equilibrium. Therefore, we start with the ansatz

$$f_{\mathbf{k}}(\mathbf{r}) = f^0_{\mathbf{k}}(\mathbf{r}) + \delta f_{\mathbf{k}}(\mathbf{r}) \tag{2.25}$$

where $f^0_{\mathbf{k}}(\mathbf{r})$ is a local Fermi function, and we assume that $\delta f_{\mathbf{k}}(\mathbf{r})$ is small. Using this decomposition, the Boltzmann equation in relaxation time approximation (2.3) reads

$$(\partial_t + \mathbf{v}_{\mathbf{k}}\nabla_{\mathbf{r}} + \mathbf{F}\nabla_{\mathbf{k}})(f^0_{\mathbf{k}} + \delta f_{\mathbf{k}}) = -\frac{\delta f_{\mathbf{k}}}{\tau(\mathbf{n})} \tag{2.26}$$

Necessary ingredients to hydrodynamics are the continuity equations. These equations are formally derived from the Boltzmann Eq. (2.26) by using that

$$\begin{aligned} \int d\mathbf{k}\,(\partial_t + \mathbf{v}_{\mathbf{k}}\nabla_{\mathbf{r}} + \mathbf{F}\nabla_{\mathbf{k}})(f^0_{\mathbf{k}} + \delta f_{\mathbf{k}}) &= 0 \\ \int d\mathbf{k}\,\epsilon_{\mathbf{k}}\,(\partial_t + \mathbf{v}_{\mathbf{k}}\nabla_{\mathbf{r}} + \mathbf{F}\nabla_{\mathbf{k}})(f^0_{\mathbf{k}} + \delta f_{\mathbf{k}}) &= 0 \end{aligned} \tag{2.27}$$

where we have used that the collision term preserves the particle number and the kinetic energy. The fact that $\delta f_{\mathbf{k}}$ is a periodic function on the Brillouin zone leads to the absence of boundary terms, implying $\int \nabla_{\mathbf{k}}\delta f_{\mathbf{k}} = 0$. We also use the definition of the particle density $n = \int f_{\mathbf{k}}/(2\pi)^d$ and the kinetic energy density $e = \int \epsilon_{\mathbf{k}} f_{\mathbf{k}}/(2\pi)^d$ to derive

$$\begin{aligned} \dot{n} &= -\nabla_{\mathbf{r}}\frac{1}{(2\pi)^d}\int d\mathbf{k}\,\mathbf{v}_{\mathbf{k}}\,\delta f_{\mathbf{k}}(\mathbf{r}) \\ \dot{e} &= -\nabla_{\mathbf{r}}\frac{1}{(2\pi)^d}\int d\mathbf{k}\,\epsilon_{\mathbf{k}}\,\mathbf{v}_{\mathbf{k}}\,\delta f_{\mathbf{k}}(\mathbf{r}) + \mathbf{F}\frac{1}{(2\pi)^d}\int d\mathbf{k}\,\mathbf{v}_{\mathbf{k}}\,\delta f_{\mathbf{k}}(\mathbf{r}) \end{aligned} \tag{2.28}$$

where we used that $\int \epsilon_{\mathbf{k}}\,\nabla_{\mathbf{k}}\delta f_{\mathbf{k}} = -\int \mathbf{v}_{\mathbf{k}}\,\delta f_{\mathbf{k}}$. The above equations are already the continuity equations in terms of the Boltzmann equation, but we can bring them into a more familiar form, using the definitions for the particle and energy currents:

$$\mathbf{j}_n = \frac{1}{(2\pi)^d}\int d\mathbf{k}\,\mathbf{v}_{\mathbf{k}}\,\delta f_{\mathbf{k}}(\mathbf{r}), \qquad \mathbf{j}_e = \frac{1}{(2\pi)^d}\int d\mathbf{k}\,\epsilon_{\mathbf{k}}\,\mathbf{v}_{\mathbf{k}}\,\delta f_{\mathbf{k}}(\mathbf{r}) \tag{2.29}$$

Using the above expressions for the currents, the continuity equations can be brought to the standard form:

$$\dot{n} = -\nabla_{\mathbf{r}}\,\mathbf{j}_n, \qquad \dot{e} = -\nabla_{\mathbf{r}}\,\mathbf{j}_e + \mathbf{F}\,\mathbf{j}_n \tag{2.30}$$

The source term in the kinetic energy continuity equation reflects the fact that potential energy can be converted into kinetic energy (Joule heating) and vice versa.

The diffusive approach is valid if the scattering time is the smallest time scale in the system, i.e. the Boltzmann equation is dominated by its right-hand side. As a side remark, note that due to the dependence of the scattering time on the local densities, it is not *globally* small: in fact, it even *diverges* for vanishing particle densities. Hence, the diffusion equation can only be valid in these regions if its left hand side is also small. The validity of the diffusion equation is formally discussed in the Appendix (B.2).

As a second step, we have to calculate the particle and energy current, which amounts to calculating $\delta f_{\mathbf{k}}$. Let us formally solve Eq. (2.26) for $\delta f_{\mathbf{k}}$ in the collision-dominated regime. If the scattering time τ is the smallest parameter in the problem, i.e. much smaller that inverse forces or inverse spatial gradients, an iterative solution to the equation is given by

$$\delta f_{\mathbf{k}} = \sum_{n=1}^{\infty} \left[-\tau(\mathbf{n})(\partial_t + \mathbf{v}_{\mathbf{k}}\nabla_{\mathbf{r}} + \mathbf{F}\nabla_{\mathbf{k}})\right]^n f^0_{\mathbf{k}} \tag{2.31}$$

The *diffusive* or *hydrodynamic* limit emerges from the first-order approximation of the above solution,

$$\delta f_{\mathbf{k}} \approx -\tau(\mathbf{n})\;(\mathbf{v}_{\mathbf{k}}\nabla_{\mathbf{r}} + \mathbf{F}\nabla_{\mathbf{k}})\;f^0_{\mathbf{k}}(\mathbf{n}) \tag{2.32}$$

where we also neglected the time-derivative[3]. Most importantly, consider $f^0_{\mathbf{k}}$ as a function of $\mathbf{n}$ and momentum. In combination with the continuity equations, we can therefore derive a closed set of equations for $\mathbf{n}$, as the currents are given by

$$\begin{aligned}
\mathbf{j}_n &= -\frac{1}{(2\pi)^d}\int d\mathbf{k}\,\tau(\mathbf{n})\,\mathbf{v}_{\mathbf{k}}\,(\mathbf{v}_{\mathbf{k}}\,\nabla_{\mathbf{r}} + \mathbf{F}\nabla_{\mathbf{k}}) f^0_{\mathbf{k}}(\mathbf{n}) \qquad (2.33)\\
\mathbf{j}_e &= -\frac{1}{(2\pi)^d}\int d\mathbf{k}\,\tau(\mathbf{n})\,\epsilon_{\mathbf{k}}\,\mathbf{v}_{\mathbf{k}}\,(\mathbf{v}_{\mathbf{k}}\nabla_{\mathbf{r}} + \mathbf{F}\nabla_{\mathbf{k}})\,f^0_{\mathbf{k}}(\mathbf{n})
\end{aligned}$$

2.5.2 General case

Despite of the fact that Eqs. (2.30) and (2.33) are a closed set of equations, we have only little intuition on them. Especially the dependence of $f^0_{\mathbf{k}}(\mathbf{n})$ on $\mathbf{n}$ is somewhat counterintuitive and should be clarified. Therefore, using the chain rule of differentiation, we express the currents as

$$\begin{aligned}
\mathbf{j}_n &= -\frac{1}{(2\pi)^d}\int d\mathbf{k}\,\tau(\mathbf{n})\,\mathbf{v}_{\mathbf{k}}\cdot\mathbf{v}_{\mathbf{k}}\left(\frac{\partial f^0}{\partial\mu},\frac{\partial f^0}{\partial\beta}\right)\left(\frac{\partial(\mu,\beta)}{\partial(n,e)}\right)\begin{pmatrix}\nabla_{\mathbf{r}}n\\ \nabla_{\mathbf{r}}e\end{pmatrix} \qquad (2.34)\\
&- \frac{1}{(2\pi)^d}\int d\mathbf{k}\,\tau(\mathbf{n})\,\mathbf{v}_{\mathbf{k}}\cdot\mathbf{v}_{\mathbf{k}}\,\frac{\partial f^0}{\partial\epsilon_{\mathbf{k}}}\mathbf{F}\\
\mathbf{j}_e &= -\frac{1}{(2\pi)^d}\int d\mathbf{k}\,\tau(\mathbf{n})\,\epsilon_{\mathbf{k}}\,\mathbf{v}_{\mathbf{k}}\cdot\mathbf{v}_{\mathbf{k}}\left(\frac{\partial f^0}{\partial\mu},\frac{\partial f^0}{\partial\beta}\right)\left(\frac{\partial(\mu,\beta)}{\partial(n,e)}\right)\begin{pmatrix}\nabla_{\mathbf{r}}n\\ \nabla_{\mathbf{r}}e\end{pmatrix} \qquad (2.35)\\
&- \frac{1}{(2\pi)^d}\int d\mathbf{k}\,\tau(\mathbf{n})\epsilon_{\mathbf{k}}\mathbf{v}_{\mathbf{k}}\cdot\mathbf{v}_{\mathbf{k}}\frac{\partial f^0}{\partial\epsilon_{\mathbf{k}}}\mathbf{F}
\end{aligned}$$

---

[3] The time-derivative yields second-order spatial derivatives for $\delta f_{\mathbf{k}}$ that we neglect, as $\partial_t\, f^0_{\mathbf{k}} = \partial_{\mathbf{n}}\, f^0_{\mathbf{k}}\,\dot{\mathbf{n}} \sim \partial_{\mathbf{n}}\, f^0_{\mathbf{k}}\,\Delta_{\mathbf{r}}\mathbf{n}$

where $\mathbf{v_k} \cdot \mathbf{v_k}$ is the dyadic product in the spatial coordinate, and a matrix multiplication is involved in each integral. Let us spend a few more lines to give these equations a meaning. In a similar way as we have derived a formula for the particle conductivity in terms of the scattering rate (1.44), we can generalize this result and define a matrix of generalized conductivities

$$\hat{\sigma}(\mathbf{n}) = \frac{\tau(\mathbf{n})}{(2\pi)^d} \int d\mathbf{k} \begin{pmatrix} \mathbf{v_k} \cdot \mathbf{v_k} \frac{\partial f^0_{\mathbf{k}}}{\partial \mu} & \mathbf{v_k} \cdot \mathbf{v_k} \frac{\partial f^0_{\mathbf{k}}}{\partial \beta} \\ \epsilon_{\mathbf{k}} \mathbf{v_k} \cdot \mathbf{v_k} \frac{\partial f^0_{\mathbf{k}}}{\partial \mu} & \epsilon_{\mathbf{k}} \mathbf{v_k} \cdot \mathbf{v_k} \frac{\partial f^0_{\mathbf{k}}}{\partial \beta} \end{pmatrix} \tag{2.36}$$

where the diagonal entries are the particle and energy conductivities respectively: these terms measure the system's response in terms of particle and energy flow on gradients in chemical potential and inverse temperature. The off-diagonal entries measure the strength of thermoelectric effects. We also define a 2 × 2-matrix of "susceptibilities"

$$\hat{\chi}(\mathbf{n}) \quad = \quad \left(\frac{\partial(n, e)}{\partial(\mu, \beta)} \right), \tag{2.37}$$

which measures the response of the density n and kinetic energy e to changes in the inverse temperature and the chemical potential. We can then consider the matrix product of the generalized conductivity and the inverse susceptibility to define a matrix of *diffusion constants*,

$$\mathbf{D}(\mathbf{n}) = \hat{\sigma}(\mathbf{n}) \hat{\chi}^{\mathbf{-1}}(\mathbf{n}) \tag{2.38}$$

Importantly, the matrix of diffusion constants inherits its nonlinearity from the nonlinearities of the scattering time, $\mathbf{D}(\mathbf{n}) \propto \tau(\mathbf{n})$. Finally, the generalized diffusion equation can be expressed as

$$\begin{pmatrix} \dot{n} \\ \dot{e} \end{pmatrix} = \nabla \left(\mathbf{D}(\mathbf{n}) \nabla \begin{pmatrix} n \\ e \end{pmatrix} \right) + \begin{pmatrix} \nabla(\mathbf{F}\sigma_{11}(\mathbf{n})) \\ \nabla(\mathbf{F}\sigma_{12}(\mathbf{n})) \end{pmatrix} + \begin{pmatrix} 0 \\ \mathbf{F} \cdot \mathbf{j}_n \end{pmatrix} \tag{2.39}$$

In our concrete applications, we do not need the diffusion equations in their full generality. Instead, we consider their high temperature limit, which we will review below.

2.5.3 High temperature expansion

For the analytical studies in the context of this thesis, we need a simplified variant of the above diffusion equations. It turns out that the high-temperature limit of the diffusion equations greatly simplifies them, and even the simplified equations still give considerable agreement when comparing their solutions with simulations of the Boltzmann equation at high temperatures. Therefore, we will review the equations in the high-temperature limit in this paragraph, following the Appendix of [63].

As we want to derive simplified expressions for the currents, given in Eq. (2.33), the first goal is express $f^0_{\mathbf{k}}(\mathbf{n})$ as a function of $\mathbf{n}$ in the limit of small inverse temperatures $\beta \ll 1$, but finite fugacities z. The result can be presented in arbitrary dimensions, but we will concentrate on $d = 2$ in order to simplify the notation. We start from an expansion of $f^0_{\mathbf{k}}$ in terms of β and z:

$$\begin{aligned} f^0_{\mathbf{k}}(z, \beta) &= \frac{1}{z e^{\beta \epsilon_{\mathbf{k}}} + 1} \qquad (2.40) \\ &= \frac{1}{1+z} - \frac{z}{(1+z)^2} \epsilon_{\mathbf{k}} \beta + \frac{(z-1)z}{2(1+z)^3} \epsilon^2_{\mathbf{k}} \beta^2 - \frac{z(1+(z-4)z)}{6(1+z)^4} \epsilon^3_{\mathbf{k}} \beta^3 + \mathcal{O}(\beta^4) \end{aligned}$$

Next, we calculate the particle density as a function of the variables z and β by integrating over all momenta:

$$\begin{aligned} n(z,\beta) &= \frac{1}{4\pi^2}\int d^2\mathbf{k}\; f^0_{\mathbf{k}}(z,\beta) \\ &\approx \frac{1}{1+z} + 2\,J^2\,\frac{z(z-1)}{(z+1)^3}\beta^2 \end{aligned} \tag{2.41}$$

We took and will take advantage of the fact that integrals of the form $\int d\mathbf{k}\,\epsilon^n_{\mathbf{k}}/(2\pi)^d$ can be calculated explicitly for any integer n. These integrals give integer multiples of powers of the hopping amplitude J that generally depend on the dimension [63]. We can also calculate the kinetic energies and find

$$\begin{aligned} e(z,\beta) &= \frac{1}{4\pi^2}\int d^2\mathbf{k}\;\epsilon_{\mathbf{k}} f^0_{\mathbf{k}}(z,\beta) \\ &\approx -4\,J^2\,\frac{z}{(1+z)^2}\beta - 6\,J^4\,\frac{z(1+(z-4)z)}{(1+z)^4}\beta^3 \end{aligned} \tag{2.42}$$

These relations can be inverted up to order e^3 and plugged into equation (2.40). This yields the equilibrium distribution function in terms of the local densities and energy densities:

$$f^0(n,e) \;\approx\; n + \frac{\epsilon_{\mathbf{k}}}{4\,J^2}\,e - \frac{(1-2n)(4\,J^2-\epsilon^2_{\mathbf{k}})}{32\,J^4\,(1-n)n}\,e^2 + \mathcal{O}(e^3) \tag{2.43}$$

Using these expressions, we can calculate the currents for the particle and energy densities, which are given by

$$\begin{aligned} \mathbf{j}_n &\approx -2\,J^2\,\tau(\mathbf{n})\,\nabla_{\mathbf{r}} n + \frac{\tau(\mathbf{n})}{2}\,(\nabla_{\mathbf{r}} V)\,e - \frac{\tau(\mathbf{n})}{16}\frac{(1-2n+2n^2)}{(1-n)^2n^2}(\nabla_{\mathbf{r}} n)e^2 + \frac{\tau(\mathbf{n})}{8}\frac{(1-2n)}{(1-n)n}e\nabla_{\mathbf{r}} e \\ \mathbf{j}_e &\approx -\frac{3}{2}\,J^2\,\tau(\mathbf{n})\,\nabla_{\mathbf{r}} e + \frac{3}{8}\,\tau(\mathbf{n})\,\frac{1-2n}{(1-n)n}(\nabla_{\mathbf{r}} V)e^2 \end{aligned} \tag{2.44}$$

Again, we used that expressions of the form $\int d\mathbf{k}\,\mathbf{v}^i_{\mathbf{k}}\mathbf{v}^j_{\mathbf{k}}\,\epsilon^n_{\mathbf{k}}/(2\pi)^d$ give integer multiples of powers of J. In chapter 5 of this thesis, we will simplify these equations even further, where we combine them with the high temperature limit of the scattering rate function (2.24). A this point, we want to emphasize that in absence of external potentials and for very high temperatures, i.e. $e \approx 0$, the particle diffusion equation decouples from the energy sector, which is important for the theoretical discussion in chapter 3.

3

Fermionic transport in a homogeneous Hubbard model

3.1 Introduction

Transport properties are among the defining characteristics of materials, distinguishing insulators from metals or superconductors. Yet, they are typically more difficult to calculate than e.g. thermodynamic quantities. Foundations of fermionic transport were laid in 19th century Cologne by Georg Simon Ohm [64], followed by first ideas of how to explain the emergence of currents and dissipation in solids due to Drude [65], who wrongly assumed that the free motion of electrons gets damped by collisions with lattice ions. After the development of the band theory of solids [66], physicists became aware of the fact that the nature of dissipation and transport is a very delicate subject. Electrons collide due the presence of lattice defects, impurities, the coupling to lattice phonons, electron-electron interactions and other effects. Surprisingly, applying an electric field to a perfectly conducting lattice system should not lead to a directed flow of electrons, but instead to an oscillatory movement of the electrons. This phenomenon is called Bloch oscillations [66] and will be subject of chapter 6, where we analyze the damping of Bloch oscillations by interactions. Up to now, the quantum-mechanical description of a stationary electrical current in a metal at fixed temperature has remained a complicated problem, reflecting the general difficulty to treat non-equilibrium quantum systems.

Ultracold atoms in optical lattices open the possibility of *simulating* transport in strongly interacting systems in a well controlled experimental framework. As optical lattices are clean and defect free, one can examine the transport of fermionic particles in an environment where the particle and heat currents get only damped due to *inter-particle* interactions. But besides providing new insights with relevance for condensed matter physics, they are very interesting on their own right, *especially* in the field of non-equilibrium.

A prominent, early non-equilibrium experiment with cold atoms was the observation of the dynamics of the order parameter after a quench through the superfluid-to-Mott phase transition in 2002 [12]. This experiment was a hallmark in the field of nonequilibrium many-body dynamics and let to an increasing interest in the topic of *quantum quenches*, which also motivated the development of novel numerical techniques such as the time-dependent density-matrix renormalization group (tDMRG) [38–40] and non-equilibrium extensions of dynamical mean field theory (DMFT) [50]. Also, the realization of a quantum variant of *Newton's cradle*, performed in the group of D. Weiss [13], was an experimental breakthrough: for the first time, the theoretical debate on the presence or absence of thermalization in integrable systems could be explored experimentally. In the experiment, two one-dimensional atomic clouds of hard-core Bosons were repeatedly brought to collision, which were not found to equilibrate to a thermal state after more than 1000 collision events. The experiment has inspired further theoretical research about *thermalization of isolated systems*, exemplified by the formulation of the “eigenstate thermalization hypothesis” [67].

Most experiments have been performed with bosonic atoms, but more recently, also fermionic systems have attracted more and more attention. Early experiments by M. Zwierlein et al. in 2005 showed the crossover from a BCS superfluid of cooper pairs to a BEC of bosonic molecules at positive scattering lengths, involving fermionic atoms [6]. More recently, spin transport was measured for this system, both in the diffusive regime and also far from equilibrium [68]. While these studies were performed in absence of a lattice, fermionic atoms in optical lattices were recently used to realize a Mott-insulating state in experiment [2,3]. These experiments triggered further theoretical and experimental research on the strongly repulsive Hubbard model, exemplified by studies on the lifetime of metastable repulsively-bound fermionic pairs [69, 70]. Nonequilibrium experiments with lattice-Fermions might give an estimate for the conductivity in the Mott regime, which is subject of recent theoretical studies [10, 71] and of applied relevance for novel devices.

The expansion dynamics of an initially confined fermionic cloud in the one-dimensional Hubbard model was studied numerically using the tDMRG [46]. In a regime, where U is much larger than the bandwidth, doubly occupied sites were found to assemble in the center - a phenomenon referred to as “quantum distillation“ - which was proposed to serve as a means to cool fermionic ultracold atoms. In a recent follow-up study, the short-time expansion dynamics was analyzed numerically [72], where a linear growth of the cloud’s radius was observed numerically for short times and small clouds. Note, that the physics of the Hubbard model in $d > 1$ can be expected to be very different from $d = 1$ due to the integrability of the model in the latter case. Besides the above-mentioned studies, there are many further dynamic experiments involving bosonic [73–77] and fermionic [78–80] quantum gases.

The study that will be reviewed in this chapter emerged from a joint theoretical-experimental collaboration with the group of Immanuel Bloch (MPI Munich) and Eugene Demler (Harvard), and it is based on one of the first experiments on lattice-transport with ultracold atoms [81]. Here, we analyzed the expansion dynamics of an initially confined fermionic atomic cloud in an optical lattice in the presence of interactions. The cloud was prepared in equilibrium in the presence of a harmonic trapping potential, which was switched off subsequently. This way, it could expand in the presence of the optical lattice. The expansion velocity was found to drop dramatically in the presence of interactions, but surprisingly, the drop was independent of the attractive or repulsive character of the interactions. This could be explained by us by demonstrating a novel dynamic symmetry of the Hubbard model. Below, we will review the experimental findings and the corresponding theoretical results. Large parts of the project were done in collaboration with David Rasch and are also reviewed in his PhD thesis [56]. More details on the experimental realization can be found in the PhD thesis of Ulrich Schneider [16].

3.2 Experiment

The central technical innovation in the experiment [81] was the realization of an approximately ”flat“, i.e. spatially homogeneous optical lattice. As explained earlier in subsection 1.1.3, an atomic cloud is always naturally confined to the center of a red detuned laser beam. This fact had made experiments involving a homogeneous lattice potential impossible. An approximately flat optical lattice has been realized in the center of the trap by superimposing the red-detuned optical trapping potential with a blue-detuned optical lattice potential, such that the confinement and the deconfinement adds up to zero.

The experiment [3] is initiated as follows: in the presence of a red-detuned harmonic dipole trap, a cloud of $2-3\times10^5$ fermionic atoms is cooled down to the temperature $T/T_F = 0.13$ by evaporative cooling, where T_F is the Fermi temperature of the atoms in the harmonic trap. The cloud consists of a balanced “spin”-mixture, i.e. a mixture of potassium atoms in the two lowest hyperfine states. Subsequently, a blue-detuned 3D optical lattice at wavelength $\lambda = 738$ nm is ramped up linearly within 56 ms, until the lattice depth of 8 Er is reached[1]. During this time, the strength of the magnetic field is kept at a value that corresponds to a vanishing interaction strength (209.1 G). This procedure prepares the atoms in a band-insulating state in the middle of the lattice, surrounded by a thin metallic shell.

The aim of the next step is to prepare the cloud at infinite temperature. To do this, the lattice depth is slowly increased from 8 to 20 Er, such that tunneling between the lattice sites is almost completely suppressed. This is a done at a rate slow enough to avoid transitions into higher bands. It is then kept at the final value for another 40 ms. While the atoms are localized in the steep potential wells, their phase coherence gets lost: all momentum states get equally populated, and hence the cloud assumes an infinite temperature. This waiting time is also used to tune the magnetic field to the desired value in order to realize attractive or repulsive interactions. In the end, the lattice depth is rapidly changed to the desired final value (typically 8 Er) while simultaneously the harmonic trapping potential is eliminated. This is realized by reducing the intensity of the red-detuned dipole trap by about 90%, such that its remaining confining potential exactly compensates the anti-confinement of the blue-detuned laser beams which create the optical lattice. While the atomic cloud expands in the homogeneous optical lattice, phase-contrast images are taken of the density profile in periodic steps in time. This allows one to keep track of the time-evolution of the density profile in a non-destructive way, as opposed to destructive time-of-flight measurements. More details on the experimental parameters are given in [81]. To summarize, a interacting cloud of atoms, initially at infinite temperature in the lowest band is released from a harmonic trap and expands in an optical lattice.

3.3 Non-interacting case

3.3.1 Free expansion rate

It is observed in experiment that a striking change in the cloud's symmetry occurs during the expansion process: While it is spherically symmetric initially, it obtains a square shape while it expands. Experimental pictures of the observed density distributions are shown in Fig. 3.1: the cloud assumes the square shape of the Brillouin zone.

Due to the initial preparation, each particle is localized in a Wannier state, which is an

---

[1] $1\,\mathrm{Er} = h^2/(2m\lambda^2)$

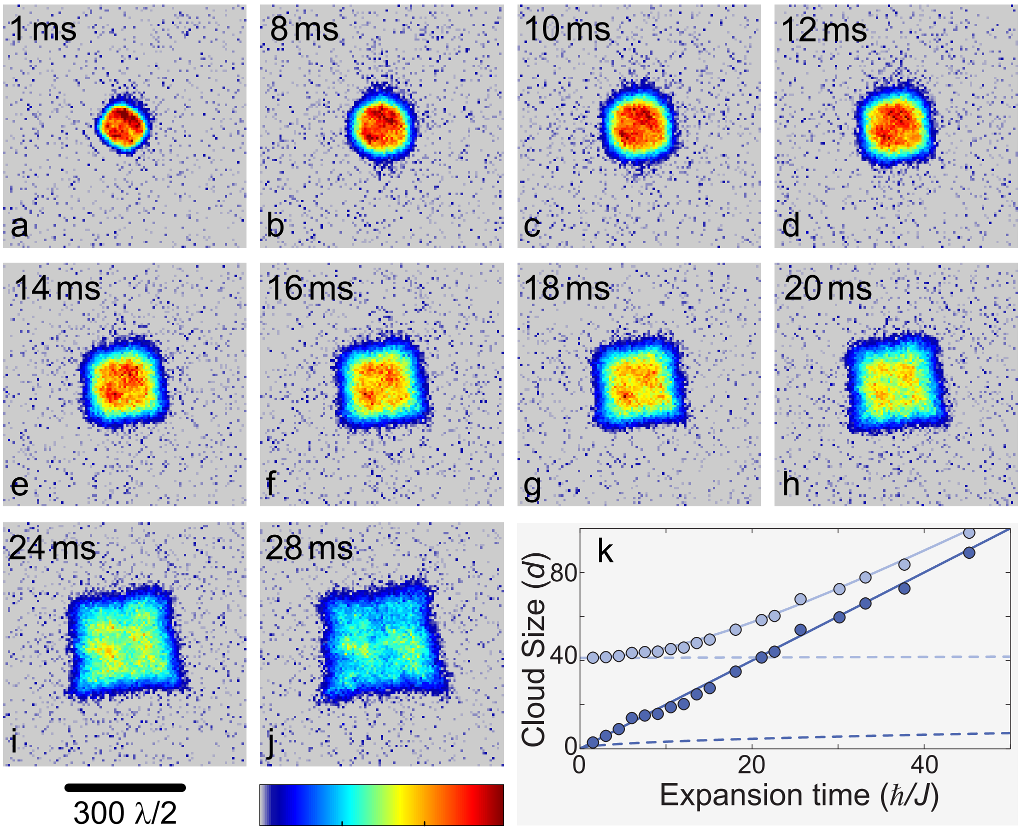

Figure 3.1: Time-evolution of the density profile of a noninteracting expanding cloud. In the course of time, the density-distribution assumes the square symmetry of the Brillouin zone. Figure k: Measured cloud width $R(t)$ and deconvolved width, $R_s(t) = \sqrt{R^2(t) - R^2(0)}$. The solid lines represent the quantum-mechanical prediction (tunneling) while the dashed lines denote the corresponding classical random walk prediction (thermal hopping). Figure made by U. Schneider

equal superposition of all Bloch waves that contain the information of the Brillouin zone. Therefore, the cloud's velocity distribution is not rotationally invariant. The cloud's mean velocity v at infinite temperatures is given by

$$v = \left(\frac{1}{4\pi^2}\int d\mathbf{k}\,{\mathbf{v}_\mathbf{k}}^2\right)^{1/2} = \sqrt{2\,d}\,J \tag{3.1}$$

where we set $\hbar = 1$, $a = 1$. This theoretical constant expansion rate agrees very well with the experimental measurements, as can be seen in the inset of Fig. 3.1. In contrast, thermal hopping can certainly be excluded, as this would result in a random walk whose radius would grow as the square-root in time (dashed curves in Fig. 3.1). In the noninteracting case, the particles evolve under the action of the tight-binding Hamiltonian alone, $H = -J\sum_{<ij>} c_i^\dagger c_j$, which can in principle easily be simulated numerically, using Slater determinants. However, also the semiclassical approach works very well in this case as the cloud is large and density gradients are small[2].

---

[2] For a noninteracting system, semiclassics just amounts to a first-order gradient expansion

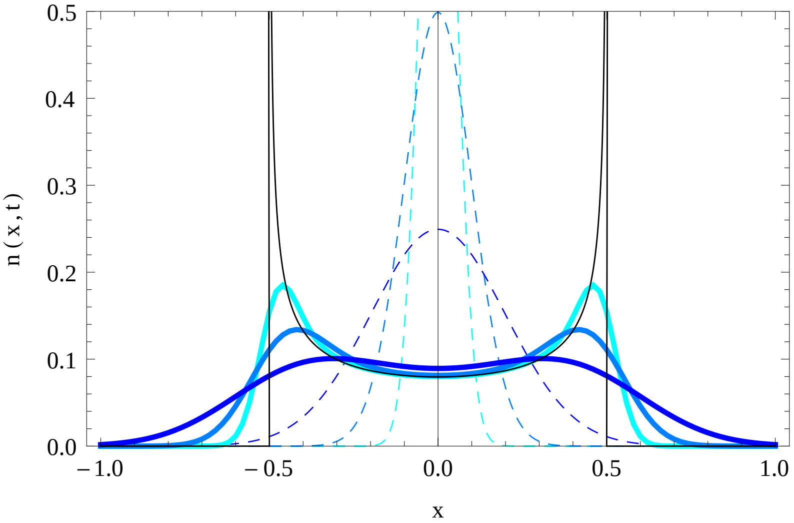

Figure 3.2: Analytic density profiles of the noninteracting expansion in $d = 1$, starting from a delta peak. The analytic result $n_0(x, t)$ (given by Eq. (3.3), thin black line) develops peaks at $x = v_{max}\, t$, where $v_{max} = 2J$ are the maximal velocities of the band. These peaks tend to wash out, when one considers the convolutions $n(x, t) = \int n_0(x, t)g(x)$ with Gaussian initial density distributions $g(x) = \text{Exp}[-x^2/(2\alpha^2)]/\sqrt{2\pi}\alpha$ where $\alpha = 0.05$, 0.1, 0.2 are the dark blue, blue and cyan curves, respectively. The curves are plotted at the times $t = 0$ (dashed) and $t = 0.25$ (solid).

3.3.2 Minimal model of free expansion

Semiclassics allows for an analytic solution of the expansion dynamics. Let us first consider the case $d = 1$. We assume that the particles are initially *sharply* localized at the origin before they expand freely. Particles travel at velocities $v_k = 2J \sin(k)$, and for the following calculation we set $J = 1$. The dynamics of a semiclassical particle at position x and momentum k, which has started at the origin $x_0 = 0$ at time t_0, is described by the distribution function

$$f(x, k, t) = \delta(x - 2 \sin k(t - t_0)) \tag{3.2}$$

The density profile $n_0(x, t) = \int f(x, k, t)\, dk/2\pi$ for an assembly of such particles, which is initially characterized by an infinite temperature, is given by

$$\begin{aligned} n_0(x, t) &= \int \frac{dk}{2\pi}\,\frac{1}{2}\,\frac{1}{|t - t_0|}\delta\Big(\frac{x/2}{t - t_0} - \sin k\Big) \\ &= \frac{2}{4\pi}\,\frac{\Theta(1 - \frac{|x/2|}{t-t_0})}{|t - t_0|}\,\frac{1}{\arcsin'(\frac{|x/2|}{t-t_0})} \\ &= \frac{1}{2\pi}\,\frac{\Theta(1 - \frac{|x/2|}{t-t_0})}{|t - t_0|}\,\frac{1}{\sqrt{1 - \frac{1}{4}(\frac{x}{t-t_0})^2}} \end{aligned} \tag{3.3}$$

Note that this density distribution is characterized by two singularities that travel at the speed of the fastest particles $v_{max} = 2J$, as can be seen in Fig. 3.2. This is an artifact

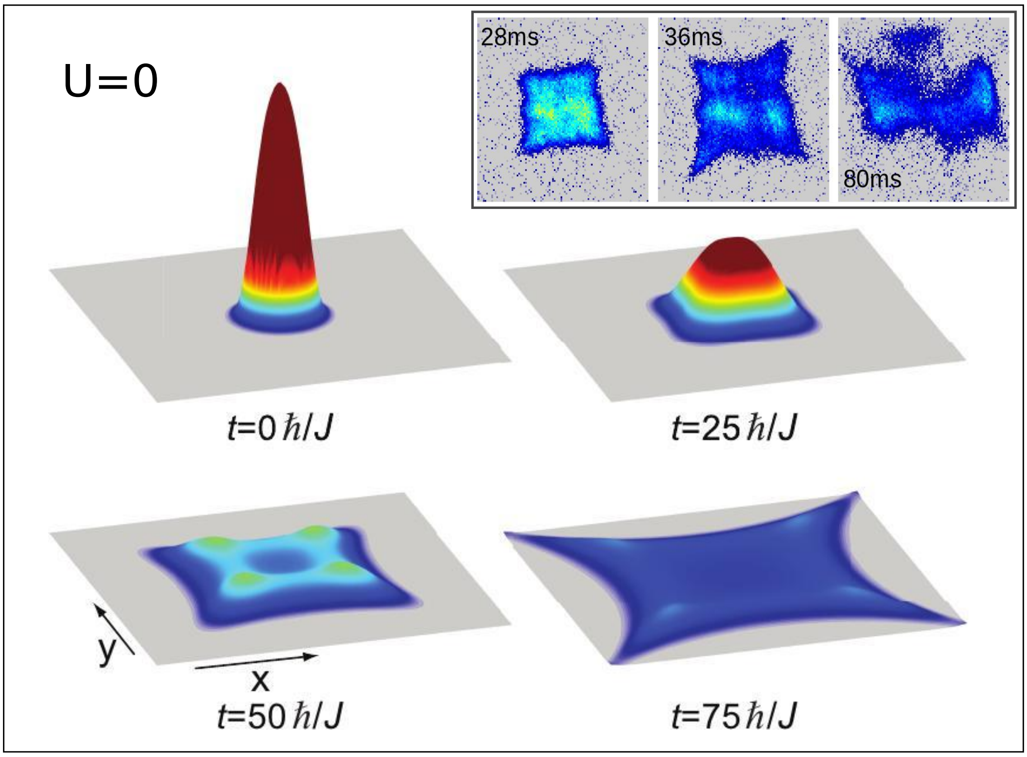

Figure 3.3: Boltzmann simulations of the noninteracting case, taking lattice inhomogeneities into account. When particles approach the "edge" of the laser beam in one direction, their hopping amplitude in the perpendicular direction increases. This leads to an enhancement of the expansion velocities along the diagonals, in agreement with the experimental observations. Inset: Experimental density profiles for $U = 0$ at long times. Pictures and experimental data by U. Schneider [81].

of the initial delta-distribution. In order to get a more realistic density profile, one has to consider the convolution of Eq. (3.3) with a broadened initial density distribution $g(x)$, i.e.

$$n(x,t) = \int dx\, n_0(x,t)\, g(x) \tag{3.4}$$

The densities $n_0(x,t)$ and $n(x,t)$ are compared in Fig. 3.2, where $g(x)$ are Gaussians of different widths. Finally, note that the analogous problem in $d = 2$ factorizes, and hence its density distribution is just given by a product of two one-dimensional distributions,

$$n_0^{d=2}(x,y,t) \propto n_0(x,t)\, n_0(y,t) \tag{3.5}$$

With a loving eye, the resulting four-peak structure of the density distribution can also be seen in the experimental data (Fig. 3.1) and also occurs visibly in the numerical simulations for $U = 0$, see Figs. 3.3 and 3.4.

3.3.3 Lattice inhomogeneities

Another experimental observation in the noninteracting case is the fact that for long times, the atomic clouds tends to deviate from the perfect square shape. Very large clouds expand faster along the diagonals of the lattice than along the lattice axes, as can be seen in Fig. 3.3. This effect can be understood as follows: when the cloud has grown large, its motion starts to become affected by lattice inhomogeneities due to the finite width of the laser beams. It is important to notice that upon approaching the laser "edge" in x direction, the hopping amplitude in y direction gets increased, and vice versa. This effect can be easily implemented in the semiclassical formalism by making the kinetic energies spatially dependent:

$$\epsilon(k_x, k_y) \longrightarrow \epsilon(x, y, k_x, k_y) = A(y)\epsilon(k_x) + A(x)\epsilon(k_y) \tag{3.6}$$

In the Appendix (B.1), we show how to calculate the factors $A(x)$ by modeling physical laser profiles. The new ansatz is such that it reproduces the original hopping rate J in the center of the trap, i.e. $A(0) = 1$, and increases it by about 25% for a distance of 100 lattice constants from the center. Our resulting simulations were in good agreement with the experimental observations, see Fig. 3.3.

3.4 Interacting case

3.4.1 Experimental observation

Interactions were found to modify the expansion dynamics drastically when compared to the noninteracting case. In the presence of interactions, the experiment as described above was repeated for different positive and negative values of the Hubbard on-site energy $U/J \in [-10, 10]$. Surprisingly, it was found that the mere presence of interactions slows down the expansion velocities drastically, *independent* of the sign of the interaction strength. Note that this observation contradicts the naive expectation that repulsive interaction push the cloud apart, while attractive interactions hold the cloud together: instead, both U and $-U$ lead to the *same* expansion dynamics. Furthermore it is found that the cloud's radius grows approximately linear in time for all values of U, but with different rates. Thus, a unique expansion velocity can be addressed to each interaction strength. Fig. 3.6 shows the expansion velocities as a function of U. Furthermore, it can be seen that while the outer parts of the cloud assume a square shape as in the noninteracting case, the core of the cloud remains spherically symmetric during its expansion. Fig. 3.4 shows the experimentally measured density profiles for different U.

3.4.2 Theoretical interpretation

Let us start our analysis with a qualitative theoretical explanation of the experimental findings. Note that the experimentally realized interaction strengths were *weak enough* to avoid the system's the Mott insulating regime. Yet, let us consider interactions *large enough* to drive the system locally to thermal equilibrium wherever the local densities are not too small and the local density gradients are not too large. In this case, most parts of the system should be in a regime where a diffusion equation applies. This diffusion equation can be expected to be highly nonlinear: the scattering rate and therefore also the diffusion constant depends crucially on the local particle density, as we have shown in chapter 2. In regions where the local density per spin is close to 1/2, the dynamics should be dominated by frequent collisions. Hence, the particles' directed motion will be suppressed, reflected by a small diffusion constant in these regions. When considering

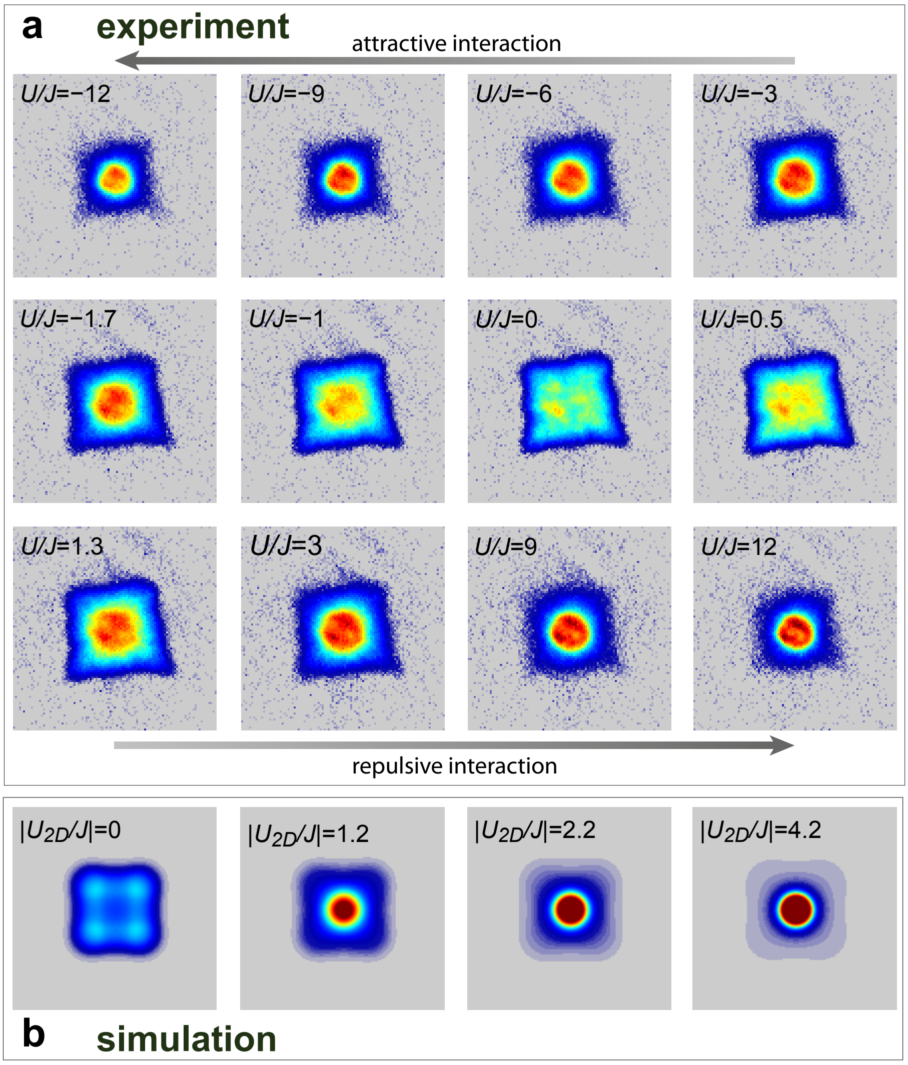
a
experiment
attractive interaction
U/J=−12
U/J=−9
U/J=−6
U/J=−3
U/J=−1.7
U/J=−1
U/J=0
U/J=0.5
U/J=1.3
U/J=3
U/J=9
U/J=12
repulsive interaction
|U2D/J|=0
|U2D/J|=1.2
|U2D/J|=2.2
|U2D/J|=4.2
b
simulation

Figure 3.4: In-situ images of the density distribution. Pictures are taken after a fixed time of expansion (25 ms) for various interaction strengths. Identical behavior for positive and negative interactions is observed. Also, an increasing number of atoms remains in the spherically symmetric regime upon increasing $|U/J|$. Bottom-line: 2D Boltzmann-simulations for various interaction strengths.

regions with lower densities[3], the mean free path and therefore the diffusion constant grows. Finally, the dynamics in the tails of the cloud is almost ballistic, because the local density is so low that particles almost never collide with each other. Therefore, the system is characterized by a spatial crossover from *diffusive* dynamics in the center of the cloud to a *ballistic* dynamics in its tails. The diffusion equation that describes the center of the cloud is rotationally symmetric, and therefore the core remains round during the expansion. In contrast, the tails of the cloud assume a square shape, as the dynamics is effectively ballistic. This crossover also becomes visible in Fig. 3.5 which shows results from a numerical simulation of the Boltzmann equation that we explain below.

For larger and larger interaction strengths U, larger and larger parts of the cloud enter the diffusive regime. Assuming that most parts of the cloud are describable by the diffusion equation, one might naively expect that the cloud's radius R grows in time t according to $R \sim t^{1/2}$, which is in contradiction to the measured growth rate $R \sim t$. Note, however, that the first mentioned scaling law does not necessarily hold for *nonlinear* diffusion equations, as we will discuss later.

The scattering rate $\tau^{-1}(\mathbf{n}) \sim U^2$ depends only on the modulus of the interaction strength U, and not on its sign. As diffusive particles expand slower than ballistic particles, we can expect the cloud's expansion velocity to decrease for large values of $\pm U$. However, this fact alone does *not* explain the observed symmetry in the expansion dynamics for attractive and repulsive interactions: interaction energies $E_{int} \sim U$ have a non-negligible impact on the system's dynamics and are obviously sensitive to the sign of U. The invariance of the expansion velocities under the transformation $U \to -U$ emerges due to a dynamic symmetry of the Hubbard model and will be explained later. We will proceed in reviewing our numerical Boltzmann simulations.

3.5 Numerical simulations

As the dynamics of the expanding atomic cloud is characterized by a crossover from diffusive dynamics in the center to ballistic dynamics in the tails, we need a model that can describe both regimes and the crossover regime in-between. One of the simplest models that has this property is the Boltzmann equation. We use it in a version of the relaxation time approximation described in chapter 2:

$$\begin{aligned} (\partial_t + \mathbf{v_k}\nabla_\mathbf{r} + \mathbf{F}\nabla_\mathbf{k})f_\mathbf{k} &= -\tau^{-1}(\mathbf{n})(f_\mathbf{k} - f^0_\mathbf{k}) \\ \mathbf{F} &= -U\,\nabla_\mathbf{r} n \end{aligned} \tag{3.7}$$

Here, $\mathbf{v_k} = \nabla_\mathbf{k}\epsilon_\mathbf{k}$ describes the group velocity of the particles, and the Force-term $\mathbf{F}$ takes interaction energies on the Hartree level into account. We will now describe how the problem-specific conditions are implemented numerically.

3.5.1 Geometry

We model the expansion dynamics of a two-dimensional cloud, initially prepared in a rotationally invariant trapping potential. The high symmetry of the initial state and the lattice allows us to exploit several symmetries in the system's geometry in order to minimize the computational costs. We can exploit an eightfold symmetry in the discretized phase-space, as described in detail in [56]. This discretization usually involves 100 × 100 sites in the spatial coordinates and 40 × 40 momenta, as well as a temporal discretization of $\Delta t = 10^{-3}\, J^{-1}$. We have to simulate times up to $t_{max} = 100\, J^{-1} \approx 100 \times 0.57\,\mathrm{ms}$ for the given experimental parameters, as we derive as a side result in Appendix (B.6).

---

[3] Due to particle-hole symmetry, the same argument also applies to regions where the local density per spin is close to 1.

In experiment, the atomic cloud is initially prepared rotationally symmetric in a 3-dimensional optical lattice. Subsequently, the laser intensity in the vertical direction is increased such that vertical tunneling is almost completely suppressed. This leads to several two-dimensional atomic layers that spread independently in the horizontal direction. Imitating the experimental conditions, we have to simulate 21 different 2-dimensional layers with different initial cloud radii. Imitating the experimental imaging technique, the densities of the individual layers have to be integrated vertically to correspond to the measured density profiles [16]. However, the density distribution of a single two-dimensional atomic layer and the layer-averaged density profile do not differ much and yield very similar expansion velocities.

3.5.2 Adjusting initial parameters

According to the experimental procedure, the cloud is initially prepared in equilibrium, before the local temperatures are quenched to infinity. To prepare an equilibrium distribution function in the presence of a harmonic trapping potential, we need to know three parameters: The initial inverse temperature β, the prefactor of the harmonic potential V_0 and the offset of the chemical potential μ_0.

The value of V_0 is determined by measuring the trapping frequency of the optical potential and using Eq. (1.24); the resulting numerical value is given by $V_0 = 0.0097\, J/a^2$. Instead of μ_0 and β, however, we are only given the total number of particles of the three dimensional layered system, $N_{3D} = 2 \times 10^5$, and the initial cloud radii R, which can be read-off from the measured density profiles, see supplementary material to [81]. Hence, we use the equations for the total number of particles and the squared cloud radius in equilibrium

$$\begin{aligned} N_{3D} &= \sum_{z=-\infty}^{\infty} \int d^2r \int \frac{d^2k}{4\pi^2} \frac{1}{1+e^{\beta(\epsilon_{\mathbf{k}}-\mu_0+V_0(\mathbf{r}^2+z^2))}} \\ R^2 &= \mathcal{N} \int d^2r \int \frac{d^2k}{4\pi^2} \frac{\mathbf{r^2}}{1+e^{\beta(\epsilon_{\mathbf{k}}-\mu_0+V_0\mathbf{r}^2)}} \end{aligned} \tag{3.8}$$

which can be solved numerically for μ_0 and β, using Newton's algorithm. The sum runs over the different 2D layers and $\mathcal{N}$ is the normalization of the corresponding integral. Note that in order to prepare the atoms in an initial state *independent* of the interaction strength, the density profile was "frozen in" in absence of interactions before U was tuned to a finite value, as we have explained above. However, still the particle number N and also the cloud radius R may vary slightly in each experimental realization. Therefore, we also obtain slightly varying initial temperatures and chemical potentials as starting parameters for the different simulations. However, these variations turn out to not very pronounced: while β lies in the range between 0.13 and 0.19, μ_0 lies between 17.4 and 20.7 for the different numerical runs that correspond to a given value of U. The detailed values have been listed in [56].

As a last step before we start the simulation of the time evolution, we calculate the local particle densities $n(\mathbf{r})$, and we subsequently modify the initial distribution function

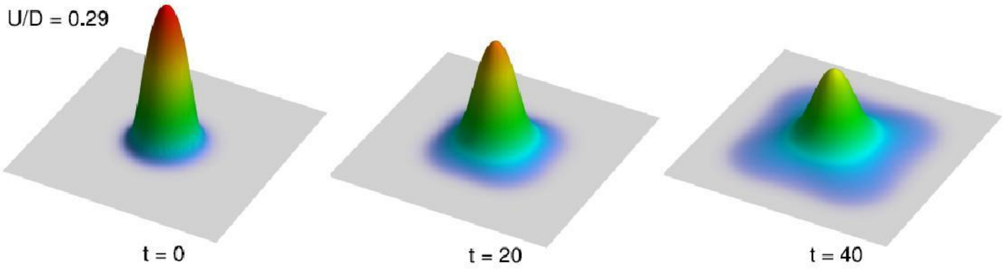

Figure 3.5: Theoretical simulation of the time-evolution of a typical density profile for $U/(4J) = 0.29$. The diffusive-to-ballistic crossover could be reproduced: round regions in the density distributions are in the diffusive regime, while the ballistic regime is characterized by a square-shape.

$f_{\mathbf{k}}$ and the local inverse temperature β according to

$$f_{\mathbf{k}}(\mathbf{r}) = n(\mathbf{r}), \qquad \beta(\mathbf{r}) = 0 \tag{3.9}$$

This procedure imitates the experimental step of destroying the phase coherence between the different lattice sites and thereby creating a fixed density profile and an infinite temperature in the lowest band.

3.6 Comparison of numerical and experimental data

3.6.1 Expansion velocities

Using the Boltzmann equation, we adjusted the initial conditions to the experimental situation as described above and simulated the expansion of the atomic cloud. The time-evolution of a typical theoretical density profile is shown in Fig. 3.5, which shows the same diffusive-to-ballistic crossover as seen in the experimental data.

An interesting quantity to observe in experiment is the growth of the cloud's radius in time, $R(t)$. The cloud radius was obtained from phase-contrast images and was defined to be the half-width at half maximum (HWHM) of the density distribution: this quantity turns out to be less sensitive with respect to noise than, e.g., the radius obtained from a Gaussian fit to the density distribution. As stated above, the expansion rate of the cloud radius is approximately constant in time, $R \sim t$, or to be more precise:

$$R(t) \approx \sqrt{R_0^2 + v_{\mathrm{exp}}^2(U)\, t^2} \tag{3.10}$$

where R_0 is the initial radius. Here, v_{exp} is a constant expansion velocity that can be addressed to each interaction strength U. Fig. 3.5 shows the velocity $v_{\mathrm{exp}}(U)$ of the expanding core as function of the interaction strength U and compares theory with experiment, where the red curve shows the numerical simulation and the black curve is a guide to the eye. The points are experimental measurements.

Note that not a full quantitative agreement could be achieved, which is discussed later. In this figure, the aforementioned $U \to -U$ symmetry becomes quantitatively visible. Expansion velocities drop dramatically already at moderate interaction strengths, which reveals the strong impact of interactions on the mass transport. Note that these velocities assume negative values for interaction strengths $|U/J| \geq 3$, both in theory and in experiment. Here, the diffusive expansion in the center is very slow compared to the ballistic velocities of the free particles in the low density regions. Therefore, the core rather "melts" like a block of ice instead of expanding: the width at half maximum therefore shrinks, $\dot{R}(t) < 0$. The asymmetric behavior for very large interactions can be attributed to light-assisted collisions on the attractive side of the Fermi gas.

3.6.2 Momentum distribution

Note that not all observables are invariant under the change of $U \to -U$: some quantities satisfy a more complicated symmetry relation. Given the noequilibrium distribution function as calculated from the Boltzmann equation at a given time $t > 0$, we can extract the *momentum-distribution* from it by integrating over the spacial coordinates:

$$n(\mathbf{k}, t) = \int d^2r \; f_{\mathbf{k}}(\mathbf{r}, t) \tag{3.11}$$

This quantity corresponds to the momentum-distribution that one would obtain when doing a time-of-flight measurement. Density plots of the simulated momentum distribution functions are shown as insets (i - v) in Fig. 3.5. Plots are made for a simulated expansion time of 40 ms and for different interaction strengths.

During the expansion, the cloud converts interaction energy into kinetic energy or vice-versa, depending on the sign of U: it reduces its kinetic energy for $U < 0$, and it further increases its kinetic energy for $U > 0$. As the distribution function is prepared at $\beta = 0$, finite inverse temperatures $\beta > 0$ emerge at attractive interactions: the cloud gets cooled during its expansion. This can be seen in Fig. 3.5 (i), where momenta accumulate around the origin while states at high momenta get reduced. However, just the *opposite* behavior is seen in Figure (v), where the occupation of states around momentum (π, π) gets *enhanced* during the expansion, while low momentum states get reduced. The enhanced population of high-energy states reflects the emergence of *negative absolute temperatures*, $\beta < 0$. A subsequent project that is subject of the thesis at hand will be exclusively devoted to negative temperatures. Therefore, we will stop the corresponding discussion here and instead interpret the emergence of the apparent (anti-) symmetry in the expansion dynamics with respect to the operation $U \to -U$. No comparison between theory and experiment is currently available for the momentum distributions.

3.7 Dynamic symmetry of the Hubbard model

The observed and simulated symmetry in the expansion dynamics turns out to be an *exact* dynamic symmetry of the Hubbard model, proposed by Eugene Demler and described in Ref. [81]. This symmetry relies on the initial state, on the observable and on the Hubbard Hamiltonian. To begin with, it is important that the initial state and the observable are symmetric under time-reversal symmetry. We will also need to introduce a "π-boost" operator that shifts all momentum states by $\mathbf{Q} = (\pi, \pi)$:

$$B_{\mathbf{Q}} \; \hat{c}_{\mathbf{q}} = \hat{c}_{\mathbf{q}+\mathbf{Q}} \tag{3.12}$$

Note that $B_{\mathbf{Q}}^2 = 1$, which will be used later. The crucial symmetry property of the Hubbard model $H(U)$ is the fact that its prefactor can be inverted by flipping U and simultaneously boosting all momentum states by $\mathbf{Q}$:

$$H(U) = -B_{\mathbf{Q}} H(-U) B_{\mathbf{Q}} \tag{3.13}$$

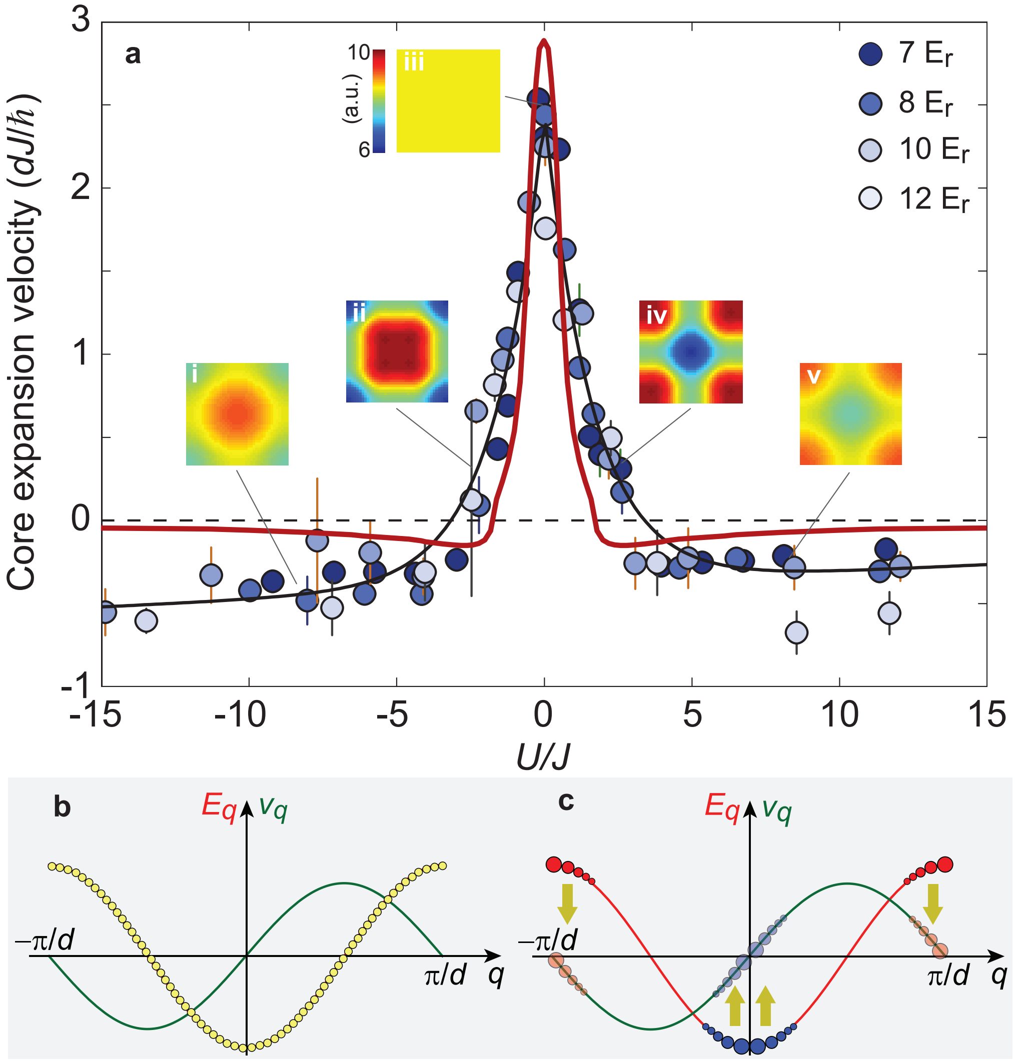

Figure 3.6: **a**: Expansion velocities of the cloud radius for various interaction strengths. The red curve is taken from a Boltzmann-simulation which includes an average over several 2D layers. While the time-evolution of the density is symmetric, the momentum-distribution (insets i-v) evolves anti-symmetrically upon changing $U \rightarrow -U$. The momentum distributions are calculated after a simulated expansion time of 40 ms. No fitting parameters are involved in the simulation. **b** & **c**: One-dimensional dispersion-relation (red line) and velocity-distribution (green line). Initial state (**b**) vs. final state (**c**), where the momentum-distribution has evolved differently for $U > 0$ (red dots) and $U < 0$ (blue dots). The resulting velocity distributions are, however, identical. Picture by U. Schneider, taken from [81].

As an artifact of the cosine-dispersion, the above equation can be traced back to the identity $\cos(q+\pi) = -\cos(q)$. Importantly, our initial state is prepared at *infinite* temperature, implying an equal population of all momentum states. Therefore, its density-matrix $\rho_0 := \rho(t=0)$ is invariant under the "π-boost", i.e.

$$\rho_0 = B_{\mathbf{Q}}\,\rho_0\,B_{\mathbf{Q}} \tag{3.14}$$

Now, let us combine these requirements and consider the time-evolution of an arbitrary time-reversal invariant observable $\hat{O}$:

$$\begin{aligned}
\langle \hat{O}\rangle_{H(U)}(t) &:= \mathrm{Tr}\left(e^{iH(U)t}\rho_0 e^{-iH(U)t}\hat{O}\right)\\
&\overset{(3.13)}{=} \mathrm{Tr}\left(B_{\mathbf{Q}}e^{-iH(-U)t}B_{\mathbf{Q}}\rho_0 B_{\mathbf{Q}}e^{+iH(-U)t}B_{\mathbf{Q}}\hat{O}\right)\\
&\overset{(3.14)}{=} \mathrm{Tr}\left(e^{-iH(-U)t}\rho_0 e^{+iH(-U)t}B_{\mathbf{Q}}\hat{O}B_{\mathbf{Q}}\right)\\
&\overset{\text{T.R.}}{=} \mathrm{Tr}\left(e^{+iH(-U)t}\rho_0 e^{-iH(-U)t}B_{\mathbf{Q}}\hat{O}B_{\mathbf{Q}}\right)\\
&= \langle B_{\mathbf{Q}}\hat{O}B_{\mathbf{Q}}\rangle_{H(-U)}(t)
\end{aligned} \tag{3.15}$$

To summarize our result: starting at infinite temperature, the time-evolution of a given observable in the repulsive Hubbard model is identical to the time-evolution of the "π - boosted" observable in the attractive Hubbard model and vice-versa.

Let us now consider two important examples. First, note that the local density operator $\hat{n}(\mathbf{r})$ is invariant under the boost, $B_{\mathbf{Q}}\hat{n}(\mathbf{r})B_{\mathbf{Q}} = \hat{n}(\mathbf{r})$, and therefore we find

$$\langle \hat{n}(\mathbf{r})\rangle_{H(U)} = \langle \hat{n}(\mathbf{r})\rangle_{H(-U)} \tag{3.16}$$

This identity explains the observed dynamic symmetry with regard to the cloud's density profile and expansion velocity: these quantities evolve exactly the same under the Hamiltonians $H(U)$ and $H(-U)$, which explains the symmetry of the expansion velocity as a function of interaction strength, see Fig. 3.6. As a second example, let us consider the momentum distribution operator, which obviously satisfies $B_{\mathbf{Q}}\hat{n}(\mathbf{k})B_{\mathbf{Q}} = \hat{n}(\mathbf{k}+\mathbf{Q})$, and therefore

$$\langle \hat{n}(\mathbf{k})\rangle_{H(U)} = \langle \hat{n}(\mathbf{k}+\mathbf{Q})\rangle_{H(-U)} \tag{3.17}$$

The above relation explains our numerical results for the momentum distributions, which are shown in the insets of Fig. 3.6: the momentum distributions of clouds that expand in the attractive or repulsive Hubbard model differ by a shift of all momentum states by $\mathbf{Q}$. Hence, momentum distributions at positive temperature correspond to momentum distributions at negative temperature at opposite values of U, and vice versa. This concludes the discussion on the dynamic symmetry of the Hubbard model.

Let us also give a more intuitive explanation of the dynamic symmetry of the Hubbard model. Counter-intuitively, the attractive or repulsive character of interactions was found to have no impact on the expansion dynamics. Repulsive forces always increase momenta, but they do not always increase *velocities*: while in free space where $\epsilon_{\mathbf{k}} \propto \mathbf{k}^2$, larger momenta imply also larger velocities $\mathbf{v}_{\mathbf{k}} = \nabla_{\mathbf{k}}\epsilon_{\mathbf{k}} \propto \mathbf{k}$, this is not necessarily the case for the Hubbard model, where the velocities for the momenta $\mathbf{k}$ and $\mathbf{Q}-\mathbf{k}$ are identical, see Fig. 3.6. Let us emphasize again that the observed dynamic symmetry is not an artifact of the Boltzmann simulation, but a general property of the Hubbard model.

3.8 Nonlinear diffusion equation

3.8.1 Validity of hydrodynamics

Our next goal is to try to gain more *analytic* insight in this complex expansion process. Although we have already simplified the problem by studying transport in the Hubbard model by using the Boltzmann equation in relaxation-time approximation, even the Boltzmann equation is still rather complex: it is characterized by several time scales given by the strength of external and internal forces, the group velocities and the rate of scattering. In order to get rid of one of these parameters, we need a controlled limit which simplifies the Boltzmann equation. An obvious choice is the hydrodynamic (or diffusive) limit, which assumes that the time between subsequent collisions, τ_{scatt}, is the smallest time scale in the problem. If other time scales are much larger, the microscopic details of scattering are not important any more and the system is close to local equilibrium. Hydrodynamic approaches are powerful and well established techniques in many different areas of physics, including not only classical systems but also quantum systems. However, hydrodynamics certainly does not describe the tails of the expanding cloud correctly, which is governed by ballistic motion.

In chapter 2, we showed how to derive coupled diffusion equations from the Boltzmann equation. Again, let us combine the particle density n and the kinetic energy density e in the container variable $\mathbf{n}(\mathbf{r}, t)$. In absence of external potentials, the hydrodynamic equations (2.39) simplify in absence of potentials according to

$$\dot{\mathbf{n}} = \nabla\left(\mathbf{D}(\mathbf{n})\nabla\mathbf{n}\right) \tag{3.18}$$

where $\mathbf{D}$ is a 2×2-matrix of diffusion constants. In the previous chapter, we determined $\mathbf{D}$ in such a way as to reproduce the diffusion constant of the Hubbard model. Using the high temperature limits of the currents given in Eq. (2.44), we can identify the coefficients of the matrix of diffusion constants to linear order in e as

$$\mathbf{D}(\mathbf{n}) \;\approx\; \frac{\tau_0}{n}\begin{pmatrix} 2\,J^2 & 0 \\ 0 & \frac{3}{2}\,J^2 \end{pmatrix} \;+\; \mathcal{O}(e^2) \tag{3.19}$$

where we used the infinite temperature and low-density limit of the scattering rate function from Eq. (2.25), which states that $\tau(\mathbf{n}) \approx \tau_0/n$ with $\tau_0 \approx 1.647\, J/U^2$. Importantly, the sectors for particle and energy diffusion approximately decouple in absence of potentials and for very high temperatures or small kinetic energy densities e. We therefore study the particle diffusion equation alone:

$$\dot{n} = \nabla(D(n)\nabla n), \qquad D(n) = 2J^2\tau_0/n \tag{3.20}$$

Note that the above hydrodynamic approach is not valid in one dimension, where the Hubbard model is integrable and the isolated system doesn't necessarily thermalize to a state solely characterized by n and e.

In order to identify the validity of the diffusive approximation, the leading nonlinear corrections to the currents can be compared to the linear currents. If we want the diffusion equation to be valid, this ratio defines dimensionless number that has to be small. In the Appendix (B.2), we show that this criterion is equivalent to

$$\frac{1}{\tau_{scatt}} \gg \frac{1}{\tau_{exp}} := \frac{|\nabla(D(n)\nabla(D(n)\nabla n))|}{|D(n)\nabla n|} \tag{3.21}$$

where $1/\tau_{scatt}$ is a typical scattering rate in the system and $1/\tau_{exp}$ is the cloud's characteristic expansion rate. This criterion can be further simplified by scaling considerations. Let us therefore replace the gradients by the inverse cloud radius, which in turn can be estimated using the total number of particles, i.e. $\nabla \sim 1/R \sim 1/N^{1/3}$. We also use that the diffusion constant can be estimated as $D \sim v^2\, \tau_{scatt} \sim J^2\, \tau_{scatt}$, which can be combined to the criterion

$$\frac{1}{\tau_{scatt}} \gg \frac{J}{1/N^{1/3}} \tag{3.22}$$

where we took the square root on both sides. There is also an alternative criterion for the validity of the diffusion equation. The other criterion states that the diffusive currents must never involve velocities larger than the maximally allowed ballistic velocities v imposed by the lattice, $j_{\text{diff}} = D(n)\nabla n \ll j_{\text{ball}} \approx n\, v$. This criterion leads to the same result after the above scaling analysis. Using that $1/\tau_{scatt} \sim n\, U^2/J$ for low densities, Eq. (3.22) can be also expressed as

$$n \gg \frac{J^2}{U^2\, N^{1/3}} \tag{3.23}$$

Therefore, one might expect naively that in the physical case of $N = 10^5$ particles, almost the entire cloud should be in the diffusive regime and that it therefore suffices to use the diffusion equation alone to model the entire system. This naive expectation turns out to be incorrect, as we will show below.

3.8.2 Fast diffusion equation

Due to divergence of the scattering time $\tau(\mathbf{n})$ for low densities n, the hydrodynamic approach looses necessarily its validity in the tails of the cloud. However, upon increasing the interaction strength U, larger and larger parts of the cloud are in the diffusive regime, as is correctly predicted by Eq. (3.23). For large enough values of U, we could hope that we can describe the entire cloud in terms of the diffusion equation alone. Here we will show that this is not the case.

Introducing the constant $C = 2J^2\tau_0 \approx 3.29\, J^3/U^2$, we will now study the particle diffusion equation (3.20) in more detail, valid at high temperatures and low densities:

$$\dot{n} = C\, \nabla \left(\frac{1}{n} \nabla n \right) \tag{3.24}$$

The interaction strength U enters quadratically in $C \sim U^{-2}$ and can be absorbed into a re-definition of the time variable, $t \to t/C$. Consequently, interactions only affect the *speed* of diffusion and nothing else. Let us generalize the diffusion equation slightly by introducing a new parameter δ such that $\delta = 1$ gives our original equation:

$$\partial_t n(\mathbf{r}, t) = \nabla \left(\frac{1}{n^\delta} \nabla n(\mathbf{r}, t) \right) \tag{3.25}$$

The above equation is called the *fast diffusion equation* and has been extensively studied in the mathematical literature, as is reviewed in a book of J. L. Vazquez [82].

In Fig. 3.7, we compare numerical simulations of the Boltzmann equation to numerical simulations of the fast diffusion equation for $\delta = 1$, starting from identical density distributions. The numerical solutions of the two equations agree in the bulk of the system for short times and large interaction strengths. There are significant deviations in the tails of the cloud even for strong interactions: while the Boltzmann equation only allows for finite spreading velocities, particles can become arbitrarily fast according to the diffusion equation.

3.8.3 Scaling solutions

A subset of solutions for nonlinear diffusion equations of the type (3.25) can usually be found by making a certain scaling ansatz. These solutions are called Barenblatt-type solutions [83]. Although scaling ansatzes clearly cannot capture *all* possible solutions of the equation, some properties of the Barenblatt solutions might be valid for a wider class of solutions as well. We make the following ansatz for the particle density, involving a scaling function f and the unknown parameter $\alpha > 0$:

$$n(\mathbf{r}, t) = \frac{1}{t^{d\,\alpha}} f(r/t^{\alpha}) \tag{3.26}$$

Note that the prefactor $t^{-d\alpha}$ is fixed, as the total integral of n over $\mathbf{r}$ gives the total number of particles and must be independent of time. The nonlinear diffusion equation for radially symmetric initial conditions in d dimensions reads

$$0 = -\,\partial_t\, n(r,t) + \frac{1}{r^{d-1}}\,\partial_r \left(\frac{r^{d-1}}{n(r,t)^{\delta}}\,\partial_r n(r,t) \right) \tag{3.27}$$

Using our scaling ansatz for this equation yields an *ordinary* differential equation for the scaling function f. Substituting $r \to q = r/t^{\alpha}$ yields

$$\begin{aligned} 0 \;&=\; d\alpha f(q) + q\alpha f'(q) \\ &-\; t^{1-2\alpha+d\alpha\delta} \left(\frac{(d+1) f(q)^{-\delta} f'(q)}{q} + f(q)^{-\delta} f''(q) - f(q)^{-\delta-1} f'(q)^2 \delta \right) \end{aligned} \tag{3.28}$$

where the first two terms on the right hand side are due to the time derivative, while the remaining terms come from the spatial derivatives. These contributions have to cancel each other for all times t, and hence the parameter α has to be adjusted such that t drops out of the equation:

$$\alpha = \frac{1}{2 - d\delta} = \frac{1}{2-d} \quad (\delta = 1) \tag{3.29}$$

The above relation is of much more interest to us than the explicit form of the scaling function, which is given as the solution of the ordinary differential equation (3.28). It tells us that in dimensions $d = 3$, no positive α exists, and hence no scaling solution exists in $d = 3$. Also note that in two dimensions, the exponent α diverges: this is the marginal case for the existence of a scaling solution. The larger the value of α, the *faster* the Barenblatt-solution expands. We therefore conclude that the diffusion equation in two dimensions for $\delta = 1$ is very fast, and it is therefore also called the *superfast* diffusion equation [82].

3.8.4 Universal particle loss rate

It turns out that the fast diffusion equation has got remarkable properties concerning the conservation of the total number of particles. By integrating equation (3.27) radially over space up to a certain radius r_{max}, we see that

$$\partial_t N \;\sim\; \left. \frac{r^{d-1}}{n^{\delta}} n'(r) \right|_{r=r_{max}} \tag{3.30}$$

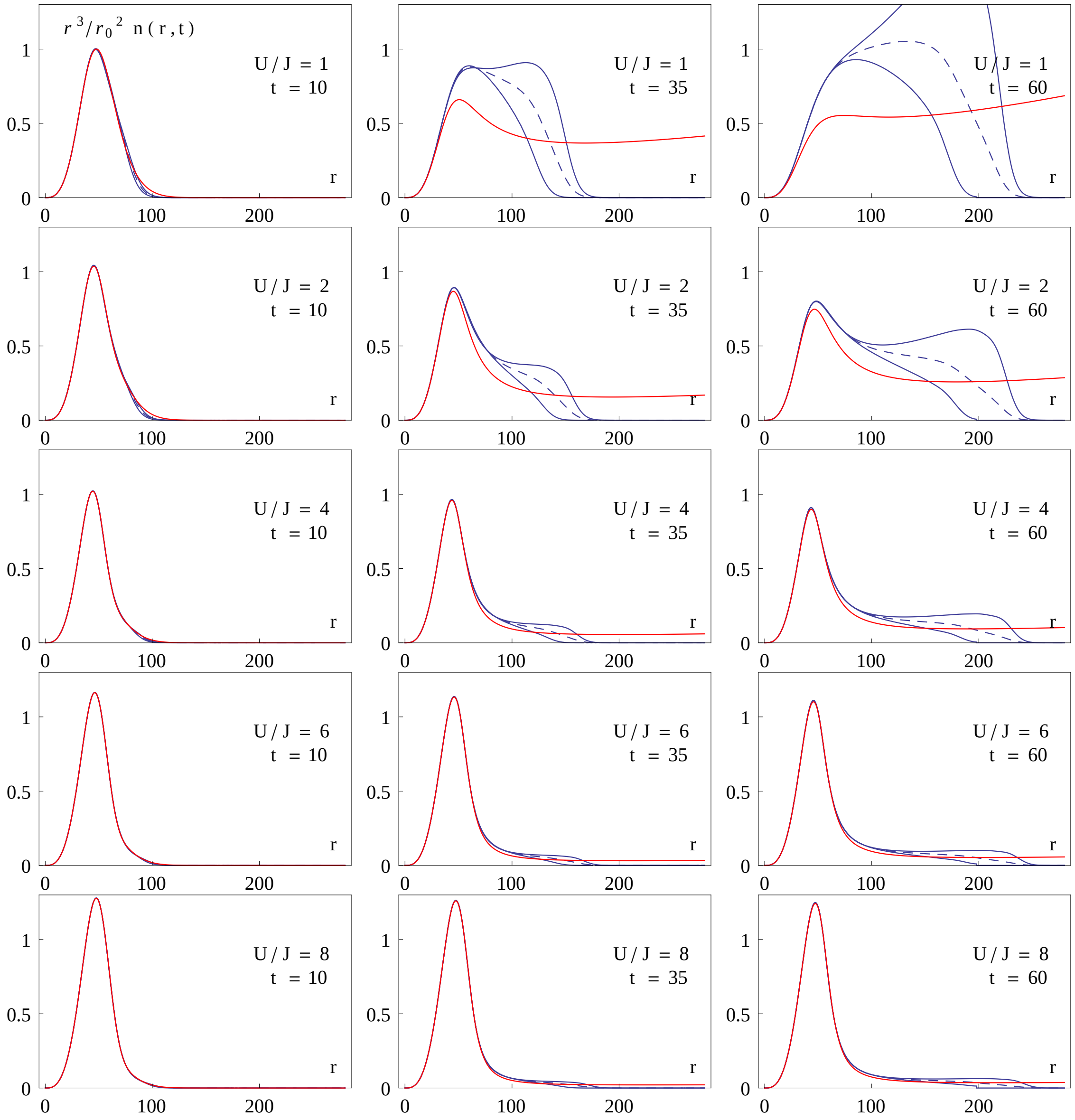

Figure 3.7: Radial density profiles multiplied by r^3/r_0^2, where $r_0 = 200$, for various interactions (increasing from top to bottom) and three subsequent times (left to right). We compare the simulated Boltzmann-data (blue) to the densities resulting from a simulation of the diffusion equation (red), given identical initial conditions. While the diffusion equation is rotationally invariant, the Boltzmann equation is not. Therefore, we show three different curves for the Boltzmann simulations: in each picture, the blue curve on the top corresponds to the density along the diagonal, while the lowest one shows the density along the x-axis. The dashed curve in-between is a radial average. The Boltzmann and diffusion equations agree in the bulk of the cloud for sufficiently large interaction strengths. Note that in contrast to the diffusion equation, the Boltzmann equation predicts a finite spreading velocity, given by the lattice dispersion relation.

For $\delta \geq 1$ the above surface-term does generally not vanish for $r_{max} \to \infty$, assuming exponential or power-law tails for n. Hence, the fast diffusion equation generally does *not* conserve the total number of particles: instead, particles may leave the system at infinity. Note that the boundary term depends on the two exponents δ and d.

From now on, we will concentrate on the physically relevant case of $\delta = 1$. The superfast diffusion equation is also called the *logarithmic* diffusion equation, as $\nabla(\frac{1}{n}\nabla n) = \Delta \log(n)$. Let us relate the spatial dimension d to the possibility to find solutions of the superfast diffusion equation which satisfy particle number conservation. In order to maintain particle number conservation, we derive from Eq. (3.30) that the asymptotic decay of the density profile n has to satisfy $|\partial_r \log(n)| < c/r^{d-1}$ for all $c > 0$, implying

$$|\log(n(r))| < c \int_{r_0}^{r} \frac{1}{\tilde{r}^{d-1}} d\tilde{r} \qquad (r \to \infty) \tag{3.31}$$

for some $r_0 > 0$. As the density goes necessarily to zero and hence the logarithm diverges, also the right hand side has to diverge, which only happens for $d < 2$. Therefore, particles get lost for $d \geq 2$. Still, solutions that do not obey particle number conservation can be found also in this case: those solutions are determined by their particle number loss rates at infinity. In fact, one can specify a time-dependent current at infinity to make the partial differential equation's solution unique [82]. In contrast, for $d < 2$, solutions with a conserved total particle number exist. In one dimension, e.g., one can check that the function $n(x,t) = 2t/(x^2 + (vt)^2)$ is a solution for arbitrary v.

In $d = 3$, it has been shown [82] that *no* solutions exists for initial conditions that involve asymptotically decaying density profiles, i.e. $n(r \to \infty, t = 0) = 0$. This can be interpreted as follows: here, the diffusion is so fast, that all particles vanish at infinity in an infinitesimally small time step. In $d = 2$, Eq. (3.29) tells us that the scaling exponent α diverges. Let us try to understand this case better and map the rotationally invariant two-dimensional diffusion equation to a one-dimensional diffusion equation, following [82]. To this end, we define the function $\tilde{n}(u,t)$ by

$$n(r,t) = \tilde{n}(\log(r), t)/r^2 \tag{3.32}$$

It can easily be checked that $\tilde{n}(u,t)$ solves the fast diffusion equation in $d = 1$ if $n(r,t)$ solves the fast diffusion equation in $d = 2$. Note that $\tilde{n}(u,t) = n(e^u,t)e^{2u}$, which leads to the identity

$$\partial_u \log(\tilde{n}(u)) \quad = \quad 2 + n'(e^u)e^u/n(e^u) \quad \longrightarrow \quad 2 \quad (u \to -\infty) \tag{3.33}$$

where we used the fact that $n'(0) = 0$ because $n(\mathbf{r},t)$ should be differentiable in the origin. We now can calculate the change in the total number of particles in the course of time:

$$\begin{aligned}
\dot{N} \quad &= \quad \int_0^\infty dr\, 2\pi r\, \partial_t n(r,t) \overset{(3.32)}{=} \int_0^\infty dr\, 2\pi r\, \partial_t \tilde{n}(\log(r),t)/r^2 \\
&= \quad 2\pi \int_{-\infty}^{\infty} du\, \partial_t \tilde{n}(u,t) = 2\pi \int_{-\infty}^{\infty} du\, \partial_u^2 \log \tilde{n}(u,t) \\
&\overset{(3.33)}{=} \quad -4\pi + 2\pi \lim_{u\to\infty} \frac{\tilde{n}'(u)}{\tilde{n}(u)} \;\leq\; -4\pi
\end{aligned} \tag{3.34}$$

In the last line, we used that the additional contribution to -4π is negative:

$$\lim_{u\to\infty} \partial_u \log(\tilde{n}(u)) \overset{(3.33)}{=} \lim_{r\to\infty} r\, n'(r)/n(r) \leq \lim_{r\to\infty} r\, \partial_r(cr^{-2})/n(r) \leq 0 \tag{3.35}$$

where we used that the asymptotic decay of n is faster than r^{-2} to give a finite total number of particles. Hence, studying the total number of particles for the two-dimensional superfast diffusion equation leads to a surprising result: there exists an unavoidable, *universal* minimal particle loss rate of 4π, which is independent of the size and shape of the density distribution. The universal loss rate can also be proved geometrically, as is reviewed in Appendix (B.3). Although the above equation is an inequality, it becomes an equality for many initial conditions. One example for such a case is given by the following initial density distribution:

$$n_\epsilon(r,0) = n_0(r) + \epsilon \tag{3.36}$$

Here, the function n_0 obeys $n_0(r \to \infty) = 0$ and the offset ϵ gives an upper bound to the diffusion constant for any finite ϵ. In the limit $\epsilon \to 0$, the system exhibits a loss rate which is given by the universal value of 4π [82]. We also used such a type of regularization when we compared the Boltzmann equation to the diffusion equation, see Fig. 3.7.

Let us come back to our original diffusion equation (3.24), including the physical parameters τ_0, J and U. In theory, the universal particle loss rate should be given by

$$\dot{N} \leq -4\pi\, 2J^2\tau_0 \approx -41.3\, J^3/U^2 \tag{3.37}$$

Due to the minimal loss rate, the total number of particles should vanish after a finite time t_{max}, which is given by

$$t_{max} = -N/\dot{N} \sim N\, U^2/J^3 \tag{3.38}$$

This result is of course *unphysical*: as atoms cannot leave the physical system, the number of particles is conserved[4]. We have shown previously that on a lattice, group velocities are bounded by the band width. Unbounded velocities are an artifact of the diffusion equation and don't reflect the physical situation. In contrast, the Boltzmann equation correctly describes that the cloud cannot expand faster than ballistically. The unphysical result of a universal loss rate reflects the *breakdown of hydrodynamics*: diffusion equations alone can *not* describe the expansion process, even for large U where almost the entire cloud is in the diffusive regime.

The ballistic particles at the cloud's edges *regularize* the diffusive dynamics in the center: they act as “traveling boundary conditions” and limit the diffusive domain of the cloud. In three dimensions, the diffusive core is literally held together by the ballistic boundary: we have stated previously that no solution for a finite total number of particles would exist in infinite space.

While the diffusive core is held together by the ballistic tails, the tails are *fed* by the diffusive core when the particles enter the low density regions. The expansion dynamics is therefore determined by the complex interplay between these two regions.

To conclude, the diffusive dynamics cannot be studied without the feedback from the ballistic particles in the tails. We will now review an analytic toy model, where we combine finite group velocities with the universal loss rate.

3.8.5 Interplay of the diffusive and ballistic regime

Despite of being unphysical, we will now investigate if the universal loss rate of 4π is nevertheless reflected in some property of the physical system. It particular, we pose the question if it can be used to estimate the rate at which the cloud's radius grows in time.

---

[4] Here, we consider an idealized situation of a perfectly conservative lattice potential and are not referring to atomic losses e.g. due to three-body collisions, which have nothing to do with the universal loss rate.

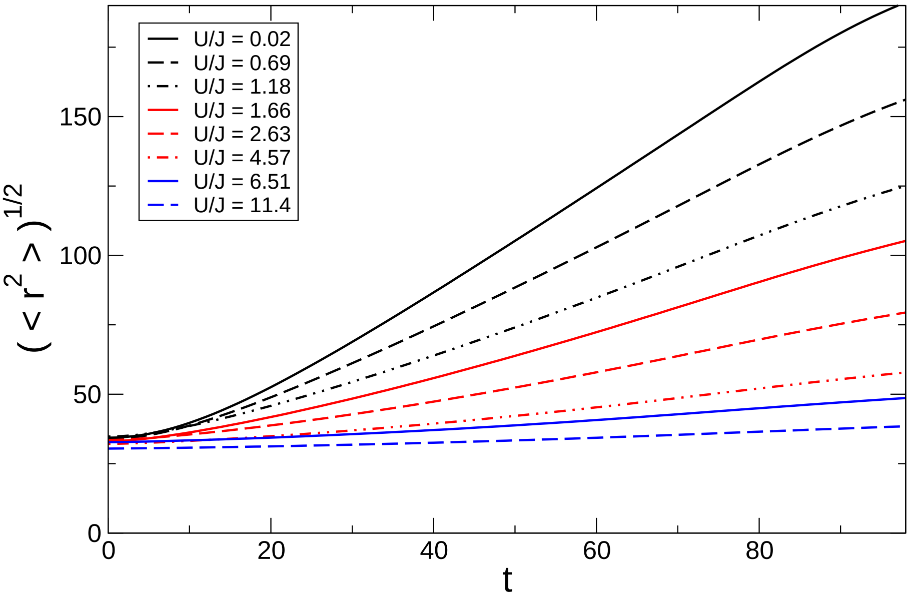

Figure 3.8: Cloud radii defined as $\sqrt{\langle r^2 \rangle}$ as function of time for different interaction strengths. Data are taken from a simulation of the Boltzmann equation. Initial conditions correspond to physical parameters.

From our Boltzmann simulation, we know that the diffusive core emits particles into the ballistic regions of the cloud at an approximately constant rate. Could it be that this rate coincides with the universal loss rate of the diffusion equation? To address this question, let us consider a toy model in which ballistic particles are released from the center of the optical lattice at a continuous rate $W(t)$. Let us assume that the momentum distribution of these particles is uniform, corresponding to an infinite temperature. In analogy to Eq. (3.3) we calculated the emerging density profile of this system:

$$n_{ball}(\mathbf{r}, t) = \int \frac{d\mathbf{k}}{(2\pi)^d} \int_0^t dt' \, W(t') \, \delta(\mathbf{r} - \mathbf{v_k}(t - t')) \tag{3.39}$$

Calculating the mean-square displacement amounts to calculating

$$\begin{aligned} \langle r^2 \rangle(t) &= \frac{1}{N} \int d^2 r \, \mathbf{r}^2 \, n_{ball}(\mathbf{r}, t) \\ &= \langle \mathbf{v_k}^2 \rangle \frac{\int_0^t W(t')(t - t')^2 \, dt'}{\int_0^t W(t') \, dt'} \end{aligned} \tag{3.40}$$

where $\langle \mathbf{v_k}^2 \rangle = \int \frac{d\mathbf{k}}{(2\pi)^d} \mathbf{v_k}^2$. Note that the rate at which particles are emitted from the core, $W(t)$, should give the total number of particles when integrated over all times, i.e. $\int_0^\infty W(t')dt' = N$. Since the universal loss rate predicts a constant flow of particles out of the diffusive core, we choose $W(t) = N/t_{max}$ for times $t < t_{max}$ and $W(t) = 0$ for $t > t_{max}$, where t_{max} was defined in Eq. (3.38). Using $\langle \mathbf{v_k}^2 \rangle = 4J^2$, this leads to the following prediction for the growth of the radius:

$$\langle r^2 \rangle \approx 4 \, J^2 \begin{cases} t^3/(3t_{max}) & (t < t_{max}) \\ t^2 & (t \gg t_{max}) \end{cases} \tag{3.41}$$

This concludes our toy model: assuming that the diffusive core emits particles at a constant rate determined by the universal loss rate, the radius grows in time according to the power-law $r \sim t^{3/2}$. Let us reformulate Eq. (3.41) again in the regime where $t < t_{max}$. By defining $r = \sqrt{\langle r^2(t) \rangle}$, $r_0 = \sqrt{\langle r^2(0) \rangle}$ and $v = \sqrt{\langle \mathbf{v_k}^2 \rangle}$, this relation can be written alternatively as

$$\frac{r}{r_0} \left(\frac{v t_{max}}{r_0} \right)^{1/2} = \frac{1}{\sqrt{3}} \left(\frac{vt}{r_0} \right)^{3/2} \tag{3.42}$$

In order to check this result, we can use the simulated density profiles from the Boltzmann equation, using $v = 2J$. The results of this analysis can be seen in Fig. 3.9, which verifies that for not too small interactions, $r \sim t^{3/2}$. But the analysis reveals more: the slopes of the curves, shown in the inset, should according to Eq. (3.42) coincide with the value of $\frac{1}{\sqrt{3}} \approx 0.577$ (dashed line). Our analytical prediction and the numerical Boltzmann data agree up to 20% for a broad span of values of U/J, which is a remarkable result. We also showed the asymptotic behavior for a much larger system than currently experimentally realizable (lower plot), where the proposed power-law behavior can be seen even clearer.

To summarize, the universal loss rate serves as an adequate analytic estimate for the rate, at which ballistic particles are emitted from the diffusive core of the atomic cloud. Characterizing the unphysical two-dimensional fast diffusion equation, it still influences the rate, at which the physical system's radius grows. This estimate seems to be valid over different orders of magnitude in the interaction strength.

3.9 Discrepancies between theory and experiment

Using the numerical simulation of the Boltzmann equation, we are able to reproduce all experimentally observed phenomena qualitatively and semi-quantitatively. This includes the $U \to -U$ symmetry, the melting of the diffusive core for strong interactions and the pronounced drop in the spreading velocity of the cloud when tuning the interaction strength away from the noninteracting case. However, the observed spreading velocities are consistently larger than predicted by our theory. Therefore one might wonder about the origins of the systematic deviations between theory and experiment.

We will not review all possible origins for systematic errors on the experimental side, which are mainly discussed in [16]. To mention a few of them, there are the possible occupation of higher bands, particle-losses due to light-assisted collisions and imaging-errors. However, we believe that these factors had only a minor effect and are probably not responsible for the observed discrepancies between theory and experiment.

On the theoretical side, there were many approximations involved to derive the Boltzmann equation in relaxation-time approximation from the full underlying quantum theory. Note that in the noninteracting case, good agreement was achieved. Therefore, there is good reason to believe that the use of semi-classical methods, in which the noninteracting cloud follows the Liouvillian dynamics, is well justified.

The main discrepancies occur in the presence of interactions. First, note that even the full Boltzmann equation (1.49) originates from a Keldysh perturbative expansion to second order in $U/(4J)$ [34]. If this expansion were the main origin of deviations, one would expect that the discrepancies become larger with increasing interaction strength. However, such a tendency is not apparent in the numerical data.

We therefore believe that the most important deviations between theory and experiment probably come from the relaxation-time approximation. Note that the relaxation-time

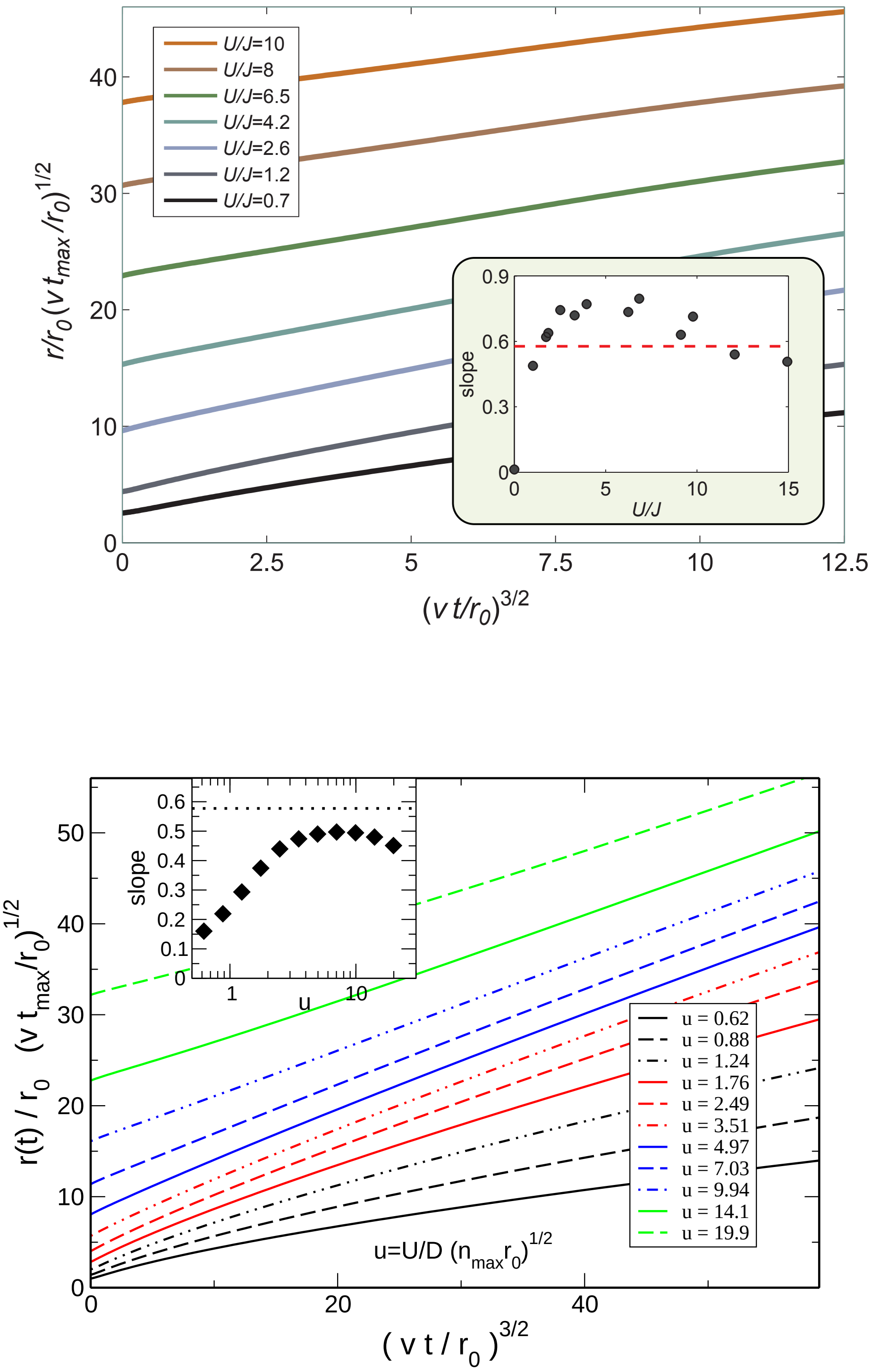

Figure 3.9: Upper figure: Growth of the cloud radius as function of $t^{3/2}$ in renormalized units (data taken from Boltzmann simulations). Units are chosen such that the slope of the curves yields $\frac{1}{\sqrt{3}} \approx 0.577$ according to (3.42)(dashed line in the inset). For large interactions, $r \sim t^{3/2}$, while for small interactions, $t \sim r$ (overall ballistic expansion). Lower figure: Same plot for a larger system. We give the interaction strength in units of $u = U/D\sqrt{n_{max}r_0}$, where n_{max} is the maximal density, r_0 the initial radius and D is half of the band width.

approximation is derived from the full collision integral in two steps: first, the collision-integral is linearized, and second, the diffusion constant is calculated variationally, based on the linearized Boltzmann equation. However, after having tested the variational estimate with different numbers of variational parameters, we do not believe that the variational method is a serious source of error in our approach.

Instead, we believe that the *linearization* of the Boltzmann equation is probably the main source of the observed discrepancies between theory and experiment. Linearization of the collision integral is well justified if the entire system is approximately in local equilibrium. While this assumption is certainly true in the center of the cloud for not too small interactions, it is not valid in the regions of the cloud which are characterized by a crossover between diffusive and ballistic dynamics. Note that although the major part of the cloud may be in local equilibrium, there is a strong feedback from the ballistic tails to the diffusive core. The error that stems from the incorrect description of the crossover regime is uncontrolled and can be large, thus we expect it to be mainly responsible for the observed discrepancies between theory and experiment.

3.10 Summary and outlook

We studied the expansion dynamics of a cloud of fermionic atoms in an optical lattice after releasing it from a trapping potential. The system was modeled numerically using a Boltzmann equation in relaxation-time approximation, whose hydrodynamic limit results in a highly singular diffusion equation. Identical growth rates of the cloud radius for $+U$ and $-U$ were found both in theory and in experiment, which we explained by revealing a novel dynamic symmetry of the Hubbard model. For the case of an expanding repulsively interacting cloud, we predicted the emergence of local negative absolute temperatures, which have however not been addressed experimentally. Furthermore, the system is characterized by a crossover from a diffusive regime in the center of the cloud to a ballistic regime in the tails. While the diffusion equation alone predicts an unphysical particle loss rate and therefore cannot be used alone to describe the physical system, the loss rate serves as an estimate for the rate at which ballistic particles are emitted from the diffusive core.

Experimentally, it would be interesting to observe the expansion dynamics in the presence of a linear potential, as will be discussed theoretically in chapter 5. From a mathematical point of view, it would be interesting to work out a regularization scheme for a proper hydrodynamic limit of the Boltzmann equation for lattice-particles, taking the limited group velocities into account.

4

Equilibration rates and negative absolute temperatures

4.1 Introduction

Nothing can be colder than absolute zero. And yet, the notion of negative absolute temperatures, $T < 0$, exists. They are, however, not *colder* than infinitely cold, but characterize states that have more kinetic energy than any other equilibrium state at $T > 0$; in this sense, they are *hotter* than infinitely hot. The present chapter reviews one possibility to realize negative absolute temperatures in experiments with cold atoms, following an article by Akos Rapp, Achim Rosch and the author [84, 85].

Negative temperatures describe equilibrated systems that are characterized by an inverted population of energy states. To realize negative temperatures in experiment, one needs a system that is thermally very well isolated from its environment, which is usually at $T > 0$. The first system with this property was realized with nuclear spins [86–88]. Coupled nuclear spins that are forced to align with an external magnetic field can be brought to a state at negative absolute temperature by rapidly reversing the magnetic field, so that the spins can not react fast enough and rearrange. As the system is very well isolated from its environment, the spins cannot get rid of their excess energy and equilibrate to a thermal state at negative temperature. It has been also observed that *antiferromangetically* coupled nuclear spins order *ferromagnetically* at negative temperature. This example shows that negative temperatures give access to new regions of the phase diagram for a given system.

Ultracold atoms in optical lattices are ideal candidates to realize negative temperature in experiment, as they are almost perfectly isolated from their environment. The first proposal of realizing negative temperatures with cold atoms in optical lattices is due to Mosk [89], who proposed to realize $T < 0$ by inverting a trapping potential, which we will discuss below. In his article, he mainly studies the system's tunneling rate into higher bands, which has to be small in order to realize gases at $T < 0$ that are sufficiently stable.

The group of W. Ketterle recently realized negative absolute "spin" temperatures in an experiment with bosonic atoms [90]. A balanced mixture of bosonic atoms at two internal states with different magnetic moments was prepared in the presence of a strong magnetic field gradient. This way, the cloud splits in two parts with opposite spin polarizations. Subsequently the lattice depth was increased such that the system entered the Mott insulating regime. In analogy to the realization of negative temperatures with nuclear spins, the magnetic field gradient was quickly reversed. Consequently, negative absolute spin

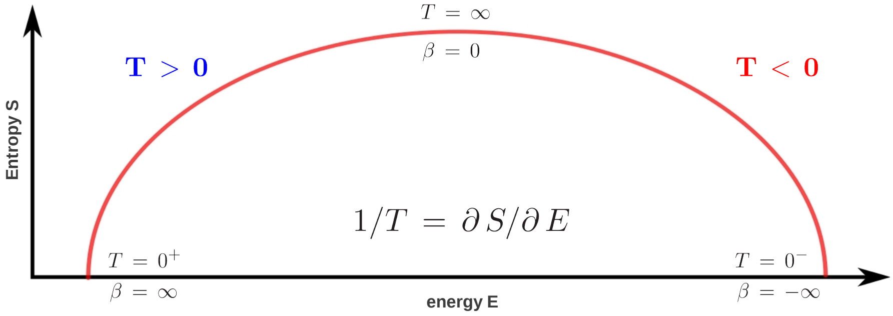

Figure 4.1: Schematic plot of entropy as a function of energy for a system with a bounded continuous spectrum. The inverse temperature is defined as the slope of the entropy curve, as $1/T = \partial S/\partial E$. If the system is bounded both from above and from below, both positive and negative temperatures are possible.

temperatures emerged, which could be estimated by measuring the width of the mixed region of spins at the border between the two polarized regions.

In a recent study, A. Rapp discusses the possibility of exploiting negative temperatures to explore new regions of phase diagrams: in particular, he suggests to use negative temperatures to study the attractive $SU(3)$ Hubbard model with repulsively interacting ^{173}Yb atoms [91], which have been recently used to experimentally realize a lattice model with $SU(6)$ symmetry [92]. An experimental realization of the $SU(3)$ Hubbard model with ultracold atoms would be highly desirable, as it shows similarities to quantum chromodynamics [93]. For practical reasons, ^{173}Yb atoms are a promising sort of fermionic atoms to experimentally realize the attractive $SU(3)$ Hubbard model, as Akos Rapp points out in his article. Unfortunately, however, their scattering length is positive [92]. Negative absolute temperature would reverse the character of interactions and thereby allow for an experimental simulation of the $SU(3)$ Hubbard model at attractive interactions.

In our article [84], we study Mosk's qualitative proposal of realizing $T < 0$ with emphasis on the *dynamics* of the corresponding non-equilibrium process. We also point out that a bosonic condensate at negative absolute temperature will condense in the band *maxima* instead of the band minima. Hence, a time-of-flight image of such a condensate will show peaks at finite momentum (π, π, π), setting the lattice constant $a = 1$. A schematic plot of this scenario is shown in Fig. 4.2. Note that in our aforementioned study on a freely expanding cloud in chapter 3, we already predicted the emergence of negative *local* temperatures for repulsive interactions if the cloud is initially prepared at infinite temperature. In this chapter, we will discuss the possibility of realizing *equilibrated* negative temperatures.

4.2 Qualitative discussion

4.2.1 General properties of negative temperatures

Negative absolute temperatures are a well known and established concept [94, 95]. They describe systems with an inverted population of energy states: states at higher energy have a higher occupation than states at lower energy. Recall the definition of the partition function that describes all thermodynamic quantities ($k_B = 1$),

$$Z = \mathrm{Tr}\ \exp\left(-\hat{H}/T\right) \tag{4.1}$$

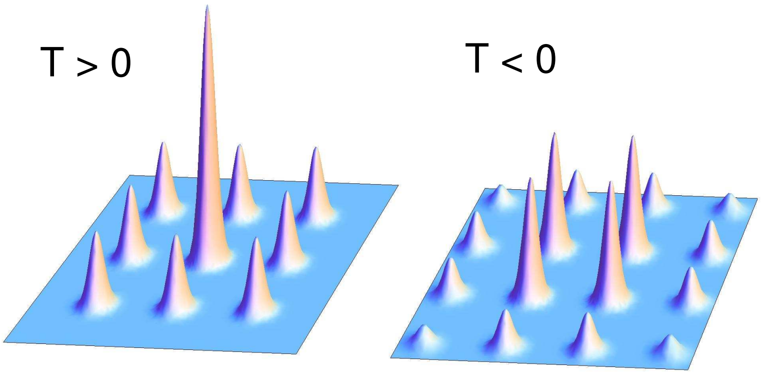

Figure 4.2: Expected time-of-flight image for Bose-condensates at positive temperature (left) and negative temperature (right). While the usual BEC at $T > 0$ condenses at zero momentum, a BEC at $T < 0$ will condense in the band-maxima at momentum (π, π, π).

A system at $T < 0$ with an spectrum that is *unbounded from above* would have a divergent partition function, and thus is not well defined. Therefore, negative absolute temperatures are only possible if a (many-body) state of highest energy exists, i.e. when the energy spectrum is bounded from *above*.

States at negative temperature are in thermodynamic equilibrium unlike other systems with population inversion such as lasers, whose population inversion is created artificially by some external drive. All laws of thermodynamics equally apply for negative temperatures as well. Recall the definition of temperature,

$$1/T = \partial S/\partial E \tag{4.2}$$

where E is the energy and S is the system's entropy. When the entropy of a system *decreases* with increasing energy, negative temperatures emerge. Such a situation is sketched in Fig. 4.1.

Counter-intuitively, a Carnot engine that operates between two reservoirs, one of them having a positive temperature and the other one having a negative temperature, has an efficiency larger than 1. When heat is extracted from a system at negative temperature, its entropy *increases*, as can be seen in Fig. 4.1. Therefore, heat can be extracted from both reservoirs simultaneously, while the total entropy still increases.

Let us try do develop some intuition on negative temperatures. In equilibrium, each state at temperature T of the Hamiltonian H is *equivalent* to a reference state at $\tilde{T} = -T$ of the Hamiltonian $\tilde{H} = -H$: their equilibrium density matrices, which describe all physical properties, coincide due to the identity

$$\exp(-H/k_B T) = \exp(-\tilde{H}/k_B \tilde{T}) \tag{4.3}$$

Therefore, states at negative temperatures can generally be understood as states of the inverted Hamiltonian at positive temperatures. This mapping will be especially important to understand the nonequilibrium processes that we want to study below, which result in a thermal final state at $T < 0$.

4.2.2 Negative temperatures in the Hubbard model

We will concentrate mainly on fermionic systems, described by the Fermi Hubbard model

$$H = -J \sum_{<ij>,\sigma} (c^\dagger_{i\sigma} c_{j\sigma} + h.c.) + U \sum_i n_{i\uparrow} n_{i\downarrow} + V_0(t) \sum_{i\sigma} \mathbf{r}_i^2 n_{i\sigma} \tag{4.4}$$

where $V_0(t)\mathbf{r}^2$ is a time-dependent trapping potential and $\sigma = \uparrow, \downarrow$ is the hyperfine index for the Fermions. We consider a balanced population of hyperfine states. As shown in [89], it is sufficient to concentrate on the lowest band alone, as transitions into higher bands which might result from non-adiabatic manipulations of $V_0(t)$ can be neglected for our purposes.

How can negative temperatures be realized in optical lattices? Obviously, initially a cloud of Fermionic atoms has to be prepared at a positive temperature, as it is usually first cooled down by evaporative cooling before the optical lattice is switched on. This means that one has to realize negative temperatures *dynamically* within the optical lattice. We model the corresponding process by varying certain coupling constants of the Hubbard model in time. As already indicated in Eq. (4.4), it will suffice to manipulate the trapping potential.

For Bosons, negative absolute temperatures are only possible at *attractive* interactions. The bosonic interaction Hamiltonian reads

$$H^B_{int} = \frac{U}{2} \sum_i n_i(n_i - 1) \tag{4.5}$$

where n_i counts the number of Bosons on site i. As the occupation number is not restricted for Bosons, the Bose-Hubbard model as a whole is unbounded from above for $U > 0$, as all interacting Bosons can accumulate on a single lattice site. In contrast, the corresponding *fermionic* variant of the interaction operator (4.4) is bounded both from below *and* from above, as no more than two spin $\frac{1}{2}$ Fermions can coexist on one lattice site. A bosonic system at $U > 0$ will collapse at $T < 0$, just as it would collapse at $T > 0$ and $U < 0$. In Ref. [84], we discuss a scheme how a BEC at negative temperatures can nevertheless be realized in experiment.

As stated previously, the Fermi Hubbard model H at $T < 0$ is equivalent to the Hubbard model $\tilde{H}$ at $T > 0$ with parameters $-V_0$,$-U$ and $-J$. It is important to remember that flipping the sign of the kinetic energy is equivalent to shifting all momenta by $Q = (\pi, \pi, \pi)$, where we have set the lattice constant $a = 1$. This property of the Hubbard model is based on the relation $-J\cos(k) = J\cos(k + \pi)$ and is also related to the dynamical symmetry of the Hubbard model, as discussed in the previous chapter. As a consequence, the phase diagrams of H and $\tilde{H}$ have to coincide upon shifting all momenta by Q. For Bosons at $T < 0$, this explains the aforementioned condensation at momentum Q.

Is there a similar striking signature of negative temperatures for *fermionic* atoms? Note that also condensates of "cooper pairs" of attractively interacting fermionic atoms have been realized in optical traps [6]. Using optical lattices, it should be possible to realize such a fermionic condensate also at negative temperatures for $U > 0, T < 0$, in analogy to the fermionic condensate at $U < 0, T > 0$. Unfortunately, the fermionic superfluid at $T < 0$ will still be condensed at *zero* momentum due to the identity

$$\sum_k c^\dagger_{k\uparrow} c^\dagger_{-k\downarrow} = \sum_k c^\dagger_{k+Q\uparrow} c^\dagger_{-k-Q\downarrow} \tag{4.6}$$

Therefore, it cannot be easily distinguished from a condensate at positive temperatures by simple time-of-flight measurements.

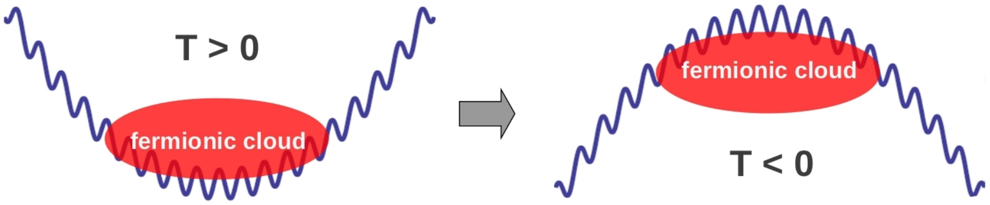

Figure 4.3: Experimental scheme of realizing negative absolute temperatures as proposed in [84, 89]. Fermionic atoms in an optical lattice are exposed to a sudden change of the trapping potential, $V(\mathbf{r}) \to -V(\mathbf{r})$. For energetic reasons, the system is still trapped and equilibrates to a new thermal state at $T < 0$.

4.2.3 Proposed scheme of realizing $T < 0$

In order to reach thermodynamic equilibrium at $T < 0$, the external trapping potential has to be chosen such that the inhomogeneous Hubbard Hamiltonian (4.4) is only bounded from above and not from below. It is important to notice that the Fermi Hubbard model without external potentials is bounded both from below *and* from above: it is the external trapping potential that decides about the boundedness of the inhomogeneous Hubbard Hamiltonian. Initially, V_0 is necessarily positive, but when the trapping potential is inverted, the system does only allow for equilibrium at negative temperatures:

$$V_0 \longrightarrow -V_0 \qquad \Longrightarrow \qquad T > 0 \longrightarrow T < 0 \tag{4.7}$$

Lattice-particles subject to an *inverted* trapping potential, $V_0 < 0$, are also confined: as the kinetic energy of each atom is bounded, particles cannot accelerate in the inverted trapping potential and escape. Instead, they remain trapped in energetically allowed regions around the center of the trapping potential, just as it is the case for $V_0 > 0$. We therefore propose to invert the trapping potential in a time-dependent way, as depicted in Fig. 4.3. Note that the system, subject to $V_0 \to -V_0$, will equilibrate to a thermal state: its dynamics can be mapped to the dynamics of a reference system, characterized by $-U$ and $-J$ and $V_0 > 0$. As the reference system will equilibrate to positive temperatures, the original system will necessarily equilibrate to negative temperatures. Hence, reversing the harmonic potential in some time-dependent way is the basic idea of realizing negative temperatures in optical lattices.

Manipulating the prefactor of the trapping potential $V_0(t)$ in time necessarily implies that the system's entropy increases. In [84], a protocol for the creation of a bosonic BEC at $T < 0$ was given. The generated total entropy was shown to be small enough for a sufficiently large condensate fraction to exist in the final state. The associated amount of heat that is created for different time-dependent manipulations of V_0 will be studied below for *Fermions*.

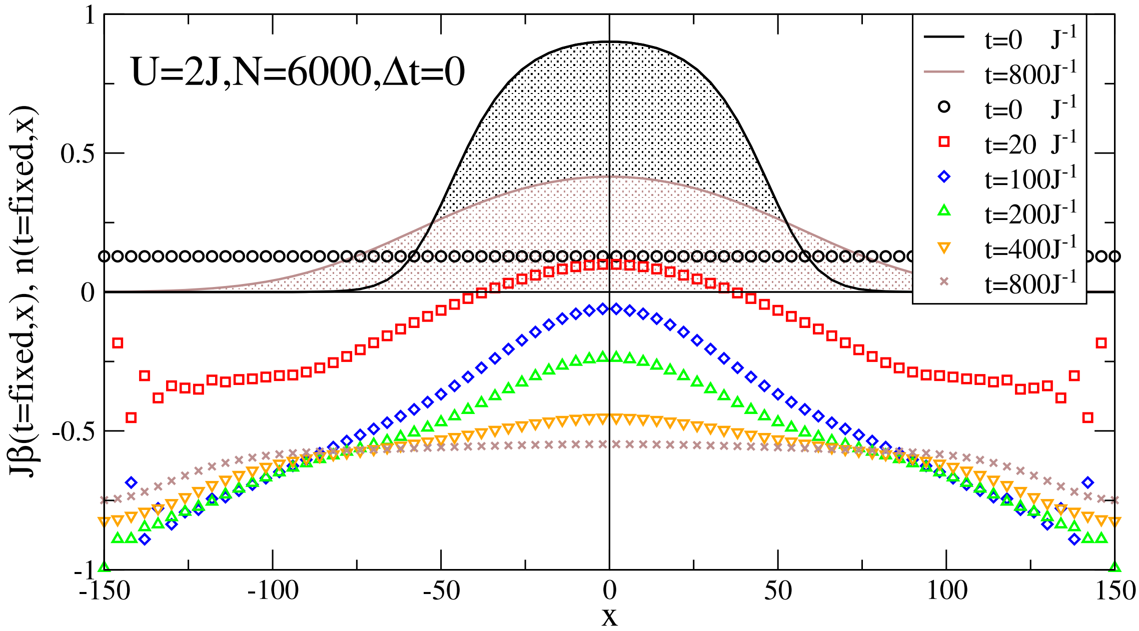

Figure 4.4: Instantaneous quench of the trapping potential $V_{0i} \to -0.05V_{0i}$ for $U/J = 2$. Solid lines: cuts through the density profile at time $t = 0\,J^{-1}$ (black) and at time $t = 800\,J^{-1}$ (brown). Symbols: corresponding local inverse temperatures at various times. At $t = 800\,J^{-1}$, equilibrium is reached to good approximation, reflected in an almost spatially constant inverse temperature.

4.3 Quantitative analysis

4.3.1 Numerical simulations

We studied the relaxation dynamics towards negative temperatures using the version of the Boltzmann equation introduced in chapter 2. To shorten the duration of numerical simulations, we chose a two-dimensional setup. In contrast to the simulations reviewed in the previous study of the expanding atomic cloud, we simulated only a single two-dimensional layer of atoms. However, an explicitly time-dependent external trapping potential had to be implemented in the Runge-Kutta scheme.

Initially, the system is prepared in equilibrium in the presence of a trapping potential $V_i(x) = V_{0i}\,x^2$ with $V_{0i} = 0.01J/a^2$, $N = 3000, 6000$ and 12000 particles, various values of U and $\beta = 0.13$, which characterizes the system uniquely and which mimics the experimental conditions realized in [81] for $N = 6000$ particles in the central layer. Resulting initial entropies are $S/N = 1.2k_B$, consistent with current experiments. Note that time is measured in units of the inverse hopping amplitude J, which translates to SI units according to $1\,\hbar/J = 0.568\,\text{ms}$ for a lattice depth of $8\,\text{E}_\text{r}$, as reviewed in Appendix (B.6).

4.3.2 Instantaneous quench

Let us first study the case of a "quench" in the trapping potential: $V_{0i} > 0$ is switched instantaneously to the negative final value $V_{0f} < 0$. The time-evolution of the local densities and temperatures are shown in Fig. 4.4. As previously, local temperatures are defined for a local reference system in equilibrium which has got the same filling and kinetic energy.

As we have explained above, the system at inverted V_0 equilibrates to a thermal state at $T < 0$. This is shown in Fig. 4.4, where the symbols show the time-evolution of the local inverse temperatures: starting from a homogeneous $\beta > 0$, local temperatures evolve in time and finally equilibrate to a homogeneous, negative value.

In contrast to e.g. a quench in the interaction strength, not all particles are affected by the quench of the trapping potential instantly and in the same way: particles in the middle of the trap are not immediately affected, because they only feel the *gradients* of the trapping potential which are always small in the center of the trap. In contrast, particles in the tails are exposed to a very large difference in potential gradients. Therefore, changes in the local temperatures first emerge in the tails of the cloud. We observe numerically that the new local negative temperatures slowly diffuse from the tails of the cloud into the bulk, until a global equilibrium at $\beta < 0$ is reached. However, due to the small scattering rates and large potential gradients in the tails, it takes longer to equilibrate to the new homogeneous negative temperature there. This can be seen in Fig. 4.4.

4.3.3 Time scales of global equilibration

We will now try to learn more about the time scale of equilibration to a homogeneous negative temperature after the quench in the trapping potential.

There are two relevant time scales involved in the Boltzmann equation: one time-scale is obviously given by the local scattering time $\tau(n, e)$ which drives the system to *local* equilibrium. Note, however, that the collision term of the Boltzmann equation preserves the local energy and local particle density by construction. Hence, it can not lead to a redistribution of kinetic energy in the cloud, which is necessary for global equilibration. Therefore, we need to consider a second time scale that describes how long it takes for particles and energies to redistribute within the system. Under the assumption that most parts of the system remain close to local equilibrium even after the quench, this time scale can be extracted from a diffusion equation and we will refer to it as τ_D. We have argued before that transport in optical lattices for moderate interactions will be diffusive and not convective. Although the diffusion constant depends on the local density, one can crudely postulate an averaged diffusion constant D that describes the entire system. If $R = \sqrt{\langle r^2 \rangle}$ measures the extend of the cloud, the time-scale related to diffusion can be estimated to be

$$\tau_D \sim \frac{R^2}{D} \tag{4.8}$$

To further investigate the scaling of τ_D with the system parameters, we approximate the diffusion constant as $D \sim v^2\,\tau$, where $v \sim Ja$ is a typical velocity and τ is a typical inverse scattering rate. Using $1/\tau \sim n\,U^2/J$ for a small averaged density n and $n\,R^2/a^2 \sim N$, we obtain

$$\tau_D \sim \frac{U^2 N}{J^3} \tag{4.9}$$

Note that this time scale has just the opposite dependency on U and n as the *local* scattering time, which according to Eq. (2.25) is approximately given by

$$\tau \sim \frac{J}{n\,U^2} \tag{4.10}$$

Using our numerical simulations, we were able to check numerically how long the system

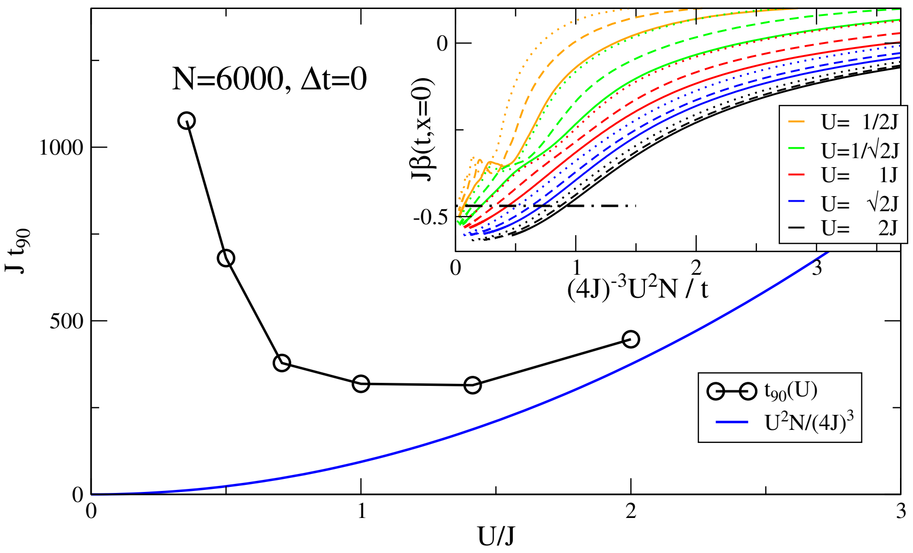

Figure 4.5: Instantaneous quench. Time required to approximately reach equilibrium in the center of the trap, as a function of U. $J\,t_{90}$ is the time after which the critical temperature β_{90} is reached, where β_{90} is 90% of the final temperature in the limit $U \to 0$. Inset: Inverse temperature in the center of the trap as a function of τ_D/t, where $\tau_D = U^2N/(4J)^3$, for various values of U and particle numbers N (solid, dashed and dotted curves for $N = 3000, 6000, 12000$ respectively). Dashed-dotted curve: β_{90}. The fastest equilibration rate is obtained for intermediate values of U.

takes to relax into global equilibrium. To this end, we ran simulations for systems with $N = 3000, 6000$ and 12000 particles for various interaction strengths. We were considering an *instantaneous* quench, in which the trapping potential is directly switched to its final value, $V_{0i} \to V_{0f}$.

The results of the simulation are shown in Fig. 4.5. The inset shows the temperature in the middle of the trap as a function of τ_D/t, where we defined $\tau_D = U^2N/(4J)^3$. For large N and not too small U, the curves with different values of U and N have a tendency to collapse on a single curve. This means that τ_D is indeed the right time scale that determines how long it takes to equilibrate globally. However, as our scaling predictions are based on the hydrodynamic (diffusive) limit, they do not hold for too small values of U. This can be seen by the fact that the yellow, green and red curve in Fig 4.5 do not lie on top of each other. Note that there is a regime where $(\beta - \beta_{eq}) \sim 1/t$ for long times: in this regime, the cloud's density distribution has approximately reached its equilibrium configuration, while the energy density still needs to re-distribute. Hence, the long time dynamics should be governed by ordinary (linear) energy diffusion, which obeys this scaling law.

The main plot of Fig. 4.5 shows the time t_{90}, at which 90% of the final equilibrium temperature is reached in the *center* of the trap as a function of U/J. We observed that this time scale increases both for small *and* for large values of U. For small U, the diffusive time scale τ_D is formally small, however, *local* relaxation is slow due to $\tau \sim J/U^2$. On the other hand, for *large* U, local relaxation is fast, but $\tau_D \sim U^2\,N/J^3$ is large, i.e. it takes very long to redistribute heat within the system. Therefore, also here the global relaxation time diverges in the limit $U \to \infty$. We find that there is an optimal value

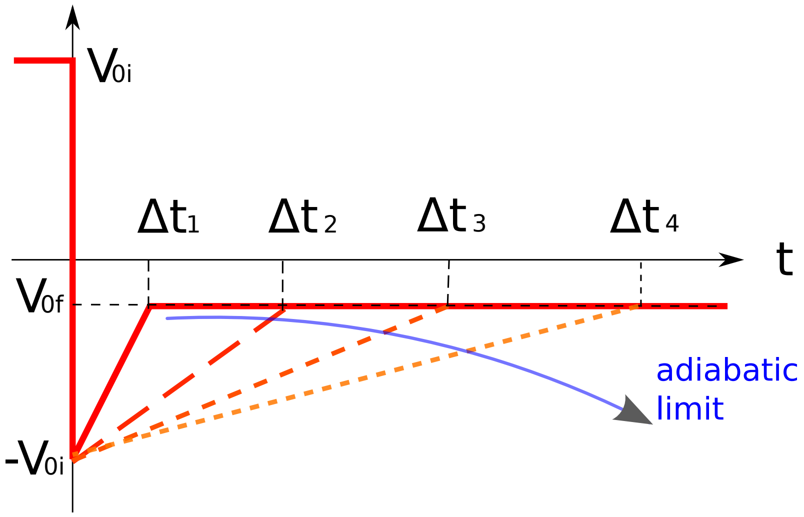

Figure 4.6: Time-dependent ramping of the harmonic trapping potential. The different curves show the prefactor $V_0(t)$ of the harmonic potential, following Eq. (4.13), for four different values of Δt. In all cases, the trapping potential is first switched instantaneously from $+V_{0i}$ to $-V_{0i}$, followed by a linear reduction of $|V_0|$ up to the value V_{0f} within the time span Δt. The larger Δt, the close is the system to the adiabatic limit and the smaller $|T_\infty|$, where $T_\infty < 0$ is the equilibrated final temperature, as can be seen in Fig. 4.7.

U_{opt} of intermediate magnitude, where the time to reach global equilibrium is fastest by demanding that $\tau \sim \tau_D$, which leads to

$$U_{\text{opt}} \sim \frac{J}{N^{1/4}} \tag{4.11}$$

and hence to the optimal global equilibration time τ_{opt}:

$$\tau_{\text{opt}} \sim \frac{U_{\text{opt}}^2 N}{J^3} \sim \sqrt{N}\, J^{-1} \tag{4.12}$$

Note that in all cases it takes long time to equilibrate globally, as we have found numerically that $t_{90} > 300/J \approx 170$ms. This time scale is much larger than the time scales associated to *local* equilibration.

4.3.4 Continuous ramping and adiabaticity

Our simulations have shown that in the case of an instantaneous quench, relaxation to equilibrium at $T < 0$ can be realized in an experimentally accessible time. However, the final values of β are close to zero in the equilibrated final state. For different reasons however, one might be interested in realizing states at large negative β, meaning small $|T|$. Therefore, one needs to realize a refined scheme, where the trapping potential is varied in an almost *adiabatic* way from $V_0 > 0$ to $V_0 < 0$.

A first idea for such an almost adiabatic ramping protocol might be to first increase the laser intensities slowly such that hopping becomes completely suppressed. After flipping the confining potential $V_0 \to -V_0$ instantaneously, the lattice intensities could be slowly reduced to arrive at the original value for J. The problem is that the time scales of equilibration will *diverge* upon sending $J \to 0$. Unfortunately, the duration of every experiment

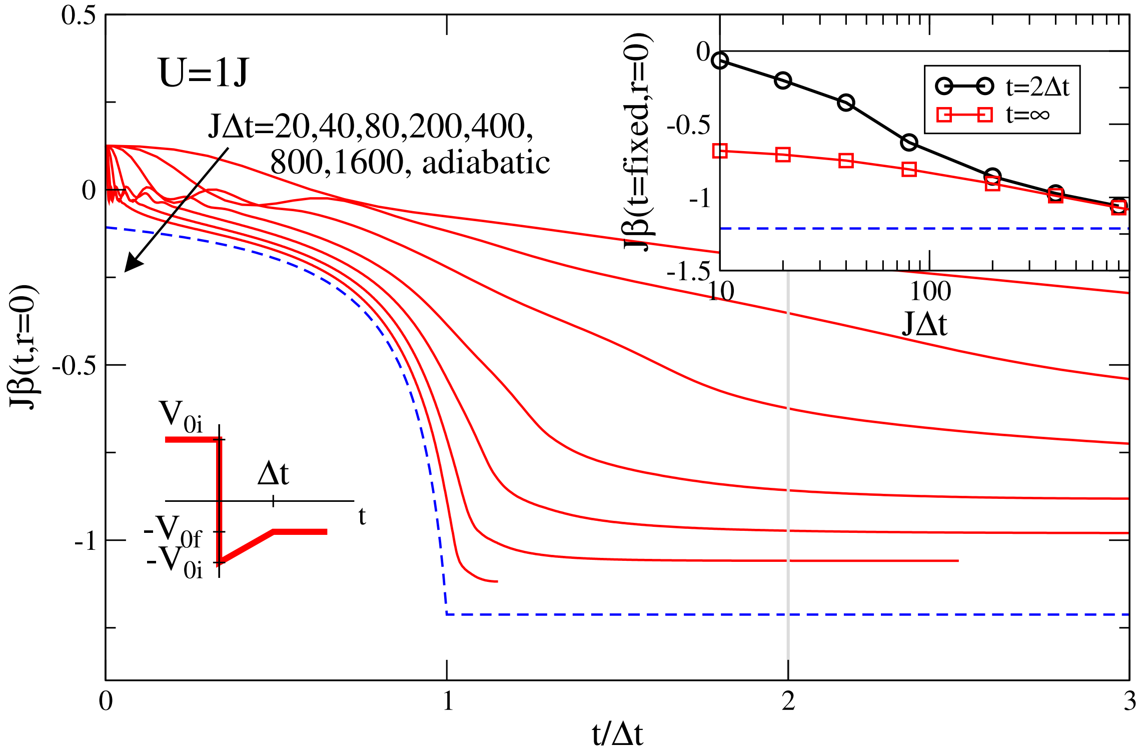

Figure 4.7: Inverse temperatures in the center of the trap as function of $t/\Delta t$. The trapping potential $V_0(t)$ is ramped according to (4.13), depicted in Fig. 4.6 and in the left inset. The right inset compares the inverse temperatures $\beta(0, t = \infty)$ and $\beta(0, t = 2\Delta t)$ as a function of Δt. Blue dashed curves denote the adiabatic limit.

involving optical lattices is limited due to particle losses and heating by inelastic scattering with the laser photons. We therefore propose another scheme where negative temperatures can be realized within experimentally accessible time scales. The proposed scheme is based on a time-dependent trapping potential. In order to reach low final entropies, it is important to restrict the phase space volume that is accessible to the Fermions after inverting the trapping potential. To this end, we propose to compress the fermionic cloud tightly, which results in a band-insulating state at large V_0. As a first step, the trapping potential is reversed abruptly, $V_{0i} \to -V_{0i}$. Due to the tight compression of the cloud, the density distribution can only redistribute very little, so that only a small amount of entropy is produced in the process of equilibration. As a second step, we propose to reduce the strength of the trapping potential slowly, $-V_{0i} \to V_{0f}$ in a time span referred to as Δt. This way, the cloud can expand and thereby "cool", i.e. assume smaller values of $|T|$ with $T < 0$. Hence, we propose the following time-dependent protocol for $V_0(t)$:

$$V_0(t) = \begin{cases} V_{0i} & t = 0 \\ -V_{0i} + (V_{0i} + V_{0f})\, t/\Delta t & 0 < t \leq \Delta t \\ V_{0f} & t > \Delta t \end{cases} \tag{4.13}$$

This protocol is graphically depicted in Fig. 4.6. It has the advantage of allowing for lower temperatures in the equilibrated final state than in the case of an instantaneous quench. Ideally, the strength of the trapping potential is reduced *adiabatically*, $\Delta t \to \infty$ (see Fig. 4.6), which is, however, experimentally obviously not practicable. In Appendix (C.1), we show how the final temperatures for the adiabatic limit can be calculated, based on LDA. We used the Boltzmann simulations to predict how close we are to this adiabatic limit, when opening the trap within the time span Δt.

Fig. 4.5 shows the time evolution of the inverse temperature in the center of the trap for different rates $1/\Delta t$, at which the strength of the trap is reduced. The horizontal axis denotes the rescaled time $t/\Delta t$. The larger we choose Δt, the more we approach the adiabatic limit, reflected in lower and lower entropies in the final state (larger $|\beta|$ for the same V_{0f} and N). Our numerics revealed that even for $\Delta t = 1600 J^{-1} \approx 1\,\text{sec}$ under typical experimental conditions [81], deviations from the adiabatic limit are considerable. In the adiabatic limit, entropy is only generated during the initial switch $V_{0i} \to -V_{0i}$ in the band-insulating state. We found that entropy production due to this switch is tiny for our initial conditions, as $\Delta S/N \approx 0.12\,k_B$. This results in a final value of $\beta \approx -1.2\,J^{-1}$ for $\Delta t \to \infty$. Hence, $|T|$ remains relatively high even for adiabatic conditions due to the high entropy in the initial state. However, it is possible to reach $T \approx -2J$ within the time $200/J \approx 100\,\text{ms}$.

The right inset of Fig. 4.7 compares two different inverse temperatures as a function of the parameter Δt: while the lower curve shows the expected equilibrated final inverse temperature, the upper curve shows the inverse temperature in the center of the trap at $2\Delta t$. The dashed curve at the bottom of the plot shows the adiabatic limit. Again, the plot provides a measure for the adiabaticity: the larger Δt, the larger $|\beta(t \to \infty)|$ and the closer we are to this limit already at $2\Delta t$.

4.4 Summary

We proposed a scheme to experimentally realize negative absolute temperatures for ultracold atoms in optical lattices. Negative temperatures are an established concept in statistical physics, but in the context of ultracold atoms they might help to enable the experimental realization of novel phases. The scheme is based on an inversion of the trapping potential in a time-dependent way. Fermionic ultracold atoms are first prepared in a band insulating state before the potential is flipped. While this process already induces negative temperatures, we propose to reduce the strength of the potential subsequently to achieve lower $|T|$. Using our Boltzmann simulations, we determined the emergent final temperatures for different rates $1/\Delta t$ at which the strength of the trapping potential is reduced, and found that deviations from the adiabatic case are still pronounced even for $\Delta t \approx 1$ sec. For the case of an instantaneous quench in the trapping potential to the final value, we identified the relevant time-scales of *global* equilibration, which is approximately given by $\tau_D = (4J)^{-3} U^2 N$. This time scale describes how fast the kinetic energy can diffuse and redistribute in the system after the quench in the trapping potential, as required to achieve global equilibrium. We found that equilibration is fastest for intermediate values of U, as $\tau_D \sim U^2$ competes with the time-scale $\tau \sim U^{-2}$ of *local* equilibration. These results are not only important in problems related to negative temperatures, but play a role whenever time-dependent manipulations are performed on the external trapping potential.

5

Symmetric expansion in a gravitational potential

5.1 Introduction

Probing the conductivity of a metal by applying an electric field belongs to the most fundamental experiments one can think of. The physics of a quantum particle in a periodic potential in the presence of a linear potential is an old topic, pioneered by Felix Bloch shortly after the birth of quantum mechanics [96]: non-interacting particles show the phenomenon of Bloch oscillations, which emerge due to the coherent Bragg-scattering of the wave packets from the periodic potential. While these oscillations have not been observed for electrons in solids due to the large impact of scattering on impurities, phonons or other electrons, they have been observed in semiconductor-superlattices [97], optical waveguide arrays [98] and ultracold atoms in optical lattices [74, 99, 100]. Bloch oscillations have also been applied to measure masses of atoms with ultrahigh precision [101]. Constant forces for ultracold atoms in optical lattices are naturally realized by the gravitational potential. For harmonically trapped systems, the presence of gravity has the only effect of shifting the potential minimum. However, the atoms are exposed to the linear gravitational potential when the harmonic trapping potential has been eliminated, as described in [81]. Alternatively, constant forces can be realized using accelerated lattices [74, 102]. In the present chapter we study the dynamics of an interacting fermionic cloud in an optical lattice, subject to a linear (gravitational) potential, which was analyzed in collaboration with Akos Rapp and Achim Rosch [63].

In the presence of interactions, Bloch oscillations get damped, which has been observed in experiment with bosonic atoms [76]. The damping of Bloch oscillations has been studied in various situations and is also the subject of chapter 6 of this thesis. Most theoretical studies have been concerned about homogeneous systems [51, 103–111]. As Bloch oscillations were originally observed for bosonic atoms in optical lattices rather than fermionic atoms, the earlier theoretical studies have been also carried out for bosonic systems [106, 108, 109]. Fermions have not been studied until recently. Using nonequilibrium extensions of DMFT, lattice-electrons in the presence of a constant force have been simulated first for the Falicov-Kimball model [104, 105] and later for the fermionic Hubbard model [10, 51, 111], often with focus on the regime of strong interactions. This problem is often associated with the question of how electric fields can lead to a breakdown of a Mott insulator. This so-called dielectric breakdown is a topic of great relevance for novel solid state devices and been studied recently in experiments [112, 113] and in theory, where it has been approached analytically [11,71,107,114,115] and numerically by means of DMFT and DMRG methods [10,116].

When studying the dynamics of ultracold atomic clouds, it is very important to realize that these systems are very well thermally isolated from their environment. Therefore, total energy conservation will play a central role in our discussion. This condition is in stark contrast to the typical conditions in solid state experiments, where the coupling to a heat bath (e.g., the phonon system) fixes the temperature. Let us first comment on an infinite and homogeneously filled system in the presence of a constant force, that we are going to study in detail in chapter 6. In contrast to condensed matter systems, in which the linear steady-state particle currents are usually characterized by a fixed temperature, an isolated system, such as the Hubbard model, will get heated up due to Joule heating. The system will get hotter and hotter in the course of time, and the final state will be characterized by an *infinite* temperature and a vanishing current. This physical necessity holds true in many different parameter regimes of the Hubbard model: at moderate interactions, it applies both for the collision-dominated linear response regime and for the opposite regime, characterized by weakly damped Bloch oscillations, which will be also subject of chapter 6. But also in the Mott insulating regime, where currents are exponentially suppressed, we expect heating up to infinite temperatures in the very long time limit, which seems to be consistent with the short-time behavior observed with non-equilibrium DMFT [10].

In contrast to homogeneously filled systems, a *finite* cloud of lattice-particles in a gravitational field behaves very differently, as we will argue below. But also here, energy conservation plays a major role when studying the long time dynamics. Using a discrete version of the Gross-Pitaevskii equation, the dynamics of an interacting bosonic cloud in a tilted optical lattice was studied by Kolovsky, Gómez and Korsch [117] and by Krimer, Khomeriki and Flach [118]. The Gross-Pitaevskii equation has recently been rigorously derived for the dilute limit of a many-body Schrödinger equation [119] by Erdös, Schlein and Yau. However, bosonic atoms out equilibrium are known to be characterized by a nontrivial interplay of their condensed and uncondensed fractions. An approach that involves condensed and uncondensed Bosons as two coupled hydrodynamic fluids has already been worked out by Landau [120] in the context of superfluid Helium. Going beyond hydrodynamics, Kirkpatrick and Dorfman [121] have derived equations for a condensate which is coupled to a Boltzmann equation for the uncondensed fraction of particles. These equations were later generalized by Zaremba, Nikuni and Griffin [55,122] and for the first time applied to trapped ultracold bosonic atoms, e.g. to predict the damping of the breathing mode.

We consider the nontrivial coupling between the mean-field and the uncondensed Bosons in tilted optical lattices to be very important, especially when one is interested in the long time limit which we expect to be characterized by very high temperatures. Studying the dynamics of the Gross-Pitaevskii equation alone yields theoretical predictions that can be expected to be very different from the results one would obtain from a calculation that respects both bosonic components. The Gross-Pitaevskii equation without coupling to the uncondensed Bosons has been studied in Refs. [117] and [118]. In these studies, a sub-diffusive spreading of the cloud's radius R as a function of time t was postulated, i.e. $R \sim t^{1/\gamma}$, where $\gamma > 2$. While the numerical value of $\gamma \approx 5.3$ was obtained in Ref. [118], the scaling law $\gamma = 4$ was postulated in Ref. [117], by approximating the dynamics of the mean-field equation by an effective nonlinear diffusion equation. In this framework, the diffusion constant was assumed to be proportional to the square of the local density, thus claiming the porous medium equation to be valid, which can be shown

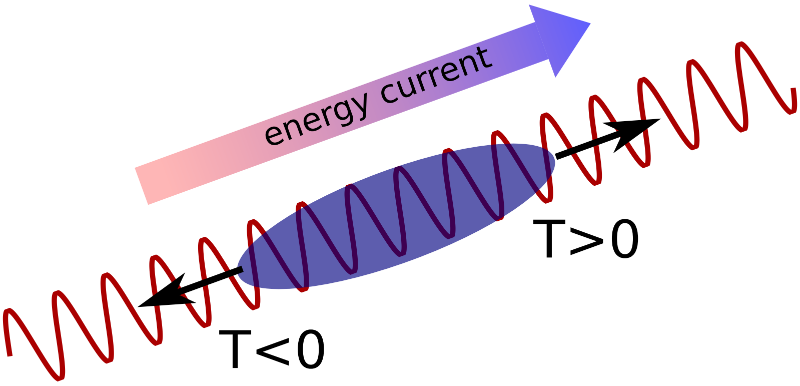

Figure 5.1: Finite atomic cloud in an optical lattice subject to a linear potential. A symmetric expansion preserves the cloud's total energy balance. Heat currents transport kinetic energy "uphill", as atoms loose potential energy at the bottom and gain it at the top of the cloud. The heat current is driven by a gradient of inverse temperature, with $T > 0$ at the top, $T = \infty$ in the center, and $T < 0$ at the bottom of the cloud.

to obey the claimed scaling law [82]. However, as we will show in the present chapter and in chapter 6, the coupling between particle and energy diffusion is qualitatively important for different density dependences of the diffusion constant. In our opinion, studying the dynamics of a finite cloud of bosonic atoms in a tilted optical lattice, taking the interplay between condensed and uncondensed atoms into account, is still a challenging and interesting open problem.

In the present chapter, we consider a finite cloud of interacting *fermionic* atoms in a tilted optical lattice, described by the Fermi Hubbard model in the presence of an additional linear potential. While we will consider the regime of over-damped Bloch oscillations in the present chapter, the opposite regime of weakly damped Bloch oscillations will be discussed in chapter 6.

5.2 Qualitative discussion

We argue that the physics of a finite atomic cloud in an optical lattice is very different from the homogeneous system: energy conservation prevents the cloud from moving up or down over long distances, as illustrated in Fig. 5.1. Without interaction, the particles are Bloch oscillating and their individual total energies are conserved. This assumption is justified as long as the optical lattice is sufficiently deep and inter-band transitions are suppressed.

In presence of interactions, the dynamics is more complex: particles can exchange their kinetic energies by collisions. Therefore, the atoms' individual energies are not conserved any more, but now the cloud's *total* energy is conserved. Total energy conservation allows the cloud to expand *symmetrically upwards and downwards* the gravitational potential: descending particles at the "bottom" of the cloud convert potential energy into kinetic energy, while other particles at the "top" of the cloud rise upwards and convert kinetic energy back into potential energy. This process is possible in the presence of interactions, which induce a non-vanishing heat conductivity in the system and thus allow for the transport of energy from the bottom to the top of the cloud.

So far we have only argued that a symmetric expansion is an energetically allowed option for the dynamics of the cloud. This argument alone does not necessarily imply that the system will evolve accordingly, as the energy balance would also be satisfied differently, e.g. when the system does not move at all. However, if the cloud *does* expand symmetrically, it will certainly increase its phase space volume that way. Therefore, we can expect that the proposed phenomenon will happen: the cloud expands symmetrically upwards and downwards the gravitational potential.

A large cloud in the presence of a force that is not too strong will be approximately in local equilibrium, such that it is characterized by local temperatures. Let us therefore try to predict the distribution of local temperatures in the cloud. Given that the cloud expands symmetrically, the particle current vanishes in the center of the trap. However, the energy current is finite, as it is necessary for the exchange of energies between the upper part and the lower part of the cloud. The presence of an energy current without a particle current implies an approximately constant gradient in inverse temperature, $\beta = 1/T$, around the center. In analogy to the homogeneous system, we can expect that the center of the cloud will be at infinite temperature, $\beta = 0$, for large times. As the inverse temperature vanishes in the center and it is positive in the cloud's upper half, it is necessarily *negative* in the lower half of the cloud, as we have argued that β has an approximately constant gradient around the center. This is the situation sketched in Fig. 5.1: the cloud expands, using an energy current that mediates between positive and negative temperatures. This implies that we have identified another nonequilibrium process where negative absolute temperatures emerge dynamically.

So far we just presented a qualitative picture of what to expect to happen. Our main results to be presented below show (i) that all proposed phenomena indeed show up in an appropriate Boltzmann simulation and (ii) that the simulated problem can even be solved *analytically* in the long-time limit.

5.3 Numerical analysis

We expect the dynamics of a two-dimensional fermionic cloud in the presence of a linear potential to be describable with the following extended fermionic Hubbard model,

$$H = -J \sum_{\langle ij \rangle,\sigma} c^\dagger_{i\sigma} c_{j\sigma} + U \sum_i n_{i\uparrow} n_{i\downarrow} + g \sum_{i,\sigma} x_i \, n_{i\sigma} \tag{5.1}$$

where x_i denotes the distance of the x coordinate of the site i from the origin. Again, we will set the lattice constant $a = 1$. The force $-g$ thus points in the x direction, and it distinguishes our analysis from the previous study presented in chapter 3, where we studied the free expansion of an initially confined atomic cloud in an optical lattice. As we will see below, the dynamics in the presence of a constant force is very different. Studying the dynamics for a two-dimensional system instead of a three-dimensional one has another advantage with regard to experimental realizations: the strength of the gravitational potential can easily be increased or reduced by *tilting* the two-dimensional lattice vertically.

For typical experimental parameters, the gravitational force is of the same order of magnitude as the hopping amplitude, $g \approx J$. However, we are more interested in a regime where g is much weaker. This allows us to approximate the dynamics of the Hubbard model by the two-dimensional variant of the Boltzmann equation that we established in chapter 2, which in the presence of a linear potential reads

$$\begin{aligned} \partial_t f + \mathbf{v_k} \nabla_\mathbf{r} f + \mathbf{F} \nabla_\mathbf{k} f &= -\tau^{-1}(\mathbf{n})(f - f^0(\mathbf{n})) \\ \mathbf{F} &= -\nabla_\mathbf{r}(gx) - U \nabla_\mathbf{r} n(\mathbf{r}, t) \end{aligned} \tag{5.2}$$

Note that the linear potential prevents equilibrium at finite T. We prepare the system in equilibrium in the presence of an additional trapping potential at a temperature $T = J$ (a typical temperature of current experiments), taking interaction energies into account. This initial trapping potential $V_i(\mathbf{r}) = 0.01\, {x_i}^2$ is switched-off in the beginning of the time-evolution. Note that we chose initial conditions translationally invariant in the y direction, i.e. the direction perpendicular to the force. This has the advantage that the spatial y dependence completely drops out of the equation. Thus, the problem reduces in dimensionality to two momentum coordinates and only one spatial coordinate, which allows us to study the dynamics for longer times. From a theoretical perspective, these initial conditions are useful, as we can study the expansion along the direction of the linear potential without considering an additional spreading of the cloud in the direction perpendicular to the force, which would complicate the situation. We simulated intermediate interaction strengths $U/J \leq 2$ and times up to $5000J^{-1}$. As observables, we computed the particle- and energy densities, local temperatures, the center of mass and the local currents.

Fig. 5.2 shows results from a numerical simulation of the Boltzmann equation (5.2). Let us first focus on the short-time dynamics. Starting initially in equilibrium at finite $\beta > 0$, the cloud drifts downwards and thereby converts potential energy into kinetic energy until its total kinetic energy has vanished. For sufficiently strong interactions such that Bloch oscillations are over-damped, the center of mass $x_0(t) \sim \int dx\, n(x) x$ becomes stationary. This can be seen in the inset of Fig. 5.3, which shows the movement of the center of mass for different interaction strengths. In the Appendix (D.1) we study the short-time dynamics of the center of mass in more detail.

The characteristics of the long-time dynamics are even more prominent. Fig. 5.2 shows that after a short transient, temperatures in the center of the cloud become infinite. Also, the entire temperature profile of the cloud becomes antisymmetric with respect to the cloud's center of mass, implying negative absolute temperatures at the bottom of the cloud. Gradients in inverse temperature are approximately linear and quasi-stationary, i.e. they change only on very long time scales. On these scales, the slow symmetric expansion of the cloud also becomes visible in the figure. The tails of the cloud are characterized by Bloch oscillations, where the local densities are too low and scattering events too rare for local equilibration. To conclude, all properties of our above qualitative discussion could be verified by the Boltzmann simulation. We will proceed in studying the expansion dynamics *analytically.*

5.4 Hydrodynamic theory

Similarly to the previous studies, the dynamics in terms of the Boltzmann equation is too complex to be predicted analytically, as the system is characterized by the interplay of several competing time and length scales. The diffusive limit reduces the $2d$-dimensional phase space dynamics to a coupled set of d-dimensional diffusion equations for the conserved quantities, which in our case are the particle and energy densities [1]. Formally, the diffusive limit is justified if the time between two scattering events is smaller than the

---

[1] As stated previously, momentum is not conserved due to the presence of umklapp scattering processes.

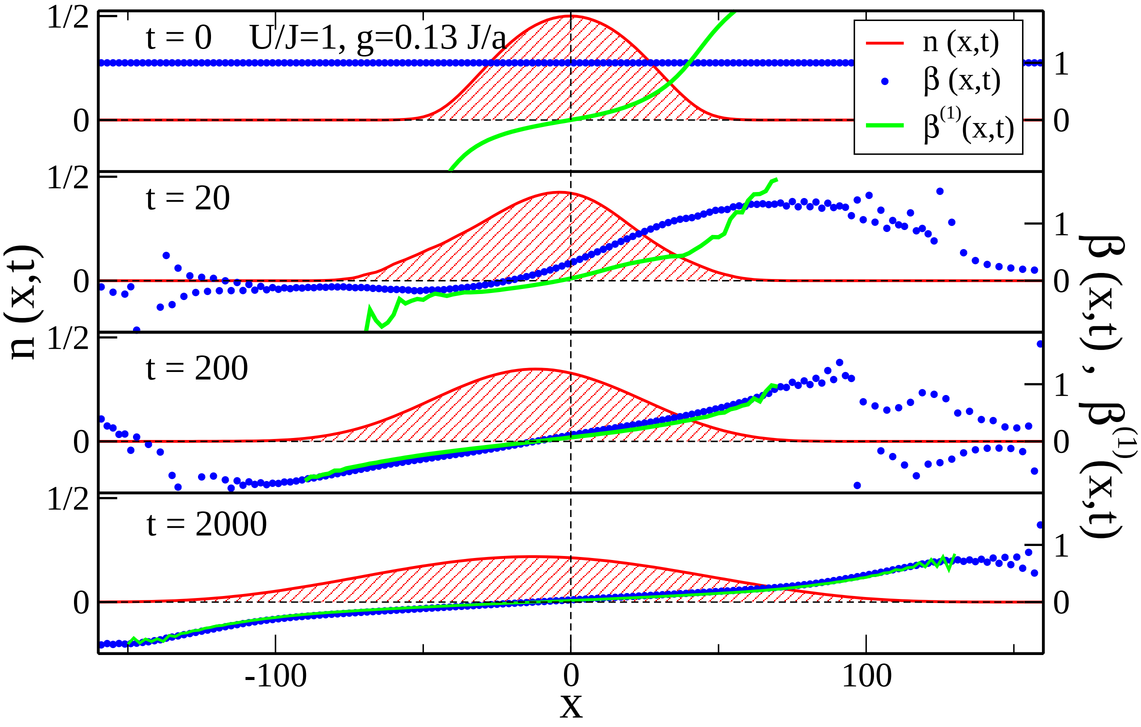

Figure 5.2: Time-evolution of the density profile (red) and inverse local temperatures (blue dots) from a simulation of the Boltzmann equation for $U/J = 1$ and $g = 0.13J$. Starting at positive local temperatures, the cloud initially drifts in the direction of the force and thereby heats up. Soon, it reaches a state whose dynamics is very slow and which is characterized by $T > 0$ at the top, $T = \infty$ in the center and $T < 0$ at the "bottom" of the cloud, accompanying the cloud's symmetric expansion. The green line denotes the quantity $\beta^{(1)} = -\partial_x n/(n\partial_x V)$, which according to the analytic formula (5.13) is expected to agree with β in the diffusive regime. The non-trivial prediction becomes apparent for long times.

Bloch oscillation period, i.e. $g\tau/2\pi \ll 1$. In addition to this criterion, the linear potential has to be weak, as has been discussed in chapter 1. The opposite limit of weakly damped Bloch oscillations is subject to chapter 6.

In addition to studying the problem in the diffusive limit, we use two more additional simplifications: first, we use that local kinetic energies and hence inverse temperatures are typically high during the expansion process. Note that

$$\beta \approx -\frac{e}{4\,J^2\,n} \tag{5.3}$$

holds approximately for high temperatures. We simplify the diffusion constant further, using the *high temperature expansion* that was carried out in chapter 2 and where the particle and energy currents were perturbatively expressed in terms of n and e. We combine those equations with the relaxation rate in its dilute *and* infinite temperature limit, using that

$$\tau^{-1}(n,e) \approx n/\tau_0 \tag{5.4}$$

where $\tau_0 \approx 1.647\,J/U^2$ as given in Eq. (2.25). This approximation is justified, as we are mainly interested in the dynamics at long times when the density has become dilute, i.e. $n \ll 1$. The above assumptions result in coupled diffusion equations for the local particle and kinetic energy densities:

$$\begin{aligned} \partial_t n \quad &+ \quad \nabla \mathbf{j}_n = 0, \qquad \partial_t e + \nabla \mathbf{j}_e = -\mathbf{j}_n \nabla V, && (5.5)\\ \mathbf{j}_n \quad &= \quad -\frac{J^2\tau_0}{n}\left(2 + \frac{e^2}{16J^2n^2}\right)\nabla n + \frac{\tau_0 e}{2n}\nabla V + \frac{\tau_0 e}{8n^2}\nabla e + \mathcal{O}(e^3) && \\ \mathbf{j}_e \quad &= \quad -\frac{3J^2\tau_0}{2n}\nabla e + \frac{3\tau_0 e^2}{8n^2}\nabla V + \mathcal{O}(e^3) && (5.6) \end{aligned}$$

The source term in the continuity equation for the kinetic energy takes into account that the *total* energy density and not the kinetic energy density is conserved. Above, we listed all terms of the high temperature expansion that turn out to contribute in the long-time limit according to the following analysis.

As an alternative to the above equations, one could also have derived similar equations directly from the linearized Boltzmann equation (1.55): to this end, one could use the variational principle presented in chapter 1 to calculate the matrix of diffusion constants for n and e variationally. However, here we derived the hydrodynamic equations from the relaxation-time approximation in order to allow for a quantitative comparison between our numerical simulations and our analytical predictions. Both versions of hydrodynamic equations agree up to changes in numerical prefactors. In this sense, Eqs. (5.5) and (5.6) are *exact* for the high temperature limit of the Hubbard model in dimensions $d > 1$ for large clouds and not too strong forces g. Note that in $d = 1$, the Hubbard model is integrable and is characterized by infinitely many conservation laws. Therefore, this hydrodynamic approach does not apply there.

5.5 Analytic solution of the hydrodynamic equations

5.5.1 Scaling ansatz

The hydrodynamic equations (5.5) and (5.6) form a closed set of equations that should describe the same expansion dynamics as the Boltzmann equation (5.2), given that the required approximations were justified. Despite of being non-trivially coupled and highly nonlinear, these equations can be solved *analytically.* The analytic solution is based on a *scaling ansatz.*

In the following, we are going to measure the distance x relative to the center of mass. We start our asymptotic analysis with the following scaling ansatz for the particle density:

$$n(x,t) = N_0 \frac{1}{R(t)} F[x/R(t)] \; , \tag{5.7}$$

We impose the normalization conditions $\int dz\, F[z] = \int dz\, z^2 F[z] = 1$ on the scaling function. Then, N_0 is the total number of particles and R is the radius of the cloud. Note that we also assume that $F[z] = F[-z]$. The scaling ansatz postulates that the expansion dynamics depends only on the ratio of $x/R(t)$, where the function $R(t)$ is unknown for the moment and measures the diameter of the density profile, i.e. $R^2(t) = \int dx\; x^2 n/N_0$. Our goal is to calculate both functions, i.e. $R(t)$ and $F[z]$, in the long-time limit. Note that we don't have the option to choose the prefactor in front of the scaling function other than $1/R(t)$: only this way, the total integral over the x-coordinate remains independent of time, which means that the total number of particles is constant.

The coupled hydrodynamic equations also require a second scaling ansatz for the kinetic energy density. This second ansatz is more sophisticated, and relies on the idea that to leading order, energy conservation prevents the cloud from rapidly expanding, making the expansion dynamics very slow. We decompose the kinetic energy density into a dominant contribution e_0 and a subleading correction Δe,

$$e = e_0 + \Delta e \tag{5.8}$$

where we *define* the leading order contribution to the kinetic energy density e_0 such as to make the particle current vanish. Following this idea, we use Eq. (5.6) for the particle current $\mathbf{j}_n$ and set to zero, where we consider only the lowest power in e. We then identify e_0 as the term that fulfills that relation exactly:

$$0 = -2\frac{J^2 \tau_0}{n} \nabla n + \frac{\tau_0 e_0}{2n} \nabla V \tag{5.9}$$

This equation can be solved for e_0, which yields

$$e_0(x,t) = \frac{4J^2}{\partial_x V} \partial_x n \tag{5.10}$$

It can be checked easily that e_0 does not generally solve the energy continuity equation. It is important to also consider the corrections $\Delta e = (e - e_0)$, which finally leads to the fact that the cloud expands. We therefore make a second scaling ansatz for Δe,

$$\Delta e(x,t) = \frac{J}{R(t)^{1+\gamma}} G[x/R(t)] \; , \tag{5.11}$$

involving a second scaling function $G[z]$ and an unknown scaling exponent γ. In accordance with its subleading character, we assume that $\gamma > 0$. Combining Eqs. (5.7),(5.10) and (5.11), we arrive at the scaling form for the total kinetic energy density:

$$e(x,t) \;=\; \frac{4J^2}{\partial_x V} N_0 \frac{1}{R(t)^2} F'[x/R(t)] + \frac{J}{R(t)^{1+\gamma}} G[x/R(t)] \tag{5.12}$$

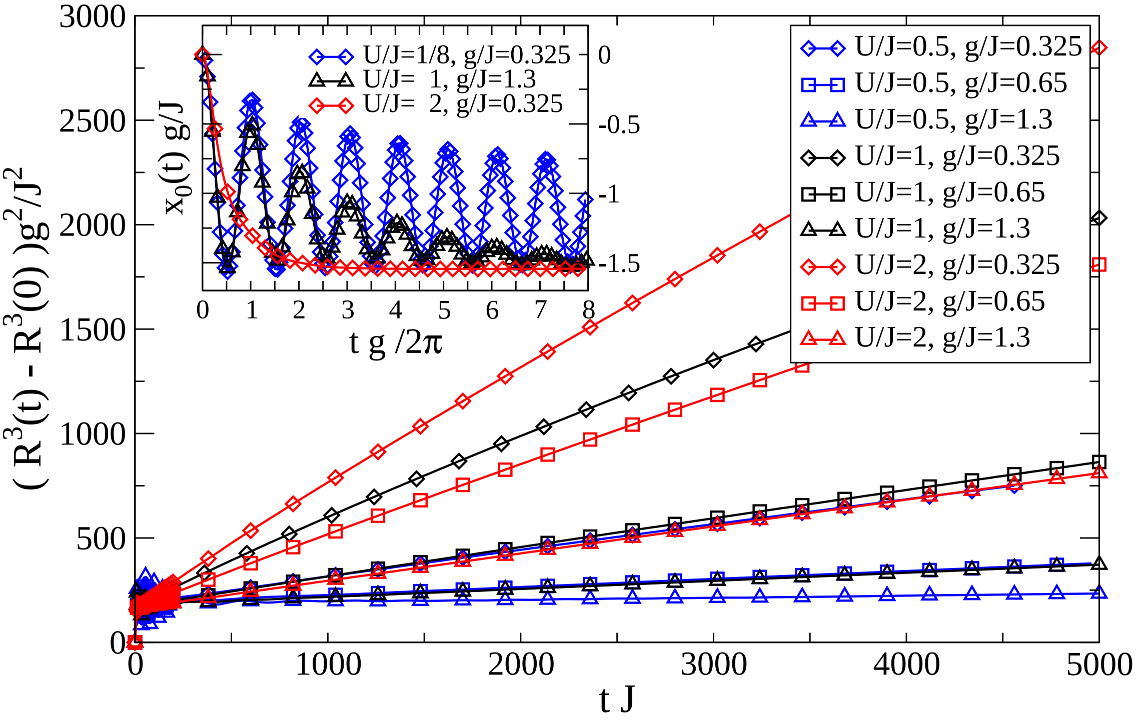

Figure 5.3: Cubed radius of the cloud as a function of time for different interaction strengths U and different strengths of gravity g. To a good approximation, $R^3(t) \sim (t - t_0)$. Inset: Damped Bloch oscillations of the center of mass $x_0(t)$ in a regime beyond the range of validity of the diffusion equation (strong forces).

This concludes our scaling ansatz. Before we proceed, let us check if e_0 is indeed the dominant contribution to the kinetic energy, such that Δe is really small. To this end, we combine (5.10) with (5.3) to derive

$$\beta(x) \approx -\frac{\partial_x n(x)}{n(x)\, \partial_x V(x)} \tag{5.13}$$

If $e \approx e_0$, this relation should be almost an identity. We test this relation numerically in Fig. 5.2, where $\beta(x)$ is plotted blue, and the right hand side of Eq. (5.13) is plotted green. In the long-time limit, we see that this identity is satisfied to a very good approximation, which confirms the fact that Δe is very small.

In the following, we are going to solve the coupled diffusion equations asymptotically, using Eq. (5.7) and Eq. (5.12). The problem amounts to solving a problem that involves two (continuity) equations and two unknowns $R(t)$ and γ.

5.5.2 Particle number continuity

As a first step, we will relate the scaling exponent γ to the function $R(t)$ that describes the growth of the radius. To this end, we use the particle number continuity equation in combination with our scaling ansatz. Note that there are two different ways to calculate the particle current, using the scaling ansatz: it can be obtained either from the right or the left hand side of the particle number continuity equation (5.5),(5.6). Using the left hand side, the particle current $\tilde{j}_n$ can be obtained via integration over x:

$$\tilde{j}_n(x,t) = -\int_{-\infty}^{x} \partial_t\, n(x',t)\, dx' = N_0 \frac{x}{R(t)^2} F[x/R(t)]\dot{R}(t) \tag{5.14}$$

Alternatively, the right hand side of equation (5.6), neglecting terms of order e^2, gives

$$\begin{aligned} j_n(x,t) &= -2\frac{J^2\tau_0}{n}\partial_x n + \frac{\tau_0(e0+\Delta e)}{2n}\partial_x V \\ &\overset{(5.9)}{=} \frac{\tau_0 \Delta e}{2n}\partial_x V \\ &= \frac{\partial_x V\, J\, \tau_0\, G[x/R(t)]\, R(t)^{-\gamma}}{2\, N_0\, F[x/R(t)]} \end{aligned} \tag{5.15}$$

The two expressions (5.14) and (5.15) have to be identical, i.e. $j_n = \tilde{j}_n$. This identification yields

$$R(t)^{\gamma-1}\dot{R}(t) = \frac{\partial_x V J \tau_0 G[z]}{2N_0^2 z F[z]^2} =: \frac{\alpha^\gamma}{\gamma} \tag{5.16}$$

where we have substituted x by the new variable $z = x/R(t)$, and $\alpha > 0$ is an unknown constant. We also used that the partial differential equation factorizes in the new variables t and z. The ordinary differential equation for $R(t)$ is solved for

$$R(t) = (R_0^\gamma + \alpha^\gamma t)^{1/\gamma} \approx \alpha\, t^{1/\gamma} \quad (t \to \infty) \tag{5.17}$$

where we used that we are interested in asymptotically long times, and where R_0 is the radius at the initial time zero. As a result, we have achieved to relate $R(t)$ and γ, using the particle number continuity equation.

5.5.3 Energy continuity equation

It remains to determine γ, using the energy continuity equation. We calculate the necessary currents with the scaling ansatzes

$$\begin{aligned} n(x,t) &= \frac{N_0}{\alpha}\, t^{-1/\gamma}\, F[x\, t^{-1/\gamma}/\alpha] \\ e(x,t) &= \frac{4J^2 N_0}{\partial_x V\, \alpha^2} t^{-2/\gamma} F'[x\, t^{-1/\gamma}/\alpha] + \frac{J}{\alpha^{1+\gamma}} t^{-1-1/\gamma} G[x\, t^{-1/\gamma}/\alpha] \end{aligned} \tag{5.18}$$

which are nothing but (5.7) and (5.12) in combination with the fact that $R(t) = \alpha\, t^{1/\gamma}$. Note that we can calculate the particle current in two equivalent ways, using either j_n or $\tilde{j}_n$, given by (5.15) and (5.14) respectively. To reduce the number of terms, we use $\tilde{j}_n$, i.e. we calculate

$$0 \;=\; \partial_t e + \partial_x\, j_e + \tilde{j}_n\, \partial_x V \tag{5.19}$$

We use the full expressions for the particle and energy currents including Hartree-corrections, i.e. $V(x) = gx + Un(x)$, and higher order terms in e. The expressions for the currents and the resulting energy continuity equation are very lengthy and are given in section D.2 of the Appendix. When having calculated the energy continuity equation with the ansatzes (5.18), we again substitute the spatial variable x by

$$z = x\, t^{-1/\gamma}/\alpha \tag{5.20}$$

which eliminates the time-dependence in the arguments of the scaling functions F and G. For later convenience, we also replace α by the new variable α_0, where

$$\alpha_0 = \alpha \left(\frac{J^4 \tau_0}{g^2 N_0} \right)^{-1/\gamma} \tag{5.21}$$

We can now calculate the energy continuity equation, involving the ansatzes and variables mentioned above. The resulting equation is extremely lengthy, but it can be represented as a fractional polynomial in t of the form

$$0 \;=\; C_0[z]\, t^{-1} + C_1[z]\, t^{-\frac{2}{\gamma}-1} + C_2[z]\, t^{-\frac{1}{\gamma}-2} + C_3[z]\, t^{-3/\gamma} + ... \tag{5.22}$$

which involves the coefficient functions $C_i[z]$ that depend on the variable z, and on the scaling functions and the parameters J, g, τ_0 and N_0, but *not* on t. Importantly, we neglected all powers in t which are subleading in the large t limit for *any choice* of γ. As an example, we neglected terms proportional to $t^{-5/\gamma}$, which are a priori smaller than terms proportional to $t^{-3/\gamma}$ for any $\gamma > 0$.

We want Eq. (5.22) to be asymptotically satisfied in the large t limit. The non-vanishing coefficient $C_0[z] = \alpha_0^3\, z\, F[z]/(6\gamma)$ stems from the time derivative of the energy continuity equation. It needs at least one other coefficient $C_i[z]$ that decays with the same power law, i.e. as t^{-1}, in order to be canceled asymptotically. It turns out that there is only a single choice for γ which makes this possible, namely the choice of

$$\gamma = 3 \tag{5.23}$$

Let us reflect this important result for a moment: the scaling functions depend on the argument $r/t^{1/3}$, which tells us that the cloud's radius R increases *subdiffusively* as the *third* root of time,

$$R \;\sim\; t^{1/3} \quad (t \to \infty) \tag{5.24}$$

This remarkable analytic result explains the numerical observation of the slow expansion dynamics in the Boltzmann simulations. To test the result, we plotted the cube of the cloud's radius as a function of time in Fig. 5.3. For a wide range of parameters we obtain straight lines, which verifies our result and justifies the approximations involved in the analytical derivation.

5.5.4 Formulas for the scaling functions

Having already achieved our main result, i.e. proving the asymptotic scaling law $R \sim t^{1/3}$, we will show now that even an explicit formula for the scaling functions $F[z]$ and $G[z]$ can be obtained for large times. To do so, we consider Eq. (5.22) in combination with $\gamma = 3$. The terms proportional to C_1 and C_2 become subleading in the limit of long times,

$$C_0[z]t^0 + C_1[z]t^{-\frac{2}{3}} + C_2[z]t^{-\frac{1}{3}-1} + C_3[z]t^0 \;\longrightarrow\; C_0[z] + C_3[z] \quad (t \to \infty) \tag{5.25}$$

Using the explicit formulas for the coefficient functions from the Appendix (D.2), we arrive at the following ordinary differential equation for F, valid asymptotically in the long-time limit:

$$\begin{aligned} 0 \;&=\; C_0[z] + C_3[z] \\ &=\; -\frac{F^{(3)}[z]}{F[z]} - \frac{2F'[z]^3}{F[z]^3} + \frac{3F'[z]F''[z]}{F[z]^2} + \frac{1}{18}\alpha_0^3 z F[z] \end{aligned} \tag{5.26}$$

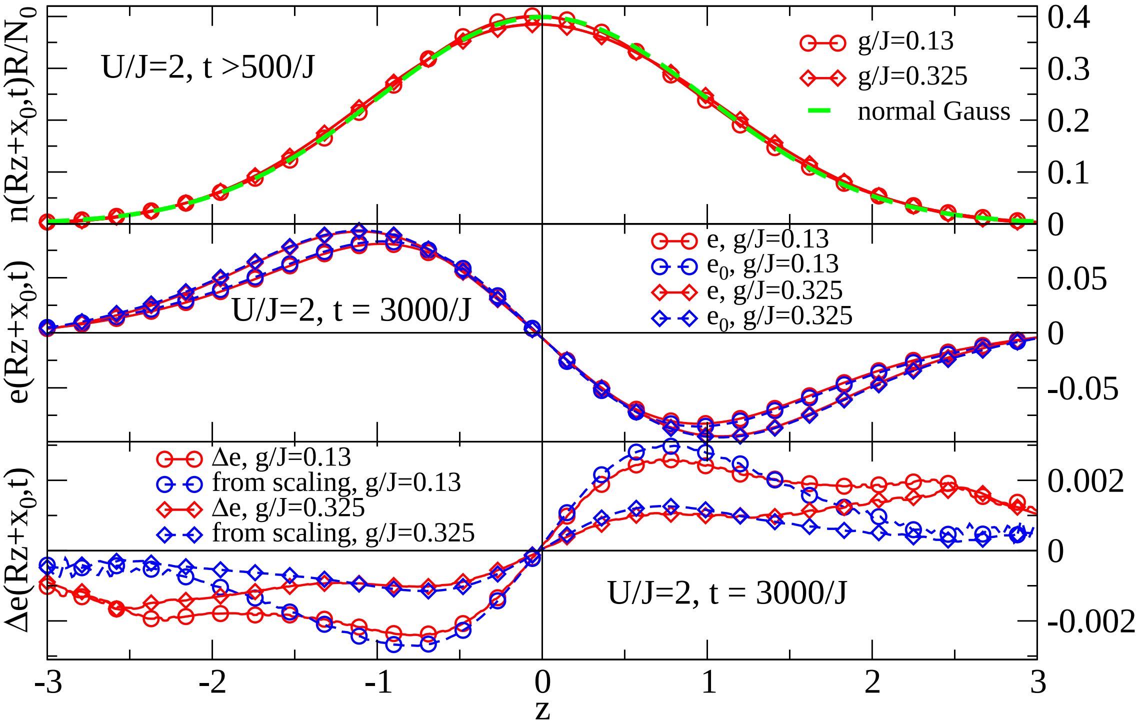

Figure 5.4: Top panel: Rescaled density profile as a function of $z = x/R(t)$ for $tJ = 500, 1500, 2500, 3500$. Under the scaling transformation, the rescaled densities at different times collapse and agree with the predicted scaling form (normalized Gaussian) to a high precision. Middle panel: Energy densities e and e_0, defined in Eq. (5.10). Bottom panel: Comparison of two different expressions for Δe (Eq. (5.10) and Eq. (5.33)). Currents, energies and densities are taken from the Boltzmann simulation.

This equation can be alternatively written as

$$\partial_z^3 \log F[z] = \frac{\alpha_0^3}{18}\, z\, F[z] \tag{5.27}$$

Surprisingly, a simple analytic solution can be found even for the scaling function under the assumption that $\alpha_0 \ll 1$: the above differential equation is solved approximately by a Gaussian function,

$$F[z] \approx \frac{e^{-z^2/2}}{\sqrt{2\pi}} + O(\alpha_0^3) \tag{5.28}$$

We are also able to derive a formula that expresses $G[z]$ in terms of $F[z]$. To this end, we proceed in almost the same way, starting from the continuity equation for the energy density. This time, however, we use the alternative expression j_n for the particle current from Eq. (5.15) instead of using $\tilde{j}_n$ from Eq. (5.14), resulting in

$$0 \;=\; \partial_t e + \partial_x\, j_e + j_n\, \partial_x V \tag{5.29}$$

Also here, we use the ansatz (5.18) and repeat the previous steps, but this time we immediately set $\gamma = 3$ and we are only interested in the limit $t \to \infty$. The resulting equation is similar to Eq. (5.26), but now involves both scaling functions F and G:

$$0 = -6F^{(3)}[z] - \frac{13F'[z]^3}{F[z]^2} + \frac{20F'[z]F''[z]}{F[z]} + \frac{g^3 G[z]}{2J^3 N_0} \tag{5.30}$$

Using Eq. (5.26) to get rid of the third derivative $F^{(3)}[z]$ yields

$$G[z] \;=\; \frac{2N_0 J^3}{g^3}\left(\frac{\alpha_0^3 z F[z]^2}{3} + \frac{F'[z]^3}{F[z]^2} - \frac{2F'[z]F''[z]}{F[z]}\right) \tag{5.31}$$

Finally, we want to use Eq. (5.31) to derive a new relation: we relate the corrections to the kinetic energy Δe to the particle currents and the gradients of the particle density. Using the scaling ansatz for the density and substituting $x = z\, R(t)$ yields the scaling function

$$F[z] = \frac{R(t)\, n(zR(t), t)}{N_0} \tag{5.32}$$

Now, using Eq. (5.31) in combination with Eq. (5.32) and (5.11) yields

$$\Delta e \approx \frac{2}{g\tau_0} n j_n + \frac{2J^4(\partial_x n)^3}{g^3 n^2} - \frac{4J^4 n(\partial_x n)(\partial_x^2 n)}{g^3 n^2} \tag{5.33}$$

where we have used $j_n = x\dot{R}(t)n(x,t)/R(t)$ according to (5.14). As will be shown below, we use the last relation to compare our analytical findings with the Boltzmann simulations. This concludes our analytical solution of the asymptotic expansion dynamics in the diffusive limit. Most importantly, we have found asymptotic scaling of $R \sim t^{1/3}$, but we have also derived explicit formulas for the scaling functions in the long time limit. We have also shown that the scaling function for the density profile is almost a Gaussian.

5.5.5 Comparison of the analytical and numerical results

We can now use our analytic predictions and compare it with the numerical results. For not too strong forces and large clouds, the Boltzmann equation is in its diffusive regime, and we can expect that its dynamics is very close to the dynamics predicted by the coupled diffusion equations (5.5),(5.6). The top panel of Fig. 5.4 shows a scaling plot of the density profile. Here, we compare the particle densities for a range of time between 500 and 3500, in which the cloud's radius changes significantly, see also Fig. 5.2. The plot shows the scaling function $F[z]$, obtained by rescaling the densities according to Eq. (5.32), where $R(t)$ is the instantaneous second moment of $n(x,t)$. All curves lie on top of each other to surprising accuracy, reflecting that the numerically simulated densities are close to a self-similar form, justifying our scaling ansatz. We also compare the scaling functions with a normalized Gaussian function (green, dashed line), which according to Eq.(5.28) is its theoretically expected shape for a small parameter α_0. This parameter depends on the initial conditions and can be extracted from the slope of the curves in Fig. 5.3, using that

$$g^2 R^3 \approx \alpha_0^3 \frac{J^4 \tau_0}{N_0} t \tag{5.34}$$

which can be derived from Eqs. (5.17) and (5.21). α_0 is not small for the numerical data shown in Fig. 5.4: in fact, for $U/J = 2, g/J = 0.325$ we find that $\alpha_0 \approx 3$. However, the top panel of Fig. 5.4 shows that the Gaussian form of the scaling function, predicted in Eq. (5.28), is still approximately satisfied. In the second panel of Fig. 5.4, we show the kinetic energy density $e(x,t)$ and compare it with $e_0(x,t)$ from Eq. (5.10), rescaled according to the scaling ansatz. We find that the curves for e (blue curves) and e_0 (red curves) are so close to each other that they can hardly be distinguished from one another, reflecting the smallness of Δe.

In the lowest panel, we compare two different quantities that are identified with each other only according to our analytical study: while the red curves show the original Δe defined as the tiny difference between e and e_0 (second panel), the blue curves show Δe according to Eq. (5.33). Note that a priori, these two quantities seem completely unrelated to each other, as the first one mainly contains information on the energy density, while the second quantity knows only about particle densities and currents. However, also here, the blue and red curves agree to a high precision. This nontrivial fact substantiates our analytical study. Note that the quantities in the lowest panel are an order of magnitude smaller than the previous quantities and should be very sensitive to discrepancies between Boltzmann numerics and analytics. For large z, the blue and red curves deviate from each other. This fact is to be expected, as in the cloud's tail regions, the local interparticle scattering rates are too small to drive the system to local equilibrium. Hence, the hydrodynamic approximation is not valid there.

5.6 Summary and outlook

To summarize, we have analyzed the dynamics of interacting fermionic ultracold atoms in optical lattices in the presence of a gravitational potential. We concentrated on the diffusive limit, where $\tau \ll \tau_B = 2\pi/g$. After a short transient, the cloud expands symmetrically. We systematically derived coupled diffusion equations for the particle- and kinetic energy density. Using a scaling ansatz, we were able to solve the equations *analytically* in the long time limit. We found that the cloud radius R grows in time as $R \sim t^{1/3}$ as opposed to ordinary diffusion, where $R \sim t^{1/2}$. We were also able to find the scaling function, which turns out to be very close to a normalized Gaussian. Comparing the analytical theory with numerical data from a Boltzmann simulation, we found excellent agreement even to *subleading* order in the sense of our previous discussion.

Yet, the above study does not describe the *ultimate* long time limit of the problem. Note that the diffusive approximation relied on the fact that the scattering time is much shorter than the period of Bloch oscillations, i.e. $\tau_0/n \ll \tau_B$. As the density profile gets more and more dilute, i.e. $n \to 0$, the cloud will sooner or later reach a regime where inter-particle scattering is not strong enough any more to over-damp Bloch oscillations. This regime is necessarily reached when $\tau_0/n \gg \tau_B$. Using the scaling ansatz (5.18) for $n(x,t)$ with the result $\gamma = 3$, the diffusive approximation looses its validity when

$$t \gg N_0^4/(\alpha_0^3\, g\, J^4\, \tau_0^4) \tag{5.35}$$

For much longer times, the cloud willl enter the opposite regime, where Bloch oscillations are only weakly damped. This regime will be studied in chapter 6, where we show the emergence of a different scaling law. Experimentally, however, it will be very difficult to observe the dynamics of the system at such long times. As mentioned before, it is also a challenging and highly relevant follow-up study to solve the corresponding bosonic problem, which is characterized by a non-trivial interplay between the dynamics of condensed and uncondensed bosonic atoms.

6

Damping of Bloch oscillations and stroboscopic diffusion

6.1 Introduction

The observation of Bloch oscillations belongs to the pioneering experiments with ultracold atoms [99] and has been achieved several years even before the regime of strong correlations has been accessed in these systems. The basics of Bloch oscillations can be easily understood in a semi-classical picture e.g. in one dimension. Let us consider the dynamics of a wave packet at position x and initial momentum k in the presence of a constant force F in a lattice model, whose energy dispersion is given by $\epsilon_k = -2J\cos(k)$. Solving the semi-classical equations of motion (1.31), one finds

$$x(t) - x(0) \; = \; -2JF^{-1}\left(\cos(k+Ft) - \cos(k)\right) \tag{6.1}$$

Hence, the wave packet is not uniformly accelerated by the constant force, but keeps *oscillating* instead. Bloch oscillations have been first predicted for electrons in periodic potentials by Felix Bloch [96], but they have never been observed for crystalline solids due to the fast scattering on impurities, phonons, lattice defects or other electrons. Besides ultracold atoms, there are more quantum systems that show these oscillations, among which are semiconductor-superlattices [97], and optical waveguide arrays [98].

We will be interested in the damping of Bloch oscillations in the fermionic Hubbard model. When such a system exhibits Bloch oscillations, it is in a state far from thermodynamic equilibrium. In the presence of interactions, the dynamics is characterized by a competition between the static driving force F and the scattering rate $\tau_{\text{scatt}}^{-1} \sim U^2$, which drives the system back to equilibrium. As we have pointed out in chapter 5, it is very important to take into account that the Hubbard model describes a thermally isolated system, such that the particle currents will lead to an intrinsic heating in the long time limit. Therefore, if interactions are weak enough not to over-damp Bloch oscillations, scattering will nevertheless lead to a damping of the amplitude of Bloch oscillations. Due to the exponential decay of all momentum modes, the system will be characterized by a constant momentum distribution in the long time limit, which can be interpreted as an infinite temperature as well.

The damping of Bloch oscillations has been observed in experiment with bosonic atoms [76], and it has been studied theoretically in many physical realizations [51,103–111]. For various fermionic lattice models, the damping of Bloch oscillations has been studied numerically using DMFT [51, 104, 105, 111]. In particular, Eckstein and Werner simulated the damping of Bloch oscillations for the fermionic Hubbard model [51], where they especially analyzed the regime of intermediately strong and weak interactions. In their study, the decay of the current mode was observed numerically. For weak interactions, it was found to decay exponentially on top of its oscillatory dynamics, while for stronger interactions, these oscillations were found to be over-damped and the current was exponentially decaying. In this chapter, we will present an analytic theory of the damping of Bloch oscillations, whereupon we also explain the numerical findings by Eckstein and Werner.

When a *finite* cloud of interacting lattice-particles is exposed to a constant force, we have shown in chapter 5 that its dynamics is strongly influenced by energy conservation: the cloud as a whole can not move upwards or downwards over large distances. While we were interested in the collision-dominated regime in chapter 5, we will consider here the opposite limit of weakly damped Bloch oscillations. As can be seen e.g. in Eq. (6.1), Bloch oscillations *localize* the particles in a region whose width is determined by the inverse force. Non-interacting particles can not leave this region, in which they are periodically oscillating up and down. However, in the presence of interactions, the particles can be kicked out of their periodic orbits by scattering processes. As a consequence, the cloud as a whole can expand by collisions. In this chapter, we will derive an effective diffusion equation for the cloud's dynamics on top of its rapid oscillatory movement, which is very different from the conventional diffusion that emerges in the collision-dominated regime.

The present chapter is organized as follows. In sections 6.2 and 6.3, we analyze the damping of Bloch oscillations in the *homogeneous* Hubbard model, where we will present an analytic theory for the decay of Bloch oscillations, based on the Boltzmann equation. In section 6.2, we introduce two perturbative schemes to calculate the system's heating rate in the two limits of over-damped and weakly damped Bloch oscillations. While this section is conceptually important for the study of the *inhomogeneous* system, it can be skipped by readers who are only interested in the homogeneous system, because we introduce a more powerful way to address the homogeneous system in section 6.3. Here, we systematically derive coupled differential equations for the dynamics of the kinetic energy mode and map it to a damped harmonic oscillator equation, which can be solved exactly. The analytic results are also compared to a numerical solution of the full Boltzmann equation in one dimension. Finally, in section 6.4 we study the dynamics of an *inhomogeneous*, finite cloud of fermionic particles in the Hubbard model, driven by a linear potential at weak interactions, such that Bloch oscillations are only weakly damped. We show that the dynamics of the system can be semi-quantitatively approximated by a nonlinear, *stroboscopic* diffusion equation that governs the cloud's dynamics on top of its rapid oscillatory movement. The equations for the particle density and kinetic energy density are structurally similar to the diffusion equations derived in chapter 5, however, their dependence on the scattering time and on the local density is found to be *inverse* to the aforementioned study. This leads to the peculiar sub-diffusive scaling law or $R \sim t^{1/5}$ at which the cloud expands, where R is the cloud's radius and t is the time variable.

6.2 Two perturbative limits for the homogeneous system

6.2.1 Over-damped Bloch oscillations

As a very first step, let us consider the rate at which a thermally isolated system heats up in the presence of a constant force in the *linear response* regime, which is characterized by local equilibrium. This approach is conceptually very similar to deriving the Diffusion equation from the Boltzmann equation.

We first consider the regime where the Bloch oscillation period $\tau_B = 2\pi/F$, is much *larger* than the time between two scattering events, $\tau_B \gg \tau_{scatt}$. In this case, the system is always close to local equilibrium. Therefore, we decompose the non-equilibrium distribution function $f_{\mathbf{k}}$ as the sum of an equilibrium Fermi function $f^0_{\mathbf{k}}$ and a tiny perturbation $\delta f^0_{\mathbf{k}}$,

$$f_{\mathbf{k}} = f^0_{\mathbf{k}} + \delta f_{\mathbf{k}} \tag{6.2}$$

This ansatz is chosen such that it approximately solves the right-hand side of the Boltzmann equation, i.e. it minimizes the collision integral. Plugging this ansatz into the Boltzmann equation and neglecting δf on the left-hand side yields

$$\left(\partial_t + \mathbf{F}\nabla_{\mathbf{k}}\right) f^0_{\mathbf{k}} = -\int \frac{d\mathbf{k}'}{(2\pi)^d} M_{\mathbf{k}\mathbf{k}'} \delta f_{\mathbf{k}} \tag{6.3}$$

A formal solution of the equation can be obtained, provided the inverse of the scattering matrix $M_{\mathbf{k}\mathbf{k}'}$ is known:

$$\delta f_{\mathbf{k}} = -\int \frac{d\mathbf{k}'}{(2\pi)^d} M^{-1}_{\mathbf{k}\mathbf{k}'} \left(\partial_t + F\partial_{\mathbf{k}'}\right) f^0_{\mathbf{k}'}[z(t), \beta(t)] \tag{6.4}$$

Here, we regard $f^0_{\mathbf{k}}$ as a function of inverse temperature and fugacity. This will be of later convenience as z and β converge to finite values in the infinite temperature limit, in contrast to μ and T. We will now use the fact that by the chain rule,

$$\begin{aligned}
\nabla_{\mathbf{k}} f^0_{\mathbf{k}} &= \mathbf{v}_{\mathbf{k}} \frac{\partial f^0_{\mathbf{k}}}{\partial \epsilon_{\mathbf{k}}} && (6.5)\\
\partial_t f^0_{\mathbf{k}} &= \frac{\partial f^0_{\mathbf{k}}}{\partial \beta}\dot{\beta} + \frac{\partial f^0_{\mathbf{k}}}{\partial z}\dot{z} \\
&= \frac{\epsilon_{\mathbf{k}}}{\beta}\frac{\partial f^0_{\mathbf{k}}}{\partial \epsilon_{\mathbf{k}}}\frac{\partial \beta}{\partial e}\dot{e} + \frac{\partial f^0_{\mathbf{k}}}{\partial z}\frac{\partial z}{\partial e}\dot{e} \\
&= \frac{\partial f^0_{\mathbf{k}}}{\partial \epsilon_{\mathbf{k}}}\left(\frac{\epsilon_{\mathbf{k}}}{\beta}\frac{\partial \beta}{\partial e} + \frac{1}{z\,\beta}\frac{\partial z}{\partial e}\right)\dot{e} && (6.6)
\end{aligned}$$

Combining the above equations with Eq. (6.4), we can calculate the particle current, which yields

$$\begin{aligned}
\mathbf{j}_n &= \int \frac{d\mathbf{k}}{(2\pi)^d} \mathbf{v}_{\mathbf{k}} \delta f_{\mathbf{k}} \\
&= -\int \frac{d\mathbf{k}}{(2\pi)^d}\frac{d\mathbf{k}'}{(2\pi)^d} \mathbf{v}_{\mathbf{k}} M^{-1}_{\mathbf{k}\mathbf{k}'} \frac{\partial f^0_{\mathbf{k}'}}{\partial \epsilon_{\mathbf{k}'}} \left[\mathbf{F}\mathbf{v}_{\mathbf{k}'} + \left(\frac{\epsilon_{\mathbf{k}'}}{\beta}\frac{\partial \beta}{\partial e} + \frac{1}{z\,\beta}\frac{\partial z}{\partial e}\right)\dot{e}\right] && (6.7)
\end{aligned}$$

Using the continuity equation, the time-evolution of the kinetic energy is determined by

$$\dot{e} = -\nabla \mathbf{j}_e + \mathbf{F}\,\mathbf{j}_n = \mathbf{F}\,\mathbf{j}_n \tag{6.8}$$

Combining Eqs. (6.7) and (6.8) gives us an equation for the time-evolution of the kinetic energy

$$\dot{e} = -\mathbf{F}\int \frac{d\mathbf{k}}{(2\pi)^d}\frac{d\mathbf{k}'}{(2\pi)^d} \mathbf{v}_{\mathbf{k}} M^{-1}_{\mathbf{k}\mathbf{k}'} \frac{\partial f^0_{\mathbf{k}'}}{\partial \epsilon_{\mathbf{k}'}} \left[\mathbf{F}\mathbf{v}_{\mathbf{k}'} + \left(\frac{\epsilon_{\mathbf{k}'}}{\beta}\frac{\partial \beta}{\partial e} + \frac{1}{z\,\beta}\frac{\partial z}{\partial e}\right)\dot{e}\right] \tag{6.9}$$

Let us have a closer look on this equation: its right hand side carries an overall prefactor of $|M^{-1}|F \ll 1$ where $|M^{-1}|$ is a characteristic scattering rate addressed to M. We can therefore solve the equation iteratively and concentrate on the leading term, neglecting $\dot{e}$ on the right hand side. The result can be expressed by the conductivity in terms of the linearized Boltzmann equation,

$$\sigma = \sigma_{xx} = -\int \frac{d\mathbf{k}}{(2\pi)^d}\frac{d\mathbf{k}'}{(2\pi)^d}\, \mathbf{v}^x_{\mathbf{k}} M^{-1}_{\mathbf{k}\mathbf{k}'} \mathbf{v}^x_{\mathbf{k}'} \frac{\partial f^0_{\mathbf{k}'}}{\partial \epsilon_{\mathbf{k}'}}, \tag{6.10}$$

which leads to the most general result for the heating rate of the homogeneous system close to equilibrium,

$$\dot{e} = \sigma(e)\,\mathbf{F}^2 \tag{6.11}$$

The implicit dependence of the conductivity σ on the kinetic energy e can be worked out explicitly for high temperatures. We can use the high temperature version of $f^0_{\mathbf{k}}$ as given in Eq. (2.43) or Eq. (6.42), which leads to $\partial f^0_{\mathbf{k}}/\partial\epsilon_{\mathbf{k}} \approx e/(2J^2 d)$. Then, the conductivity (6.10) simplifies to

$$\sigma \approx -\int \frac{d\mathbf{k}}{(2\pi)^d}\frac{d\mathbf{k}'}{(2\pi)^d}\, \frac{\mathbf{v}^x_{\mathbf{k}} M^{-1}_{\mathbf{k}\mathbf{k}'} \mathbf{v}^x_{\mathbf{k}'}}{2J^2 d}\, e \;=:\; -\frac{e\,\tau_{\text{sc}}}{2} \tag{6.12}$$

which implicitly defines the scattering time τ_{sc}. Hence, the final result can be expressed as

$$\dot{e} \approx -\frac{F^2\,\tau_{\text{sc}}}{2}\, e, \qquad e(t) = e_0\, \exp(-\frac{1}{2}F^2\,\tau_{\text{sc}}\, t) \tag{6.13}$$

At high temperatures, the scattering operator $M_{\mathbf{k}\mathbf{k}'} \sim \tau_{\text{sc}}^{-1} \sim U^2/J$ becomes approximately independent of temperature. Using $\mathbf{v}_{\mathbf{k}} \sim 2J$, Eq. (6.13) can be approximated as

$$\dot{e} \sim -\frac{4\,J\,F^2}{U^2} e \tag{6.14}$$

By using the time scale $\tau_B = 2\pi/F$, which measures the time of one Bloch oscillation period in absence of interactions, the heating rate can be finally estimated as

$$1/\tau_{\text{heat}} \sim \tau_{\text{sc}}/\tau_B^2 \tag{6.15}$$

6.2.2 Weakly damped Bloch oscillations

General philosophy

After having studied the heating rate of an isolated lattice system in the collision dominated linear response regime, we want to study the opposite limit, where the scattering rate is much smaller than the driving force, $\tau_{\text{scatt}}^{-1} \ll F$. The perturbative calculation that we are going to present here is mostly conceptually important, as it can be generalized to a spatially inhomogeneous situation, which will be done in section 6.4. A more direct way of addressing the homogeneous system will be presented in section 6.3.

We are interested in a situation where the Fermions are dominantly Bloch oscillating; yet, from time to time the particles scatter on each other. Again, we want to calculate the heating rate of the system, reflected in the decay of the kinetic energy and current mode. As the Bloch oscillations are only weakly damped, the solution of the Boltzmann equation will be a distribution function far from thermal equilibrium. Usually, the linearization of the Boltzmann equation around an equilibrium Fermi function would therefore be inappropriate. However, as we expect that the particle current will get damped in the long time limit, the non-equilibrium distribution function will get closer and closer to a constant distribution function, $f_{\mathbf{k}} \to n \;\; (t \to \infty)$, in momentum space. As a constant distribution is formally the same as an equilibrium distribution at *infinite temperature*, we can linearize the distribution function around $T = \infty$. Hence, we study the linearized Boltzmann equation

$$(\partial_t + \mathbf{F}\nabla_{\mathbf{k}})\, f_{\mathbf{k}} = -\int \frac{d\mathbf{k}'}{(2\pi)^d}\, M_{\mathbf{k}\mathbf{k}'}(f_{\mathbf{k}'} - n) \tag{6.16}$$

Here, n is the constant density of the system and M is the linearized collision integral of the Boltzmann equation at infinite temperature, specified in Appendix (E.1). Similarly to the collision-dominated case, an approximate solution to the Boltzmann equation can be found using a proper decomposition of the distribution function. In the linear response regime, the non-equilibrium distribution function was decomposed into the Fermi function f^0 and a tiny perturbation δf. The ansatz was designed to approximately solve the right hand side of the Boltzmann equation. Here, we are considering the opposite case, where the Boltzmann equation is dominated by its *left* hand side. An appropriate decomposition of the non-equilibrium distribution function should almost solve the left-hand side. Therefore, we decompose $f_{\mathbf{k}}$ according to

$$f = f^B + \delta f \tag{6.17}$$

where f^B is an *exact* solution of the non-interacting Boltzmann equation

$$(\partial_t + \mathbf{F}\nabla_{\mathbf{k}})\, f^B(\mathbf{k}, t) = 0 \tag{6.18}$$

and $\delta f \ll f^B$ is a tiny correction which describes the deviation from the purely Bloch-oscillating behavior. Note that δf nevertheless is an important contribution that takes the damping of the oscillations into account. Let us now construct f^B. At time $t = 0$, the system shall be described by the momentum distribution function $f(\mathbf{k}, 0)$ as an initial condition. In defining

$$f^B(\mathbf{k}, t) := f(\mathbf{k} - \mathbf{F}t, 0) \tag{6.19}$$

one immediately recognizes that the above definition of f^B solves Eq. (6.18) for *any* $f(\mathbf{k}, 0)$. The function f^B can be considered as a zeroth order solution of the Boltzmann equation in the expansion parameter τ_B/τ_{sc}, and we will use it as a starting point for a perturbative expansion. For the linearization of the collision integral to be justified, we have to assume that

$$|f^B(\mathbf{k}) - n| \ll n \tag{6.20}$$

for all $\mathbf{k}$. Using our proposed decomposition, the Boltzmann equation reads

$$(\partial_t + \mathbf{F}\nabla_{\mathbf{k}})\, \delta f_{\mathbf{k}} \;=\; -\frac{1}{(2\pi)^d}\int d\mathbf{k}' M_{\mathbf{k}\mathbf{k}'}(f^B_{\mathbf{k}'} + \delta f_{\mathbf{k}'} - n) \tag{6.21}$$

As we will show below, the inverse of the Liouvillian operator $(\partial_t + \mathbf{F}\nabla_{\mathbf{k}})$ is proportional to $F^{-1} \sim \tau_B$. Therefore, the contribution of $\delta f_{\mathbf{k}}$ on the right hand side of Eq. (6.21) is suppressed by another factor of $\tau_B\, M_{\mathbf{k}\mathbf{k}'} \sim \tau_B/\tau_{\text{scatt}} \ll 1$. Omitting this term yields

$$(\partial_t + \mathbf{F}\nabla_{\mathbf{k}})\, \delta f_{\mathbf{k}} \;\approx\; -\frac{1}{(2\pi)^d}\int d\mathbf{k}' M_{\mathbf{k}\mathbf{k}'}(f^B_{\mathbf{k}'} - n) \tag{6.22}$$

The strategy will be to solve the equation for $\delta f_{\mathbf{k}}$ by applying the inverse Liouvillian operator on both sides.

Perturbative solution

We will proceed in deriving an explicit expression for the function $\delta f_{\mathbf{k}}$ in terms of the known function $f^B_{\mathbf{k}}$. The perturbation $\delta f_{\mathbf{k}}$ describes the net flow of particles that get scattered out of their free, periodic motion. To simplify the resulting expressions, we will be only interested in the *integrated* flow of particles that get scattered within one Bloch cycle. As this approach involves an integration over the Bloch period, it will be crucial that the function $f^B_{\mathbf{k}}$ is *periodic* in the Bloch period $\tau_B = 2\pi/F$. While this is *always* the case in one dimension, it is not necessarily the case in dimensions larger than one for incommensurate ratios of the vector components of $\mathbf{F}$. For simplicity, we consider a situation where

$$\mathbf{F} \;=\; F \begin{pmatrix} 1 \\ 1 \\ \vdots \\ 1 \end{pmatrix} \tag{6.23}$$

points into the diagonal direction of the lattice[1]. In order to solve Eq. (6.22) for $\delta f_{\mathbf{k}}$, we have to find the operator inverse of the Liouvillian. To find its inverse, let us consider the equation

$$(\partial_t + \mathbf{F}\nabla_{\mathbf{k}})\, a(\mathbf{k},t) \;=\; b(\mathbf{k},t) \tag{6.24}$$

It can be checked straightforwardly that its solution is given by

$$a(\mathbf{k},t) \;=\; \int_0^t dt'\, b(\mathbf{k}-\mathbf{F}(t-t'),t') \;+\; a(\mathbf{k}-\mathbf{F}t,0) \tag{6.25}$$

We now combine the definition of f^B in Eq. (6.19) with the defining Eq. (6.22) for δf and its formal solution Eq. (6.25) to derive

$$\delta f_{\mathbf{k}}(t) \;=\; -\int \frac{d\mathbf{k}'}{(2\pi)^d} \int_0^t dt'\, M_{\mathbf{k}-\mathbf{F}(t-t'),\mathbf{k}'} \;\big(f(\mathbf{k}'-\mathbf{F}t',0) - n\big) \tag{6.26}$$

where we used that $\delta f_{\mathbf{k}}$ is initially zero, as it grows to a finite value only due to scattering processes at $t > 0$. Furthermore, we will not be interested in the rapid Bloch oscillations on top of the weak damping. Therefore, integrate the solution $\delta f_{\mathbf{k}}$ over one Bloch cycle and normalize by τ_B, where we define

$$\overline{\delta f_{\mathbf{k}}} \;:=\; \frac{1}{\tau_B}\int_0^{\tau_B} dt\, \delta f_{\mathbf{k}}(t) \tag{6.27}$$

We can also substitute $\mathbf{k}' \to \mathbf{k}' + \mathbf{F}t'$ in Eq. (6.26) in order to get rid of the oscillations in the momentum argument of the initial distribution function $f(\mathbf{k},0)$. The resulting equation is the analog of Eq. (6.4) in the case of linear response, which relates the first order perturbative correction of the Boltzmann equation to the instantaneous distribution function $f(\mathbf{k},0)$:

$$\overline{\delta f_{\mathbf{k}}} \;=\; -\int \frac{d\mathbf{k}'}{(2\pi)^d}\, \overline{M}_{\mathbf{k}\mathbf{k}'} \;\big(f(\mathbf{k}',0) - n\big) \tag{6.28}$$

---

[1] Note that F does not denote the *absolute value* of $\mathbf{F}$, but rather its projection on one of the coordinate axes. This notation is extremely useful and will be kept throughout the chapter.

Here, we defined

$$\overline{M}_{\mathbf{k}\mathbf{k}'} \;:=\; \frac{1}{\tau_B}\int_0^{\tau_B} dt \int_0^t dt'\, M_{\mathbf{k}-\mathbf{F}(t-t'),\mathbf{k}'+\mathbf{F}t'} \tag{6.29}$$

Note that when estimating $M \sim U^2/J$, we find that $\overline{M} \sim F^{-1}U^2/J$ has a different dimensionality from the original scattering matrix.

In order to proceed in the spirit of the previous study, we have to parametrize the instantaneous distribution function $f(\mathbf{k},0)$ by the relevant momentum modes of the system. In the case of linear response, the instantaneous distribution function was a Fermi function and uniquely parametrized by the density n and kinetic energy e. As we will discuss in more detail in section 6.3, far from equilibrium the system is only fully characterized by the set of *all* modes. However, as a first approximation, it makes sense to parametrize the instantaneous distribution function $f(\mathbf{k},0)$ also by its density and energy density mode,

$$f(\mathbf{k},0) \;\approx\; n + \frac{1}{2J^2d}\, e\,\epsilon_{\mathbf{k}} \tag{6.30}$$

where $2J^2d = \int d\mathbf{k}\,\epsilon_{\mathbf{k}}^2/(2\pi)^d$ is a normalization constant. The quality of this approximation will be discussed in section 6.3. Note that it is not necessary to include the current mode $\mathbf{v}_{\mathbf{k}}$ in the above ansatz, as it is periodically converted into the energy mode and vice versa by the Bloch oscillations. As we have the freedom to define our initial time as we wish, we can choose $t = 0$ such that the particle current due to Bloch oscillations is at its turning point, i.e. such that it is zero.

We now use the energy continuity equation $\dot{e} = \mathbf{F}\,\mathbf{j_n}$ for the homogeneous system, where we calculate the current with Eq. (6.28) and use the ansatz (6.30) for $f(\mathbf{k},0)$:

$$\begin{aligned} \dot{e} \;&\approx\; \mathbf{F}\int \frac{d\mathbf{k}}{(2\pi)^d}\,\mathbf{v}_{\mathbf{k}}\,\overline{\delta f_{\mathbf{k}}} \\ &\approx\; -\mathbf{F}\int \frac{d\mathbf{k}}{(2\pi)^d}\frac{d\mathbf{k}'}{(2\pi)^d}\,\frac{\mathbf{v}_{\mathbf{k}}\,\overline{M}_{\mathbf{k}\mathbf{k}'}\,\epsilon_{\mathbf{k}'}}{2J^2d}\, e \end{aligned} \tag{6.31}$$

We will show in Eq. (6.44) that the continuity equation is valid arbitrarily far from equilibrium. As the force points into the diagonal direction of the lattice, it is convenient to introduce a scalar variant of the velocity mode:

$$v_{\mathbf{k}} = \mathbf{v}_{\mathbf{k}} \cdot (1,1,...,1)^T \tag{6.32}$$

This allows us to relate the matrix elements of $\overline{M}$ to matrix elements of M:

$$\begin{aligned} \int d\mathbf{k}d\mathbf{k}'\, v_{\mathbf{k}}\,\overline{M}_{\mathbf{k}\mathbf{k}'}\,\epsilon_{\mathbf{k}'} \;&\overset{(6.29)}{=}\; \frac{1}{\tau_B}\int_0^{\tau_B} dt \int_0^t dt' \int d\mathbf{k}d\mathbf{k}'\; v_{\mathbf{k}}\; M_{\mathbf{k}-\mathbf{F}(t-t'),\mathbf{k}'+\mathbf{F}t'}\;\epsilon_{\mathbf{k}'} \\ &\overset{\text{subst.}}{=}\; \frac{1}{\tau_B}\int d\mathbf{k}d\mathbf{k}'\; M_{\mathbf{k}\mathbf{k}'}\int_0^{\tau_B} dt \int_0^t dt'\; v_{\mathbf{k}+\mathbf{F}(t-t')}\;\epsilon_{\mathbf{k}'-\mathbf{F}t'} \\ &\overset{(E.14)}{=}\; \frac{1}{2F}\int d\mathbf{k}d\mathbf{k}'\; v_{\mathbf{k}}\, M_{\mathbf{k}\mathbf{k}'}\, v_{\mathbf{k}'} \end{aligned} \tag{6.33}$$

where we shifted the momentum integration variables. The remaining integral identity relies on trigonometric identities and leads to the fact that the time integrals can be performed exactly, as is shown in Appendix (E.14). Combining this result with Eq. (6.31), we arrive at the final result for the damping rate of the kinetic energy mode on top of strong Bloch oscillations, which reads

$$\dot{e} \;\approx\; -\frac{1}{2}\int \frac{d\mathbf{k}}{(2\pi)^d}\frac{d\mathbf{k}'}{(2\pi)^d}\;\frac{v_{\mathbf{k}}\,M_{\mathbf{k}\mathbf{k}'}\,v_{\mathbf{k}'}}{2J^2 d}\;e \tag{6.34}$$

Remarkably, the damping rate is completely independent of the force F and depends only on the current-current matrix element of the scattering matrix M. In contrast to Eq. (6.15) that we derived for the linear response limit, here we can identify the heating rate with the microscopic scattering rate of the system,

$$1/\tau_{\mathrm{heat}} \sim 1/\tau_{\mathrm{sc}} \tag{6.35}$$

This concludes the study of the heating rate of the homogeneous system in the regime of weakly damped Bloch oscillations. Before we proceed with the next section, let us emphasize that naively, one could also have calculated the energy change after one Bloch period differently, namely by using that

$$\dot{e} \;\approx\; \frac{e(\tau_B)-e(0)}{\tau_B} \;\overset{(?)}{=}\; \frac{1}{\tau_B}\int \frac{d\mathbf{k}}{(2\pi)^d}\,\epsilon_{\mathbf{k}}\,\delta f_{\mathbf{k}}(\tau_B) \tag{6.36}$$

The question mark above shall signify that the relation is not an exact identity, but only holds if $\delta f_{\mathbf{k}}$ is an exact solution of the Boltzmann equation. If this were the case, both ways of calculating $\dot{e}$ were indeed equivalent:

$$\begin{aligned}
\frac{1}{\tau_B}\int \frac{d\mathbf{k}}{(2\pi)^d}\,\epsilon_{\mathbf{k}}\,\delta f_{\mathbf{k}}(\tau_B) \;&=\; \frac{1}{\tau_B}\int \frac{d\mathbf{k}}{(2\pi)^d}\,\epsilon_{\mathbf{k}}\int_0^{\tau_B} dt\,\delta \dot{f}_{\mathbf{k}}(t) \\
&\overset{\text{Boltzm.}}{=}\; -\frac{1}{\tau_B}\int \frac{d\mathbf{k}}{(2\pi)^d}\,\epsilon_{\mathbf{k}}\int_0^{\tau_B} dt\,\mathbf{F}\nabla_{\mathbf{k}}\delta f_{\mathbf{k}}(t) \\
&\overset{\underline{P.I.}}{=}\; \mathbf{F}\frac{1}{\tau_B}\int \frac{d\mathbf{k}}{(2\pi)^d}\,\mathbf{v}_{\mathbf{k}}\int_0^{\tau_B} dt\,\delta f_{\mathbf{k}}(t) \\
&=\; \mathbf{F}\int \frac{d\mathbf{k}}{(2\pi)^d}\,\mathbf{v}_{\mathbf{k}}\,\overline{\delta f_{\mathbf{k}}}
\end{aligned} \tag{6.37}$$

where we assumed that $\delta f_{\mathbf{k}}$ fulfills the Boltzmann equation and $\int d\mathbf{k}'\, M_{\mathbf{k}\mathbf{k}'}\epsilon_{\mathbf{k}'} = 0$. Importantly, however, $\delta f_{\mathbf{k}}$ does *not* fulfill the Boltzmann equation exactly, as it is only an approximation to the solution. Hence, we have to use Eq. (6.31) to calculate $\dot{e}$, and *not* the right hand side of Eq. (6.36) in order to satisfy the conservation laws exactly. This is especially important in the spatially inhomogeneous generalization of the approach, where the total particle number and total energy must be conserved.

6.3 Generalized continuity equations

We will now present an alternative framework in which the dynamics of the system's momentum modes can be studied in various regimes. We will refer to this approach as the method of deriving *generalized continuity equations.* We will show below that this approach is more general than the perturbative schemes described before: it allows us not only to study the over-damped and the weakly damped regime, but also various regimes in between. But it also has the disadvantage that it is not obvious how to generalize the new approach to spatially inhomogeneous systems, while we are successful in doing so with the first approach, as we will show in section 6.4. Again, we start from the linearized Boltzmann equation

$$(\partial_t + \mathbf{v_k}\nabla_\mathbf{r} + \mathbf{F}\nabla_\mathbf{k})\, f_\mathbf{k} = -\int d\mathbf{k}'\, M_{\mathbf{k}\mathbf{k}'}\,(f_{\mathbf{k}'} - n) \tag{6.38}$$

where M is the matrix of the linearized collision integral at infinite temperature. Let us discuss the possibility of deriving effective diffusion equations from the Boltzmann equation. In usual (collision-dominated) diffusion, it is assumed that the smallest time scale is given by the relaxation rate, i.e. the matrix $M_{\mathbf{k}\mathbf{k}'}$ is large and therefore the right hand side dominates the Boltzmann equation. If this is satisfied, it is guaranteed that the non-equilibrium distribution function $f_\mathbf{k}$ is always close to an equilibrium distribution function, and in particular it is fully determined by the system's conserved quantities, which are the particle density n and kinetic energy density e, i.e. $f_\mathbf{k} = f_\mathbf{k}(n, e)$. In a regime far beyond the conventional diffusive limit, things are much more complicated.

A priori, there is no reason to assume that a generic non-equilibrium distribution function should be parametrized only by two parameters; instead it can be *any* function of momentum $\mathbf{k}$. In terms of its Fourier representation, the distribution function is therefore characterized by an *infinite* set of momentum modes.

In the spatially homogeneous case, Eq. (6.38) formally simplifies in the Fourier representation; however, we are still left with an infinite set of coupled ordinary differential equations for the different mode occupation coefficients. The basic idea of this section is to truncate the number of momentum modes to a "physically relevant" subset.

Let us introduce a scalar product in the space of momentum-dependent functions,

$$\langle f(\mathbf{k})|g(\mathbf{k})\rangle := \frac{1}{(2\pi)^d}\int d\mathbf{k}\, f(\mathbf{k})\, g(\mathbf{k}) \tag{6.39}$$

The minimal modes that are needed to describe the system's dynamics in the *diffusive* limit are the particle density n, the kinetic energy density e, the particle current $\vec{v}$ and the heat current $\vec{h}$:

$$n = \langle 1|f_\mathbf{k}\rangle, \quad e = \langle \epsilon_\mathbf{k}|f_\mathbf{k}\rangle, \quad \vec{v} = \langle \mathbf{v_k}|f_\mathbf{k}\rangle, \quad \vec{h} = \langle \epsilon_\mathbf{k}\mathbf{v_k}|f_\mathbf{k}\rangle, \quad ... \tag{6.40}$$

Above, the dots shall indicate that out of equilibrium, the list of modes is in principle not restricted. In a similar way of how we derived the continuity equations (2.28) from the Boltzmann equation, we can derive a more general set of coupled equations,

$$\begin{aligned}
\langle 1|\,(\partial_t + \mathbf{v_k}\nabla_\mathbf{r} + \mathbf{F}\nabla_\mathbf{k})\, f_\mathbf{k}\rangle &= 0 \\
\langle \epsilon_\mathbf{k}|\,(\partial_t + \mathbf{v_k}\nabla_\mathbf{r} + \mathbf{F}\nabla_\mathbf{k})\, f_\mathbf{k}\rangle &= 0 \\
\langle \mathbf{v_k}|\,(\partial_t + \mathbf{v_k}\nabla_\mathbf{r} + \mathbf{F}\nabla_\mathbf{k})\, f_\mathbf{k}\rangle &= -\langle \mathbf{v_k}|M|f_\mathbf{k}\rangle \\
\langle \epsilon_\mathbf{k}\mathbf{v_k}|\,(\partial_t + \mathbf{v_k}\nabla_\mathbf{r} + \mathbf{F}\nabla_\mathbf{k})\, f_\mathbf{k}\rangle &= -\langle \epsilon_\mathbf{k}\mathbf{v_k}|M|f_\mathbf{k}\rangle
\end{aligned} \tag{6.41}$$

where $|1\rangle$ denotes the constant function in momentum space. Above, we used that the scattering terms vanish for the particle number and energy modes, i.e. $\langle 1|M|f_\mathbf{k}\rangle = 0, \langle \epsilon_\mathbf{k}|M|f_\mathbf{k}\rangle = 0$. Again, also here the list of equations for the different momentum modes is in principle not limited. Due to the orthogonality of these modes, the non-equilibrium distribution function $f_\mathbf{k}$ close to infinite temperature at time t can be expressed uniquely as

$$f_\mathbf{k}(\mathbf{r}, t) = n(\mathbf{r}, t) + \frac{e(\mathbf{r}, t)}{2J^2 d}\epsilon_\mathbf{k} + \frac{\vec{v}(\mathbf{r}, t)}{2J^2}\mathbf{v_k} + \frac{\vec{h}(\mathbf{r}, t)}{6J^4}\epsilon_\mathbf{k}\mathbf{v_k} + ... \tag{6.42}$$

where the normalization of the coefficients stems from the following integral identities:

$$\int \frac{d\mathbf{k}}{(2\pi)^d}\, \epsilon_{\mathbf{k}}^2 = 2J^2 d, \quad \int \frac{d\mathbf{k}}{(2\pi)^d}\, \mathbf{v}_{\mathbf{k}}^i \mathbf{v}_{\mathbf{k}}^j = 2J^2 \delta_{ij}, \quad \int \frac{d\mathbf{k}}{(2\pi)^d}\, \epsilon_{\mathbf{k}}^2 \mathbf{v}_{\mathbf{k}}^i \mathbf{v}_{\mathbf{k}}^j = 6J^4 \delta_{ij} \tag{6.43}$$

The scalar products in Eq. (6.41) can then be carried out, where the orthogonality of the different modes is used. Using the ansatz for the distribution function (6.42) and the orthogonality of the modes, they can be equivalently expressed as

$$\begin{aligned} \dot{n} + \nabla_{\mathbf{r}} \vec{v} &= 0 \qquad\qquad (6.44) \\ \dot{e} + \nabla_{\mathbf{r}} \vec{h} - \mathbf{F} \vec{v} &= 0 \\ \dot{\vec{v}} + 2J^2\, \nabla_{\mathbf{r}} n + \mathbf{F}\, e &= -\frac{1}{2J^2} \langle \mathbf{v}_{\mathbf{k}} | M | \mathbf{v}_{\mathbf{k}} \rangle \vec{v} - \frac{1}{6J^4} \langle \mathbf{v}_{\mathbf{k}} | M | \epsilon_{\mathbf{k}} \mathbf{v}_{\mathbf{k}} \rangle \vec{h} + \ldots \\ \dot{\vec{h}} + \frac{3}{d} J^2\, \nabla_{\mathbf{r}} e + \langle \epsilon_{\mathbf{k}} \mathbf{v}_{\mathbf{k}} | \mathbf{F} \nabla_{\mathbf{k}} f_{\mathbf{k}} \rangle &= -\frac{1}{2J^2} \langle \epsilon_{\mathbf{k}} \mathbf{v}_{\mathbf{k}} | M | \mathbf{v}_{\mathbf{k}} \rangle \vec{v} - \frac{1}{6J^4} \langle \epsilon_{\mathbf{k}} \mathbf{v}_{\mathbf{k}} | M | \epsilon_{\mathbf{k}} \mathbf{v}_{\mathbf{k}} \rangle \vec{h} + \ldots \end{aligned}$$

among which the first two equations are nothing else but the continuity equations for the particle and energy density, respectively. All other modes are damped and coupled to each other by the corresponding matrix elements of the scattering matrix $M_{\mathbf{k}\mathbf{k}'}$. The above set of coupled differential equations can now be used to study the many-body dynamics of the system. In general, the above selection of modes does not suffice to characterize the system's full dynamics: all higher modes may couple to the lower modes by the scattering terms on the right hand side. For a situation far from local equilibrium, there is unfortunately no good reason why the higher modes should not contribute, because they are not necessarily damped much faster than the lower modes. In units of one scattering time, basically all modes are significantly damped. However, if the off-diagonal matrix elements of the scattering matrix M are small, many of the momentum modes decouple from each other, and therefore we can restrict our attention to a selection of relevant modes. Note that neglecting off-diagonal scattering elements also amounts to neglecting thermo-electric effects, where the particle current is scattered into the energy current channel and vice versa.

6.3.1 Reproducing conventional diffusion

As a first application and test of the set of equations (6.44), we show that the (conventional) diffusion equations for the particle and energy density at high temperatures can be derived from them. Let us start from the generalized continuity equations, where we restrict our attention to the case $\mathbf{F} = 0$. Furthermore, let us define

$$\hat{M} = \begin{pmatrix} \langle \mathbf{v}_{\mathbf{k}} | M | \mathbf{v}_{\mathbf{k}} \rangle / (2J^2) & \langle \mathbf{v}_{\mathbf{k}} | M | \epsilon_{\mathbf{k}} \mathbf{v}_{\mathbf{k}} \rangle / (6J^4) \\ \langle \epsilon_{\mathbf{k}} \mathbf{v}_{\mathbf{k}} | M | \mathbf{v}_{\mathbf{k}} \rangle / (2J^2) & \langle \epsilon_{\mathbf{k}} \mathbf{v}_{\mathbf{k}} | M | \epsilon_{\mathbf{k}} \mathbf{v}_{\mathbf{k}} \rangle / (6J^4) \end{pmatrix} \tag{6.45}$$

as the projection of the scattering matrix M on the subspace spanned by the current and energy current modes. The equations for the dynamics of the particle and heat currents in Eq. (6.44) can be formulated as

$$\begin{pmatrix} \dot{\vec{v}} \\ \dot{\vec{h}} \end{pmatrix} + \begin{pmatrix} 2J^2\, \nabla_{\mathbf{r}} n \\ (3/d) J^2\, \nabla_{\mathbf{r}} e \end{pmatrix} \approx -\hat{M} \begin{pmatrix} \vec{v} \\ \vec{h} \end{pmatrix} \tag{6.46}$$

where we neglected the scattering from higher momentum modes into the particle and energy current modes and vice versa. If the rate, at which $\nabla_{\mathbf{r}} n$ and $\nabla_{\mathbf{r}} e$ change in time, is much smaller than the scattering rate associated to M, they can be regarded as approximately constant. Then, this set of equations is solved by

$$\begin{pmatrix}\vec{v}\\ \vec{h}\end{pmatrix} = -\hat{M}^{-1}\begin{pmatrix}2J^2\,\nabla_{\mathbf{r}}n\\ (3/d)J^2\,\nabla_{\mathbf{r}}e\end{pmatrix} + e^{-\hat{M}t}\mathbf{C} \tag{6.47}$$

where $\mathbf{C} = (C_1, C_2)^T$ is some constant. If the dynamics is dominated by collisions, the exponential term will decay very rapidly and therefore will not contribute. Alternatively, this result can also be obtained by setting $\dot{\vec{v}} = \dot{\vec{h}} = 0$ in Eq. (6.46). We can define the matrix $\tilde{D}$ as the matrix that mediates between the currents and the density gradients:

$$\tilde{D} = -\hat{M}^{-1}\cdot\begin{pmatrix}2J^2 & 0\\ 0 & \frac{3}{d}J^2\end{pmatrix} \tag{6.48}$$

We claim that the matrix $\tilde{D}$ is an approximation to the matrix of diffusion constants D at high temperatures, which we are going to show now. To this end, we give a short derivation of the diffusion constant in the language of the linearized Boltzmann Eq. (6.38) in absence of the force. In the same way as we have shown for the relaxation time approximation in chapter 2, one can show that

$$\delta f_{\mathbf{k}} = -\int \frac{d\mathbf{k}'}{(2\pi)^d}\, M^{-1}_{kk'}\, v_{\mathbf{k}'}\nabla_{\mathbf{r}} f^0_{\mathbf{k}'}(n,e) \tag{6.49}$$

which is the analog of Eq. (2.32), and which expresses the corrections to local equilibrium in terms of $f^0_{\mathbf{k}}$. We can express the same equation in the language of vectors and the scalar product (6.39) as

$$\begin{aligned} |\delta f_{\mathbf{k}}\rangle &= -M^{-1}\,|\mathbf{v}_{\mathbf{k}}\nabla_{\mathbf{r}} f^0_{\mathbf{k}}(n,e)\rangle \qquad (6.50)\\ &= -M^{-1}\,\left(|\mathbf{v}_{\mathbf{k}}\partial_n f^0_{\mathbf{k}}\rangle,\,|\mathbf{v}_{\mathbf{k}}\partial_e f^0_{\mathbf{k}}\rangle\right)\begin{pmatrix}\nabla_{\mathbf{r}}n\\ \nabla_{\mathbf{r}}e\end{pmatrix}\\ &\approx -M^{-1}\left(|\mathbf{v}_{\mathbf{k}}\rangle,\,\frac{|\epsilon_{\mathbf{k}}\mathbf{v}_{\mathbf{k}}\rangle}{2J^2d}\right)\begin{pmatrix}\nabla_{\mathbf{r}}n\\ \nabla_{\mathbf{r}}e\end{pmatrix}\end{aligned}$$

where we used the chain rule of differentiation and the fact that for high temperatures, $\partial_n f^0_{\mathbf{k}} \approx 1$ and $\partial_e f^0_{\mathbf{k}} \approx \epsilon_{\mathbf{k}}/(2J^2d)$ as can be seen e.g. from Eq. (6.42). Furthermore, from

$$\mathbf{j}_n = \langle\mathbf{v}_{\mathbf{k}}|\delta f_{\mathbf{k}}\rangle, \qquad \mathbf{j}_e = \langle\epsilon_{\mathbf{k}}\mathbf{v}_{\mathbf{k}}|\delta f_{\mathbf{k}}\rangle \tag{6.51}$$

we can identify the matrix of diffusion constants as

$$\begin{aligned} D &= -\begin{pmatrix}\langle\mathbf{v}_{\mathbf{k}}|\\ \langle\epsilon_{\mathbf{k}}\mathbf{v}_{\mathbf{k}}|\end{pmatrix} M^{-1}\left(|\mathbf{v}_{\mathbf{k}}\rangle,\,\frac{|\epsilon_{\mathbf{k}}\mathbf{v}_{\mathbf{k}}\rangle}{2J^2d}\right) \qquad (6.52)\\ &= -\begin{pmatrix}\langle\mathbf{v}_{\mathbf{k}}|M^{-1}|\mathbf{v}_{\mathbf{k}}\rangle & \langle\mathbf{v}_{\mathbf{k}}|M^{-1}|\epsilon_{\mathbf{k}}\mathbf{v}_{\mathbf{k}}\rangle/(2J^2d)\\ \langle\epsilon_{\mathbf{k}}\mathbf{v}_{\mathbf{k}}|M^{-1}|\mathbf{v}_{\mathbf{k}}\rangle & \langle\epsilon_{\mathbf{k}}\mathbf{v}_{\mathbf{k}}|M^{-1}|\epsilon_{\mathbf{k}}\mathbf{v}_{\mathbf{k}}\rangle/(2J^2d)\end{pmatrix}\\ &= -\widetilde{M}\cdot\begin{pmatrix}2J^2 & 0\\ 0 & \frac{3}{d}J^2\end{pmatrix}\end{aligned}$$

where we used Eq. (6.50), and where we have defined

$$\widetilde{M} = \begin{pmatrix}\langle\mathbf{v}_{\mathbf{k}}|M^{-1}|\mathbf{v}_{\mathbf{k}}\rangle/(2J^2) & \langle\mathbf{v}_{\mathbf{k}}|M^{-1}|\epsilon_{\mathbf{k}}\mathbf{v}_{\mathbf{k}}\rangle/(6J^4)\\ \langle\epsilon_{\mathbf{k}}\mathbf{v}_{\mathbf{k}}|M^{-1}|\mathbf{v}_{\mathbf{k}}\rangle/(2J^2) & \langle\epsilon_{\mathbf{k}}\mathbf{v}_{\mathbf{k}}|M^{-1}|\epsilon_{\mathbf{k}}\mathbf{v}_{\mathbf{k}}\rangle/(6J^4)\end{pmatrix} \tag{6.53}$$

By comparing Eqs. (6.48) and (6.52), we see that if $\hat{M}$ and $\widetilde{M}$ are inverse to each other, we have proven that $D = \tilde{D}$. Indeed, $\hat{M}$ and $\widetilde{M}$ are *almost* inverse to each other:

$$\widetilde{M} \;\approx\; \hat{M}^{-1} \tag{6.54}$$

While $\hat{M}^{-1}$ is the inverse of the projected scattering matrix on the subspace of the particle and energy currents, $\widetilde{M}$ is the projection of the *full* inverse matrix. To a good approximation, these two matrices coincide, because the current and energy current modes are the weakly damped, “slow” modes in the system [30]. Therefore, the matrix elements $\langle \mathbf{v_k}|M|\mathbf{v_k}\rangle$, $\langle \epsilon_\mathbf{k}\mathbf{v_k}|M|\mathbf{v_k}\rangle$, $\langle \mathbf{v_k}|M|\epsilon_\mathbf{k}\mathbf{v_k}\rangle$ and $\langle \epsilon_\mathbf{k}\mathbf{v_k}|M|\epsilon_\mathbf{k}\mathbf{v_k}\rangle$ are comparatively *small*, and they hence contribute *strongly* to the inverse matrix. Hence, the generalized continuity equations allow us to reproduce the conventional hydrodynamic (diffusive) limit of the Boltzmann equation.

6.3.2 Damping of Bloch oscillations and the harmonic oscillator

We will now analyze the spatially homogeneous system. Again, we consider the situation where the force $\mathbf{F} = F\,(1, 1, ..., 1)^T$ points in the diagonal direction of the lattice[2]. The case where the force points in the direction of an individual lattice coordinate can be also treated with our method, but is is slightly more complicated as it leads to a splitting of the energy mode in the direction of the force and the perpendicular directions, whose dynamics are coupled. As the force points into the diagonal direction, the current mode will deviate from equilibrium in the diagonal direction. As the scattering matrix M has no preferred lattice coordinate, the momentum distribution can be expected to remain the same for each lattice coordinate. We therefore simplify the ansatz (6.42) according to

$$f_\mathbf{k}(t) = n + \frac{e(t)}{2J^2 d}\,\epsilon_\mathbf{k} + \frac{v(t)}{2J^2 d}\,v_\mathbf{k} + ... \tag{6.55}$$

where $v_\mathbf{k}$ is the scalar current or velocity mode defined in Eq. (6.32) and $v(t)$ is its coefficient. Spatial homogeneity reduces the complexity of Eqs. (6.44), which simplify to

$$\begin{aligned} \dot{e} - F\,v &= 0 \\ \dot{v} + F\,e &= -\frac{1}{2J^2 d}\,\langle v_\mathbf{k}|M|v_\mathbf{k}\rangle\, v \end{aligned} \tag{6.56}$$

whereby we neglected the dynamics of the heat current mode and the possibility to scatter between the current and heat current modes, which means that we neglected thermoelectric effects. For the following analysis, it will be convenient to define the damping parameter

$$\tau^{-1} \;:=\; \frac{1}{2}\frac{\langle v_\mathbf{k}|M|v_\mathbf{k}\rangle}{2J^2 d} \tag{6.57}$$

As a side remark, note that we have encountered τ^{-1} before: it is exactly the rate at which we have shown the energy mode to get damped in the limit of weakly damped Bloch oscillations, as can be seen in Eq. (6.34). Let us now combine the two coupled first-order ordinary differential equations (6.56) and create a single second-order differential equation out of them, which reads

$$\ddot{v} = F^2\,v - 2\tau^{-1}\,\dot{v} \tag{6.58}$$

---

[2] As before, scalar parameter F signifies the projection of the force on the individual lattice coordinates.

Surprisingly, this is nothing but the equation of the classical damped harmonic oscillator. As it is known from textbooks [123], the harmonic oscillator is characterized by three regimes: the over-damped regime, the under-damped regime, and the critically damped regime in between. All regimes carry over to the damping of Bloch oscillations, and we will discuss them below. Let us emphasize that the full solution of Eq. (6.58) is given by

$$v(t) = e^{-t/\tau} \left[A \exp\left(t \sqrt{\frac{1}{\tau^2} - F^2} \right) + B \exp\left(-t \sqrt{\frac{1}{\tau^2} - F^2} \right) \right] \tag{6.59}$$

but we are going to discuss the limits of this solution instead, as they correspond exactly to the two regimes that we have been studying before.

a.) Over-damped limit

Let us first study the case where $F\tau \ll 1$. In this case we can approximate the square root in the full solution Eq. (6.59) as

$$\sqrt{1/\tau^2 - F^2} \;\approx\; \tau^{-1} \left(1 - \frac{1}{2} (\tau F)^2 \right) \tag{6.60}$$

Therefore, the velocity and hence also the kinetic energy mode decays according to

$$e(t) = e_0 \exp\left(-\frac{1}{2}\, t\, \tau\, F^2 \right) \tag{6.61}$$

in this limit. As we will show now, this is an approximation to a previous result that we obtained in the over-damped regime, given by Eq. (6.13). First let us demonstrate that the factor $-e\tau/2$ is an approximation to the system's *conductivity* σ:

$$\sigma \overset{(6.12)}{\approx} -\frac{\langle \mathbf{v_k} | M^{-1} | \mathbf{v_k} \rangle}{2J^2 d}\, e \approx -\frac{2J^2 d}{\langle \mathbf{v_k} | M | \mathbf{v_k} \rangle}\, e \overset{(6.57)}{=} -\frac{e\,\tau}{2} \tag{6.62}$$

where we approximated the matrix element of the inverse matrix of M by the inverse matrix element of M. As discussed before, the current-current matrix element is small, as the current is only weakly damped by umklapp scattering. Hence, this matrix element becomes *dominant* in the inverse matrix, and therefore the approximation is well justified. Using this approximation and combine it with Eq. (6.61), we find that

$$e(t) \sim \exp(-\frac{\tau\, t}{2}\, F^2) \tag{6.63}$$

which is nothing but Eq. (6.13) from the first section of this chapter. Therefore, the over-damped limit gives the analogous result to the diffusive limit.

b.) Weakly damped Bloch oscillations

In the limit of $F\,\tau \gg 1$, the square roots in Eq. (6.59) become negative. Introducing

$$\omega = \sqrt{F^2 - 1/\tau^2} \tag{6.64}$$

the dynamics of the kinetic energy is approximately given by

$$e(t) = e_0\, e^{-t/\tau}\, \cos(\omega t) \tag{6.65}$$

Most prominently, the envelope of the oscillations decay exponentially at the rate τ^{-1}. This result is in correspondence with the perturbative result (6.34) obtained earlier, which exactly contains the definition of the factor $1/\tau$ as the decay rate. Therefore, also the limit of weakly damped Bloch oscillations is describable with the method of deriving generalized continuity equations as we have done in this section. However, here we were able to derive an expression for the interaction-dependent frequency shift of these oscillations, too.

c.) Marginal case

In the marginal case of $F\tau = 1$, Bloch oscillations get critically damped. For the initial condition that $e(0) = e_0$ and $\dot{e}(0) = 0$, the dynamics of the kinetic energy mode is given by

$$e(t) = (e_0 + e_0 t/\tau)\, e^{-t/\tau} \tag{6.66}$$

which contains corrections to a purely exponential decay of the energy mode. Note that this limit is highly non-perturbative in the ratios $\tau_B/\tau_{\mathrm{sc}}$ or $\tau_{\mathrm{sc}}/\tau_B$ and can not be derived from the perturbative approaches that we have discussed before.

6.3.3 Comparison with Boltzmann simulations

We can now proceed and compare our analytic findings with a numerical simulation of a Boltzmann equation. As a minimalistic model that describes the physics of inter-particle scattering and relaxation to equilibrium, we decided to do the comparison for a one-dimensional, *discrete* homogeneous Boltzmann equation, including the full collision integral:

$$\begin{aligned}(\partial_t + F\,\partial_k)\; f_k(t) \;\; = \;\; & -\frac{U^2}{J}\frac{1}{N}\sum_{k_1,k_2,k_3} \delta(k + k_2 - k_2 - k_3 \bmod \pi, 0) \\ & \times (f_k f_{k_1}(1 - f_{k2})(1 - f_{k3}) - f_{k2} f_{k3}(1 - f_k)(1 - f_{k_1})) \\ & \times \delta\,(\epsilon_k + \epsilon_{k_1} - \epsilon_{k_2} - \epsilon_{k_3}, 0)\end{aligned} \tag{6.67}$$

Here, the operator $\partial_k f = (f_{i+1} - f_{i-1})/2\Delta k$ with $\Delta k = 2\pi/N$ stands for the discrete derivative and δ signifies the Kronecker δ-symbol. Note that in contrast to the continuous equation, the collision integral carries a prefactor of U^2/J instead of U^2 as the discrete delta-constraint for the energy is dimension-less. As in previous studies, the presence of umklapp processes is crucial to ensure equilibration to the fixed frame of reference give by the lattice. The distribution function $f_{\mathbf{k}}$ was initially prepared as a Fermi function at $T = J$, a typical temperature for current experiments with ultracold fermionic atoms.

Note that the one-dimensional Boltzmann equation has got very peculiar relaxation and scattering properties and does not properly describe the one-dimensional Hubbard model, as we discuss in more detail in Appendix (E.2). However, we will be interested in using it as a simplistic, well defined discrete model that allows us to easily compare our analytic findings with numerical simulations. To this end, we need to calculate the current-current matrix element $\langle v_k|M|v_k\rangle \sim \tau^{-1}$ of the corresponding *linearized* Boltzmann equation. This matrix element is particularly easy to calculate in one dimension, and we calculate it for the discrete linearized Boltzmann equation in Appendix (E.2). Following Eq. (E.12), it is approximately given by

$$\langle v_k|M|v_k\rangle \;\approx\; 4\,n(1-n)\,U^2\,J \qquad (N \gg 1) \tag{6.68}$$

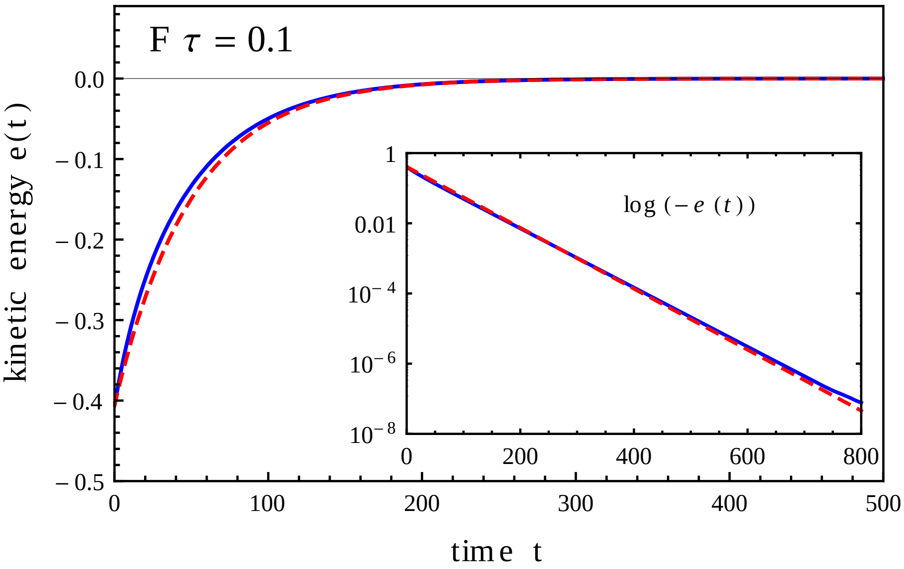

Figure 6.1: *Over-damped* Bloch oscillations of the kinetic energy at filling 1/2. Blue curve: numerical simulation of the Boltzmann Eq. (6.67) for the parameters $U/J = 4$ (yielding $\tau = 0.25$) and $F = 0.4J$ such that $F\tau = 0.1$ guarantees the validity of the diffusive regime. Red dashed curve: analytic result from Eq. (6.61).

such that when using the defining Eq. (6.57) for τ, the latter at filling $n = 1/2$ is given by

$$\tau \;=\; 4\,J/U^2 \tag{6.69}$$

We can now study the three regimes of the harmonic oscillator equation and compare it with simulations of the Boltzmann equation.

Figures 6.1, 6.2 and 6.3 show the cases of *over*-damped, *weakly* damped and *marginally* damped Bloch oscillations, respectively. While the blue curves show the numerical simulations of the Boltzmann Eq. (6.67), the dashed red curves show the analytic predictions given by Eqs. (6.61), (6.65) and (6.66), respectively. Note that the analytic results only depend on the initial kinetic energy e_0, which was adjusted to the initial kinetic energy in the numerical simulations. As the analytic formulas depend only on the force F and on the calculated damping rate τ^{-1}, no fitting parameters were involved. Surprisingly, the analytic formulas describe the complex dynamics of the Boltzmann equation extremely well, despite of the fact that they are based on a high temperature expansion of the collision integral and neglect thermoelectric couplings. Note that the weakly damped and over-damped regimes of Bloch oscillations have also been observed numerically for the Hubbard model by Eckstein and Werner [51], using DMFT. Our quantitative mapping to the harmonic oscillator equation gives a first analytic explanation for this numerical observation.

This concludes the study of the homogeneous system, where we essentially neglected the scattering between the damped momentum modes. In the presence of inter-mode scattering, the equations (6.44) are probably not analytically solvable. Having solved the homogeneous system with this approach, one could ask about the possibility to fully solve the spatially inhomogeneous system as well. However, we are not aware how to solve the complicated coupled equations (6.44) in the presence of spatial gradients. Instead, we will continue with our earlier approach that we introduced in subsection 6.2.2 to derive effective

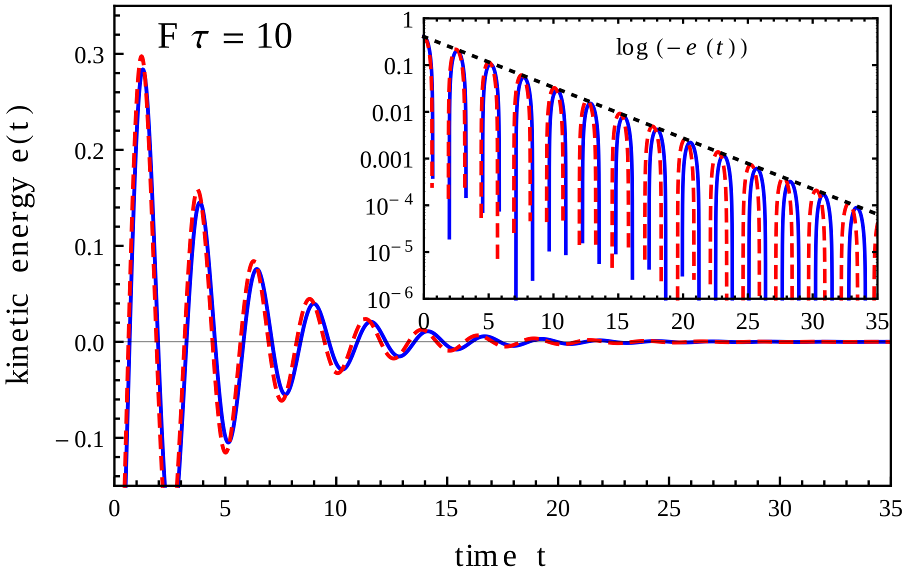

Figure 6.2: *Weakly* damped Bloch oscillations of the kinetic energy at filling 1/2. Blue curve: numerical simulation of the Boltzmann Eq. (6.67) for the parameters $U/J = 1$ (yielding $\tau = 4$) and $F = 2.5J$ such that $F\tau = 10$ gives rise to the regime of weak damping. Red dashed curve: analytic result from Eq. (6.65).

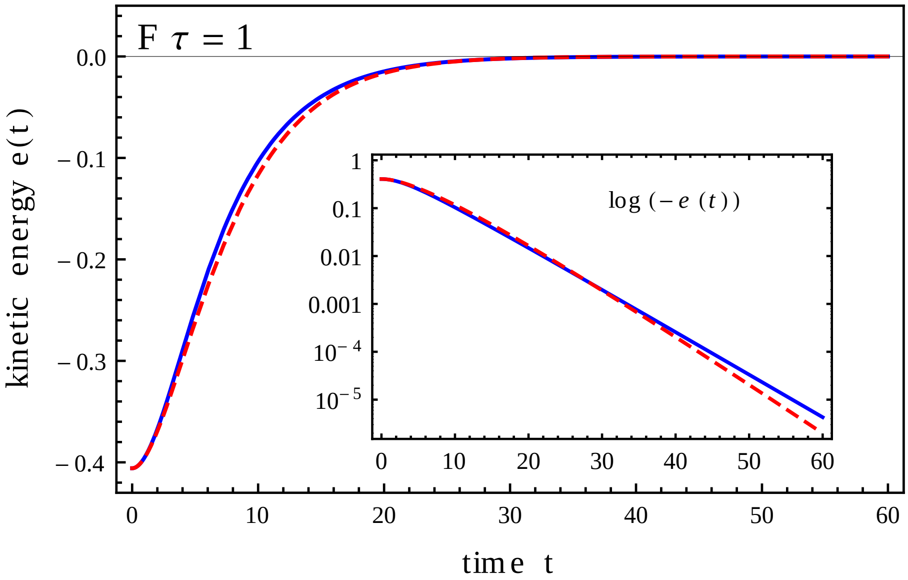

Figure 6.3: *Marginally* damped Bloch oscillations of the kinetic energy at filling 1/2. Blue curve: numerical simulation of the Boltzmann Eq. (6.67) for the parameters $U/J = 1$ (yielding $\tau = 4$) and $F = 0.25J$ such that $F\tau = 1$ gives rise to the marginal case. Red dashed curve: analytic result from Eq. (6.66).

equations for the inhomogeneous system in the limit $F\tau \gg 1$, where again we average the oscillatory dynamics over the Bloch period.

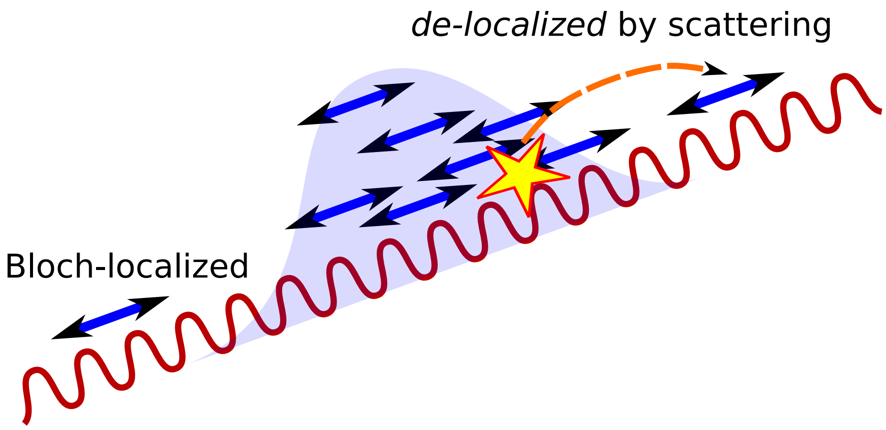

Figure 6.4: Sketch of the situation described by the stroboscopic diffusion equation: at very weak interactions, particles are dominantly Bloch-oscillating in the restricted region indicated by the blue double-arrows, and scatter only rarely. Only by inter-particle scattering, they can be kicked out of their periodic motion. On top of the fast periodic Bloch oscillations, we can therefore expect a nonlinear diffusion process to occur, where the speed of diffusion, reflected by the diffusion constant $D \sim n$, is proportional to the local density.

6.4 The stroboscopic diffusion equation

6.4.1 Introduction

We will now study the spatially *inhomogeneous* situation. Just as in chapter 5, we will be interested in the dynamics of an interacting, finite cloud of Fermions in a tilted optical lattice, described by the Hubbard model with an additional linear potential. However, in contrast to the previous study which was based on the collision-dominated diffusive regime where $F\tau_{\text{sc}} \ll 1$, we will now be interested in the opposite limit of weakly damped Bloch oscillations, where $F\tau_{\text{sc}} \gg 1$. Our study is nevertheless based on the validity of the Boltzmann equation, which requires smooth external potentials. In this sense, one should better have very small scattering rates in mind, instead of strong forces.

Let us now try to derive effective equations of motion for the cloud of atoms. In chapter 5, we derived coupled diffusion equations and found that the coupling of the energy and particle diffusion was essential. We can still expect that this is also the case in the limit of strong Bloch oscillations, as the system is still thermally isolated. As we are interested in the opposite limit, where the system is dominantly Bloch oscillating, the conventional diffusion equations which rely on being close to local equilibrium obviously are not valid in this regime. Instead, we may hope to derive alternative equations of motion for the lowest momentum modes.

Scattering events are rare, but they are crucial for the long time dynamics of the system, as they break the periodicity of the cloud's Bloch oscillating motion. This situation is sketched in Fig. 6.4, which shows that the cloud can only move over long distances by scattering: the isolated, Bloch oscillating particles at the edge of the cloud are *localized* on a length scale given by the inverse force. When looking at those particles *stroboscopically* in units of the Bloch oscillation period, they do not move at all. Instead, only the rare collisions between particles can break the periodicity in the dynamics and lead to a spreading of the cloud. Having this picture in mind, we are interested in deriving a *stroboscopic diffusion equation*, that describes the expansion of the cloud whereby we ignore its rapid Bloch oscillating motion.

The regime of weakly damped Bloch oscillations is highly relevant in the context of ultracold atoms in optical lattices exposed to a linear (gravitational) potential. As we have pointed out in the conclusions of chapter 5, a finite cloud of atoms that expands in an optical lattice in the presence of gravity will in the long time limit always enter the regime of weakly damped Bloch oscillations. The reason is that while the cloud expands, its density goes to zero and therefore the scattering rate decreases, while the strength of the force remains always the same. While we found in chapter 5 for the collision-dominated regime that the cloud's radius R grows according to the law $R \sim t^{1/3}$ in time t, the system will display a different scaling law in the regime dominated by Bloch oscillations, which we will identify at the end of this chapter.

The system is characterized by three different macroscopic length scales: the radius R of the cloud, the length scale J/F on which the external potential changes, and the scattering length $J\tau_{\mathrm{sc}}$. While $J/F \ll J\tau_{\mathrm{sc}}$ already characterizes the regime of strong Bloch oscillations, we still have the option to study a small cloud in a weak potential, i.e. $R \ll J/F$, or a large cloud in a steep potential, $R \gg J/F$. We will be interested in the second case, such that we consider the following hierarchy of length scales:

$$1/R \ll 1/(\tau_{\mathrm{sc}} J) \ll F/J \tag{6.70}$$

We will study the system using the perturbative scheme introduced in section 6.2.2. While this method may have seemed rather formal and complicated compared with the method of deriving generalized continuity equations, it reveals its full use in a spatially inhomogeneous situation. In the presence of spatial gradients, we are not aware of how to extract any information about the long time dynamics from Eq. (6.44). However, the perturbative method is easily generalizable to a spatially inhomogeneous situation. It turns out that we have done most of the work already in section 6.2.2.

How well can we expect the stroboscopic diffusion equation to reproduce the full dynamics of the Boltzmann equation? As we stated previously, there is no principle reason to describe the system's dynamics only in terms of the particle and energy density alone in a situation far from local equilibrium. In fact, here the situation is even worse than in the homogeneous system: previously, the dynamics of the energy and velocity mode were separated from all other momentum modes when neglecting inter-mode scattering. In the inhomogeneous case, all modes are in addition coupled to each other by spatial gradients, as can be seen in Eq. (6.44). This makes the inhomogeneous system much more complicated. Here, we review the derivation of a *minimalistic* variant of a diffusion equation with a minimal number of momentum modes. We claim that our approach is *semi-quantitative*: the final diffusion equation is only qualitatively correct, but we show how to principally calculate the numerical parameters of the diffusion constant and how to systematically improve the quality of the approximation by considering a larger number of modes. The goal of the section will be to analyze the scaling of the growth of the cloud's radius as a function of time. This scaling relation does not depend on the numerical values of the diffusion constant, but might also be modified when considering a larger number of momentum modes.

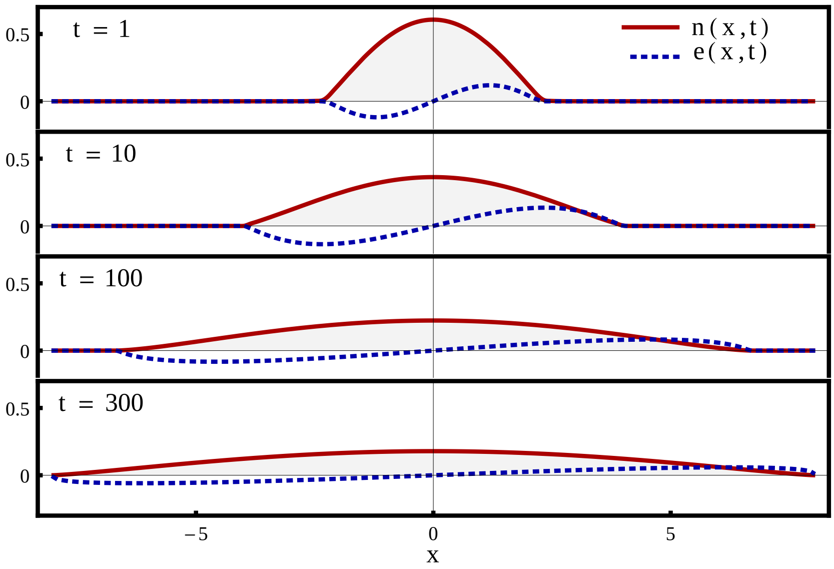

Figure 6.5: Numerical simulation of the nonlinear *stroboscopic* diffusion equations (6.102). We simulated the case $F = 1\,J$ and measure time in units of $\tau_0\,F^2/J^2$. Initially, the system was prepared at zero kinetic energy and with a Gaussian density profile $n(x,0) = \exp(-x^2)$. Within one time unit, the density approximately assumes the shape of its scaling function, as can be seen in Fig. 6.7. This characteristic shape drastically varies from the conventional diffusive limit studied in chapter 5, where it was found to be approximately a Gaussian.

6.4.2 Decomposition of the distribution function

In order to derive effective diffusion equations in the case of strong Bloch oscillations, we will follow and extend the approach of section 6.2.2. This time, we will be interested in finding an approximate solution to the *inhomogeneous* linearized Boltzmann equation in the presence of a constant force $\mathbf{F}$,

$$(\partial_t + \mathbf{v}_\mathbf{k}\nabla_\mathbf{r} + \mathbf{F}\nabla_\mathbf{k})\, f_\mathbf{k}(\mathbf{r},t) \;=\; -\int \frac{d\mathbf{k}'}{(2\pi)^d}\, M_{\mathbf{k}\mathbf{k}'}\, \left(f_{\mathbf{k}'}(\mathbf{r},t) - n(\mathbf{r},t)\right) \tag{6.71}$$

Beyond the standard diffusive limit that we have derived from this equation in chapter 2, this is a non-trivial problem. Again, we consider a situation where the force $\mathbf{F}$ points in the diagonal direction of the lattice:

$$\mathbf{F} \;=\; F \begin{pmatrix} 1 \\ \vdots \\ 1 \end{pmatrix} \tag{6.72}$$

In analogy to the homogeneous case, we start from the decomposition

$$f_\mathbf{k} = f^B_\mathbf{k} + \delta f_\mathbf{k} \tag{6.73}$$

where $f^B_\mathbf{k}$ solves the non-interacting problem,

$$(\partial_t + \mathbf{v}_\mathbf{k}\nabla_\mathbf{r} + \mathbf{F}\nabla_\mathbf{k})\, f^B_\mathbf{k}(\mathbf{r},t) \;=\; 0 \tag{6.74}$$

In the presence of spatial gradients, the construction of $f^B_{\mathbf{k}}$ is a bit more subtle than in the homogeneous situation. To simplify the problem, let us consider a situation where the initial distribution function is *translationally invariant* in the direction perpendicular to the force. By the symmetry of the initial state and by the fact that the projection of the force F on every lattice coordinate is the same, we can expect the distribution function to remain translationally invariant in this direction. Let therefore r be the component of $\mathbf{r}$ along the diagonal. Let us now consider the function

$$\xi_{\mathbf{k},t} \;=\; F^{-1}\left(\epsilon_{\mathbf{k}-\mathbf{F}t} - \epsilon_{\mathbf{k}}\right) \tag{6.75}$$

which has the dimensionality of a length. One can easily check that

$$\left(\partial_t + v_{\mathbf{k}}\partial_r + \mathbf{F}\nabla_{\mathbf{k}}\right)\left(r + \xi_{\mathbf{k},t}\right) \;=\; 0 \tag{6.76}$$

In fact, *any* function that depends on the composite argument $(r + \xi_{\mathbf{k},t})$ solves the non-interacting Boltzmann equation. The function $\xi_{\mathbf{k},t}$ is related to the displacement of a Bloch-oscillating particle at time t from its initial position r. If at time $t = 0$, the system is characterized by the distribution function $f(\mathbf{r}, \mathbf{k}, 0)$, one can check easily that

$$f^B(\mathbf{r}, \mathbf{k}, t) \;=\; f\left(r + \xi_{\mathbf{k},t},\, \mathbf{k} - \mathbf{F}t,\, 0\right) \tag{6.77}$$

is a solution to Eq. (6.74) with the given initial condition. Let us now calculate the scattering integral of this zeroth-order solution in order to obtain the first order correction to the non-interacting result. To this end, we define

$$\begin{aligned}
b(r, \mathbf{k}, t) \quad &= \quad -\frac{1}{(2\pi)^d}\int d\mathbf{k}'\, M_{\mathbf{k},\mathbf{k}'}\; f^B(r, \mathbf{k}', t) \qquad (6.78)\\
&= \quad -\frac{1}{(2\pi)^d}\int d\mathbf{k}'\, M_{\mathbf{k},\mathbf{k}'}\; f\left(r + \xi_{\mathbf{k}',t},\, \mathbf{k}' - \mathbf{F}t,\, 0\right)\\
&\overset{\mathbf{k}'\to\mathbf{k}'+\mathbf{F}t}{=} \quad -\frac{1}{(2\pi)^d}\int d\mathbf{k}'\, M_{\mathbf{k},\mathbf{k}'+\mathbf{F}t}\; f\left(r + \xi_{\mathbf{k}'+\mathbf{F}t,t},\, \mathbf{k}',\, 0\right)
\end{aligned}$$

In order to find the deviation from the non-interacting solution f^B, we have to invert the Liouvillian operator, which amounts to solving the following equation for $\delta f(\mathbf{r}, \mathbf{k}, t)$:

$$\left(\partial_t + v_{\mathbf{k}}\partial_r + \mathbf{F}\nabla_{\mathbf{k}}\right)\delta f(r, \mathbf{k}, t) \;=\; b(r, \mathbf{k}, t) \tag{6.79}$$

In analogy to Eq. (6.25), it can be checked straightforwardly that the solution is given by

$$\begin{aligned}
\delta f(r, \mathbf{k}, t) \quad &= \quad \int_0^t dt'\, b(r + \xi_{\mathbf{k}-\mathbf{F}(t-t'),t'},\, \mathbf{k} - \mathbf{F}(t-t'),\, t')\\
&\overset{(6.78)}{=} \quad -\int_0^t dt' \int \frac{d\mathbf{k}'}{(2\pi)^d}\, M_{\mathbf{k}+\mathbf{F}(t-t'),\mathbf{k}'+\mathbf{F}t'}\\
&\qquad\quad \times f(r + \xi_{\mathbf{k}'+\mathbf{F}t',t'} + \xi_{\mathbf{k}-\mathbf{F}(t-t'),t'},\, \mathbf{k}',\, 0)
\end{aligned}$$

This is the analog equation of Eq. (6.26) in the inhomogeneous case, but for our purposes it is still too complicated. We would like to take advantage of the fact that the cloud radius R is much larger than the length scale associated to the Bloch oscillations $\xi_{\mathbf{k},t} \sim JF^{-1}$. We can therefore expand the Bloch oscillating distribution function in its spatial argument:

$$\begin{aligned}
f(r + \xi_{\mathbf{k}'+\mathbf{F}t',t'} + \xi_{\mathbf{k}-\mathbf{F}(t-t'),t'},\, \mathbf{k}',\, 0) \quad \approx \quad & f(r,\, \mathbf{k}',\, 0)\\
& + \partial_r\, f(r,\, \mathbf{k}',\, 0)\left(\xi_{\mathbf{k}'+\mathbf{F}t',t'} + \xi_{\mathbf{k}-\mathbf{F}(t-t'),t'}\right)
\end{aligned}$$

Again we define

$$\delta\overline{f_{\mathbf{k}}}(r) \;=\; \frac{1}{\tau_B}\int_0^{\tau_B} \delta f(r,\mathbf{k},t) \tag{6.80}$$

In analogy to Eq. (6.28), we then find

$$\delta\overline{f_{\mathbf{k}}}(r) \;=\; -\int \frac{d\mathbf{k}'}{(2\pi)^d}\,\overline{M}_{\mathbf{k}\mathbf{k}'}\,\big(f(r,\mathbf{k}',0)-n(r,0)\big) \;-\; \int \frac{d\mathbf{k}'}{(2\pi)^d}\,\overline{\overline{M}}_{\mathbf{k}\mathbf{k}'}\,\partial_r\, f(r,\mathbf{k}',0) \tag{6.81}$$

In a similar way as in Eq. (6.29), we have defined

$$\begin{aligned}\overline{M}_{\mathbf{k}\mathbf{k}'} &= \frac{1}{\tau_B}\int_0^{\tau_B} dt \int_0^t dt'\, M_{\mathbf{k}-\mathbf{F}(t-t'),\mathbf{k}'+\mathbf{F}t'} \qquad (6.82)\\ \overline{\overline{M}}_{\mathbf{k}\mathbf{k}'} &= \frac{1}{\tau_B}\int_0^{\tau_B} dt \int_0^t dt'\, M_{\mathbf{k}-\mathbf{F}(t-t'),\mathbf{k}'+\mathbf{F}t'}\,\big(\xi_{\mathbf{k}'+\mathbf{F}t',t'}+\xi_{\mathbf{k}-\mathbf{F}(t-t'),t'}\big)\end{aligned}$$

In order to derive effective, coupled diffusion equations for the lowest modes, we again have to parametrize the initial distribution function $f_{\mathbf{k}}(r)$ by those modes. As we have discussed before, the system's dynamics far from equilibrium may be highly complex and characterized by the interplay of *all* momentum modes, but we will restrict our attention to the dynamics of the density and energy density. At time $t=0$, we approximate

$$f(r,\mathbf{k},0) \;\approx\; n(r) \,+\, \frac{e(r)}{\langle\epsilon_{\mathbf{k}}|\epsilon_{\mathbf{k}}\rangle}\,\epsilon_{\mathbf{k}} \tag{6.83}$$

where $\langle\epsilon_{\mathbf{k}}|\epsilon_{\mathbf{k}}\rangle = 2J^2 d$. This initial condition approximately emerges when preparing the system in local equilibrium at high temperature, before the constant force is switched on. However, at longer times, the system might be characterized by a spatially varying phase shift in the kinetic energy mode, i.e. $\epsilon_{\mathbf{k}} \to \epsilon_{\mathbf{k}-\phi(\mathbf{r})}$. Including this phase shift as a third mode and studying its impact on the dynamics will be left for future studies. As discussed before, we will continue studying the system's dynamics qualitatively, by deriving a minimal variant of the stroboscopic diffusion equation that is characterized by the coupled dynamics of the density and the kinetic energy alone.

In analogy to our previous study of the homogeneous system, we will be interested in the net flow of particles and energy, integrated over one Bloch period and divided by τ_B. Therefore we use Eq. (6.81) and calculate the particle current $j_n(n,e)=\int v_{\mathbf{k}}\delta\overline{f_{\mathbf{k}}}(r)$ and energy current $j_e(n,e)=\int \epsilon_{\mathbf{k}}v_{\mathbf{k}}\delta\overline{f_{\mathbf{k}}}(r)$ from it, where we use the above parametrization (6.83) for $f(r,\mathbf{k},0)$. Those currents are given by

$$\begin{pmatrix} j_n\\ j_e\end{pmatrix} = -\underbrace{\begin{pmatrix}\langle v_{\mathbf{k}}|\overline{\overline{M}}|1\rangle & \langle v_{\mathbf{k}}|\overline{\overline{M}}|\epsilon_{\mathbf{k}}\rangle/\langle\epsilon_{\mathbf{k}}|\epsilon_{\mathbf{k}}\rangle\\ \langle\epsilon_{\mathbf{k}}v_{\mathbf{k}}|\overline{\overline{M}}|1\rangle & \langle\epsilon_{\mathbf{k}}|\overline{\overline{M}}|\epsilon_{\mathbf{k}}\rangle/\langle\epsilon_{\mathbf{k}}|\epsilon_{\mathbf{k}}\rangle\end{pmatrix}}_{=D}\cdot\begin{pmatrix}\partial_r\, n\\ \partial_r\, e\end{pmatrix} - \begin{pmatrix}\langle v_{\mathbf{k}}|\overline{M}|\epsilon_{\mathbf{k}}\rangle\\ \langle\epsilon_{\mathbf{k}}v_{\mathbf{k}}|\overline{M}|\epsilon_{\mathbf{k}}\rangle\end{pmatrix}\,\frac{e}{\langle\epsilon_{\mathbf{k}}|\epsilon_{\mathbf{k}}\rangle} \tag{6.84}$$

We then use those currents in combination with the continuity equations

$$\dot n = -\partial_r\, j_n, \qquad \dot e = -\partial_r\, j_e + F\, j_n \tag{6.85}$$

We can identify the matrix D in Eq. (6.84) as the diffusion constant of the problem. So far, we have only derived an abstract result, which is the generalization of Eq. (6.31) that we derived in the homogeneous case. Again, we need to relate the matrix elements of $\overline{M}$ and $\overline{\overline{M}}$ to matrix elements of M in order to make the equation transparent. As previously, we will be able to do so due to several trigonometric identities.

Let therefore be $a_{\mathbf{k}} \in \{v_{\mathbf{k}},\, \epsilon_{\mathbf{k}} v_{\mathbf{k}}\}$ and $b_{\mathbf{k}} \in \{1,\, \epsilon_{\mathbf{k}}\}$. Calculating the entries of the matrix of diffusion constants D then amounts to calculating matrix elements of the structure $\langle a_{\mathbf{k}} | \overline{\overline{M}} | b_{\mathbf{k}} \rangle$. According to the definition of $\overline{\overline{M}}$ in Eq. (6.82), we find that

$$\langle a_{\mathbf{k}} | \overline{\overline{M}}_{\mathbf{k}\mathbf{k}'} | b_{\mathbf{k}'} \rangle = \frac{1}{\tau_B} \int_0^{\tau_B} dt \int_0^t dt' \, \langle a_{\mathbf{k}+\mathbf{F}(t-t')} | M_{\mathbf{k}\mathbf{k}'} \left(\xi_{\mathbf{k}',t'} + \xi_{\mathbf{k},t'} \right) | b_{\mathbf{k}'-\mathbf{F}t'} \rangle \tag{6.86}$$

where we have made the substitutions in the momentum integrals $\mathbf{k} \to \mathbf{k} + \mathbf{F}(t - t')$ and $\mathbf{k}' \to \mathbf{k}' - \mathbf{F}t'$ involved in the scalar products. Furthermore, we can take advantage from the following trigonometric identities:

$$\begin{aligned} \epsilon_{\mathbf{k}-\mathbf{F}t} &= \epsilon_{\mathbf{k}} \cos(Ft) - v_{\mathbf{k}} \sin(Ft) \\ v_{\mathbf{k}-\mathbf{F}t} &= v_{\mathbf{k}} \cos(Ft) + \epsilon_{\mathbf{k}} \sin(Ft) \\ \xi_{\mathbf{k},t} &= F^{-1} \left(\epsilon_{\mathbf{k}} \cos(Ft) - v_{\mathbf{k}} \sin(Ft) - \epsilon_{\mathbf{k}} \right) \end{aligned} \tag{6.87}$$

These identities help us to separate the momentum integrals from the time integrals, and perform the time integrals exactly. In Appendix (E.3), we will present the calculation of the matrix elements in more detail. As a result, we find the following relations:

$$\begin{aligned} \langle v_{\mathbf{k}} | \overline{\overline{M}} | 1 \rangle &= \frac{1}{2\,F^2} \, \langle v_{\mathbf{k}} | M | v_{\mathbf{k}} \rangle \\ \langle v_{\mathbf{k}} | \overline{\overline{M}} | \epsilon_{\mathbf{k}} \rangle &= -\frac{3}{2\,F^2} \, \langle \epsilon_{\mathbf{k}} v_{\mathbf{k}} | M | v_{\mathbf{k}} \rangle \\ \langle \epsilon_{\mathbf{k}} v_{\mathbf{k}} | \overline{\overline{M}} | 1 \rangle &= 0 \\ \langle \epsilon_{\mathbf{k}} v_{\mathbf{k}} | \overline{\overline{M}} | \epsilon_{\mathbf{k}} \rangle &= \frac{1}{4\,F^2} \, \left(\langle \epsilon_{\mathbf{k}} v_{\mathbf{k}} | M | \epsilon_{\mathbf{k}} v_{\mathbf{k}} \rangle \, + \, R \right) \end{aligned} \tag{6.88}$$

where the remaining terms

$$\begin{aligned} R \;=\; & \frac{1}{4} \{ \langle v_{\mathbf{k}}^2 | M | \epsilon_{\mathbf{k}}^2 \rangle - \langle \epsilon_{\mathbf{k}}^2 v_{\mathbf{k}} | M | v_{\mathbf{k}} \rangle - 3 \langle \epsilon_{\mathbf{k}}^2 | M | v_{\mathbf{k}}^2 \rangle \\ & - \langle \epsilon_{\mathbf{k}}^2 | M | \epsilon_{\mathbf{k}}^2 \rangle + 3 \langle v_{\mathbf{k}}^3 | M | v_{\mathbf{k}} \rangle + 3 \langle v_{\mathbf{k}}^2 | M | v_{\mathbf{k}}^2 \rangle \} \end{aligned} \tag{6.89}$$

contain matrix elements involving higher momentum modes. To be consistent with describing the system qualitatively in terms of the lowest modes, we negelect all matrix elements involving modes that are orthogonal to the particle- and energy current modes. When submitting this thesis, we therefore wrongly concluded that R could be neglected. However, later we became aware of the fact that R contains contributions that can *not* be neglected, e.g. due to the finite overlap between $v_{\mathbf{k}}^3$ and $v_{\mathbf{k}}$. Carrying out the calculation in the presence of those contributions may modify the following scaling analysis and will be left for future studies. In the following, we will present the analysis for $R = 0$.

The matrix of diffusion constants is approximately given by

$$D \;=\; \frac{1}{4F^2} \begin{pmatrix} 2 \, \langle v_{\mathbf{k}} | M | v_{\mathbf{k}} \rangle & -6 \, \left(\langle \epsilon_{\mathbf{k}} v_{\mathbf{k}} | M | v_{\mathbf{k}} \rangle + R \right) / (2J^2 d) \\ 0 & \langle \epsilon_{\mathbf{k}} v_{\mathbf{k}} | M | \epsilon_{\mathbf{k}} v_{\mathbf{k}} \rangle / (2J^2 d) \end{pmatrix} \tag{6.90}$$

The matrix entries involving $\overline{M}$ can be calculated in the same way (see Appendix (E.3)), and we find that

$$\langle v_{\mathbf{k}} | \overline{M} | \epsilon_{\mathbf{k}} \rangle \;=\; \frac{1}{2\,F} \langle v_{\mathbf{k}} | M | v_{\mathbf{k}} \rangle \tag{6.91}$$

$$\langle \epsilon_{\mathbf{k}} v_{\mathbf{k}} | \overline{M} | \epsilon_{\mathbf{k}} \rangle \;=\; 0 \tag{6.92}$$

To conclude, ignoring R as discussed before, the diffusive currents read

$$\begin{pmatrix} j_n \\ j_e \end{pmatrix} = -\frac{1}{4F^2} \begin{pmatrix} 2\,\langle v_\mathbf{k}|M|v_\mathbf{k}\rangle & -6\,\langle \epsilon_\mathbf{k} v_\mathbf{k}|M|v_\mathbf{k}\rangle/(2J^2d) \\ 0 & \langle \epsilon_\mathbf{k} v_\mathbf{k}|M|\epsilon_\mathbf{k} v_\mathbf{k}\rangle/(2J^2d) \end{pmatrix} \cdot \begin{pmatrix} \partial_r\, n \\ \partial_r\, e \end{pmatrix} - \begin{pmatrix} \frac{1}{2\,F} \frac{\langle v_\mathbf{k}|M|v_\mathbf{k}\rangle}{2J^2d}\; e \\ 0 \end{pmatrix} \tag{6.93}$$

6.4.3 Relaxation-time approximation

The coupled diffusion equations (6.93) describe the stroboscopic diffusion for a general scattering matrix $M_{kk'}$ and depend on the matrix elements of M in terms of the current and heat current modes. Let us now study the equations in the easiest approximation one can think of, which is the relaxation time approximation. Hence, let us express the relaxation time approximation in terms of the scattering matrix M. At high temperatures, the non-equilibrium distribution function $f_\mathbf{k}$ and the reference Fermi function $f^0_\mathbf{k}$ are given by

$$f_\mathbf{k} \;=\; n + \frac{e}{2J^2d}\epsilon_\mathbf{k} + r_\mathbf{k} \tag{6.94}$$

$$f^0_\mathbf{k} \;\overset{(2.43)}{=}\; n + \frac{e}{2J^2d}\epsilon_\mathbf{k} + \mathcal{O}(e^2) \tag{6.95}$$

where $\langle \epsilon_\mathbf{k}|\epsilon_\mathbf{k}\rangle = 2J^2d$ and where we introduced the function $r_\mathbf{k}$ that contains the information about all higher momentum modes of $f_\mathbf{k}$. Neglecting terms of order e^2, the collision term of the relaxation time approximation can be expressed as

$$-\frac{1}{\tau}\left(f_\mathbf{k} - f^0_\mathbf{k}\right) \;=\; -\frac{1}{\tau} r_\mathbf{k} \;\overset{!}{=}\; -\int \frac{d\mathbf{k}}{(2\pi)^d}\, M_{\mathbf{k}\mathbf{k}'}\left(f_{\mathbf{k}'} - n\right) \tag{6.96}$$

which leads to the obvious identification of

$$M \;=\; \tau^{-1}\left(\mathbb{1} - \frac{|\epsilon_\mathbf{k}\rangle\langle\epsilon_\mathbf{k}|}{\langle\epsilon_\mathbf{k}|\epsilon_\mathbf{k}\rangle}\right) \tag{6.97}$$

The matrix M preserves the kinetic energy mode by construction and damps all other modes at the same scattering rate τ^{-1}. The different matrix elements in (6.93) can be calculated explicitly using this definition of M, which yield

$$\begin{aligned} \langle \mathbf{v}_\mathbf{k}|M|\mathbf{v}_\mathbf{k}\rangle &= & \tau^{-1}\langle \mathbf{v}_\mathbf{k}|\mathbf{v}_\mathbf{k}\rangle &= & \tau^{-1}\,2J^2d \qquad (6.98)\\ \langle \epsilon_\mathbf{k}\mathbf{v}_\mathbf{k}|M|\epsilon_\mathbf{k}\mathbf{v}_\mathbf{k}\rangle &= & \tau^{-1}\langle \epsilon_\mathbf{k}\mathbf{v}_\mathbf{k}|\epsilon_\mathbf{k}\mathbf{v}_\mathbf{k}\rangle &= & \tau^{-1}\,6J^4d \\ \langle \epsilon_\mathbf{k}\mathbf{v}_\mathbf{k}|M|\mathbf{v}_\mathbf{k}\rangle &= & \tau^{-1}\langle \epsilon_\mathbf{k}\mathbf{v}_\mathbf{k}|\mathbf{v}_\mathbf{k}\rangle &= & 0\,+\mathcal{O}(e^2) \end{aligned} \tag{6.99}$$

Consequently, the relaxation time approximation excludes scattering from the particle current mode to the heat current mode. One could, however, easily consider a situation where $\langle \epsilon_\mathbf{k}\mathbf{v}_\mathbf{k}|M|\mathbf{v}_\mathbf{k}\rangle \neq 0$ as well, but here we would like to draw the connection to our previous study in chapter 5, which was also based on the relaxation time approximation. Furthermore, let us consider the case of low densities n and high temperatures, where the scattering rate is approximately given by

$$\tau^{-1} \;=\; \tau_0^{-1}\, n \tag{6.100}$$

where $\tau_0^{-1} \approx 0.609\, U^2/J$ as we have shown in Eq. 2.25. In this case, the coupled diffusion equations (6.93) simplify towards

$$\dot{n} = -\partial_r j_n, \quad \dot{e} = -\partial_r j_e + F\, j_n$$

$$\begin{pmatrix} j_n \\ j_e \end{pmatrix} = -\frac{\tau_0^{-1}\, n}{4F^2} \begin{pmatrix} 4\, J^2 d & 0 \\ 0 & 3\, J^2 \end{pmatrix} \cdot \begin{pmatrix} \partial_r\, n \\ \partial_r\, e \end{pmatrix} - \frac{\tau_0^{-1}\, n}{4F^2} \begin{pmatrix} 2\, F\, e \\ 0 \end{pmatrix} \tag{6.101}$$

As discussed in the previous subsection, for $R \neq 0$ there will be a constant thermoelectric coupling, leading to a particle current induced by energy gradients. Let us now predict the growth rate of the density profile as predicted by the above equations. In chapter 5, we studied a similar problem, where we analyzed the scaling properties of the energy and particle diffusion equation in the conventional sense, i.e. close to local thermodynamic equilibrium. In the regime of stroboscopic diffusion, we proceed with the same philosophy. First of all, let us set $\tau_0^{-1} = 1$, i.e. we measure time in units of the scattering period. Also, the dimensionality d just enters as a numerical factor in these equations, so let us also set $d = 1$, although we are actually interested in $d > 1$ as the one-dimensional Boltzmann equation and therefore also the diffusion equation does not correctly describe the physics of the Hubbard model in $d = 1$ due to the integrability of the latter. To keep the notation as simple as possible, we also set $J = 1$. Furthermore, we rename the projected force $F = -g\, J$ to compare the result with chapter 5, so that our equations read

$$\begin{aligned} \dot{n} &= -\partial_r\, j_n, \qquad & \dot{e} &= -\partial_r\, j_e - g\, j_n \\ j_n &= -\frac{1}{g^2} n\, \partial_r n + \frac{1}{2g}\, n\, e, \qquad & j_e &= -\frac{3}{4g^2}\, n\, \partial_r e \end{aligned} \tag{6.102}$$

6.4.4 Scaling solution

We start our analysis with a proper scaling ansatz for the particle density n. In analogy to Eq. (5.7), we write

$$n(r,t) = \frac{1}{t^\alpha} F[r/t^\alpha] \tag{6.103}$$

which involves a scaling function $F[z]$ and an unknown exponent α. In the spirit of chapter 5 and motivated by numerical simulations to be discussed below, we can expect that to leading order, energy conservation prevents the cloud from expanding. Setting $j_n = 0$ in the equation for the particle current yields

$$e(r,t) \approx e_0(r,t) = \frac{2}{g}\, \partial_r\, n(r,t) \tag{6.104}$$

However, only corrections to this result lead to an expansion of the cloud. Therefore, we need the second scaling ansatz

$$e(r,t) = \frac{2}{g}\, \partial_r\, n(r,t) + \frac{1}{t^\beta} G[r/t^\alpha] \tag{6.105}$$

In order to determine the two unknown scaling exponents α and β, we use the two continuity equations. First, let us consider the particle continuity equation. Using its left hand side, the particle current is given by

$$\tilde{j_n}(r,t) = -\int_{-\infty}^{r} \partial_t\, n(r',t)\, dr' = \frac{r\, \alpha}{t^{1+\alpha}}\, F[r/t^\alpha] \tag{6.106}$$

while the right hand side yields

$$\begin{aligned} j_n(r,t) &= \frac{1}{2g}\, n\,(e-e_0) \\ &= \frac{1}{2g}\,\frac{1}{t^{(\alpha+\beta)}}\, F[r/t^{\alpha}]\, G[r/t^{\alpha}] \end{aligned} \tag{6.107}$$

By setting $j_n = \tilde{j}_n$ and by substituting $r \to z = r/t^{\alpha}$, we find the relation

$$\beta = 1-\alpha \tag{6.108}$$

Next, we consult the energy continuity equation. In contrast to the results of chapter 5, the energy continuity equation yields a manageable number terms that we are able to list completely:

$$0 = \dot{e} + \partial_r j_e + g\,\tilde{j}_n \tag{6.109}$$

$$\begin{aligned} = & -\frac{3F[z]F^{(3)}[z]t^{-5\alpha}}{2g^3} - \frac{2\alpha z t^{-2\alpha-1}F''[z]}{g} - \frac{4\alpha t^{-2\alpha-1}F'[z]}{g} \\ & -\frac{3}{4g^2}t^{-2\alpha-1}F'[z]G'[z] - \frac{3t^{-5\alpha}F'[z]F''[z]}{2g^3} + \frac{\alpha g z F[z]}{t} \\ & -\frac{3}{4g^2}F[z]t^{-2\alpha-1}G''[z] - \alpha z t^{\alpha-2}G'[z] - (1-\alpha)G[z]t^{\alpha-2} \end{aligned} \tag{6.110}$$

In order to have energy conservation for long times, the exponent α has to be adjusted in such a way to have at least one term that cancels the contribution $\alpha g z F[z]/t$ which stems from the time derivative. Apart from $\alpha = 0$ and $\alpha = 1$ which would spoil our scaling ansatzes, the only choice we have is to set

$$\alpha = 1/5 \tag{6.111}$$

As a consequence, also the cloud's radius $R(t) = \left(\int r^2\, n(r,t)/\int n(r,t)\right)^{1/2}$ grows according to the scaling law

$$R(t) \sim t^{1/5} \tag{6.112}$$

which can be checked numerically by simulating the diffusion equations (6.102). The comparison will be carried out in subsection 6.4.6.

6.4.5 Approximate solution of the scaling function

Before we carry out the comparison between numerics and analytics, note that Eq. (6.109) also provides us with an ordinary differential equation for the scaling function $F[z]$, obtained by setting $\alpha = 1/5$:

$$3\Big(F[z]F^{(3)}[z] + F'[z]F''[z]\Big) - \frac{2}{5}\, g^4\, z\, F[z] \;=\; 0 \tag{6.113}$$

First, note that the parameter g^4 can be absorbed by a scaling transformation, and can be in fact replaced by an arbitrary constant $C \in \mathbb{R}_+$. To this end, we implicitly define a new scaling function $\widetilde{F}$ and a new variable $\tilde{z}$ according to

$$F[z] =: C^{-1/5}g^{4/5}\, \widetilde{F}[C^{-1/5}g^{4/5}\, z], \qquad \tilde{z} := z\, C^{-1/5}g^{4/5} \tag{6.114}$$

For later convenience, let us however rename $\widetilde{F} \to F$ and $\tilde{z} \to z$. Under this transformation, Eq. (6.113) straightforwardly becomes

$$3\left(F[z]F^{(3)}[z] + F'[z]F''[z]\right) - \frac{2C}{5}\,zF[z] \;=\; 0 \tag{6.115}$$

The scaling symmetries of the particle density as a function of time t and the parameter g is checked numerically in Fig. 6.7. While we are not aware of an *exact* analytical solution of Eq. (6.115) for $C \neq 0$ which most likely does not exist, we will now demonstrate the calculation of an *approximate* analytical solution of the scaling function F. Let us first postulate the solution and later verify our claim. The approximate solution is given by

$$F_0[z] \;:=\; \frac{A}{b}\frac{\sqrt{3}}{2}\mathrm{Exp}[-2\;(\mathrm{InvErf}(z/b))^2] \tag{6.116}$$

where InvErf denotes the inverse error function. It can be checked that A gives the function's total integral, while its compact support is given by $[-b, b]$. This function is plotted in Fig. 6.7 for $A = b = 1$. Together with an allowed constant shift of the parameter z which would spoil the scaling function's symmetry around the origin, the parameters A and b uniquely fix the third order ordinary differential equation's solution.

Let us emphasize again that Eq. (6.116) gives only an *approximate* solution to Eq. (6.115). To see this, one can check that

$$\frac{3\left(F_0[z]F_0^{(3)}[z] + F_0'[z]F_0''[z]\right)}{\frac{2}{5}\,zF_0[z]} \;\approx\; \frac{15}{2}\sqrt{3}A\pi^2\left[1 + \frac{\pi}{12}\left(\frac{z}{b}\right)^2 + \mathcal{O}\left(\left(\frac{z}{b}\right)^4\right)\right] \tag{6.117}$$

is approximately constant if $z \lesssim b$, and hence F_0 solves Eq. (6.115) for not too large z with $C = \frac{15}{2}\sqrt{3}A\pi^2$, which is also tested numerically in the inset of Fig. 6.7 and discussed below. For $z \sim b$, the differential Eq. (6.115) is not satisfied any more, however, as F_0 decays to zero for $z \to b$, the total error turns out to be small. In the following subsection we will compare the numerically simulated density profiles with the approximate scaling form (6.116), and the quality of our approximation will be tested.

6.4.6 Comparison of the analytic and numerical results

Let us now compare our asymptotic analytic scaling prediction with numerics, where we simulate the dimensionless stroboscopic diffusion equations (6.102). Figure 6.5 shows the time evolution of the particle and energy density, where we started from a Gaussian distribution $n(r, 0) = \exp(-r^2)$ centered around the origin and a vanishing kinetic energy. The physical process which governs the expansion is very similar to the one described in chapter 5: the cloud expands symmetrically while the kinetic energy becomes anti-symmetric around the origin. As the most prominent difference to the collision-dominated case, the density dependence of the diffusion constant $D \sim n$ now is *inverse* to the previous case where $D \sim 1/n$. Therefore, the diffusion is fast in the bulk, and slow in the tail regions of the cloud. This explains the emergence of very different characteristic density profiles, which can be seen in Figs. 6.5 and 6.7.

The scaling law $R \sim t^{1/5}$ is tested numerically in Fig. 6.6, which shows the growth of the radius, raised to different integer powers, as a function of time. Only the integer $1/\alpha = 5$ makes the resulting curve a straight line.

Figure 6.7 shows the rescaled particle densities of a numerical simulation of the diffusion Eq. (6.102), simulated for different values of g and taken at different times t with

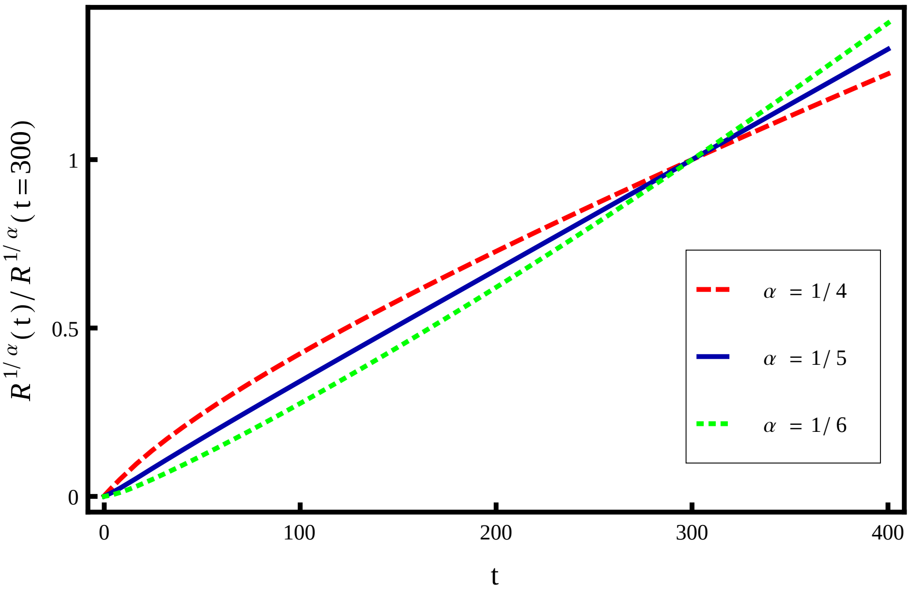

Figure 6.6: Radius $R(t) = \left(\int r^2\, n(r,t)/\int n(r,t)\right)^{1/2}$ of the numerically simulated density profiles, raised to the power $1/\alpha$ for $\alpha = 1/4, 1/5, \text{and}\, 1/6$ and normalized to its value at $t = 300\,\tau_0$. In agreement with our analytic results, $\alpha = 1/5$ is the physically realized exponent. $n(r,t)$ is obtained from a numerical simulation of the coupled stroboscopic diffusion equations (6.102) for $g = 1$.

a normalized Gaussian curve as initial condition. The rescaling was done according to Eqs. (6.103) and (6.114) involving $\alpha = 1/5$, such that the curves can be expected to show the scaling function $F[z]$. Under the scaling transformations, all numerically simulated densities collapse onto a single curve. Here, we introduced an additional non-universal scaling parameter $c \approx 2.48$ (fixed for all curves) which is chosen such that the “edges” of the simulated, rescaled density profiles coincide with -1 and 1. The plot reveals that our scaling predictions are indeed fulfilled. We can now compare the rescaled density profiles with our approximate analytical version of the scaling function $F_0[z]$ of Eq. (6.116) with area $A = 1$ and support $[-1, 1]$, i.e. $b = 1$. To a good approximation, F_0 agrees with the rescaled particle densities of the numerically simulated stroboscopic diffusion equations. In the inset of Fig. 6.7, we compare $F_0[z]$ with a numerical solution of the ordinary differential Eq. (6.115) that determines the scaling function. Here, we adjusted the initial conditions at $z = 0$ to the analytic result F_0 and chose $C = \frac{15}{2}\sqrt{3}\pi^2$ in Eq. (6.115) as required by Eq. (6.117). Also here, the numerical result agrees with the analytical estimate to a high precision without any fitting.

To conclude, we have found that $F[z] \approx \frac{\sqrt{3}}{2}\text{Exp}[-2\,(\text{InvErf}(z))^2]$ is a good approximation to the scaling function. For comparison, very different scaling functions may emerge for other non-linear diffusion equations. As an example, in chapter 5 we have identified $F[z] \approx \frac{1}{\sqrt{2\pi}}\exp[-z^2/2]$, involving a density dependence of the diffusion constant according to $D \sim 1/n$ (as opposed to $D \sim n$ as studied in this chapter), and the coupling of particle and energy diffusion. For $D \sim n^2$ without the coupling to the energy sector, the scaling function assumes a semi-circular shape [117].

As a final remark, let us again comment on the aforementioned study of an expanding

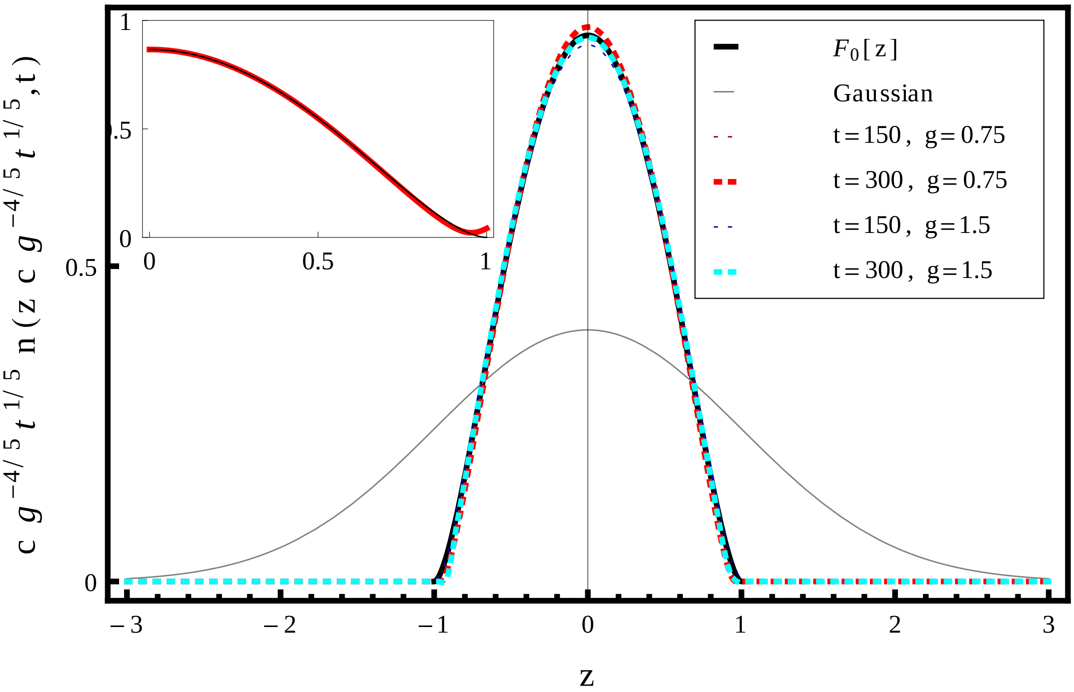

Figure 6.7: Scaling function $F[z] = c\,g^{-4/5}t^{1/5}\; n(z\,c\,g^{-4/5}t^{1/5}, t)$ of the density profile for different potential strengths g and times t (colored dashed curves). The non-universal constant $c \approx 2.48$ is chosen such that the "edges" of the rescaled density profiles simultaneously coincide with ± 1. These curves are compared to the approximate analytic scaling function $F_0[z] = \frac{\sqrt{3}}{2}\mathrm{Exp}[-2\ (\mathrm{InvErf}(z))^2]$ (black line) of Eq. (6.116) with $A = b = 1$. The scaling function F differs drastically from the initial normalized Gaussian density distribution (gray line). **Inset**: Comparison of $F_0[z]$ (black line) with a numerical solution of Eq. (6.115) that determines the scaling function $F[z]$ (red line) with initial values $F^{(i)}[0] = F_0^{(i)}[0]$ for $i = 0, 1, 2$ and $C = 15\sqrt{3}\pi^2/2$.

bosonic cloud of atoms in a tilted optical lattice [117]. The authors approximated the dynamics of the Gross Pitaevskii equation by a single nonlinear diffusion equation for the particle density with $D \sim n^2$, resulting in $R \sim t^{1/4}$. The results obtained in the last two chapters of this thesis have shown, however, that the scaling exponents get drastically modified when the sectors of particle and energy diffusion are coupled to each other.

6.5 Summary and outlook

We studied the dynamics of interacting fermionic particles in the Hubbard model, subject to a static force, in the strongly Bloch oscillating regime far beyond local equilibrium. Based on the Boltzmann equation, we derived effective equations of motion for the system's lowest momentum modes, such as the particle density and the kinetic energy density. For a homogeneous system, we presented two alternative ways to predict how Bloch oscillations get damped in the regime of weak scattering. Based on the linearized Boltzmann equation, we derived analytic formulas for the damping of Bloch oscillations by mapping the problem to a damped harmonic oscillator equation, where the damping rate is given by the current-current matrix element of the scattering matrix. Excellent agreement between numerical simulations of the Boltzmann equation and the analytic results were found for all three regimes of the system, characterized by over-damped, weakly damped and marginally damped Bloch oscillations. Two of these regimes were also observed numerically by Eckstein and Werner [51] using DMFT and could thus be analytically explained by us. For a finite, weakly damped Bloch oscillating cloud of Fermions, we derived effective, *stroboscopic* diffusion equations that describe the system's dynamics on top of its periodic oscillations. These diffusion equations were found to look structurally similar to the coupled diffusion equations studied in chapter 5, where we studied the same problem in the collision-dominated regime. However, as an important difference, the dependence of the two diffusion constants on the local density n and on the scattering rate was found to be *inverse* to each other: while at high temperatures, we found $D \sim 1/n$ in the case of ordinary diffusion, we derived $D \sim n$ for stroboscopic diffusion. As a result, the growth rate of the cloud's radius R as a function of time t was found to obey $R \sim t^{1/5}$ in the case of stroboscopic diffusion, in contrast to $R \sim t^{1/3}$ for conventional (collision-dominated) diffusion.

As a follow-up study, it would be interesting to analyze the damping of Bloch oscillations and sub-diffusive spreading of a finite cloud when the force points in a different direction of the lattice, such as in the direction of a single lattice axis. Furthermore, one could also study the expansion dynamics of a finite cloud in the stroboscopic regime which is *not* translationally invariant in the direction perpendicular to the force. Here, one can expect that the cloud expands faster on the equipotential lines in the horizontal directions than in the vertical direction, as the coupling of the particle diffusion to the energy diffusion is essential in the vertical direction, while it is probably less important in the horizontal direction.

It would be also conceptually interesting to find out if the stroboscopic diffusion equation can be derived directly from the generalized continuity equations presented in section 6.3, or if the generalized continuity equations can be used also for other problems related to non-linear transport. Furthermore, it would be desirable to simulate the sub-diffusive expansion dynamics using the inhomogeneous Boltzmann equation also in the case of weakly damped Bloch oscillations. However, as Boltzmann simulations can only be carried out up to a limited time due to the unavoidable increase of numerical noise, the scaling or

$R \sim t^{1/5}$ would probably be too slow to become visible in the Boltzmann data.

7

Summary

Ultracold atoms may act as quantum simulators of strongly correlated materials, but they also show a plethora of novel dynamic effects that have no analogues in condensed matter physics. Energy conservation has a crucial impact on the many-body dynamics in optical lattices. In this thesis, we reviewed different out-of-equilibrium processes involving fermionic ultracold atoms.

We first described in chapter 2 how we addressed a transport scattering rate to the Hubbard model, and we derived hydrodynamic equations and their high temperature limits from our version of the Boltzmann equation in relaxation time approximation.

In chapter 3, we analyzed the expansion dynamics of an initially confined cloud of fermionic atoms after the release from a trap. Modeling the system numerically with a Boltzmann equation, we could reproduce semi-quantitatively the experimentally observed dramatic drop in the expansion velocities in the presence of interactions. Counterintuitively, identical expansion rates for attractive and repulsive interactions were found in theory and in experiment, which we could explain in terms of a novel dynamic symmetry of the Hubbard model. We also found that the expansion dynamics is governed by a crossover from a ballistic expansion in the tail regions of the cloud to a diffusive expansion in the center. However, the system's dynamics can *not* be described by the diffusive part of the cloud alone, but relies on the interplay of the diffusive bulk and the ballistic tails: while the ballistic tails get fed by the diffusive core, they hold the core region together and thereby regularize the otherwise singular diffusive dynamics. The singular diffusion equation that characterizes the bulk predicts a universal loss rate of particles, and we showed that it can be used as an estimate for the rate at which the diffusive core emits particles into the ballistic tails.

In chapter 4, we analyzed a dynamic process and the corresponding time scales of realizing *negative absolute temperatures* in experiments with cold atoms in optical lattices. The scheme is based on changing the sign of the external trapping potential, which inverts the boundedness of the system's energy spectrum. As a consequence, the system relaxes to a new thermal state at $T < 0$. We then proposed to almost adiabatically reduce the strength of the inverted potential, so that the trapped cloud can expand slowly and thereby "cool", i.e. reach smaller values of $|T|$ with $T < 0$. Using a numerical simulation of the Boltzmann equation, we determined the amount of heat that is produced when the potential strength is changed non-adiabatically within a finite time span Δt. We found that Δt has to be of the order of several hundreds of milli-seconds in order to be close to the adiabatic limit. For the case of an instantaneous switch of the trapping potential to the final shape, we identified the relevant time-scale of *global* equilibration, which is approximately given by $\tau_D = (4J)^{-3}U^2N$, where N is the number of particles and U and J are the Hubbard parameters. This time scale is associated to the redistribution of heat and particles among the system by particle and energy diffusion.

The dynamics of a finite interacting cloud of fermionic atoms in a tilted optical lattice was studied in chapter 5. Here, we were interested in a regime where the Bloch oscillation rate $1/\tau_B \sim F$ is much smaller than the typical scattering rate $1/\tau_{\text{sc}}$, i.e. $1/\tau_B \ll 1/\tau_{\text{sc}}$, so that Bloch oscillations are over-damped. Instead of “dropping downwards”, the cloud was found to diffuse *symmetrically* upwards and downwards the gravitational potential. The associated diffusive process is driven by an energy current that runs through the cloud and supplies the particles that climb upwards with the necessary energy, gained by the particles that go downwards. We showed analytically that the cloud's radius R grows in time according to $R \sim t^{1/3}$, which is in excellent agreement with a direct numerical simulation of the Boltzmann equation.

The opposite limit of weakly damped Bloch oscillations, i.e. $1/\tau_B \gg 1/\tau_{\text{sc}}$, was subject of chapter 6. We first demonstrated two alternative approaches to calculate the decay rate of the Bloch-oscillating current for the homogeneous system. Based on the linearized Boltzmann equation, we derived coupled ordinary differential equations for the different momentum modes of the system. Neglecting thermoelectric effects, these formulas simplified to the classical damped harmonic oscillator equation for the particle current mode, which has an analytic solution. Using this mapping, we could analytically explain the transition from weakly damped to over-damped Bloch oscillations, which was observed numerically within dynamical mean field theory by Eckstein and Werner [51]. We also found very good agreement with a numerical simulation of the one-dimensional Boltzmann equation. We then analyzed the spatially inhomogeneous problem of a strongly Bloch-oscillating, weakly interacting finite cloud of Fermions, which we studied in chapter 5 for the opposite limit. Here, we derived an effective “stroboscopic” diffusion equation that describes the cloud's dynamics on top of its rapid Bloch-oscillating movement. Most prominently, the diffusion constant $D \sim n$ was found to be *proportional* to the local density n and scattering rates, whereas we previously derived $D \sim 1/n$ for ordinary diffusion at high temperatures. Performing a similar scaling analysis as in chapter 5, we find $R \sim t^{1/5}$ for the growth of the cloud's radius in time, consistent with a numerical simulation of the stroboscopic diffusion equation.

Appendix A

Fundamentals and Method

A.1 Variational principle

Let us give a proof of the following theorem, following [30]:
Theorem *The solution ϕ of the integral equation (1.59) minimizes the functional*

$$\phi \longmapsto \frac{\langle \phi, P\phi \rangle}{\langle \phi, X \rangle^2} \tag{A.1}$$

Proof
The scattering operator P has some characteristic properties. Obviously, it is *linear*. Importantly, the operator is also *symmetric*, as can clearly be seen in (1.61), i.e. $\langle \phi, P\psi \rangle = \langle \psi, P\phi \rangle$. As the individual entries in $P_{\mathbf{k_0}\,\mathbf{k_1}}^{\mathbf{k_2}\mathbf{k_3}}$ are all positive as physical transition rates, it is also *positive definite* by the same argument, i.e. $\langle \phi, P\phi \rangle \geq 0$.

The remaining proof consists of two parts. First, we will show that among all functions ϕ that satisfy (1.62), the solution of the integral equation (1.59) *maximizes* the value of $\langle \phi, P\phi \rangle$.
To show this, assume ψ is another function that satisfies (1.62), but not (1.59). Then, by *linearity, symmetry* and *positive-definiteness* of P,

$$\begin{aligned}
0 \;&\leq\; \langle (\phi - \psi), P(\phi - \psi) \rangle \\
&=\; \langle \phi, P\phi \rangle + \langle \psi, P\psi \rangle - \langle \phi, P\psi \rangle - \langle \psi, P\phi \rangle \\
&=\; \langle \phi, P\phi \rangle + \langle \psi, P\psi \rangle - 2\langle \psi, P\phi \rangle \\
&=\; \langle \phi, P\phi \rangle + \langle \psi, P\psi \rangle - 2\langle \psi, X \rangle \\
&=\; \langle \phi, P\phi \rangle - \langle \psi, P\psi \rangle
\end{aligned} \tag{A.2}$$

and hence

$$\langle \phi, P\phi \rangle \;\geq\; \langle \psi, P\psi \rangle \tag{A.3}$$

Second, assume that ϕ solves the integral equation (1.59), and hence also (1.62). Therefore,

$$\frac{\langle \phi, P\phi \rangle}{\langle \phi, X \rangle^2} = \frac{1}{\langle \phi, P\phi \rangle} \tag{A.4}$$

which gets minimized by ϕ, as we have shown before. □

A.2 Stability analysis of the Boltzmann equation

The Boltzmann equation in relaxation-time approximation is a nonlinear first-order partial differential equation. We explicitly evolved the equation in time, using a fourth-order Runge-Kutta scheme. Here, we want to explain why the numerical implementation of the Boltzmann equation is numerically not stable, following [57]. But instead of considering the Boltzmann equation in use, let us consider a simpler first-order partial differential equation, for which we present a *von Neumann stability analysis.* Let the simpler equation be given by

$$\partial_t f(x,t) = -v\, \partial_x f(x,t) \tag{A.5}$$

In analogy to the Runge-Kutta scheme used for the Boltzmann equation, we also want to consider a simple scheme that evolves the equation *explicitly* in time. Let us therefore consider the discrete difference equation

$$\frac{f_j^{n+1} - f_j^n}{\Delta t} = -v\, \frac{f_{j+1}^n - f_{j-1}^n}{2\Delta x} \tag{A.6}$$

where n is a discrete time-index while j is a discrete position index. A solution of the difference equation can be found with the ansatz

$$f_j^n = \xi(k)^n\, e^{i\,k\,\Delta x\, j} \tag{A.7}$$

where one finds that

$$\xi(k) = 1 - i\frac{v\,\Delta t}{\Delta x}\sin(k\,\Delta x) \tag{A.8}$$

Note that $\xi(k)$ is an eigenmode of the system. The stability analysis reveals that if $|\xi(k)| \geq 1$ for *some* k, the eigenmode is growing. Given this is the case, the approach is unstable, and Eq. (A.8) reveals that this is indeed always the case. Hence, the approach of *explicitly* evolving the equation in time leads to exponentially growing noise. Interestingly, the rate at which the noise grows in time depends on the ratio $\Delta t/\Delta x$: the growth of the noise can be temporarily suppressed by either increasing the time discretization, or by *reducing* the (phase-)space discretization. In practice, we need a very fine discretization in the time-direction to simulate long times, which makes our computations very expensive.

Appendix B

Expansion in a homogeneous lattice

B.1 Effects of the laser beam curvature

Spatially varying laser intensities modify the local hopping amplitudes. Such an effect can be implemented easily in the Boltzmann equation. It is important to realize that approaching the "edge" of the the laser in x direction modifies the hopping amplitude in y direction and vice versa. This effect can be easily implemented into the kinetic part of the Hamiltonian, which we generalize to

$$\epsilon(k_x, k_y) \longrightarrow \epsilon(x, y, k_x, k_y) = A(y)\epsilon(k_x) + A(x)\epsilon(k_y) \tag{B.1}$$

with a certain space-dependent amplitude $A(x)$ that recovers the old result in the center of the lattice, i.e. $A(0) = 1$. The goal of this section is to calculate $A(x)$ and to explain how it is obtained from the experimental parameters.

Before we do so, let us understand how the space-dependent amplitude modifies the Boltzmann equation. In order to obtain the left-hand side of the Boltzmann equation, we have to evaluate the Poisson bracket of the Hamiltonian with the distribution function, which generates new kinetic terms:

$$\begin{aligned} \{\epsilon(\mathbf{r}, \mathbf{k}), f(\mathbf{r}, \mathbf{k})\}_{\mathbf{r},\mathbf{k}} &= A(y)v(k_x)\partial_x f_{\mathbf{k}} + A(x)v(k_y)\partial_y f_{\mathbf{k}} \\ &\quad + A'(y)\epsilon(k_x)\partial_{k_y} f_{\mathbf{k}} + A'(x)\epsilon(k_y)\partial_{k_x} f_{\mathbf{k}} \end{aligned} \tag{B.2}$$

Note that the spatially varying laser intensities thus not only modify the local velocities, but also act as additional forces. Let us proceed in demonstrating how to determine $A(x)$. The problem reduces to calculating

(a) $J(V_0)$, i.e. how the hopping parameter J depends on the lattice depth V_0 and

(b) $V_0(x)$, i.e. how the local lattice depth V_0 depends on the spatial coordinate x.

For step (a), let us temporarily assume that V_0 is constant. We are interested in a two-dimensional geometry, but as the Schrödinger equation separates in the two coordinates for the given potential, the problem can be reduced to one dimension. In order to determine the functional relation between the lattice depth and the kinetic energy, we have to diagonalize the one-dimensional Hamiltonian

$$H = \frac{1}{2m}\Delta + \frac{1}{2}V_0 \cos(2\pi\, x) \tag{B.3}$$

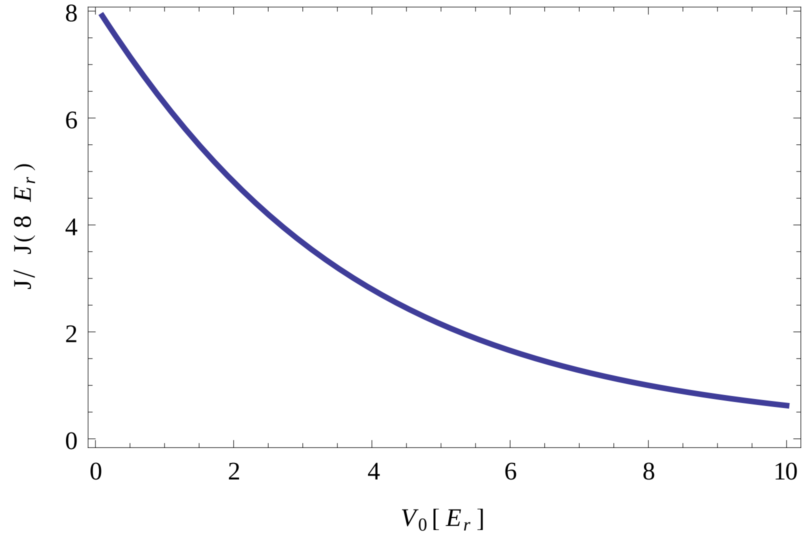

Figure B.1: Rescaled hopping parameter $J(V_0)/J(V_0 = 8\,\mathrm{E_r})$ as a function of the laser intensity in units of the recoil energy, where $V_0 = 8\,\mathrm{E_r}$ is the lattice depth in the center of the laser which was realized in the experiment.

where we measure distance in units of the lattice constant $a = \lambda/2$, given by half the wave length $\lambda = 738$ of the laser. We are considering potassium atoms, with mass $m = 40\,u$ where u is the proton mass. We measure energy in terms of the recoil energy, $\mathrm{E_r} = h^2/(2m\lambda^2)$. Following [15], the Schrödinger equation can be conveniently formulated in momentum space, it maps to a tight-binding model where V_0 determines the hopping amplitude. We can thus diagonalize the Hamiltonian for a large, but finite system. The Hamiltonian has the following structure, shown here for only 7 lattice sites:

$$H = \begin{pmatrix} \frac{\left(k+\frac{12\pi}{\lambda}\right)^2}{2m} & \frac{V_0}{4} & 0 & 0 & 0 & 0 & 0 \\ \frac{V_0}{4} & \frac{\left(k+\frac{8\pi}{\lambda}\right)^2}{2m} & \frac{V_0}{4} & 0 & 0 & 0 & 0 \\ 0 & \frac{V_0}{4} & \frac{\left(k+\frac{4\pi}{\lambda}\right)^2}{2m} & \frac{V_0}{4} & 0 & 0 & 0 \\ 0 & 0 & \frac{V_0}{4} & \frac{k^2}{2m} & \frac{V_0}{4} & 0 & 0 \\ 0 & 0 & 0 & \frac{V_0}{4} & \frac{\left(k-\frac{4\pi}{\lambda}\right)^2}{2m} & \frac{V_0}{4} & 0 \\ 0 & 0 & 0 & 0 & \frac{V_0}{4} & \frac{\left(k-\frac{8\pi}{\lambda}\right)^2}{2m} & \frac{V_0}{4} \\ 0 & 0 & 0 & 0 & 0 & \frac{V_0}{4} & \frac{\left(k-\frac{12\pi}{\lambda}\right)^2}{2m} \end{pmatrix} \tag{B.4}$$

We perform the diagonalization numerically for 60 lattice sites, where finite-size effects are negligible. This allows us to extract the band-width D of the lowest band numerically as a function of V_0. Using the physically realized lattice depth of $8\,E_r$, we obtain that the hopping amplitude $J = D/4$ of the lowest band in units of the recoil energy is given by

$$J \;=\; 0.0308201\,E_r \tag{B.5}$$

As a side result, the relation $\Delta\, t = h/J[E_r]$ allows us to relate the time step Δt in the numerical simulation to the physical time in milli-seconds, which yields

$$\Delta t \;=\; 0.568\,\mathrm{ms} \tag{B.6}$$

The relative dependence of the hopping amplitude on the lattice depth is shown in Fig. B.1, which shows the function $J(V_0)/J(V_0 = 8\,\mathrm{E_r})$ ($8\,\mathrm{E_r}$ is the lattice depth that was used in experiment). This concludes step (a).

For step (b), we calculate how the the lattice depth $V_0(x)$ depends on the spatial coordinate x, as this tells us how the hopping parameter $J = J(V_0(x))$ changes in space. As V_0 is a measure for the laser intensity, we only have to know how the laser intensity depends on space. According to [16], the beam has a waist of about $x_0 = 150\ \mu m \approx 406.5$ in units of the lattice constant. This corresponds to an intensity profile proportional to $V_0(x) = V_0(0)\, e^{-2(x/x_0)^2}$.

The above result allows us to calculate the dependence of the hopping strength as a function of the spatial coordinate. As all we have are numerical data and no analytical formulas, we fit a quartic polynomial to our numerical result, which is given by

$$A(x) = \frac{J(8\,\mathrm{E_r}\,e^{-2(x/x_0)^2})}{J(8\,\mathrm{E_r})} \approx 1 + 2.012208(x/x_0)^2 + 0.871425(x/x_0)^4 \tag{B.7}$$

The spatially varying hopping parameter $A(x)$ can easily be implemented in the Boltzmann equation.

B.2 Validity of the diffusion equation

In order to derive a criterion for the validity of the diffusion equation, we estimate the magnitude of the second order term in the series expansion (2.31). The coefficients of this expansion are given by

$$\delta f_{\mathbf{k}}^{(n)} = [-\tau(n)(\partial_t + \mathbf{v_k}\nabla_{\mathbf{r}})]^n \; f_{\mathbf{k}}^0 \tag{B.8}$$

where we assumed for simplicity that τ depends only on the particle density n, which is a good approximation at high temperatures. We would like to derive a simple expression for the criterion that the leading order current is much larger than its first nonlinear correction:

$$|\mathbf{j}_n^{(2)}|/|\mathbf{j}_n^{(1)}| \ll 1 \tag{B.9}$$

Above, we have defined

$$\mathbf{j}_n^{(n)} \;=\; \frac{1}{(2\pi)^2}\int d\mathbf{k}\,\mathbf{v_k}\,\delta f_{\mathbf{k}}^{(n)} \tag{B.10}$$

While $\mathbf{j}_n^{(1)} = -D(n)\nabla_{\mathbf{r}} n$ is known, we still need to calculate $\mathbf{j}_n^{(2)}$. For the following calculation, we will use the following identities,

$$\int d\mathbf{k}\,\mathbf{v_k}\,f_{\mathbf{k}}^0 \;=\; 0 \qquad \int d\mathbf{k}\,\mathbf{v}_{\mathbf{k}}^2\,\mathbf{v_k} f_{\mathbf{k}}^0 \;=\; 0 \tag{B.11}$$

where we used that $f^0_{\mathbf{k}}$ is an even function in momentum space and $\mathbf{v_k}$ is odd, such that the integrated product vanishes. The second-order current is therefore given by

$$\begin{aligned}
\mathbf{j}_n^{(2)} &= \frac{1}{(2\pi)^2}\int d\mathbf{k}\,\mathbf{v_k}\,\left[-\tau(n)(\partial_t+\mathbf{v_k}\nabla_{\mathbf{r}})\right]^2 f^0_{\mathbf{k}} \\
&\overset{(B.11)}{=} \frac{1}{(2\pi)^2}\,\tau(n)\int d\mathbf{k}\,\mathbf{v_k}^2\,\left[\partial_t\circ\tau(n)\nabla_{\mathbf{r}}+\nabla_{\mathbf{r}}\circ\tau(n)\partial_t\right] f^0_{\mathbf{k}} \\
&= \tau(n)\partial_t\left(\frac{1}{(2\pi)^2}\int d\mathbf{k}\,\mathbf{v_k}^2\,\tau(n)\frac{\partial f^0_{\mathbf{k}}}{\partial n}\nabla_{\mathbf{r}}n\right)+\tau(n)\nabla_{\mathbf{r}}\left(\frac{1}{(2\pi)^2}\int d\mathbf{k}\,\mathbf{v_k}^2\,\tau(n)\frac{\partial f^0_{\mathbf{k}}}{\partial n}\partial_t n\right) \\
&= \tau(n)\partial_t\left(D(n)\nabla_{\mathbf{r}}n\right)+\tau(n)\nabla_{\mathbf{r}}\left(D(n)\dot{n}\right) \\
&\approx \tau(n)\partial_t\left(D(n)\nabla_{\mathbf{r}}n\right)+\tau(n)\nabla_{\mathbf{r}}\left(D(n)\nabla_{\mathbf{r}}(D(n)\nabla_{\mathbf{r}}n)\right)
\end{aligned} \tag{B.12}$$

where $\circ$ denotes the composition of two differential operators, and in the last line we used that $\dot{n}\approx\nabla_{\mathbf{r}}D(n)\nabla_{\mathbf{r}}n$. Assuming that the emerging terms are all of approximately the same size and don't cancel each other, we concentrate on the second term and estimate

$$\left|\frac{j^{(2)}}{j^{(1)}}\right|\sim\left|\frac{\tau(n)\nabla_{\mathbf{r}}(D(n)\nabla_{\mathbf{r}}(D(n)\nabla_{\mathbf{r}}n))}{D(n)\nabla_{\mathbf{r}}n}\right|\sim\frac{v^2\tau^2}{r^2}\ll 1 \tag{B.13}$$

Above, we made the very crude approximation of identifying $\nabla_{\mathbf{r}}\sim 1/r$ as the cloud's inverse radius, and we approximated $D\sim v^2\,\tau$ for a characteristic velocity v and a typical scattering time τ.

B.3 Geometric interpretation of the universal loss rate

The minimal loss rate of 4π in $d=2$ can be also derived geometrically [82]. It is in close connection to the Euler characteristic $\chi(M)$ of a two-dimensional orientable manifold M, which is a topological invariant. In our context, M has the topology of a two-dimensional disc, where $\chi(M)=1$. Let us specify a metric g on that manifold by

$$g=n(x_1,x_2)\,dx_1\wedge dx_2 \tag{B.14}$$

where $n(x_1,x_2)$ is our initial two-dimensional density distribution. Note that the volume of the manifold then corresponds to the total number of particles N:

$$Vol(M)=\int_M n=N \tag{B.15}$$

Let us now consider the Ricci-flow of that given manifold, $\partial_t\,g_{ij}=-2R_{ij}$, which describes the flow of the manifold's metric towards vanishing curvature[1]. As the curvature tensor consists of second order spatial derivatives of the metric, one can show that the superfast diffusion equation and the Ricci flow are equivalent [82] for the special choice of g, i.e.

$$\partial_t\,g_{ij}=-2R_{ij}\quad\Leftrightarrow\quad\dot{n}=\Delta\log(n) \tag{B.16}$$

The integrated version of the Ricci flow in absence of surface terms for the given metric reads

$$\partial_t N\;=\;-2\int_M K\;\overset{\text{G.–B.}}{=}\;-4\pi\,\chi(M) \tag{B.17}$$

---

[1] More generally, the Ricci flow drives the metric towards the unique metric of *constant* curvature, which is specified by topology. A manifold that has the topology of a disc can only assume a vanishing constant curvature.

where K is the Gaussian curvature of the metric, and we used the Gauss-Bonnet theorem, which relates the integrated Gaussian curvature of a manifold to 2π times its Euler characteristic. As $\chi(M) = 1$, this concludes the geometrical proof.

Appendix C

Negative absolute temperatures in optical lattices

C.1 Final temperatures, two limiting cases

There exists no simple way to calculate the amount of heat created in the system after a time-dependent manipulation of the external trapping potential. In chapter 4, we perform a time-dependent manipulation of the prefactor $V_0(t)$ of the harmonic potential according to the protocoll (4.13) . However, there are two limits in which the final temperatures can be calculated exactly: the adiabatic limit of $\Delta t \to \infty$, and the instantaneous quench with $\Delta t = 0$, involving an infinite "waiting" time afterwards. In these two limits, we calculated the final temperature and density profiles using the local density approximation (LDA), in which the external trapping potential is absorbed by a shift in the local chemical potential.

Immediately after the quench, the density and kinetic energy distribution is still the same as before, as the kinetic energy and particle densities need a finite amount of time to adjust to the new trapping potential. Therefore, the total energy after the quench $E_>$ is just determined by the total change in potential energy, which changes instantly after the quench. Let us assume that we quench the trapping potential at $t = 0$. Then, the total energy after the quench $E_>$ is given by

$$\begin{aligned} E_> &:= E(t<0) + \Delta E \qquad \text{(C.1)} \\ \Delta E &= \lim_{t\to 0+} \int d^2r \; \left(V_0(t) - V_0(-t)\right) \mathbf{r}^2 \, n(\mathbf{r}, 0) \end{aligned}$$

Given $E_>$, we can determine two limits exactly: the adiabatic limit (i) of going from $-V_{0i}$ to V_{0f} infinitesimally slowly, i.e. $\dot{S}(t > 0) = 0$, and (ii) the limit of an instantaneous quench where $\dot{E}(t > 0) = 0$.

In the following, we are going to demonstrate this approach in more detail. Let the interaction strength U be fixed. For given μ_0, β and V_0, let

$$n(\mathbf{r}) \equiv n_{(\mu_0,\beta,V_0)}(\mathbf{r}) \qquad \text{(C.2)}$$

denote the local equilibrium particle density including Hartree-corrections, calculated self-consistently as specified in Eq. (2.15). We introduce the following functions:

$$\begin{aligned} N(\mu_0, V_0, \beta) &:= \int d\mathbf{r}\, n(\mathbf{r}) \\ E_{\text{kin}}(\mu_0, V_0, \beta) &:= \int d\mathbf{r} \int \frac{d\mathbf{k}}{(2\pi)^d} \frac{\epsilon_{\mathbf{k}}}{1 + e^{\beta(\epsilon_{\mathbf{k}} - (\mu_0 + Un(\mathbf{r}) + V_0 \mathbf{r}^2))}} \\ E_{\text{pot+int}}(\mu_0, V_0, \beta) &:= \int d\mathbf{r} \left(V_0 \mathbf{r}^2 n(\mathbf{r}) + \frac{U}{2} n(\mathbf{r})^2 \right) \\ E(\mu_0, V_0, \beta) &:= E_{\text{kin}}(\mu_0, V_0, \beta) + E_{\text{pot+int}}(\mu_0, V_0, \beta) \end{aligned} \tag{C.3}$$

N and E denote the total number of particles and the total energy of the trapped system as a function of the global inverse temperature β, the prefactor of the harmonic trapping potential V_0 and the offset of the chemical potential μ_0. First, let us consider the simpler case of an instantaneous quench (ii). In this case, the total energy after the quench at $t = 0$ is conserved. Hence, the final equilibrium temperature is uniquely determined by N, the final trap configuration $V_{0f} < 0$ and the total energy immediately after the quench, $E_>$, calculated with Eq. (C.1). Using a two-dimensional variant of Newton's algorithm, we solve the following equations for μ_0 and β, which characterize the equilibrated system in the long time limit:

$$\begin{aligned} N &= N(\mu_0, V_{0f}, \beta) \\ E_> &= E(\mu_0, V_{0f}, \beta) \end{aligned} \tag{C.4}$$

This concludes case (ii). Second, let us consider the adiabatic limit (i). Here, the trapping potential is first inverted, $V_{0i} \to -V_{0i}$ and let to equilibrate. Therefore, we first calculate the corresponding equilibrium configuration by numerically solving the equations

$$\begin{aligned} N &= N(\mu', -V_{0i}, \beta') \\ E_> &= E(\mu', -V_{0i}, \beta') \end{aligned} \tag{C.5}$$

for μ' and β'. After the quench, we open the trapping potential *adiabatically*, i.e. from now on, the system's *entropy* is conserved. Let us therefore define

$$\begin{aligned} s(\omega, \beta) &:= \beta^2 \partial_\beta \left(\frac{1}{\beta} \log \left(\frac{1}{1 + e^{\beta\omega}} \right) \right) \\ S(\mu_0, V_0, \beta) &:= \int d\mathbf{r} \int d\omega\, \nu(\omega)\, s(\omega - (\mu_0 + V_0 \mathbf{r}^2 + Un(\mathbf{r})), \beta) \end{aligned} \tag{C.6}$$

where $\nu(\omega)$ is the density of states of the two-dimensional Hubbard model, and S is the system's total equilibrium entropy. We first calculate the system's entropy $S_>$ after the quench, followed an infinite waiting time, which is given by

$$S_> := S(\mu', -V_{0i}, \beta') \tag{C.7}$$

To calculate the final inverse temperature β and chemical μ_0 potential after the adiabatic opening of the trap to the final trap configuration characterized by V_{0f}, we numerically solve the equations

$$\begin{aligned} N &= N(\mu_0, V_{0f}, \beta) \\ S_> &= S(\mu_0, V_{0f}, \beta) \end{aligned} \tag{C.8}$$

for β and μ_0. This concludes case (i).

Appendix D

Expansion in a gravitational potential

D.1 Short time dynamics

The short time dynamics is characterized by a rapid drift of the cloud's center of mass in the direction of the force, assuming that initially $T > 0$. During this process, potential energy is converted into kinetic energy. We want to calculate the motion of the cloud's center of mass,

$$x_0(t) = \frac{1}{N_0} \int dx\, x\, n(x,t) \tag{D.1}$$

where $N_0 = \int dx\, n(x,t)$. The motion of the cloud is determined by the conservation of the total energy,

$$E_{tot} = \int dx \, \left(e(x,t) + g\, x\, n(x,t) + \frac{U}{2}\, n^2(x,t) \right) \tag{D.2}$$

Let us assume that $x_0(0) = 0$. Then, using the definition of x_0, we obtain

$$x_0(t) = \frac{1}{g\, N_0} \int dx (e(x,0) - e(x,t)) + \frac{U}{2\, N_0\, g} \int dx (n(x,0)^2 - n(x,t)^2) \tag{D.3}$$

This equation can be used to analyze both the short time dynamics and the long time dynamics of x_0. The Hartree interaction energy decreases only on very long time scales. For the short time dynamics it can be regarded as constant, as can be seen in Fig. D.1.

Let us focus on the center of mass motion at very weak interactions, such that strong Bloch oscillations become apparent. The inset of Fig. 5.3 in the main text shows the decay of the center of mass oscillations. In particular, the center of mass at odd multiples of half the Bloch period approximately assumes its asymptotic value at long times. This can be understood as follows: at very weak interactions and at $t = (2n+1)\pi/g$ for $n \in \mathcal{N}$, the kinetic energy vanishes in $d = 2$, because all momenta in the direction of the force are shifted by π, while all momenta in perpendicular direction are unaltered. Note that also the Hartree energy is approximately zero. Therefore,

$$x_0(t = (2n+1)\pi/g) \approx \frac{1}{g\, N_0} \int dx\, e(x,0) \tag{D.4}$$

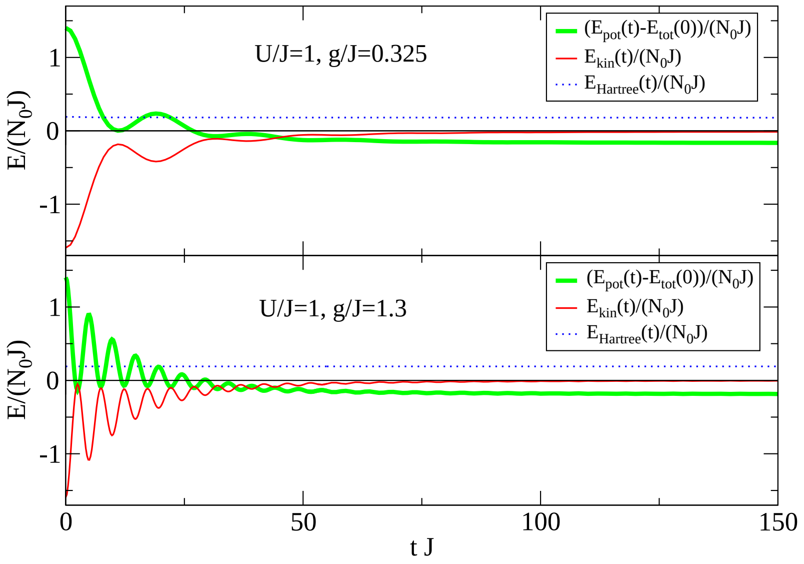

Figure D.1: Decay of the kinetic and potential energy oscillations: potential energy (green), kinetic energy (red) and Hartree energy (blue dots). The upper panel shows in intermediately strong driving force, while the lower panel shows a strong driving force for $U/J = 1$. The Hartree energy decays only on very long time scales.

Using the parameter $T = 1J$ as used in our numerical simulations and approximating $e \approx -4J^2 n/T$ yields the numerical value of $x_0(\pi/g) \approx -1.59J/g$, which agrees very well with the center of mass minima in our numerical data, shown in the inset of Fig. 5.3. Note that in the limit of very long times, the center of mass gets shifted due to the slowly decreasing Hartree energy,

$$x_0(t \to \infty) = x_0(\pi/g) + \frac{U}{2N_0 g} \int dx\, n(x,0)^2 \tag{D.5}$$

D.2 Scaling analysis of the energy continuity equation

In the main text, the scaling ansatz (5.18) is plugged into the the energy continuity equation. The resulting equation can be expressed as a fractional power series in t, with coefficients $C_i[z]$, such that the equation reads

$$0 = C_0[z]\, t^{-1} + C_1[z]\, t^{-\frac{2}{\gamma}-1} + C_2[z]\, t^{-\frac{1}{\gamma}-2} + C_3[z]\, t^{-3/\gamma} + \ldots$$

where we neglected the series coefficients of $t^{-5/\gamma}, t^{-7/\gamma}, t^{-9/\gamma}, t^{-1-4/\gamma}, t^{-1-6/\gamma}, t^{-2-3/\gamma}$ which are a priori subleading. Hence we do not list the corresponding coefficients. The remaining coefficients $C_i[z]$ are given by

$$\begin{aligned}
C_0[z] &= \frac{\alpha_0^3 z F[z]}{6\gamma} \\
C_1[z] &= \frac{\alpha_0^{1-\gamma}\tau_0^{-2/\gamma} g^{\frac{4}{\gamma}+1} G[z] J^{-\frac{8}{\gamma}-1} N_0^{\frac{2}{\gamma}-1} F''[z]}{2F[z]^2} - \frac{2\alpha_0 z \tau_0^{-2/\gamma} g^{\frac{4}{\gamma}-2} J^{2-\frac{8}{\gamma}} N_0^{2/\gamma} F''[z]}{3\gamma} \\
&\quad + \frac{3\alpha_0^{1-\gamma}\tau_0^{-2/\gamma} g^{\frac{4}{\gamma}+1} J^{-\frac{8}{\gamma}-1} N_0^{\frac{2}{\gamma}-1} F'[z] G'[z]}{4F[z]^2} - \frac{\alpha_0^{1-\gamma}\tau_0^{-2/\gamma} g^{\frac{4}{\gamma}+1} G[z] J^{-\frac{8}{\gamma}-1} N_0^{\frac{2}{\gamma}-1} F'[z]^2}{F[z]^3} \\
&\quad + \frac{\alpha_0 U z \tau_0^{-2/\gamma} F[z] g^{\frac{4}{\gamma}-1} J^{-8/\gamma} N_0^{\frac{2}{\gamma}+1} F'[z]}{6\gamma} - \frac{4\alpha_0 \tau_0^{-2/\gamma} g^{\frac{4}{\gamma}-2} J^{2-\frac{8}{\gamma}} N_0^{2/\gamma} F'[z]}{3\gamma} \\
&\quad - \frac{\alpha_0^{1-\gamma}\tau_0^{-2/\gamma} g^{\frac{4}{\gamma}+1} J^{-\frac{8}{\gamma}-1} N_0^{\frac{2}{\gamma}-1} G''[z]}{4F[z]}
\end{aligned}$$

$$\begin{aligned}
C_2[z] &= -\frac{\alpha_0^{2-2\gamma}\tau_0^{-\frac{1}{\gamma}-1} g^{\frac{2}{\gamma}+4} G[z]^2 J^{-\frac{4}{\gamma}-6} N_0^{\frac{1}{\gamma}-1} F'[z]}{8F[z]^3} + \frac{\alpha_0^{2-2\gamma}\tau_0^{-\frac{1}{\gamma}-1} g^{\frac{2}{\gamma}+4} G[z] J^{-\frac{4}{\gamma}-6} N_0^{\frac{1}{\gamma}-1} G'[z]}{8F[z]^2} \\
&\quad - \frac{z\alpha_0^{2-\gamma}\tau_0^{-\frac{1}{\gamma}-1} g^{\frac{2}{\gamma}+1} J^{-\frac{4}{\gamma}-3} N_0^{\frac{1}{\gamma}} G'[z]}{6\gamma} - \frac{1}{6}\alpha_0^{2-\gamma}\tau_0^{-\frac{1}{\gamma}-1} g^{\frac{2}{\gamma}+1} G[z] J^{-\frac{4}{\gamma}-3} N_0^{\frac{1}{\gamma}} \\
&\quad - \frac{\alpha_0^{2-\gamma}\tau_0^{-\frac{1}{\gamma}-1} g^{\frac{2}{\gamma}+1} G[z] J^{-\frac{4}{\gamma}-3} N_0^{\frac{1}{\gamma}}}{6\gamma}
\end{aligned}$$

$$\begin{aligned}
C_3[z] &= -\frac{\tau_0^{1-\frac{3}{\gamma}} F^{(3)}[z] g^{\frac{6}{\gamma}-2} J^{4-\frac{12}{\gamma}} N_0^{\frac{3}{\gamma}-1}}{F[z]} - \frac{2\tau_0^{1-\frac{3}{\gamma}} g^{\frac{6}{\gamma}-2} J^{4-\frac{12}{\gamma}} N_0^{\frac{3}{\gamma}-1} F'[z]^3}{F[z]^3} \\
&\quad + \frac{3\tau_0^{1-\frac{3}{\gamma}} g^{\frac{6}{\gamma}-2} J^{4-\frac{12}{\gamma}} N_0^{\frac{3}{\gamma}-1} F'[z] F''[z]}{F[z]^2}
\end{aligned}$$

Appendix E

Damping of Bloch oscillations

E.1 Linearized collision integral

Let us consider the matrix M that emerges from the linearization of the collision integral of the Boltzmann equation (6.16). We want to relate this matrix to the microscopic transition rates Z explicitly, which are given by

$$Z_{\mathbf{k}\,\mathbf{k_1}}^{\mathbf{k_2 k_3}} = U^2 \sum_{\mathbf{G}} \delta\left(\mathbf{k} + \mathbf{k}_1 - \mathbf{k}_2 - \mathbf{k}_3 + \mathbf{G}\right) \delta\left(\epsilon_{\mathbf{k}} + \epsilon_{\mathbf{k}_1} - \epsilon_{\mathbf{k}_2} - \epsilon_{\mathbf{k}_3}\right) \tag{E.1}$$

In analogy to Eq. (1.50), we start from the following ansatz of the non-equilibrium distribution function $f_{\mathbf{k}}$ close to infinite temperature:

$$f_{\mathbf{k}} = n + n(1-n)\phi_{\mathbf{k}} \tag{E.2}$$

As shown in section 1.3.8, the linearized collision integral can be expressed as

$$\begin{aligned} I_{\text{lin}}[\phi] &= -\int \frac{d\mathbf{k_1}}{(2\pi)^d} \frac{d\mathbf{k_2}}{(2\pi)^d} \frac{d\mathbf{k_3}}{(2\pi)^d} \left(\phi_{\mathbf{k}} + \phi_{\mathbf{k_1}} - \phi_{\mathbf{k_2}} - \phi_{\mathbf{k_3}}\right) P_{\mathbf{k}\,\mathbf{k_1}}^{\mathbf{k_2 k_3}}, & \text{(E.3)} \\ P_{\mathbf{k}\,\mathbf{k_1}}^{\mathbf{k_2 k_3}} &= U^2\, n^2\, (1-n)^2 \sum_{\mathbf{G}} \delta\left(\mathbf{k} + \mathbf{k}_1 - \mathbf{k}_2 - \mathbf{k}_3 + \mathbf{G}\right) \delta\left(\epsilon_{\mathbf{k}} + \epsilon_{\mathbf{k}_1} - \epsilon_{\mathbf{k}_2} - \epsilon_{\mathbf{k}_3}\right) & \text{(E.4)} \end{aligned}$$

Here we have used that P simplifies drastically in the infinite temperature limit, as the Pauli blocking factors simplify accoring to

$$f^0_{\mathbf{k}} f^0_{\mathbf{k_1}} (1 - f^0_{\mathbf{k_2}})(1 - f^0_{\mathbf{k_3}}) \longrightarrow n^2(1-n)^2 \qquad (T \to \infty) \tag{E.5}$$

Substituting $\delta f_{\mathbf{k}} = n(1-n)\phi_{\mathbf{k}}$, such that $f_{\mathbf{k}} = n + \delta f_{\mathbf{k}}$, we arrive at the following form of the collision integral:

$$\begin{aligned} -\int \frac{d\mathbf{k}'}{(2\pi)^d} M_{\mathbf{k}\mathbf{k}'} \delta f_{\mathbf{k}'} &\overset{!}{=} -\int \frac{d\mathbf{k_1}}{(2\pi)^d} \frac{d\mathbf{k_2}}{(2\pi)^d} \frac{d\mathbf{k_3}}{(2\pi)^d} \left(\delta f_{\mathbf{k}} + \delta f_{\mathbf{k_1}} - \delta f_{\mathbf{k_2}} - \delta f_{\mathbf{k_3}}\right) \tilde{P}_{\mathbf{k}\,\mathbf{k_1}}^{\mathbf{k_2 k_3}} \\ &= -\delta f_{\mathbf{k}} \int \frac{d\mathbf{k_1}}{(2\pi)^d} \frac{d\mathbf{k_2}}{(2\pi)^d} \frac{d\mathbf{k_3}}{(2\pi)^d} \tilde{P}_{\mathbf{k}\,\mathbf{k_1}}^{\mathbf{k_2 k_3}} \\ &\quad -\int \frac{d\mathbf{k_1}}{(2\pi)^d} \frac{d\mathbf{k_2}}{(2\pi)^d} \frac{d\mathbf{k_3}}{(2\pi)^d} \delta f_{\mathbf{k_1}} \left(\tilde{P}_{\mathbf{k}\,\mathbf{k_1}}^{\mathbf{k_2 k_3}} - \tilde{P}_{\mathbf{k}\,\mathbf{k_2}}^{\mathbf{k_1 k_3}} - \tilde{P}_{\mathbf{k}\,\mathbf{k_3}}^{\mathbf{k_2 k_1}}\right) \end{aligned} \tag{E.6}$$

where we defined $\tilde{P} = P/(n(1-n))$, and we have just re-labeled the integration variables. We can therefore identify the matrix of the linearized collision integral as

$$M_{\mathbf{k}\mathbf{k}'} = \delta_{\mathbf{k}\mathbf{k}'} \int \frac{d\mathbf{k_1}}{(2\pi)^d} \frac{d\mathbf{k_2}}{(2\pi)^d} \frac{d\mathbf{k_3}}{(2\pi)^d} \tilde{P}_{\mathbf{k}\,\mathbf{k_1}}^{\mathbf{k_2 k_3}} + \int \frac{d\mathbf{k_2}}{(2\pi)^d} \frac{d\mathbf{k_3}}{(2\pi)^d} \left(\tilde{P}_{\mathbf{k}\,\mathbf{k}'}^{\mathbf{k_2 k_3}} - \tilde{P}_{\mathbf{k}\,\mathbf{k_2}}^{\mathbf{k}' \mathbf{k_3}} - \tilde{P}_{\mathbf{k}\,\mathbf{k_3}}^{\mathbf{k_2 k}'}\right) \tag{E.7}$$

Finally let us also give the current-current matrix element of $M_{\mathbf{k}\mathbf{k}'}$. In analogy to Eq.(1.61), this matrix elements is given by

$$\begin{aligned} M_{vv} &:= \frac{1}{(2\pi)^{2d}} \int d\mathbf{k} d\mathbf{k}' \, \mathbf{v}_{\mathbf{k}} \, M_{\mathbf{k}\mathbf{k}'} \, \mathbf{v}_{\mathbf{k}'} \qquad \text{(E.8)} \\ &= \frac{1}{4} U^2 n(1-n) \, \frac{1}{(2\pi)^{4d}} \sum_{\mathbf{G}} \int d\mathbf{k_0} d\mathbf{k_1} d\mathbf{k_2} d\mathbf{k_3} \, \left(\mathbf{v}_{\mathbf{k_0}} + \mathbf{v}_{\mathbf{k_1}} - \mathbf{v}_{\mathbf{k_2}} - \mathbf{v}_{\mathbf{k_3}}\right)^2 \\ &\quad \times \delta\left(\mathbf{k}_0 + \mathbf{k}_1 - \mathbf{k}_2 - \mathbf{k}_3 + \mathbf{G}\right) \, \delta\left(\epsilon_{\mathbf{k}_0} + \epsilon_{\mathbf{k}_1} - \epsilon_{\mathbf{k}_2} - \epsilon_{\mathbf{k}_3}\right) \end{aligned}$$

E.2 Damping of the particle current

Let us now calculate the current-current matrix element $\langle v_k | M | v_k \rangle$ of the scattering matrix M for the linearization of the discrete Boltzmann equation (6.67) explicitly in $d = 1$. As we have shown before, this quantity determines the damping rate of the current mode $v_{\mathbf{k}}$.

As stated before, we only study the equation as a minimal model that describes the dynamics of interparticle scattering. It is a special constraint for a one-dimensional system to satisfy energy and momentum conservation at the same time. Trivially, scattering processes that simply exchange the incoming and outgoing momenta statisfy the energy and momentum constraint,

$$k_0, k_1 \to k_1, k_0 \qquad \text{(E.9)}$$

Obviously, this process does not lead to a damping of the particle current. Let us therefore address the question, which scattering processes can lead to relaxation to equilibrium.

For the discrete Boltzmann equation (6.67), the is a macroscopic number of scattering processes that satisfy energy and lattice momentum conservation, but also allow for a non-trivial change of the momentum states. This type of process is graphically depicted in Fig. (E.1): the scattering process is possible if the two momentum states before the collision are positioned *symetrically* around the momentum $\pi/2$ or $-\pi/2$. As a consequence, the sum of their kinetic energies adds up to zero, and their momenta add up to $\pm\pi$. This pair of states can now scatter in *any* other pair of momentum states that satisfies the same condition (of having zero total kinetic energy and a total momentum of $\pm\pi$).

Note that the number of states that can undergo this scattering process is suppressed by a factor $1/N$ due to the fine-tuning of the two momenta. However, the set of possible *final* states is proportional to N, where N is the number of discrete momenta. Therefore, the scattering process described above is relevant and survives for large values of N. Note that in a more physically realistic model, the outgoing momenta after the scattering event may eventually be determined by further conservation laws, which are not taken into account in the Boltzmann equation. We can now consider the discrete Botzmann equation and calculate the discrete variant of the matrix element of the collision kernel. Following Eq. (E.8) and adjusting the formula to the discrete Boltzmann Eq. (6.67), it is given by

$$\langle v_k | M | v_k \rangle = n(1-n) \frac{U^2}{4\,J\,N^2} \sum_{k_0, k_1, k_2} \left(v_{k_0} + v_{k_1} - v_{k_2} - v_{k_0+k_1-k_2}\right)^2 \delta(\epsilon_{k_0} + \epsilon_{k_1} - \epsilon_{k_2} - \epsilon_{k_0+k_1-k_2}) \qquad \text{(E.10)}$$

where $\delta(\epsilon) = \delta_{\epsilon,0}$ is the discrete (Kronecker) delta. Let us further simplify this sum. First, note that the two particles of a given pair of scattering partners must have the same velocity

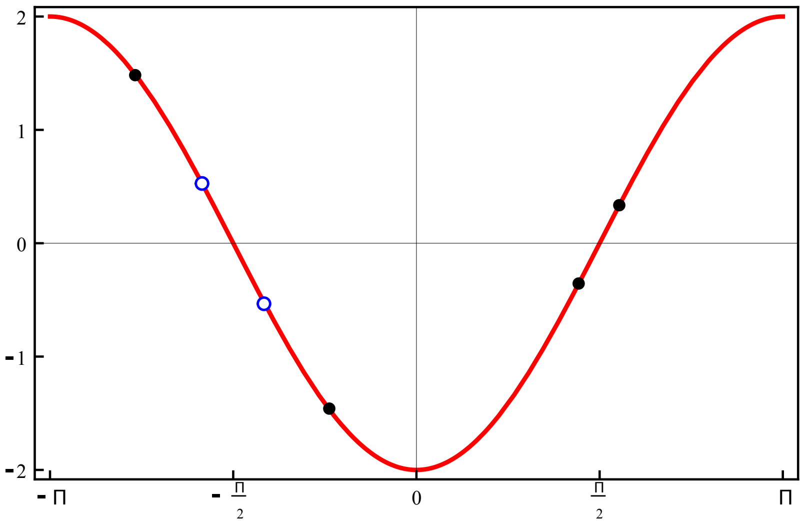

Figure E.1: Energy and momentum preserving scattering processes in 1D. The red curve shows the energy dispersion. The initial momentum states (blue circles) before scattering have to be centered around the momentum $\pm\pi/2$ in order to have vanishing total kinetic energy and total momentum $\pm\pi$. In order to satisfy energy and momentum conservation, they can scatter in *any* pair of final momentum states with vanishing total kinetic energy and total momentum $\pm\pi$ (pairs of black points as two examples for a continuum of possibilities).

before *and* after the collision, as

$$\begin{aligned} |k_0 + k_1| &= \pi \implies v_{k_1} = 2J\sin(k_1) = 2J\sin(\pm\pi - k_0) = 2J\sin(k_0) = v_{k_0} \\ v_{k_0+k_1-k_2} &= v_{\pm\pi-k_2} = v_{k_2} \end{aligned} \tag{E.11}$$

and which becomes also graphically apparent from Fig. (E.1). Now, using our knowledge about the possibility of scattering, we can simplify Eq. (E.10) and let the sum run only over those momenta that satisfy the energy and momentum constraint of scattering. From our above discussion, we know that $|k_0+k_1| = \pi$ must hold and leads to the only scattering process that can relax the current mode. Therefore, the discrete matrix element reduces to

$$\begin{aligned} \langle v_k|M|v_k\rangle &= n(1-n)\frac{U^2}{4\,J\,N^2}\sum_{k_0,k_1,k_2}(v_{k_0}+v_{k_1}-v_{k_2}-v_{k_0+k_1-k_2})^2\,\delta(|k_0+k_1|-\pi) \\ &\overset{(E.11)}{=} n(1-n)\frac{U^2}{4\,J\,N^2}\sum_{k_0,k_2}(2v_{k_0}-2v_{k_2})^2 \\ &\xrightarrow{N\gg 1} n(1-n)\frac{U^2}{4\,J}\frac{1}{4\pi^2}\int dk_0\,dk_2\,(2v_{k_0}-2v_{k_2})^2 \\ &= 4\,n(1-n)U^2\,J \end{aligned} \tag{E.12}$$

where we approximated the discrete sum in absence of the delta-constraint by a continuous integral. This approximation works very well, as we have also calculated the discrete matrix element $\langle v_k|M|v_k\rangle$ numerically using Eq. (E.10), and found excellent agreement with (E.12) already for $N = 20$.

E.3 Oscillatory integrals

The goal of this section is to provide some integral identities needed in chapter 6. As the force points into the diagonal direction of the lattice, the following identities hold:

$$\begin{aligned}
\epsilon_{\mathbf{k}-\mathbf{F}t} &= \epsilon_{\mathbf{k}}\,\cos(Ft) - v_{\mathbf{k}}\,\sin(Ft) \qquad \text{(E.13)}\\
v_{\mathbf{k}-\mathbf{F}t} &= v_{\mathbf{k}}\cos(Ft) + \epsilon_{\mathbf{k}}\,\sin(Ft)\\
\xi_{\mathbf{k},t} &= F^{-1}\left(\epsilon_{\mathbf{k}}\,\cos(Ft) - v_{\mathbf{k}}\,\sin(Ft) - \epsilon_{\mathbf{k}}\right)
\end{aligned}$$

Now, we can calculate

$$\begin{aligned}
\langle v_{\mathbf{k}}|\overline{M}|\epsilon_{\mathbf{k}}\rangle &= \frac{1}{\tau_B}\int d\mathbf{k}d\mathbf{k}'\,M_{\mathbf{k}\mathbf{k}'}\int_0^{\tau_B}dt\int_0^t dt'\,v_{\mathbf{k}+\mathbf{F}(t-t')}\,\epsilon_{\mathbf{k}-\mathbf{F}t'} \qquad \text{(E.14)}\\
&= \frac{1}{\tau_B}\int d\mathbf{k}d\mathbf{k}'\,v_{\mathbf{k}}\,M_{\mathbf{k}\mathbf{k}'}\,v_{\mathbf{k}'}\int_0^{\tau_B}dt\int_0^t dt'\,\left(-\sin(Ft')\cos(F(t-t'))\right)\\
&= \frac{1}{2\,F}\int d\mathbf{k}d\mathbf{k}'\,v_{\mathbf{k}}\,M_{\mathbf{k}\mathbf{k}'}\,v_{\mathbf{k}'}\\
&= \frac{1}{2\,F}\langle v_{\mathbf{k}}|M|v_{\mathbf{k}}\rangle \qquad \text{(E.15)}
\end{aligned}$$

where we have used the fact that $\int d\mathbf{k}'\,M_{\mathbf{k}\mathbf{k}'}\epsilon_{\mathbf{k}'} = 0$ and $\int d\mathbf{k}\,\epsilon_{\mathbf{k}}\,M_{\mathbf{k}\mathbf{k}'} = 0$. Similarly, we can calculate $\langle\epsilon_{\mathbf{k}}v_{\mathbf{k}}|\overline{M}|\epsilon_{\mathbf{k}}\rangle$. Applying the trigonometric identities (E.13) on $\epsilon_{\mathbf{k}+\mathbf{F}(t-t')}v_{\mathbf{k}+\mathbf{F}(t-t')}\epsilon_{\mathbf{k}-\mathbf{F}t'}$ and doing the time integration results is a collection of terms, each one of them being proportional to one of the following integrals:

$$\begin{aligned}
0 &= \int_0^{\tau_B}dt\int_0^t dt'\,\sin\left(Ft'\right)\sin\left(Ft-Ft'\right)\cos\left(Ft-Ft'\right) \qquad \text{(E.16)}\\
0 &= \int_0^{\tau_B}dt\int_0^t dt'\,\sin\left(Ft'\right)\cos^2\left(Ft-Ft'\right)\\
0 &= \int_0^{\tau_B}dt\int_0^t dt'\,\sin\left(Ft'\right)\sin^2\left(Ft-Ft'\right)\\
0 &= \int_0^{\tau_B}dt\int_0^t dt'\,\sin\left(Ft-Ft'\right)\cos\left(Ft'\right)\cos\left(Ft-Ft'\right)\\
0 &= \int_0^{\tau_B}dt\int_0^t dt'\,\cos\left(Ft'\right)\cos^2\left(Ft-Ft'\right)\\
0 &= \int_0^{\tau_B}dt\int_0^t dt'\,\sin^2\left(Ft-Ft'\right)\cos\left(Ft'\right)
\end{aligned}$$

As each integral vanishes, we find that $\langle\epsilon_{\mathbf{k}}v_{\mathbf{k}}|\overline{M}|\epsilon_{\mathbf{k}}\rangle = 0$.

Now, let us proceed in calculating the matrix elements involving $\overline{\overline{M}}$, which we need to calculate the diffusion constant (6.84). First of all, note that $\langle v_{\mathbf{k}+\mathbf{F}(t-t')}|M_{\mathbf{k}\mathbf{k}'}\xi_{\mathbf{k},t'}|1\rangle = 0$

because of $\int d\mathbf{k}' M_{\mathbf{k}\mathbf{k}'} = 0$. Therefore, we omit $\xi_{\mathbf{k},t'}$ in Eq. (6.86) and calculate

$$\begin{aligned}
\langle v_{\mathbf{k}}|\overline{\overline{M}}|1\rangle &\overset{(6.86)}{=} \frac{1}{\tau_B}\int_0^{\tau_B} dt \int_0^t dt' \int \frac{d\mathbf{k}d\mathbf{k}'}{(4\pi^2)^d}\, v_{\mathbf{k}+\mathbf{F}(t-t')}\, M_{\mathbf{k}\mathbf{k}'}\, \xi_{\mathbf{k}',t'} \\
&\overset{(6.87)}{=} \int \frac{d\mathbf{k}d\mathbf{k}'}{(4\pi^2)^d}\, v_{\mathbf{k}}\, M_{\mathbf{k}\mathbf{k}'}\, v_{\mathbf{k}'} \left(\frac{1}{\tau_B}\int_0^{\tau_B} dt \int_0^t dt'(-1)F^{-1} \sin\left(Ft'\right) \cos\left(F\left(t-t'\right)\right)\right) \\
&= \int \frac{d\mathbf{k}d\mathbf{k}'}{(4\pi^2)^d}\, v_{\mathbf{k}}\, M_{\mathbf{k}\mathbf{k}'}\, v_{\mathbf{k}'}\, \frac{1}{\tau_B}\int_0^{\tau_B} dt\, \frac{-t\,\sin(Ft)}{2\,F} \\
&= \frac{\pi}{F^3}\frac{1}{\tau_B}\int \frac{d\mathbf{k}d\mathbf{k}'}{(4\pi^2)^d}\, v_{\mathbf{k}}\, M_{\mathbf{k}\mathbf{k}'}\, v_{\mathbf{k}'} \\
&= \frac{1}{2\,F^2}\,\langle v_{\mathbf{k}}|M|v_{\mathbf{k}}\rangle
\end{aligned} \tag{E.17}$$

where again we omitted terms that are zero due to the identities $\int d\mathbf{k}'\, M_{\mathbf{k}\mathbf{k}'}\epsilon_{\mathbf{k}'} = 0$ and $\int d\mathbf{k}\, \epsilon_{\mathbf{k}}\, M_{\mathbf{k}\mathbf{k}'} = 0$. We can proceed in exactly the same way to calculate also the other three matrix elements in Eq. (6.84).

Bibliography

[1] R. Feynman. “Simulating physics with computers.” International Journal of Theoretical Physics **21**, 467–488 (1982). ISSN 0020-7748. 10.1007/BF02650179.

[2] R. Jördens, *et al.* “A Mott insulator of fermionic atoms in an optical lattice.” Nature **455**, 204–207 (2008).

[3] U. Schneider, *et al.* “Metallic and Insulating Phases of Repulsively Interacting Fermions in a 3D Optical Lattice.” Science **322**, 1520–1525 (2008).

[4] G. Roati, *et al.* “Anderson localization of a non-interacting Bose-Einstein condensate.” Nature **453**, 895–898 (2008).

[5] Y.-J. Lin, *et al.* “Synthetic magnetic fields for ultracold neutral atoms.” Nature **462**, 628–632 (2009).

[6] M. W. Zwierlein, *et al.* “Vortices and superfluidity in a strongly interacting Fermi gas.” Nature **435**, 1047–1051 (2005).

[7] P. Mehta and N. Andrei. “Nonequilibrium Transport in Quantum Impurity Models: The Bethe Ansatz for Open Systems.” Phys. Rev. Lett. **96**, 216802 (2006).

[8] A. Rosch, J. Kroha, and P. Wölfle. “Kondo Effect in Quantum Dots at High Voltage: Universality and Scaling.” Phys. Rev. Lett. **87**, 156802 (2001).

[9] A. Mitra and A. Rosch. “Current-Induced Decoherence in the Multichannel Kondo Problem.” Phys. Rev. Lett. **106**, 106402 (2011).

[10] M. Eckstein, T. Oka, and P. Werner. “Dielectric Breakdown of Mott Insulators in Dynamical Mean-Field Theory.” Phys. Rev. Lett. **105**, 146404 (2010).

[11] F. Queisser, P. Navez, and R. Schützhold. “Sauter-Schwinger like tunneling in tilted Bose-Hubbard lattices in the Mott phase.” arXiv:1107.3730v1 (2011).

[12] M. Greiner, O. Mandel, T. Hánsch, and I. Bloch. “Collapse and revival of the matter wave field of a Bose-Einstein condensate.” Nature **419**, 51–54 (2002).

[13] T. Kinoshita, T. Wenger, and D. S. Weiss. “A quantum Newton’s cradle.” Nature **440**, 900–903.

[14] I. Bloch, J. Dalibard, and W. Zwerger. “Many-body physics with ultracold gases.” Reviews of Modern Physics **80**, 885 (2008).

[15] N. W. Ashcroft and D. N. Mermin. *Solid state physics* (Thomson Learning, 1976).

[16] U. Schneider. *Interacting Fermionic Atoms in Optical Lattices - A Quantum Simulator for Condensed Matter Physics* (PhD thesis, Mainz, 2010).

[17] L. Landau and E. Lifshitz. *Quantum mechanics: non-relativistic theory* (Butterworth-Heinemann, 1977). ISBN 9780750635394.

[18] W. Zwerger. *The BCS-BEC Crossover and the Unitary Fermi Gas.* Lecture Notes in Physics (Springer Verlag, 2011). ISBN 9783642219771.

[19] H. Feshbach. Ann. Phys. **5**, 337 (1958).

[20] E. Tiesinga, B. J. Verhaar, and H. T. C. Stoof. "Threshold and resonance phenomena in ultracold ground-state collisions." Phys. Rev. A **47**, 4114–4122 (1993).

[21] S. Inouye, *et al.* "Stability of Spin-Aligned Hydrogen at Low Temperatures and High Magnetic Fields: New Field-Dependent Scattering Resonances and Predissociations." Nature **392**, 151–154 (1998).

[22] J. L. Roberts, *et al.* "Resonant Magnetic Field Control of Elastic Scattering in Cold ^{85}Rb." Phys. Rev. Lett. **81**, 5109–5112 (1998).

[23] P. Courteille, *et al.* "Observation of a Feshbach Resonance in Cold Atom Scattering." Phys. Rev. Lett. **81**, 69–72 (1998).

[24] V. Vuletić, A. J. Kerman, C. Chin, and S. Chu. "Observation of Low-Field Feshbach Resonances in Collisions of Cesium Atoms." Phys. Rev. Lett. **82**, 1406–1409 (1999).

[25] T. Köhler, K. Góral, and P. S. Julienne. "Production of cold molecules via magnetically tunable Feshbach resonances." Rev. Mod. Phys. **78**, 1311–1361 (2006).

[26] R. Grimm, M. Weidemüller, and Y. B. Ovchinnikov. Advances in Atomic, Molecular and Optical Physics **42**, 95–170 (2000).

[27] J. Hubbard. "Electron Correlations in Narrow Energy Bands." Proceedings of the Royal Society of London. Series A, Mathematical and Physical Sciences **276**, pp. 238–257 (1963).

[28] F. Gebhard. *The mott metal-insulator transition: models and methods.* Springer tracts in modern physics (Springer, 1997). ISBN 9783540614814.

[29] F. Essler. *The one-dimensional Hubbard model.* The One-dimensional Hubbard Model (Cambridge University Press, 2005). ISBN 9780521802628.

[30] J. M. Ziman. *Electrons and Phonons* (Oxford University Press, New York, 1960).

[31] L. Boltzmann. "Weitere Studien über das Wärmegleichgewicht unter Gasmolekülen." Wiener Berichte **66**, 275–370 (1872).

[32] J. Negele and H. Orland. *Quantum many-particle systems.* Advanced Books Classics (Perseus Books, 1998). ISBN 9780738200521.

[33] A. Garg, D. Rasch, E. Shimshoni, and A. Rosch. "Large Violation of the Wiedemann-Franz Law in Luttinger Liquids." Phys. Rev. Lett. **103**, 096402 (2009).

[34] J. Rammer and H. Smith. “Quantum field-theoretical methods in transport theory of metals.” Rev. Mod. Phys. **58**, 323–359 (1986).

[35] L. Fritz, J. Schmalian, M. Müller, and S. Sachdev. “Quantum critical transport in clean graphene.” Phys. Rev. B **78**, 085416 (2008).

[36] D. Forster. *Hydrodynamic Fluctuations, Broken Symmetry, and Correlation Functions* (Frontiers in Physics. W. A. Benjamin, Reading, 1975).

[37] J. Rammer. *Quantum transport theory.* Frontiers in physics (Perseus Books, 1998). ISBN 9780738200484.

[38] U. Schollwöck. “The density-matrix renormalization group.” Rev. Mod. Phys. **77**, 259–315 (2005).

[39] A. J. Daley, C. Kollath, U. Schollwöck, and G. Vidal. “Time-dependent density-matrix renormalization-group using adaptive effective Hilbert spaces.” Journal of Statistical Mechanics: Theory and Experiment **2004**, P04005 (2004).

[40] S. R. Manmana, A. Muramatsu, and R. M. Noack. “Time evolution of one-dimensional Quantum Many Body Systems.” AIP Conf. Proc. **789**, 269–278 (2005).

[41] S. R. Manmana, S. Wessel, R. M. Noack, and A. Muramatsu. “Strongly Correlated Fermions after a Quantum Quench.” Phys. Rev. Lett. **98**, 210405 (2007).

[42] M. Rigol, V. Dunjko, and M. Olshanii. “Thermalization and its mechanism for generic isolated quantum systems.” Nature **452**, 854 (2008).

[43] S. R. Manmana, S. Wessel, R. M. Noack, and A. Muramatsu. “Time evolution of correlations in strongly interacting fermions after a quantum quench.” Phys. Rev. B **79**, 155104 (2009).

[44] P. Barmettler, *et al.* “Relaxation of Antiferromagnetic Order in Spin-1/2 Chains Following a Quantum Quench.” Phys. Rev. Lett. **102**, 130603 (2009).

[45] M. Cheneau, *et al.* “Light-cone-like spreading of correlations in a quantum many-body system.” arXiv:1111.0776v1 (2011).

[46] F. Heidrich-Meisner, *et al.* “Quantum distillation: Dynamical generation of low-entropy states of strongly correlated fermions in an optical lattice.” Phys. Rev. A **80**, 041603 (2009).

[47] S. Langer, M. Heyl, I. P. McCulloch, and F. Heidrich-Meisner. “Real-time energy dynamics in spin-$\frac{1}{2}$ Heisenberg chains.” Phys. Rev. B **84**, 205115 (2011).

[48] A. E. Feiguin and D. A. Huse. “Spectral properties of a partially spin-polarized one-dimensional Hubbard/Luttinger superfluid.” Phys. Rev. B **79**, 100507 (2009).

[49] R. W. Helmes, T. A. Costi, and A. Rosch. “Mott Transition of Fermionic Atoms in a Three-Dimensional Optical Trap.” Phys. Rev. Lett. **100**, 056403 (2008).

[50] M. Eckstein, M. Kollar, and P. Werner. “Thermalization after an Interaction Quench in the Hubbard Model.” Phys. Rev. Lett. **103**, 056403 (2009).

[51] M. Eckstein and P. Werner. “Damping of Bloch Oscillations in the Hubbard Model.” Phys. Rev. Lett. **107**, 186406 (2011).

[52] E. Gull, *et al.* “Continuous-time Monte Carlo methods for quantum impurity models.” Rev. Mod. Phys. **83**, 349–404 (2011).

[53] M. Schiró. “Real-time dynamics in quantum impurity models with diagrammatic Monte Carlo.” Phys. Rev. B **81**, 085126 (2010).

[54] M. Schiró and M. Fabrizio. “Quantum quenches in the Hubbard model: Time-dependent mean-field theory and the role of quantum fluctuations.” Phys. Rev. B **83**, 165105 (2011).

[55] A. Griffin, T. Nikuni, and E. Zaremba. *Bose-condensed gases at finite temperatures* (Cambridge University Press, 2009). ISBN 9780521837026.

[56] D. Rasch. *Transport Theory in Low Dimensional Systems* (PhD thesis, Cologne, 2010).

[57] W. H. Press, S. A. Teukolsky, W. T. Vetterling, and B. P. Flannery. *Numerical recipes in C (2nd ed.): the art of scientific computing* (Cambridge University Press, New York, NY, USA, 1992). ISBN 0-521-43108-5.

[58] H. Mori. “Transport, collective motion, and brownian motion.” Prog. Theor. Phys. p. 423 (1965).

[59] R. Zwanzig. *Lectures in Theoretical Physics, vol 3* (Interscience, New York, 1961).

[60] E. Shimshoni, *et al.* “Large thermomagnetic effects in weakly disordered Heisenberg chains.” Phys. Rev. B **79**, 064406 (2009).

[61] D. Belitz. “Electronic transport in slids: the resolvent method revisited.” Solid State Phys. p. 2735 (1984).

[62] P. Jung and A. Rosch. “Lower bounds for the conductivities of correlated quantum systems.” Phys. Rev. B **75**, 245104 (2007).

[63] S. Mandt, A. Rapp, and A. Rosch. “Interacting Fermionic Atoms in Optical Lattices Diffuse Symmetrically Upwards and Downwards in a Gravitational Potential.” Phys. Rev. Lett. **106**, 250602 (2011).

[64] G. S. Ohm. *Die galvanische Kette, mathematisch bearbeitet* (Berlin, 1827).

[65] P. Drude. “Zur Elektronentheorie der Metalle.” Annalen der Physik **306**, 566 – 613 (1900).

[66] F. Bloch. Z. Phys. **52**, 555 (1929).

[67] M. Rigol, V. Dunjko, and M. Olshanii. “Thermalization and its mechanism for generic isolated quantum systems.” Nature **452**, 854 (2008).

[68] A. Sommer, M. Ku, G. Roati, and M. W. Zwierlein. “Universal spin transport in a strongly interacting Fermi gas.” Nature **472**, 201–204 (2011).

[69] A. Rosch, D. Rasch, B. Binz, and M. Vojta. "Metastable Superfluidity of Repulsive Fermionic Atoms in Optical Lattices." Phys. Rev. Lett. **101**, 265301 (2008).

[70] R. Sensarma, *et al.* "Lifetime of double occupancies in the Fermi-Hubbard model." Phys. Rev. B **82**, 224302 (2010).

[71] T. Oka and H. Aoki. "Ground-State Decay Rate for the Zener Breakdown in Band and Mott Insulators." Phys. Rev. Lett. **95**, 137601 (2005).

[72] S. Langer, *et al.* "Ballistic dynamics during the sudden expansion of a two-component Fermi gas in a one-dimensional lattice." ArXiv p. 1109.4364 (2011).

[73] H. Lignier, *et al.* "Dynamical Control of Matter-Wave Tunneling in Periodic Potentials." Phys. Rev. Lett. **99**, 220403 (2007).

[74] M. Ben Dahan, *et al.* "Bloch Oscillations of Atoms in an Optical Potential." Phys. Rev. Lett. **76**, 4508–4511 (1996).

[75] C. D. Fertig, *et al.* "Strongly Inhibited Transport of a Degenerate 1D Bose Gas in a Lattice." Phys. Rev. Lett. **94**, 120403 (2005).

[76] M. Gustavsson, *et al.* "Control of Interaction-Induced Dephasing of Bloch Oscillations." Physical Review Letters **100**, 080404 (2008).

[77] M. Fattori, *et al.* "Atom Interferometry with a Weakly Interacting Bose-Einstein Condensate." Physical Review Letters **100**, 080405 (2008).

[78] L. Pezzè, *et al.* "Insulating Behavior of a Trapped Ideal Fermi Gas." Physical Review Letters **93**, 120401 (2004).

[79] H. Ott, *et al.* "Collisionally Induced Transport in Periodic Potentials." Physical Review Letters **92**, 160601 (2004).

[80] N. Strohmaier, *et al.* "Interaction-Controlled Transport of an Ultracold Fermi Gas." Phys. Rev. Lett. **99**, 220601 (2007).

[81] U. Schneider, *et al.* "Fermionic transport and out-of-equilibrium dynamics in a homogeneous Hubbard model with ultracold atoms." Nature Physics **8**, 213–218 (2012).

[82] J. Vázquez. *Smoothing and decay estimates for nonlinear diffusion equations: equations of porous medium type.* Oxford lecture series in mathematics and its applications (Oxford University Press, 2006). ISBN 9780199202973.

[83] G. Barenblatt. "On some unsteady flows of fluids and gases in porous media." Akad. Nauk SSSR. Prikl. Mat. Meh. **16**, 679 (1952).

[84] A. Rapp, S. Mandt, and A. Rosch. "Equilibration Rates and Negative Absolute Temperatures for Ultracold Atoms in Optical Lattices." Phys. Rev. Lett. **105**, 220405 (2010).

[85] D. Shiga. "How to create temperatures below absolute zero." New Scientist p. 15 (2010).

[86] E. M. Purcell and R. V. Pound. "A Nuclear Spin System at Negative Temperature." Phys. Rev. **81**, 279–280 (1951).

[87] P. J. Hakonen, K. K. Nummila, R. T. Vuorinen, and O. V. Lounasmaa. "Observation of nuclear ferromagnetic ordering in silver at negative nanokelvin temperatures." Phys. Rev. Lett. **68**, 365–368 (1992).

[88] A. S. Oja and O. V. Lounasmaa. "Nuclear magnetic ordering in simple metals at positive and negative nanokelvin temperatures." Rev. Mod. Phys. **69**, 1–136 (1997).

[89] A. P. Mosk. "Atomic Gases at Negative Kinetic Temperature." Phys. Rev. Lett. **95**, 040403 (2005).

[90] P. Medley, *et al.* "Spin Gradient Demagnetization Cooling of Ultracold Atoms." Phys. Rev. Lett. **106**, 195301 (2011).

[91] A. Rapp. "Quantum Simulators at Negative Absolute Temperatures." arXiv:cond-mat/1112.4299 (2011).

[92] S. Taie, *et al.* "Realization of a SU(2) System of Fermions in a Cold Atomic Gas." Phys. Rev. Lett. **105**, 190401 (2010).

[93] A. Rapp, G. Zaránd, C. Honerkamp, and W. Hofstetter. "Color Superfluidity and "Baryon" Formation in Ultracold Fermions." Phys. Rev. Lett. **98**, 160405 (2007).

[94] L. Landau and E. Lifshitz. *Statistical physics ; 1.* Course of theoretical physics / by L. D. Landau and E. M. Lifshitz (Pergamon Press, 1980). ISBN 9780080230399.

[95] C. Kittel and H. Kroemer. *Thermal physics* (W. H. Freeman, 1980). ISBN 9780716710882.

[96] F. Bloch. Z. Phys. **52**, 555 (1928).

[97] C. Waschke, *et al.* "Coherent submillimeter-wave emission from Bloch oscillations in a semiconductor superlattice." Phys. Rev. Lett. **70**, 3319–3322 (1993).

[98] T. Pertsch, *et al.* "Optical Bloch Oscillations in Temperature Tuned Waveguide Arrays." Phys. Rev. Lett. **83**, 4752–4755 (1999).

[99] B. P. Anderson and M. A. Kasevich. "Macroscopic Quantum Interference from Atomic Tunnel Arrays." Science **282**, 1686–1689 (1998).

[100] T. Salger, *et al.* "Bloch oscillations of a Bose-Einstein condensate in a subwavelength optical lattice." Phys. Rev. A **79**, 011605 (2009).

[101] R. Battesti, *et al.* "Bloch Oscillations of Ultracold Atoms: A Tool for a Metrological Determination of h/m." Phys. Rev. Lett. **92**, 253001 (2004).

[102] O. Morsch, *et al.* "Bloch Oscillations and Mean-Field Effects of Bose-Einstein Condensates in 1D Optical Lattices." Phys. Rev. Lett. **87**, 140402 (2001).

[103] M. Schecter, D. Gangardt, and A. Kamenev. "Dynamics and Bloch oscillations of mobile impurities in one-dimensional quantum liquids." Annals of Physics **327**, 639 – 670 (2012). ISSN 0003-4916.

[104] J. K. Freericks, V. M. Turkowski, and V. Zlatić. "Nonequilibrium Dynamical Mean-Field Theory." Phys. Rev. Lett. **97**, 266408 (2006).

[105] A. V. Joura, J. K. Freericks, and T. Pruschke. "Steady-State Nonequilibrium Density of States of Driven Strongly Correlated Lattice Models in Infinite Dimensions." Phys. Rev. Lett. **101**, 196401 (2008).

[106] A. V. Ponomarev, J. Madronero, A. R. Kolovsky, and A. Buchleitner. "Atomic Current across an Optical Lattice." Physical Review Letters **96**, 050404 (2006).

[107] M. Mierzejewski and P. Prelovsek. "Nonlinear Current Response of an Isolated System of Interacting Fermions." Phys. Rev. Lett. **105**, 186405 (2010).

[108] A. R. Kolovsky, A. V. Ponomarev, and H. J. Korsch. "Damped Bloch oscillations of cold atoms in optical lattices." Phys. Rev. A **66**, 053405 (2002).

[109] A. R. Kolovsky. "New Bloch Period for Interacting Cold Atoms in 1D Optical Lattices." Phys. Rev. Lett. **90**, 213002 (2003).

[110] A. V. Ponomarev. *Dynamics of cold Fermi atoms in one-dimensional optical lattices* (PhD thesis, Freiburg, 2008).

[111] A. Amaricci, C. Weber, M. Capone, and G. Kotliar. "Non-equilibrium dynamics of the driven Hubbard model." arXiv:1106.3483v2 (2011).

[112] A. Asamitsu, Y. Tomioka, H. Kuwahara, and Y. Tokura. "Current switching of resistive states in magnetoresistive manganites." Nature **388**, 50–52 (1997).

[113] B. Wu, *et al.* "Electric-field-driven phase transition in vanadium dioxide." Phys. Rev. B **84**, 241410 (2011).

[114] T. Fukui and N. Kawakami. "Breakdown of the Mott insulator: Exact solution of an asymmetric Hubbard model." Phys. Rev. B **58**, 16051–16056 (1998).

[115] T. Oka, R. Arita, and H. Aoki. "Breakdown of a Mott Insulator: A Nonadiabatic Tunneling Mechanism." Phys. Rev. Lett. **91**, 066406 (2003).

[116] F. Heidrich-Meisner, *et al.* "Nonequilibrium electronic transport in a one-dimensional Mott insulator." Phys. Rev. B **82**, 205110 (2010).

[117] A. R. Kolovsky, E. A. Gómez, and H. J. Korsch. "Bose-Einstein condensates on tilted lattices: Coherent, chaotic, and subdiffusive dynamics." Phys. Rev. A **81**, 025603 (2010).

[118] D. O. Krimer, R. Khomeriki, and S. Flach. "Delocalization and spreading in a nonlinear Stark ladder." Phys. Rev. E **80**, 036201 (2009).

[119] L. Erdős, B. Schlein, and H.-T. Yau. "Rigorous Derivation of the Gross-Pitaevskii Equation." Phys. Rev. Lett. **98**, 040404 (2007).

[120] L. Landau. "The theory of superfluidity of helium II." J. Phys. USSR **5**, 71 (1941).

[121] T. R. Kirkpatrick and J. R. Dorfman. "Transport in a dilute but condensed nonideal Bose gas: Kinetic equations." Journal of Low Temperature Physics **58**, 301–331 (1985). ISSN 0022-2291. 10.1007/BF00681309.

[122] E. Zaremba, T. Nikuni, and A. Griffin. “Dynamics of Trapped Bose Gases at Finite Temperatures.” Journal of Low Temperature Physics **116**, 277–345 (1999). ISSN 0022-2291. 10.1023/A:1021846002995.

[123] L. Landau and E. Lifshitz. *Mechanics.* Course of theoretical physics (Butterworth-Heinemann, 1976).

[124] H. J. C. von Grimmelshausen. *Der Abentheuerliche Simplicissimus Teutsch* (Nürnberg, 1669).

Danksagung

Abenteüerlicher Simpliciſsimus.
Ich ward gleich wie Phoenix durchs Feüer geboren
Ich flog durch die Lüffte? ward doch nicht verloren
Ich wandert im waßer ich ſtreiffte zu Land,
in ſolchem Umſchwermen macht ich mir bekant
was oft mich betrübet und ſelten ergetzet.
was war das? Ich habs in dies Buch hier geſetzt
Damit ſich der Leſer gleich wie ich itzt thu,
entferne der Torheit, und Lebe in Ruh.

Titelkupfer des "Simplicissimus" [124], Nürnberg 1669

Zum Abschluss möchte ich mich gerne bei allem langjährigen Wegbegleitern meiner Dissertation bedanken. Ein besonderer Dank gilt Prof. Achim Rosch, der mit seinem fachlichen und außerfachlichen Rat sehr zum Erfolg der Arbeit, einer spannenden Zeit und einer kollegialen **G**ruppenatmosphäre beigetragen hat. Bei den Professoren Alexander Altland, Dieter Meschede, Jan Jolie und Martin Zirnbauer möchte ich mich für ein langjähriges Coaching im **R**ahmen der Bonn-Cologne Graduate School bedanken, sowie bei Petra Neubauer-Günther für ihr besonderes Engagement im Rahmen der BCGS. **I**ch danke Prof. **V**ictor Gurarie und Salvatore Manmana für das Ermöglichen eines Aufenthalts und eine erlebnisreiche Zeit an der University of Colorado. Ausserdem möchte ich mich besonders bei meinen Ko-Autoren David Rasch, Ulrich Schneider und Akos Rapp für die schöne Zeit und die gute und spannende Zusammenarbeit bedanken. Meinen Kollegen und Freunden in meiner Arbeitsgruppe und im gesamten Fachbereich Physik danke ich für eine tolle Zusammenarbeit und Freundschaft, darunter Mario Zacharias, **L**ucas Hollender, Alexander Wollny, Julia Reul, Carolin Küppersbusch, Andrej Fischer, Heidrun Weber, Norbert Braun, Philipp Carlhoff, Christian Glück, Tobias Meng, Christoph Schütte, Sebastian Schmittner, **L**ars Fritz, Karin Everschor, Matthias Sitte, Markus Garst, Karen Rodriguez, Michael Becker, Andrew Mitchell, Jonathan Lux und **E**tienne Gärtner. Ein besonderer Dank gilt meinen Eltern für ihre Unterstützung. Ganz besonders danke ich **C**hristina.

Erklärung

Ich versichere, dass ich die von mir vorgelegte Dissertation selbständig angefertigt, die benutzten Quellen und Hilfsmittel vollständig angegeben und die Stellen der Arbeit – einschließlich Tabellen, Karten und Abbildungen –, die anderen Werken im Wortlaut oder dem Sinn nach entnommen sind, in jedem Einzelfall als Entlehnung kenntlich gemacht habe; dass diese Dissertation noch keiner anderen Fakultät oder Universität zur Prüfung vorgelegen hat; dass sie – abgesehen von unten angegebenen Teilpublikationen – noch nicht veröffentlicht worden ist sowie, dass ich eine solche Veröffentlichung vor Abschluss des Promotionsverfahrens nicht vornehmen werde. Die Bestimmungen der Promotionsordnung sind mir bekannt. Die von mir vorgelegte Dissertation ist von Prof. Dr. Achim Rosch betreut worden.

Teilpublikationen:

- U. Schneider, L. Hackermüller, J. P. Ronzheimer, S. Will, S. Braun, T. Best, I. Bloch, E. Demler, S. Mandt, D. Rasch, and A. Rosch, *Fermionic transport and out-of-equilibrium dynamics in a homogeneous Hubbard model with ultracold atoms*, Nature Physics 8, 213-218 (2012).
- S. Mandt, A. Rapp, and A. Rosch, *Interacting Fermionic Atoms in Optical Lattices Diffuse Symmetrically Upwards and Downwards in a Gravitational Potential*, Phys. Rev. Lett. 106, 250602 (2011).
- A. Rapp, S. Mandt, and A. Rosch, *Equilibration Rates and Negative Absolute Temperatures for Ultracold Atoms in Optical Lattices*, Phys. Rev. Lett. 105, 220405 (2010).
- S. Mandt and M.R. Zirnbauer, *Zooming in on local level statistics by supersymmetric extension of free probability*, J. Phys. A 43 025201 (2010).

Stephan Mandt

Lebenslauf

Persönliche Daten

Geburtsdatum	31. Juli 1982
Geburtsort	Köln
Famillienstand	verheiratet

Werdegang

Seit 11/2008	**Promotion**, *Institut für Theoretische Physik, Universität zu Köln*, Betreuer: Prof. Dr. Achim Rosch.
8-12/2010	**University of Colorado**, *Boulder*, Forschungsaufenthalt.
2002-2008	**Diplomstudium Physik**, *Universität zu Köln*, Gesamtnote: "mit Auszeichnung", Diplomarbeit: "Superbosonization applied to non-Gaussian random matrix ensembles", Betreuer: Prof. Dr. Martin Zirnbauer.
2006	Vordiplom Mathematik
2001 - 2002	**Zivildienst**, *Zentren für Senioren und Behinderte der Stadt Köln*.
1993-2001	**J.-G.-Herder Gymnasium in Köln**, *Abitur*, Gesamtnote: 1,0 kürzere Schulzeit durch Überspringen eines Schuljahres.

Stipendien

2010-2012	**Studienstiftung des deutschen Volkes**.
2007-2011	**Bonn-Cologne Graduate School of Physics and Astronomy**.

Lehrerfahrung

2008 - 2012	**Übungsgruppenleiter**, *Institut für Theoretischer Physik, Köln*, Computerphysik, Klassische Mechanik, Elektrodynamik, Quantenmechanik, Statistische Physik, Quantenfeldtheorie I & II.

Ausgewählte Gastvorträge

2011	**Heidelberg**, *Ultracold fermionic atoms in optical lattices out of equilibrium: Hydrodynamics and beyond*, Finite-Temperature Non-Eq. Superfluid Systems (invited talk).
2011	**LMU München**, *Nonlinear dynamics of strongly interacting quantum fields*, Projektbericht im Rahmen des Verlängerungsantrags des SFB/TR 12.
2010	**JILA**, *Breakdown of diffusion, equilibration rates and negative absolute temperatures*, atom and molecular optics seminar, University of Colorado at Boulder.
2010	**Colorado und Wyoming**, *Breakdown of diffusion, equilibration rates and negative absolute temperatures*, Seminare der theoretischen Festkörperphysik, University of Wyoming (Laramie) und University of Colorado (Boulder).
2010	**Ecole Polytechnique**, *Breakdown of diffusion for ultracold atoms in optical lattices*, Seminar der theoretischen Festkörperphysik (Palaiseau Cedex).
2009	**Sonderforschungsbereich TR 12**, *Superbosonization applied to non-Gaussian random matrix ensembles*, Physikzentrum Bad Honnef.